ADVANCED STEEL CONSTRUCTION

An International Journal

Volume 21 Number 6

December 2025

CONTENTS

Website: *http://www.hkisc.org*
ISSN 1816-112X
Science Citation Index Expanded, Materials Science Citation Index and ISI Alerting
Cover: Greater Bay Area Cultural and Sports Center, China. Photo@ Li Hua-Bo
e-copy of IJASC is free to download at "www.ascjournal.com" in internet and mobile apps.

ADVANCED STEEL CONSTRUCTION

VOL.21, NO.6 (2025)

ADVANCED STEEL CONSTRUCTION

an International Journal

ISSN 1816-112X

Volume 21 Number 6 *December 2025*

ISSN 1816-112X

Science Citation Index Expanded, Materials Science Citation Index and ISI Alerting

Advanced Steel Construction
an international journal

Cover: Greater Bay Area Cultural and Sports Center, China. Photo@ Li Hua-Bo
e-copy of IJASC is free to download at "www.ascjournal.com" in internet and mobile apps.

General Information
Advanced Steel Construction, an international journal

Aims and scope

The International Journal of Advanced Steel Construction provides a platform for the publication and rapid dissemination of original and up-to-date research and technological developments in steel construction, design and analysis. Scope of research papers published in this journal includes but is not limited to theoretical and experimental research on elements, assemblages, systems, material, design philosophy and codification, standards, fabrication, projects of innovative nature and computer techniques. The journal is specifically tailored to channel the exchange of technological know-how between researchers and practitioners. Contributions from all aspects related to the recent developments of advanced steel construction are welcome.

Subscription inquiries and change of address. Address all subscription inquiries and correspondence to Member Records, IJASC. Notify an address change as soon as possible. All communications should include both old and new addresses with zip codes and be accompanied by a mailing label from a recent issue. Allow six weeks for all changes to become effective.

The Hong Kong Institute of Steel Construction
HKISC
c/o Prof. SL Chan,
Unit 209B, Photonics Centre, No. 2 Science Park East Avenue,
Hong Kong Science Park, Shatin, N.T., Hong Kong, China.
Tel: 852- 3595 6150 Fax: 852- 3619 7238
Email: ceslchan@connect.polyu.hk Website: *http://www.hkisc.org/*
ISSN 1816-112X
Science Citation Index Expanded, Materials Science Citation Index and ISI Alerting

ISSN 1816-112X

Science Citation Index Expanded, Materials Science Citation Index and ISI Alerting

Advanced Steel Construction
an international journal

VOLUME 21 NUMBER 6 December 2025

Technical Papers

Advanced Steel Construction – Vol. 21 No. 6 (2025) 476–487
DOI:10.18057/IJASC.2025.21.6.1

EVALUATION METHOD FOR MECHANICAL PROPERTIES OF CORRODED ANGLE STEEL IN TRANSMISSION TOWERS

Wen-Qiang Jiang [1, 2, 3, *], Heng Zhang [1], Tong-Tong Dai [1, 2, 3], Yu-Cheng Guo [1] and Yue-Ming Zhong [1]

[1] *Department of Mechanical Engineering, North China Electric Power University, Baoding, China*
[2] *Hebei Engineering Research Center for Advanced Manufacturing & Intelligent Operation and Maintenance of Electric Power Machinery，North China Electric Power University, Baoding, China*
[3] *Hebei Key Laboratory of Electric Machinery Health Maintenance & Failure Prevention, North China Electric Power University, Baoding 071003, China*
** (Corresponding author: E-mail: wenqiang.jiang@ncepu.edu.cn)*

ABSTRACT

Corrosion inevitably exists in transmission towers that have been in long-term field service. In order to study the corrosion properties of tower angle steel, the corroded steel specimens were prepared by accelerated corrosion test in this research. Combined with surface roughness and tensile test of the corroded specimens, the corrosion process of the steel specimens was explored, the degradation law of mechanical properties of the corrosion specimens was analyzed. Then, a method for estimating the corrosion rate of steel members by residual thickness was proposed. Moreover, the relationship between mechanical properties of corroded steel members and corrosion rate and surface roughness was established. The results show that the corrosion rate, the maximum pit depth and the maximum pit depth to width ratio are highly correlated with the strength degradation of corroded specimens. It is most effective to evaluate the strength of the specimens by the maximum pit depth.

ARTICLE HISTORY

Received: 5 July 2024
Revised: 27 February 2025
Accepted: 2 March 2025

KEYWORDS

Angle steel member;
Corrosion;
Surface roughness;
Tensile test;
Evaluation methods

1. Introduction

As the main material of transmission tower, structural steel is susceptible to corrosion during long-term service due to environmental and climatic factors [1,2]. Corrosion reduces the load-bearing capacity of components and affects the overall structural safety of transmission towers. Therefore, it is necessary to carry out regular inspections and evaluate the residual load-carrying capacity of corroded components to determine subsequent maintenance methods [3,4].

In the natural environment, the corrosion process of structural steel is relatively slow. It takes a long time to produce obvious corrosion phenomena [5]. Therefore, the accelerated corrosion method has been widely used to prepare corrosion specimens [6-7]. For the corrosion simulation of atmospheric environment, the commonly used methods for accelerating corrosion mainly include electrochemical accelerated corrosion method and salt spray test method. Many scholars have proved that these two methods are feasible. For example, Bazan A et al. [8] immersed steel bars with peripheral auxiliary electrodes in NaCl solution to study the effect of centripetal stress on structural properties during the corrosion of steel bars. Si Qi et al. [9] placed steel structure specimens in electrolytic corrosion solution to simulate atmospheric corrosion and analyzed the surface characteristics of corroded steel plates based on surface roughness theory and fractal theory. Cheng Ding et al. [10] conducted a neutral salt spray corrosion test on mild steel specimens and discussed the kinetic law of corrosion of mild steel. Deliang Kong et al. [11] conducted a neutral salt spray accelerated corrosion test on steel plates. An autocorrelation function model of the corrosion depth random field model is proposed based on the surface profile and 3D data of corroded steel plate. Guangchong Qin et al. [12] adopted NaCl solution spray to simulate coastal corrosion environment, the natural corrosion was well simulated within the acceptable error range. Compared with the electrochemical accelerated corrosion method, salt spray test can better simulate the natural environment, the experimental operation is simple and the results have high reliability and repeatability. Therefore, the salt spray test method will be used to prepare corrosion specimens in this research.

Corrosion rate is an important parameter to characterize the degree of corrosion damage of structural steel, which is calculated from the mass loss rate before and after corrosion of components [13-14]. The effect of corrosion rate on mechanical properties of corroded steel plate has been studied deeply by many scholars. Yuchen Ou et al. [15] conducted tensile tests on natural and artificial corroded steel bars respectively and obtained the relationship between tensile properties and corrosion rate. Zhenye Chen et al. [16] obtained high-performance steels with different degrees of corrosion through accelerated corrosion experiments with salt spray. The relationship between mechanical properties and corrosion rate was discussed by tensile test. Feng Liang et al. [17] investigated the relationship between mechanical properties and corrosion rate of S420 steel hull plates through accelerated corrosion cycle experiment and ultimate strength experiment. However, it is challenging to dismantle and weigh transmission tower components, making it difficult to obtain the corrosion rates. To solve this problem, a new method for evaluating the corrosion rate of corroded components by maximum residual thickness is proposed in this paper.

Moreover, the research shows that the surface morphology has a great influence on the residual mechanical properties of corroded components [18], especially in the aspects of deformation capacity [19-22] and fatigue behavior [23-26]. Naftary G et al. [27] obtained corroded steel specimens with different corrosion degrees through underwater accelerated corrosion tests and established a regression model for ductility estimation based on surface roughness in order to estimate the residual ductility of steel plates by roughness characteristics. Wei Wang et al. [28] established a mathematical model of the surface contour height of corroded steel based on the spectrum representation method and proved the reliability of the mathematical model taking standard deviation, arithmetic mean height and maximum height as evaluation indexes. Haipeng Song et al. [29] investigated the fatigue failure behavior of pre-corroded aluminum alloy based on experimental information such as three-dimensional rust morphology and established a data-driven fatigue life prediction model based on machine learning. Songbo Ren et al. [30] used statistical analysis to study the surface topography parameters of corroded steel and proposed a fractal reconstruction model of corroded steel surface based on W-M function. Therefore, it is necessary to consider the surface morphology parameters such as roughness when evaluating the residual mechanical properties of corroded tower members. However, the existing research results on surface morphology are mainly aimed at specific components under specific corrosion environment and lack of universality. The material and environment of transmission tower angle steel are special and their corrosion condition may be different from that of ordinary steel. Therefore, the surface morphology of transmission tower angle steel members during corrosion is deeply studied in this paper.

This paper aims to explore the corrosion process of angle steel with accelerated corrosion experiments and analyze the changes of mechanical index, corrosion rate and surface characteristic parameters during corrosion. In view of the difficulty of angle steel disassembly, evaluation methods of corrosion degree and mechanical properties are proposed, which provides a theoretical basis for practical engineering application. The layout of the paper is as follows. In section 2, the accelerated corrosion experiment is introduced, including the acquisition of experimental materials, experimental equipment and experimental methods. The experimental results are analyzed and a method for evaluating the corrosion rate of corroded steel by residual thickness is proposed in section 3. In section 4. Mechanical properties of corroded steel are evaluated by different evaluation indexes and the reliability is compared. Finally, Section 5 and Section 6 provide the discussion and conclusion respectively.

2. Experimental scheme

The section mainly introduces the experimental process. Firstly, standard tensile specimens were prepared by cutting angle steel, NaCl solution was used to simulate the atmospheric corrosion environment with high salinity, specimens with different corrosion rates were obtained by controlling the corrosion duration. Then the profile curve data of the corroded specimen surface were measured with a profile measuring instrument. Finally, the tensile test of the specimen was carried out.

2.1. Accelerated corrosion test

The purpose of this study is to explore the degradation of transmission tower components due to corrosion during service. Given that angle steel is a common component of the tower, the steel plate was obtained by cutting angle steel in the way shown in Fig.1. In order to facilitate the subsequent tensile test, the steel plate was cut and processed into the standard tensile specimen as shown in Fig.2. The material used in the test is hot-rolled Q235 steel. Q235 steel is a carbon structural steel, its chemical composition is: carbon content between 0.14% and 0.22%, silicon content is less than 0.30%, manganese content is between 0.30% and 0.70%, sulfur content is less than 0.050%, phosphorus content is less than 0.045%.

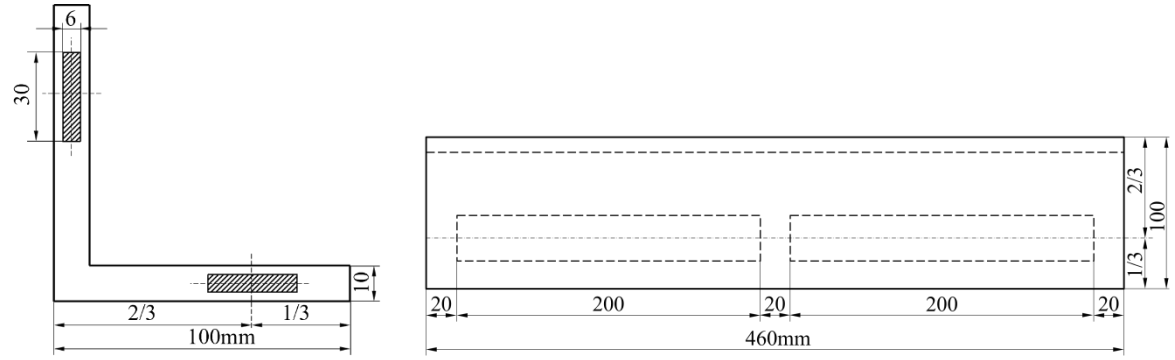

(a) Angle steel front view (b) Angle steel top view

Fig. 1 Specimen sampling

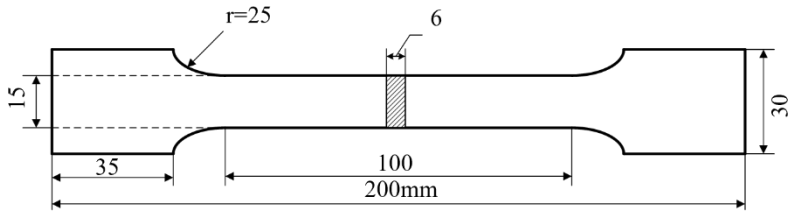

Fig. 2 Specimen size

In order to prepare corroded specimens, saturated sodium chloride solution was sprayed to simulate the environmental conditions of the coastal transmission tower, so as to accelerate the corrosion rate of the specimen and shorten the corrosion period. The experiment steps are as follows: (1) The accelerated corrosion experimental device is shown in Fig.3. A salt spray chamber with built-in specimen frames was constructed using plastic film and support. At the same time, 8 timed quantitative salt spray nozzles were arranged on both sides of the placing frame. (2) The spray settings of the salt spray nozzle are shown in Table 1. In order to ensure uniform corrosion on the surface of the specimen, the solution should be penetrated to the surface each time. (3) At the same time, the specimens were periodically turned over every 5 days to ensure consistent corrosion on both sides of the specimens.

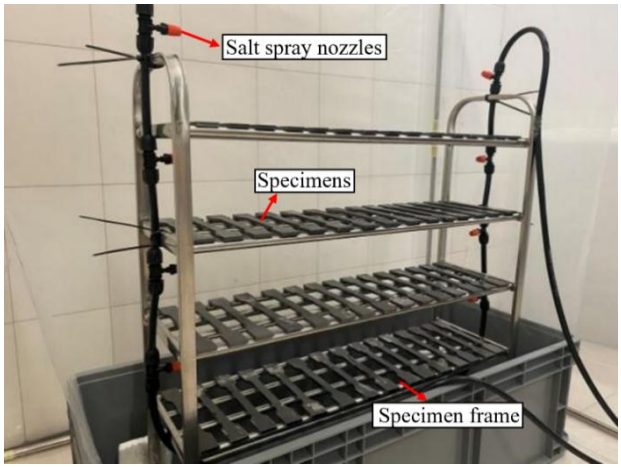

Fig. 3 Accelerated corrosion experimental device

Table 1
Salt spray rules

Interval time/hour	Spray time/min	Spray volume/liter
6	1	5.5

The processing steps of the specimens during the experiment are as follows: (1) Before the experiment, a total of 60 specimens were randomly divided into 4 groups on average, the predetermined corrosion duration of each group was shown in Table 2. After weight and size were measured, each group of specimens was placed on the corresponding specimen rack in batches. (2) For specimens that reached the predetermined corrosion days, they were removed and soaked in a hydrochloric acid solution to dissolve and wash away loose rust on the surface of the rusty parts. In order to prevent pickling damage to the corroded surface of the specimen, 10% dilute hydrochloric acid was used for pickling, the specimens were taken out every 10 minutes, the surface was wiped with a soft cloth. Repeat the above steps until the corrosion products on the specimen surface were completely removed. (3) After pickling, the specimens were placed in calcium hydroxide solution to neutralize the residual pickling solution. (4) After the specimens were cleaned and dried, the size and weight of each corroded specimen were measured. The corrosion specimen before and after rust removal is shown in Fig.4.

Table 2
Predetermined corrosion time of specimens

Group	Corrosion days/d
A	30
B	50
C	70
D	90

Fig. 4 Comparison of test pieces before and after rust removal

2.2. Surface topography measurement

The steps for extracting the surface topography data of corroded steel are as follows: (1) After the accelerated corrosion experiment, 3 specimens were randomly selected from each group A, B, C and D and numbered as shown in Table 3. (2) Three lines were selected equidistant from each of the two surfaces of the specimen, six lines were selected in total as shown in Fig.5. (3) Sanfeng FTA-H4C3000-D profile measuring instrument as shown in Fig.6 was used to measure and record the surface topography data along the selected lines. The sampling length of the instrument is 80mm, the sampling interval is 10μm and the sampling number is 8000. The two-dimensional contour curve of the measured specimen is shown in Fig.7.

Table 3
Contour measurement test piece group

Group	No.
A	A1 A2 A3
B	B1 B2 B3
C	C1 C2 C3
D	D1 D2 D3

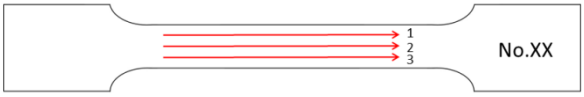

Fig. 5 Scanning position of specimen surface

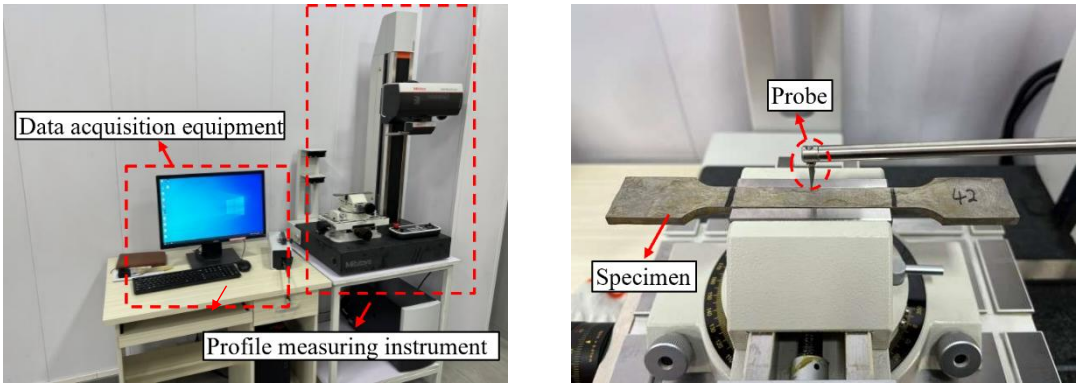

Fig. 6 Sanfeng FTA-H4C3000-D probe profilometer

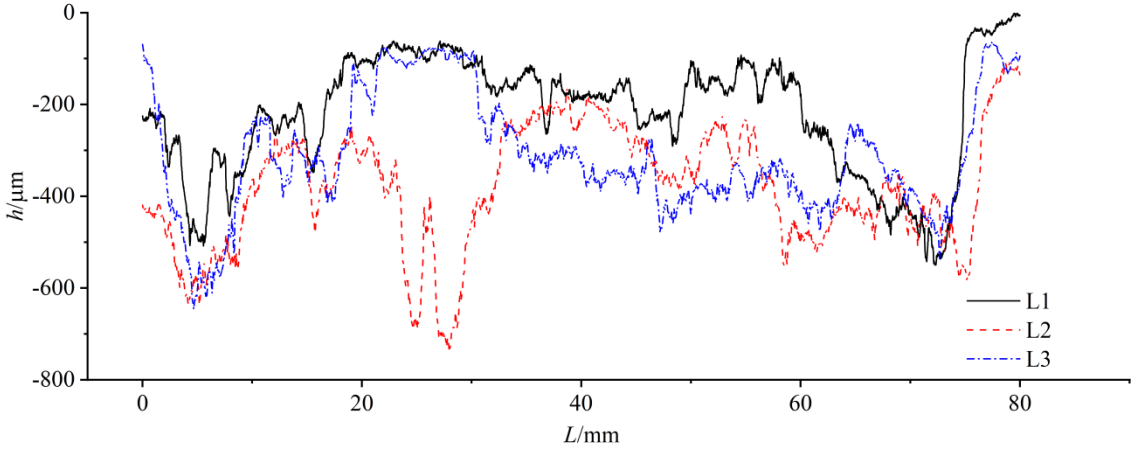

Fig. 7 Surface profile curve of specimen D1

2.3. Room temperature tensile test

MTS E45 electronic universal testing machine as shown in Fig.8 was used for the tensile test at room temperature. The experimental steps are as follows: (1) Three uncorroded specimens (numbered 01, 02 and 03 respectively) and 12 corroded specimens with contour scanning above, a total of 15 specimens, were selected for the tensile test. Before the experiment, the marking distance with an initial length of 50mm was set on the specimen (2) During the test, the system automatically collected and recorded the force and deformation in real time through the testing machine and the extensometer beam. The loading rate of the tensile test was set to 5mm/min until the specimen was pulled apart. (3) At the end of test, remove the extensometer. The stress-strain curves were obtained by data acquisition equipment.

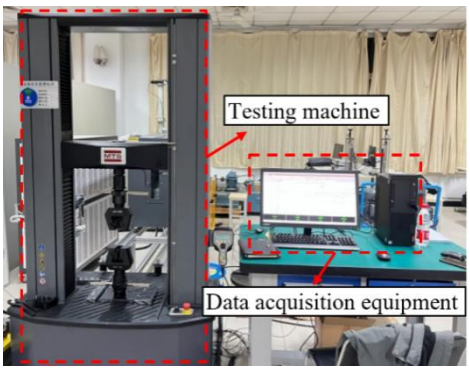

Fig. 8 MTS E45 electronic universal testing machine

3. Experimental results and analysis

The section mainly introduces and analyzes the experimental results. Firstly, the change rule of corrosion rate with time was analyzed through accelerated corrosion experiment. Then, the surface morphology index of the specimen was extracted, the microscopic change process of surface was analyzed and the relationship between the thickness of each corrosion layer and the corrosion rate was established. Finally, according to the results of tensile test at room temperature, the variation of tensile properties with corrosion degree was analyzed.

3.1. The results of the accelerated corrosion test

The weight of the specimen before and after the corrosion is m_0 and m respectively, the equation of the corrosion rate η is as follows:

$$\eta = \frac{m_0 - m}{m_0} \times 100\% \tag{1}$$

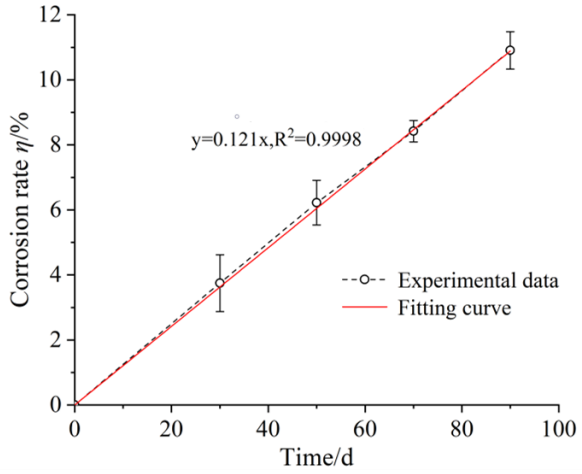

Fig. 9 Relationship between corrosion rate η and time

The corrosion rate of each specimen was calculated according to Eq. (1). The average corrosion rate of each group of specimens was taken as the corresponding corrosion rate under the corrosion duration of the group, the variation of corrosion rate over time was obtained, as shown in Fig.9. It can be seen the corrosion rate of the specimens changes roughly linearly with time when the corrosion rate is below 12%, that is, the specimens rust and lose weight at a constant rate.

3.2. The results of contour scan

The surface roughness parameters of corroded specimens were calculated based on the two-dimensional profile curve scanned by the profile measuring instrument. In this paper, the main parameters of specimen surface roughness analysis are maximum section height (R_t), arithmetic average height (R_a) and root mean square height (R_q). R_t, R_a and R_q respectively represent the sum of the maximum peak height and maximum valley depth on the contour curve, the mean value of the absolute value of the contour offset on the datum length and the root-mean-square value of the contour offset on the reference length. The calculation equation of each roughness parameter is as follows:

$$R_t = \max(R_{pi}) + \max(R_{vi}) \tag{2}$$

$$R_a = \frac{1}{l}\int_0^l |Z(x)|dx \tag{3}$$

$$R_q = \sqrt{\frac{1}{l}\int_0^l Z^2(x)dx} \tag{4}$$

The surface roughness parameters of the specimen are calculated based on the profile curves shown in Fig.7 and the above equations. The position of the component before corrosion (corresponding to h=0 in Fig.7) is taken as the reference position and the coordinates of each measurement point are the offset at this point. The calculated surface roughness parameters of each component are shown in Table 4.

Table 4
Summary of corrosion rate and average roughness parameters of corroded parts

No.	*t*/d	η/%		Average roughness parameters					
				R_t		R_a		R_q	
A1		4.30		141.7		337.0		156.7	
A2	30	4.46	4.31	209.1	159.9	386.9	348.0	216.1	170.5
A3		4.18		129.1		320.1		138.6	
B1		5.44		244.3		521.9		263.0	
B2	50	5.40	5.59	281.0	265.6	598.8	575.7	302.3	284.4
B3		5.91		271.4		606.5		288.0	
C1		8.56		275.8		601.4		294.2	
C2	70	8.26	8.56	282.9	276.2	600.1	633.6	299.3	299.0
C3		8.86		270.0		699.1		303.4	
D1		11.04		296.6		732.7		329.0	
D2	90	11.36	11.02	304.3	290.0	723.7	702.0	332.8	318.8
D3		10.67		269.1		649.7		294.5	

The relationship between surface roughness parameters and corrosion rate of corroded steel specimens is shown in Fig.10. It can be seen R_a, R_q and R_t increase with the increase of the corrosion rate when the corrosion rate of the specimen is between 0 and 6%. The growth rate of R_a, R_q and R_t slows down when the corrosion rate is between 6% and 11%, the growth of R_a and R_q almost stops and tends to be flat.

It can be seen that with the initial stage of steel surface corrosion process, dissolved oxygen reacts with steel surface materials, resulting in numerous rust pits. The steel surface starts to become rough and uneven, the surface roughness parameters increase. The corrosion becomes more and more serious with the deepening of the rust pit and the surface roughness parameters become larger. The corroded layer begins to seriously hinder the further contact between the corrosive medium and the material matrix when the corrosion process reaches a certain stage, preventing dissolved oxygen from reaching the uncorroded area of the steel, making it difficult for the steel to undergo oxidation reactions. As a result, the increase rate of the surface roughness parameters slows down.

In order to further study the deterioration of the mechanical properties of the specimens due to stress concentration caused by local rust pits on the surface of the corroded specimens, the size of the deepest rust pits on the corroded specimen was measured based on the results of surface profile scanning. The difference between the maximum depth value and the edge depth of the rust pit is denoted as the rust pit depth *d*. The edge distance between the two sides of the rust pit is denoted as the rust pit width *w*. The depth to width ratio of the rust pit is obtained by calculating *d*/*w*. The deepest rust pit was selected from the

contour curve for measurement as shown in Fig.11, the measurement data was recorded as shown in Table 5.

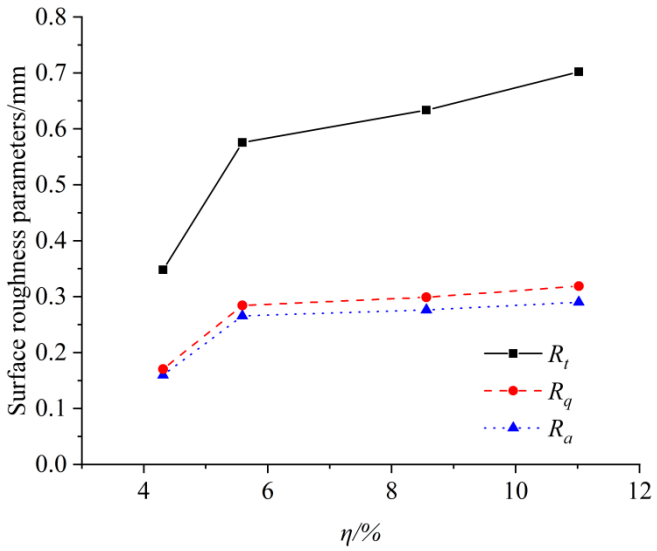

Fig. 10 Relationship between R_a, R_q, R_t and η

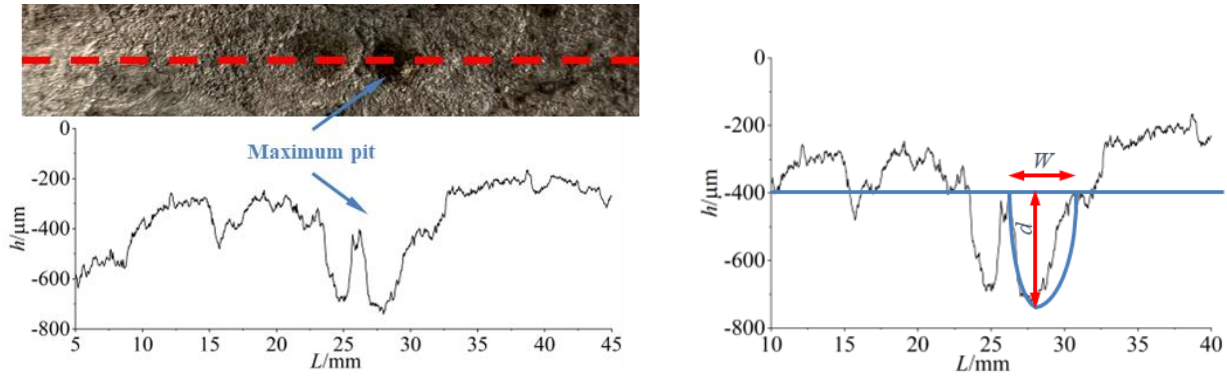

(a) Corrosion surface topography

(b) maximum rust pit size

Fig. 11 Maximum rust pit measurement process

Table 5
Maximum rust pit size for each corrosion specimen (mean value of both sides)

No.	*d*/μm		*w*/μm		*d*/*w*	
A1	132		3668		0.0361	
A2	92	130	4825	4803	0.0193	0.0279
A3	167		5917		0.0283	
B1	202		6080		0.0357	
B2	418	286	5284	5651	0.0419	0.0410
B3	239		5589		0.0453	
C1	278		4909		0.0607	
C2	296	323	6822	7498	0.0485	0.0503
C3	396		10762		0.0416	
D1	420		8660		0.0515	
D2	261	343	6856	8165	0.0402	0.0449
D3	350		8977		0.0429	

According to Table 5, the relationship between the corrosion rate of the specimen and the maximum rust pit depth and the ratio of depth to width was obtained, as shown in Fig.12. It can be seen from the figure that the maximum rust pit depth and the depth to width ratio of the specimen increase significantly with the increase of the corrosion rate when the corrosion rate of the specimen is between 0% and 8%, which indicates that corrosion pits appear on the specimen surface at the initial stage of corrosion and deepen continuously. At a certain degree of corrosion, the rate of rust pits deepening slows down. Combined with Fig.10 and Fig.12, the corrosion rate at this stage is about 6%~8%. Meanwhile, it can be seen from Fig.12 (b) that the depth to width ratio of the maximum rust pit decreases when the corrosion rate is greater than 8%, which indicates that at this stage, the development of rust pits changes from longitudinal to transverse and the bottom of rust pits becomes wider. Rust pits gradually develop from the deeper pitting pits to the wide and deep ulcer pits. The analysis of the maximum rust pit not only verifies the corrosion process of steel obtained from roughness parameters in the previous paper, but also further reveals the development law of the microscopic characteristics of the corroded surface during the corrosion process.

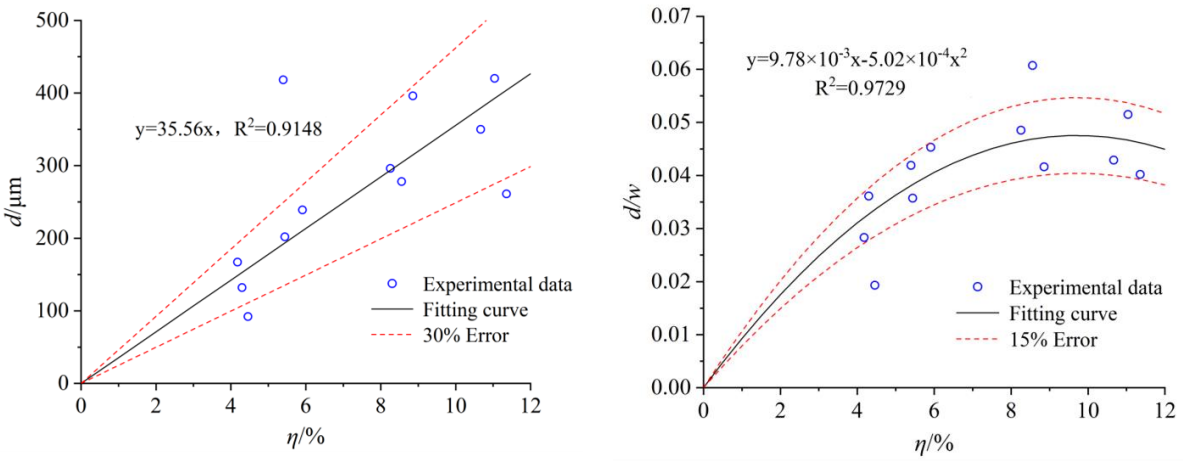

(a) Max rust pit depth

(b) Max rust pit depth to width ratio

Fig. 12 Relationship between corrosion rate and maximum rust pit size

3.3. Thickness of corrosion layer

According to the morphology of the corroded steel surface, the cross-section of the corroded specimen is divided into regions as shown in Fig.13. It can be seen from the figure that the part where the steel is thinned as a whole due to rust is the uniform rust area. There is a non-uniform rust zone between the highest peak and the deepest valley of the steel surface profile. The uncorroded part in the middle of the material is the uncorroded area.

The original thickness T_0 of the specimen was measured before the test. The maximum residual thickness T is the mean value of the measured thickness at five measuring points, as shown in Fig.14. The uniform rust layer thickness h_1 can be obtained by calculating the difference between the original thickness T_0 and the maximum residual thickness T. The thickness of the non-uniform corroded layer h_2 can be obtained from the height difference between the highest peak and the deepest valley of the profile curve of the corroded specimen. The total thickness of the rust layer h_3 is the sum of h_1 and h_2. The ratio of the thickness of each layer to the original thickness of the specimen is further calculated to obtain the proportion of each corroded layer. The thickness and proportion of each corrosion layer are summarized in Table 6.

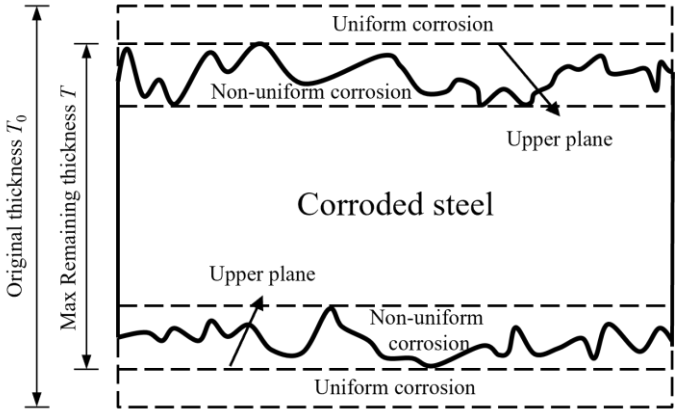

Fig. 13 Division of each corrosion layer of corrosion test piece

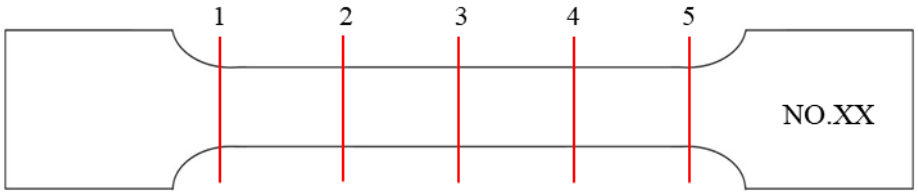

Fig. 14 Measurement of maximum residual thickness

Table 6
Summary of thickness values of specimens and proportion of each layer

No.	T_0	T		h_1		h_2		h_3	
A1	5.438	5.422	99.71%	0.016	0.29%	0.674	12.39%	0.691	12.71%
A2	5.442	5.432	99.82%	0.010	0.18%	0.774	14.22%	0.783	14.39%
A3	5.441	5.452	100.20%	-0.011	-0.20%	0.640	11.76%	0.629	11.56%
B1	5.421	5.418	99.94%	0.003	0.06%	1.044	19.26%	1.046	19.30%
B2	5.376	5.378	100.04%	-0.002	-0.04%	1.198	22.28%	1.196	22.25%
B3	5.416	5.418	100.04%	-0.002	-0.04%	1.213	22.40%	1.211	22.36%
C1	5.415	5.358	98.95%	0.057	1.05%	1.203	22.22%	1.260	23.27%
C2	5.418	5.354	98.82%	0.064	1.18%	1.200	22.15%	1.264	23.33%
C3	5.420	5.360	98.89%	0.060	1.11%	1.398	25.79%	1.458	26.90%
D1	5.446	5.258	96.55%	0.188	3.45%	1.465	26.90%	1.653	30.35%
D2	5.441	5.228	96.09%	0.213	3.91%	1.447	26.59%	1.660	30.51%
D3	5.485	5.324	97.06%	0.161	2.94%	1.299	23.68%	1.460	26.62%

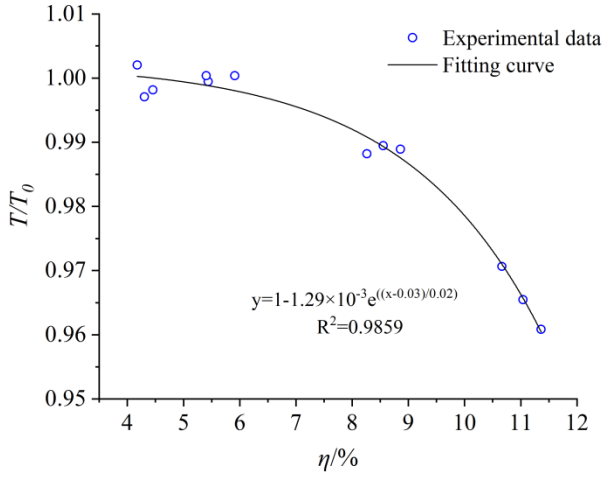

Fig. 15 Relationship between T/T_0 and corrosion rate

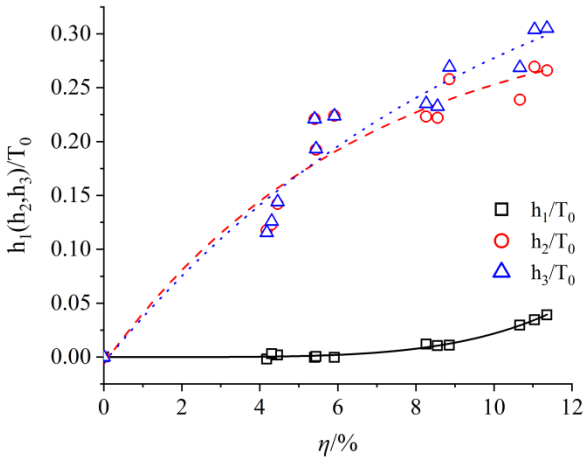

Fig. 16 Relationship between $h_{1,2,3}/T_0$ and corrosion rate

According to the thickness data of each part of the specimen obtained in Table 6, the relationship between the ratio of maximum residual thickness T/T_0 and corrosion rate is shown in Fig.15. The fitting result obtained by the exponential growth function ExpGrow1 is shown in Eq. (5). The relationship between $h_{1,2,3}/T_0$ and rust rate is shown in Fig.16. It can be seen from the figure that the thickness of uniform rust layer increases slightly with the increase of rust rate, but the growth rate accelerates. The thickness of non-uniform rust layer increased greatly, but the growth rate slowed down. This indicates that the pit develops vertically in the early stage of corrosion. However, the depth of corrosion increases with the increase of the degree of corrosion, the gradually increasing corrosion products begin to hinder the contact between the corrosion medium and the steel matrix, making it difficult for the corrosion reaction to be carried out at deeper depths of the specimen. The development of rust pits changes from longitudinal to horizontal, which also confirms the development law of rust pits obtained from the change of surface roughness parameters. For the components in the steel structure that are not easy to disassemble, the maximum residual thickness can be measured, the corrosion rate can be calculated using the following equation. However, the corrosion rate cannot be calculated by the following equation for components with corrosion rate lower than 4% or higher than 12%.

$$\frac{T}{T_0}=1-1.29\times10^{-3}e^{((\eta-0.03)/0.02)},R^2=0.9859 \quad (5)$$

3.4. Results of tensile test

The stress-strain curves of specimens obtained by tensile test are shown in Fig.17. It can be found from the figure that the mechanical properties of the same group of specimens have a certain discreteness. The dispersion of mechanical properties decreases and the degree of coincidence of stress-strain curves increases with the increase of corrosion rate. The strength of the corroded parts in groups B, C and D is significantly lower than that of the uncorroded group and group A. However, the differences of mechanical properties of nine specimens in groups B, C and D are small. It can be found that the yield strength and ultimate strength of steel plate decrease with the increase of corrosion rate when the corrosion degree is low and the decline degree becomes less and less obvious.

Fig.18 shows the morphology of 12 specimens in groups A, B, C and D after tensile failure. There are obvious necking phenomena in all specimens after tensile failure. During the corrosion process, there were two sets of contact points between the specimen and the bracket, where obvious rust pits were formed. During the stretching process, stress concentration appeared at the edge of the corrosion pit, which made the stress distribution of the specimen uneven, thus the specimen broke at this position.

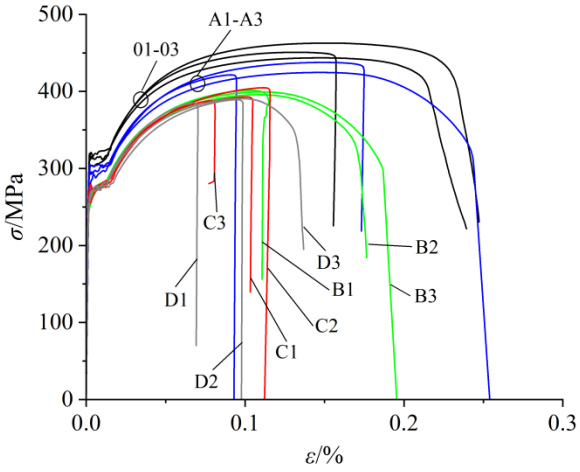

(a) Stress-strain curve

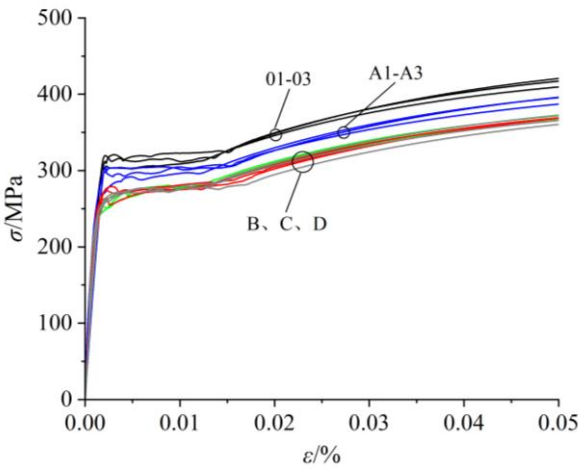

(b) Local enlarged view of stress-strain curve

Fig. 17 Stress-strain curve of each specimen

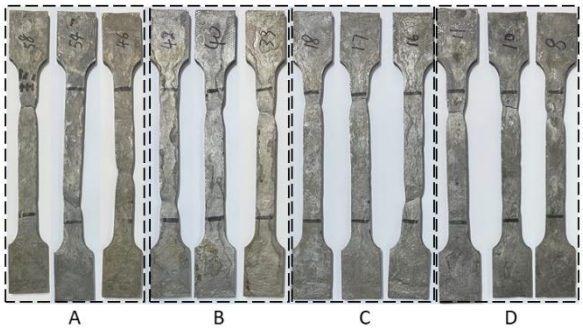

Fig. 18 Tensile failure mode of corroded specimens

4. Evaluation methods of mechanical properties of corroded steel

The section mainly analyzes the evaluation methods of mechanical properties of corroded steel. Firstly, the mechanical properties of steel specimens during tensile test are extracted. Then, the mechanical properties of the corroded steel are evaluated according to corrosion rate, surface roughness and maximum pit size. Finally, the evaluation effects of different evaluation indexes are compared.

4.1. Mechanical property index

The main mechanical properties of steel specimens are the nominal elastic modulus E_s, the nominal yield strength f_y, the nominal tensile strength f_u, the ratio of yield strength to tensile strength f_y/f_u, the elongation A and the yield platform length ε_A. In order to facilitate the study of the changes of mechanical property indexes of steel after corrosion, the curves in Fig.17 are sorted out and the indexes obtained are listed in Table 7.

Table 7
Main mechanical property indexes of specimens in the tensile test

No.	η/%		E_s/GPa	f_y/MPa	f_u/MPa	f_y/f_u	A/%	ε_A/%
01	0		197.70	319.60	450.88	0.709	22.41	1.310
02	0	0	223.80	305.80	443.65	0.689	22.07	1.046
03	0		222.30	320.80	462.76	0.693	23.34	1.074
A1	4.30		203.20	291.70	421.50	0.692	19.76	0.873
A2	4.46	4.31	206.70	305.30	437.72	0.697	23.03	1.221
A3	4.18		214.10	298.00	424.68	0.702	23.53	1.314
B1	5.44		204.80	279.60	401.43	0.697	19.76	1.124
B2	5.40	5.59	224.80	280.98	395.76	0.640	16.97	1.143
B3	5.91		199.20	278.20	399.45	0.696	19.13	1.058
C1	8.56		239.40	278.90	392.93	0.710	18.60	1.145
C2	8.26	8.56	213.80	273.80	404.82	0.676	17.24	1.026
C3	8.86		212.00	263.60	387.78	0.680	17.73	1.058
D1	11.04		233.20	277.24	385.20	0.625	17.20	1.077
D2	11.36	11.02	222.00	277.92	389.31	0.697	20.23	1.056
D3	10.67		210.10	260.60	390.72	0.667	14.71	1.013

It can be seen from Table 7 that there are certain differences in the mechanical property indexes of specimens with the same corrosion duration. This is mainly due to the fact that rust is a complex electrochemical process. In the process of accelerated corrosion test, although the same environmental conditions are set, there are still significant differences in the formation position and size of corrosion pits on the surface of different specimens under the same corrosion time (as shown in Table 5). This difference at the microscopic level will lead to different degrees of stress concentration in the tensile process of the specimen, which leads to the dispersion of the tensile strength data. But in general, under the same corrosion rate, the difference of the mechanical properties of the specimen is less than 10%, the variability of the data is not large.

4.2. Corrosion rate index

The relationship and law between mechanical properties of materials and η can reveal the process of mechanical properties deterioration of steel during corrosion. Therefore, the relationship between each indicator and η is established which is shown in Fig.19, where E_{s0}、f_{y0}、f_{u0} are the maximum values of the corresponding indexes in the groups 01 ~ 03 of uncorroded specimens.

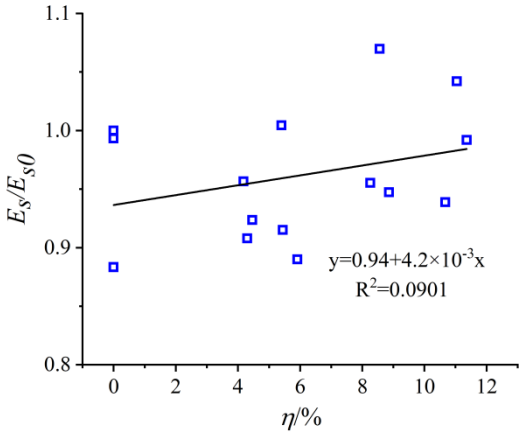

(a) Relationship between E_s/E_{s0} and η

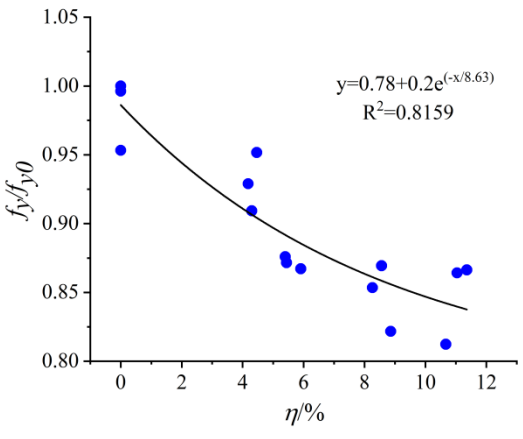

(b) Relationship between f_y/f_{y0} and η

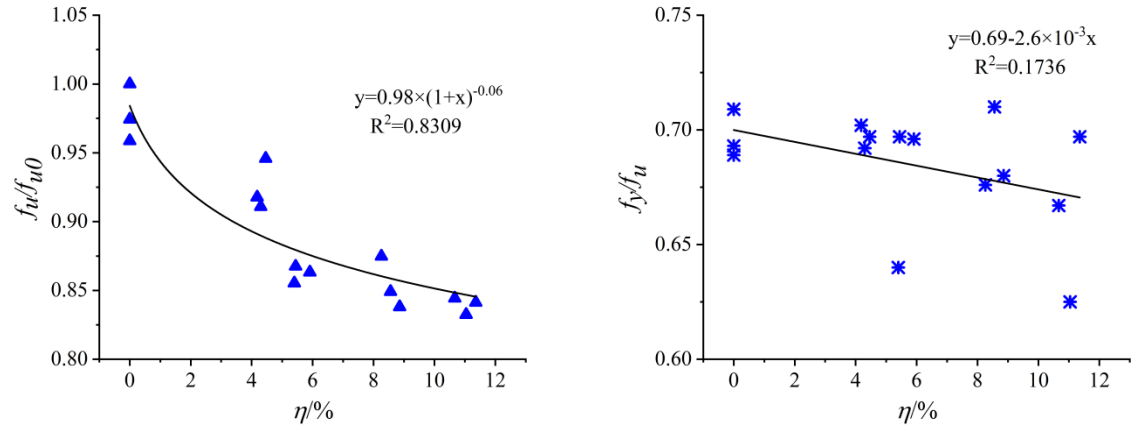

(c) Relationship between f_u/f_{u0} and η (d) Relationship between f_y/f_u and η

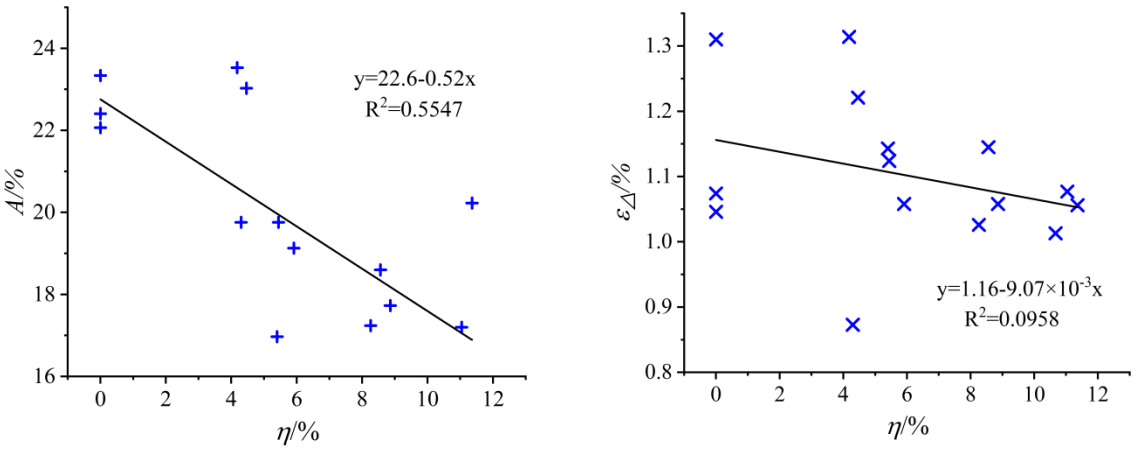

(e) Relationship between A and η (f) Relationship between ε_Δ and η

Fig. 19 Relationship between mechanical properties of corroded components and η

According to Fig.19 (a), the relative elastic modulus E_s/E_{s0} of the specimen fluctuates within the range of 0.85~1.1 with the increase of corrosion rate, corresponding to specific values of the elastic modulus from 197.7 to 239.4. The relative elastic modulus and corrosion rate of each group of specimens are fitted linearly, the correlation coefficient of the obtained relationship is only 0.0901, indicating a high degree of discreteness in the data. At the same time, the elastic modulus of the same group of specimens has great dispersion. Therefore, it can be considered that the corrosion process has little effect on the elastic modulus of the specimens.

For the data of corrosion rate and relative yield strength f_y/f_{y0} and relative tensile strength f_u/f_{u0} in Fig.19 (b) and Fig.19 (c), ExpDec1 and Pow2P2 functions are respectively used to fit the data and the following Eq. (6) and Eq. (7) are obtained.

$$\frac{f_y}{f_{y0}} = 0.78 + 0.2e^{(-\eta/8.63)}, R^2 = 0.8159 \quad (6)$$

$$\frac{f_u}{f_{u0}} = 0.98 + (1+\eta)^{-0.06}, R^2 = 0.8309 \quad (7)$$

It can be seen that correlation coefficients of the above relationships are both above 0.8, which indicates that the degree of fitting is relatively high, the yield strength and tensile strength of the steel specimen are significantly correlated with the rust rate. The f_y and f_u calculated by the above two equations have high reliability taking rust rate as the parameter.

The yield strength and tensile strength ratio f_y/f_u, elongation after fracture A and yield platform length ε_Δ all decrease with the increase of corrosion rate as can be seen from (d), (e) and (f) in Fig 19. However, R^2 is low for the fitted curves due to the large dispersion of data. Therefore, general trend of f_y/f_u, A and ε_Δ with the increase of η can only be preliminarily explained, but cannot be evaluated and predicted by η.

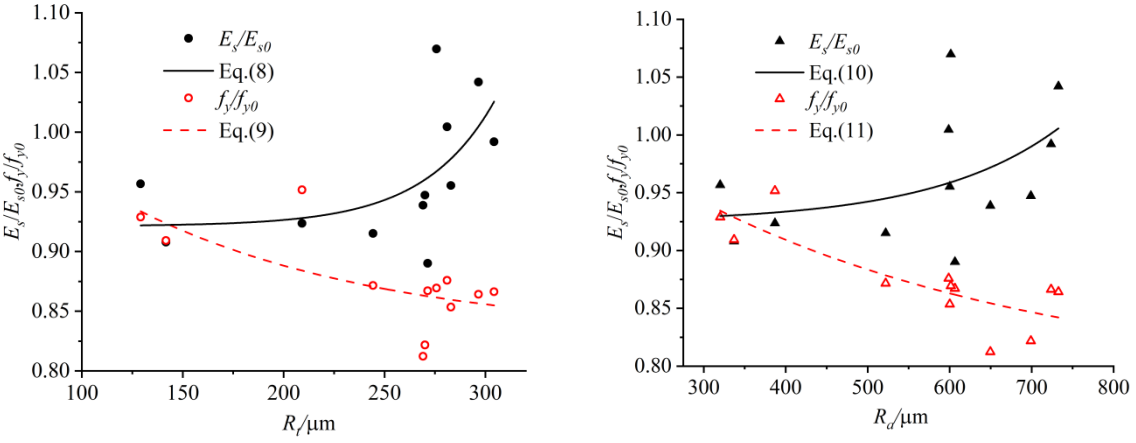

(a) Relationship of E_s/E_{s0}, f_y/f_{y0} with R_t (b) Relationship of E_s/E_{s0}, f_y/f_{y0} with R_a

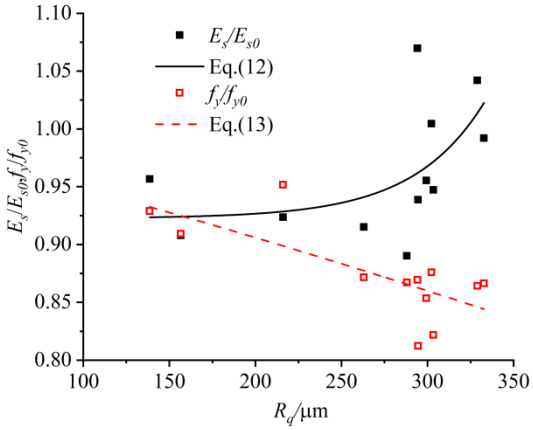

(c) Relationship of E_s/E_{s0}, f_y/f_{y0} with R_q

Fig. 20 Relationship of E_s/E_{s0}, f_y/f_{y0} with roughness parameters

4.3. Surface morphology index

Taking η as an index to evaluate the corrosion degree of steel members is an ideal treatment for the surface morphology of the corroded parts, which simplifies the corrosion effect as the overall thinning effect of components. However, in the actual corrosion process, many rust pits are formed on the surface of corroded steel components, resulting in the obvious stress concentration phenomenon appears near the rust pits when the member is subjected to external load, which is the direct cause of the deterioration of mechanical properties of the members after corrosion. Therefore, the relationship between E_s, f_y and surface roughness indexes of corroded components is established, as shown in Fig.20.

It can be seen that the values of R_t, R_a and R_q are small in the initial corrosion stage, while E_s decreases slightly with the increase of roughness. E_s increases accordingly when R_t, R_a and R_q exceed 250μm, 600μm and 250μm respectively. The stress state of the surface material of the member is changed from unidirectional stress state to triaxial stress state due to the formation of the rust pit, resulting in the increase of E_s. The yield strength of the specimen decreases nonlinearly with the increase of R_t, R_a and R_q. The discreteness of f_y increases with the increasing of R_t, R_a and R_q when R_t, R_a and R_q are greater than 250μm, 600μm and 250μm respectively, but it still shows a downward trend in general.

In order to verify the reliability of using specimen roughness parameters to evaluate E_s and f_y, ExpDec1 function is used to fit the experimental data. The results are shown in the following equations.

① R_t for the parameter

$$\frac{E_S}{E_{S0}} = 1.65\times10^{-5}\mathrm{e}^{R_t/34.78}, R^2 = 0.3345 \tag{8}$$

$$\frac{f_y}{f_{y0}} = 0.3\mathrm{e}^{(-R_t/122.83)} + 0.83, R^2 = 0.4483 \tag{9}$$

② R_a for the parameter

$$\frac{E_S}{E_{S0}} = 7.04\times10^{-4}\mathrm{e}^{R_a/154.23} + 0.92, R^2 = 0.2252 \tag{10}$$

$$\frac{f_y}{f_{y0}} = 0.31\mathrm{e}^{(-R_a/436.83)} + 0.78, R^2 = 0.6744 \tag{11}$$

③ R_q for the parameter

$$\frac{E_S}{E_{S0}} = 3.09\times10^{-5}\mathrm{e}^{R_q/41.18} + 0.92, R^2 = 0.3317 \tag{12}$$

$$\frac{f_y}{f_{y0}} = -0.54\mathrm{e}^{R_q/1400} + 1.52, R^2 = 0.5332 \tag{13}$$

Eq. (8), Eq. (10) and Eq. (12) are the fitting equations for evaluating E_s with R_t, R_a and R_q as indexes, the correlation coefficients are 0.3345, 0.2252 and 0.3317 respectively. However, the discreteness of E_s increases with the increase of R_t, R_a and R_q. In general, the reliability of evaluating the E_s of corroded steel by roughness parameters is not high, but it is better than the corrosion rate index.

Similarly, Eq. (9), Eq. (11) and Eq. (13) are the fitting equations for evaluating f_y with R_t, R_a and R_q as indexes, the correlation R^2 are 0.4483, 0.6744 and 0.5332 respectively. The discreteness of f_y is large when R_t, R_a and R_q are 250-300 μm, 600-750 μm and 250-350 μm respectively according to Fig.20. Therefore, the reliability of evaluating the yield strength of corroded components based on surface roughness is low.

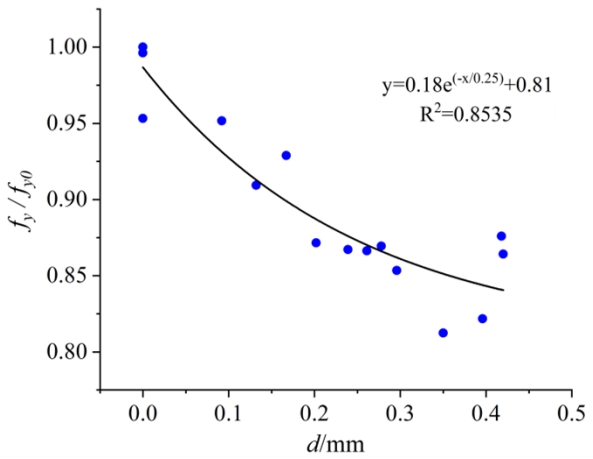

(a) Relationship between f_y/f_{y0} and d

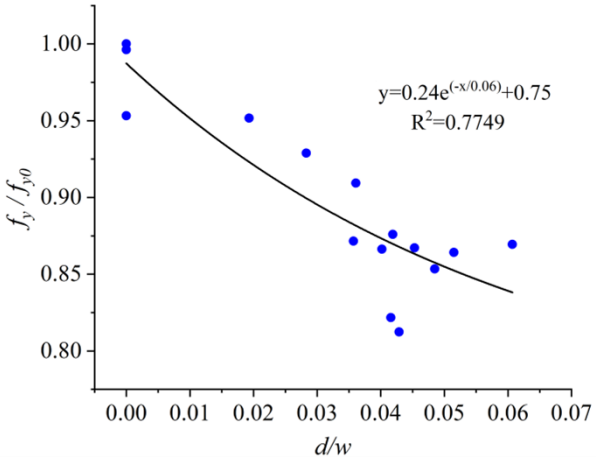

(b) Relationship between f_y/f_{y0} and d/w

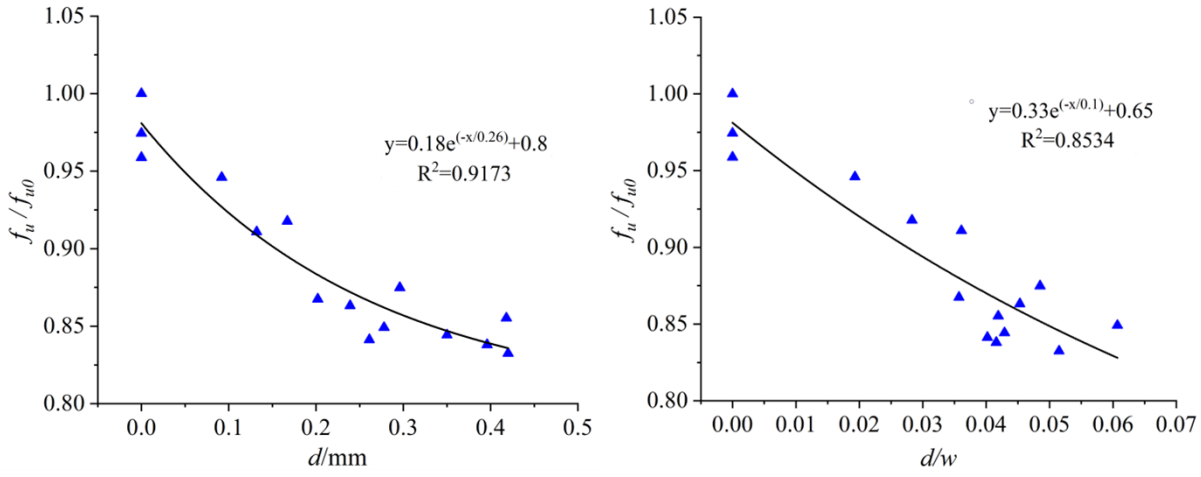

(c) Relationship between and f_u/f_{u0} and d (d) Relationship between f_u/f_{u0} and d/w

Fig. 21 Relationships between f_y and f_u and the size of the maximum rust pit

4.4. Maximum rust pit size index

There is a significant relationship between the microscopic level of corrosion surface and the mechanical properties of the component. It is found that E_s has little correlation with the size of the largest rust pit. Therefore, the reliability evaluation of f_y and f_u based on the maximum pit size is mainly discussed. The relationship between f_y and f_u of corroded specimens and the size of the maximum rust pit is established, as shown in Fig 21.

It can be seen from Fig.21 that there is a significant nonlinear correlation between the mechanical properties of corrosion specimens and the size of the maximum rust pit. Equations (14), (15), (16) and (17) are obtained by numerical fitting of ExpDec1 function.

$$\frac{f_y}{f_{y0}} = 0.18^{-\frac{d}{0.25}} + 0.81, R^2 = 0.8535 \tag{14}$$

$$\frac{f_y}{f_{y0}} = 0.24^{-\frac{d}{0.06w}} + 0.75, R^2 = 0.7749 \tag{15}$$

$$\frac{f_u}{f_{u0}} = 0.18^{-\frac{d}{0.26}} + 0.8, R^2 = 0.9173 \tag{16}$$

$$\frac{f_u}{f_{u0}} = 0.33^{-\frac{d}{0.1w}} + 0.65, R^2 = 0.8534 \tag{17}$$

The fitting curves of f_y and f_u obtained by different parameters as evaluation indexes are compared as follows. For f_y, the correlation coefficient of Eq. (14) is 0.8535, which has higher accuracy than that of equations (6) and (15), while the fitting accuracy of equations (9), (11) and (13) is poor. It can be seen that in the fitting curve of f_y, the fitting curve obtained with the maximum rust pit depth as the index has better accuracy compared with the rust rate and the depth to width ratio of the maximum rust pit, while the fitting accuracy with the surface roughness as the index is poor. For f_u, the correlation coefficient of Eq. (16) is 0.9173, which is higher than Eq. (7) and Eq. (17), indicating that the maximum rust pit depth is the most accurate fitting curve, which is higher than the rust rate index and the maximum rust pit depth to width ratio index. In general, the maximum depth of rust pit on the surface of corroded components can be used as a parameter to evaluate the strength of corroded components with high precision. At the same time, when only the corrosion rate of the component is taken as the evaluation parameter, the obtained results also have high reliability. However, component strength cannot be accurately and reliably evaluated using only surface roughness parameters.

5. Discussion

In this paper, the morphologic changes of Angle steel during corrosion are discussed, the evaluation methods of corrosion rate and mechanical properties are obtained, which has certain guiding significance for engineering practice. In the future, corrosion Angle steel needs to be further explored and studied, including the following aspects:

1) The research carried out in this paper is based on the data obtained from the artificial accelerated corrosion test which is only applicable to Angle steel members whose surface corrosion is similar to that in this paper. The environment of Angle steel in engineering is different, so it is necessary to further improve the experiment under different climatic conditions.

2) The external load in the actual environment will further affect the degree of corrosion in the Angle steel rust zone. Therefore, the evaluation of corrosion degree and bearing capacity of multi-factor coupled lower Angle steel members can be explored.

6. Conclusions

In this paper, the standard tensile specimen of angle steel is taken as the research object and the corrosion specimen is prepared by accelerated corrosion test. The morphology data and mechanical properties of the corrosion specimen are obtained by contour scanning and tensile test at room temperature. The variation of roughness parameters and the deterioration of mechanical properties of steel specimens during corrosion are investigated, the variation laws of the surface of steel specimens at macro and micro levels during corrosion are explored. The relationship between corrosion rate, surface characteristics and mechanical indexes is established, the evaluation effect of different indexes on mechanical properties is compared. The main conclusions are as follows:

1) At the initial stage of corrosion, corrosion pits appear on the specimen surface and deepen continuously with the increase of corrosion rate, the surface roughness increases. When the corrosion rate of the specimen reaches a certain extent, the corrosion products hinder the further oxidation reaction of the specimen, the deepening speed of the rust pit slows down, the bottom becomes wider and the deeper pitting pits gradually develop into wider and deeper ulcer pits, The growth rate of the specimen surface roughness slows down.

2) Transmission tower components in operation are difficult to disassemble and weigh. Considering that the thickness of the rust layer has a significant relationship with the corrosion rate during the corrosion process, the corrosion rate of the component can be evaluated by measuring the maximum residual thickness of the component, so as to judge the degree of corrosion of the component.

3) The tensile test results show that for the mechanical properties of steel specimens, except that the elastic modulus is basically not affected by corrosion, the yield strength, tensile strength, elongation and other indicators show different degrees of deterioration with the increase of corrosion degree, which indicates that rust has a significant impact on the bearing capacity and deformation capacity of steel specimens.

4) The mechanical properties of corroded components are evaluated by corrosion rate, roughness parameters and maximum pit size. By comparing different evaluation equations, it can be found that the maximum depth of rust pit on the surface of corroded members is the most accurate evaluation index for yield strength and tensile strength, the obtained results also have high

reliability taking the corrosion rate of the component as the evaluation index. It is not reliable to evaluate the elastic modulus with each index.

Acknowledgements

The authors acknowledge the financial support provided by the "333 Talent Project of Hebei Province ”(C20231056)

References

[1] Gathimba N, Kitane Y. Characterization of surface topography of corroded steel members exposed to marine environments[C]//Corrosion and Prevention 2018.2018.
[2] Oszvald K, Tomka P, Dunai L. The remaining load-bearing capacity of corroded steel angle compression members[J].Journal of Constructional Steel Research, 2016, 120(apr.):188-198.
[3] Oszvald K, Dunai, László. Effect of corrosion on the buckling of steel angle members – experimental study[J]. Periodica Polytechnica Civil Engineering, 2012, 56(2).
[4] Beaulieu L, Legeron F, Langlois S. Compression strength of corroded steel angle members[J].Journal of Constructional Steel Research,2010,66(11):1366-1373.
[5] Surahyo A. Achieving Quality in Concrete Construction: Practical Problems and Solutions[M]. 2019.
[6] Garbatov Y, Soares C G, Parunov J, et al. Tensile strength assessment of corroded small scale specimens[J]. Corrosion science, 2014, 85:296-303.
[7] Jinchao J, Yong L, Zhao L, et al. Correlation between Laboratory-Accelerated Corrosion and Field Exposure Test for High-Strength Stainless Steels[J]. Materials, 2022,15(24):9075-9075.
[8] Bazan A, Galvez J, Reyes E, et al. Study of the rust penetration and circumferential stresses in reinforced concrete at early stages of an accelerated corrosion test by means of combined SEM, EDS and strain gauges [J]. Construction and Building Materials, 2018, 184: 655-67.
[9] Qi S, Yang D, Liang Z. Electrolytic accelerated corrosion morphology for structural steel based on an improved solution[J]. Corrosion Reviews,2021,39(4):373-386.
[10] Cheng D, Jin L, Xiqing Z, et al. Corrosion Dynamics of Low Carbon Steel in Salt Spray Environment[J]. Protection of Metals and Physical Chemistry of Surfaces,2023,59(4):729-735.
[11] Deliang K, Biao N, Shanhua X. Random Field Model of Corroded Steel Plate Surface in Neutral Salt Spray Environment[J]. KSCE Journal of Civil Engineering,2021,25(7):1-11.
[12] Qin G, Xu S, Yao D, et al. Study on the degradation of mechanical properties of corroded steel plates based on surface topography[J]. Journal of Constructional Steel Research,2016,125205-217.
[13] Yafeng Z, Gemma F, Elaine A, et al. Influence of Corrosion-Induced Damage on Mechanical Integrity and Load-Bearing Capability of Cemented Carbides[J]. Metals,2022,12(12):2104-2104.
[14] Qiang L, Xianyu J, Dongming Y, et al. Study of wiring method on accelerated corrosion of steel bars in concrete[J]. Construction and Building Materials,2020,(prepublish):121286-.
[15] Ou Y C, Susanto Y, Roh H. Tensile behavior of naturally and artificially corroded steel bars[J]. Construction and Building Materials, 2016, 103(Jan.30):93-104.
[16] Zhenye C, Shidong N, Wenbing H, et al. A study on static properties of high-performance steel after corrosion damage[J]. Journal of Constructional Steel Research,2023,207.
[17] Feng L, Zheng J, Guo Z, et al. Experimental study on the mechanical properties and ultimate strength of accelerated corrosion on hull plates[J]. Marine Structures,2024,95103591-.
[18] Sheng J, Xia J. Effect of simulated pitting corrosion on the tensile properties of steel[J]. Construction and Building Materials,2017,13190-100.
[19] Wang Y, Xu S, Wang H, et al. Predicting the residual strength and deformability of corroded steel plate based on the corrosion morphology[J]. Construction and Building Materials,2017,152777-793.
[20] Zhang Z, Xu S, Nie B, et al. Experimental and numerical investigation of corroded steel columns subjected to in-plane compression and bending[J]. Thin-Walled Structures,2020,151106735-106735.
[21] Zhiwei Z, Huajie W, Hongliang Q, et al. Comparative analysis and applicability of corrosion test methods for construction steel components[J]. Case Studies in Construction Materials,2023,18.
[22] Kumar V, Tiwari K S, Sharma N. Mechanical and surface characterization of interstitial-free steel corroded under wet-dry salt spray and immersion conditions: A comparative study[J]. Materials and Corrosion,2023,74(9):1289-1300.
[23] Songquan T, Huihui X ,Ni A, et al. Experimental investigation on corrosion fatigue crack initiation and growth of heat-treated U75V rail steel[J].International Journal of Fatigue,2024,178.
[24] Hiroaki T, Natsuko Y, Sayaka M, et al. Improved corrosion fatigue performance of 316L stainless steel by surface porosification[J]. Materials Letters,2023,353.
[25] Kainuma S, Jeong Y S , Ahn J H . Investigation on the stress concentration effect at the corroded surface achieved by atmospheric exposure test[J]. Materials Science and Engineering: A, 2014.
[26] An S L, Park C Y, Kim K H. An analytical approach to predict fatigue strength of corroded steel plates using random field-based corrosion surface modeling[J].Structures,2024,63106391-.
[27] Naftary G, Yasuo K. Effect of surface roughness on tensile ductility of artificially corroded steel plates[J]. Journal of Constructional Steel Research,2021,176106392-.
[28] Wei W, Yuan W, Jingqi H, et al. Mathematical Model of Surface Topography of Corroded Steel Foundation in Submarine Soil Environment[J]. Coatings,2022,12(8):1078-1078.
[29] Haipeng S, Jing L, Hao Z, et al. Multi-source data driven fatigue failure analysis and life prediction of pre-corroded aluminum–lithium alloy 2050-T8[J]. Engineering Fracture Mechanics,2023,292.
[30] Ren S, Kong C, Gu Y, et al. Measurement pitting morphology characteristic of corroded steel surface and fractal reconstruction model[J]. Measurement,2022,190.

Advanced Steel Construction – Vol. 21 No. 6 (2025) 488–499
DOI:10.18057/IJASC.2025.21.6.2

EXPERIMENTAL STUDY ON FATIGUE CRACK GROWTH RATE OF HIGH-STRENGTH STRUCTURAL STEELS

Zhao Fang [1], Fan Yang [2], Ai-Qun Li [2, 3, *], Wen-Jie Jia [4], Hai-Yi Yang [5] and Jing-Wen Yu [1]

[1] *School of Civil Engineering and Architecture, Nanjing Institute of Technology, Nanjing 211167, China*
[2] *School of Civil Engineering, Southeast University, Nanjing 210096, China*
[3] *Beijing Advanced Innovation Center for Future Urban Design, Beijing University of Civil Engineering and Architecture, Beijing 100044, China*
[4] *Jiangsu Hydraulic Research Institute, Yangzhou 225002, China*
[5] *School of Mechanics and Engineering Sciences, Shanghai University, Shanghai 200444, China*
** (Corresponding author: E-mail: liaiqun@bucea.edu.cn)*

ABSTRACT

The static tension test on smooth specimens and the fatigue crack growth rate test on CT specimens were conducted for two mild steels, Q235B and Q355B, and three high-strength steels, Q460C, Q550D and Q690D. The digital image correlation (DIC) technique was introduced and strain results around the crack tip were verified by finite element analysis. Material constants based on stress intensity factor (SIF) range and strain energy density factor (SEDF) range were obtained by fitting. A thorough survey of fatigue crack growth test results of high-strength steels in relevant literature was conducted and test results were compared. The scatter band upper bound of fatigue crack growth curves for each steel was obtained and compared with suggested curves in various design codes. The results show that the strains at the crack tip of specimens obtained by finite element analysis and DIC analysis are in good agreement with each other; The mean+2s curve in BS7910 and DNVGL-RP-210, along with the curves in WES2805 and IIW-2259-15, are all applicable to the design of the three high-strength steels, while the mean curve in BS7910 and DNVGL-RP-210 are not applicable and the curves suggested by ASME BPVC or JSME S NA1-2008 and FKM are too conservative; The crack growth rate slows down with the increase of the yield strength, demonstrating the trend of decrease in material constants m, n and |logC| while increase in |logA|, although the trend is not strictly followed; The scatter band upper bounds established based on either SIF or SEDF are applicable to fatigue crack growth analysis and design of the three high-strength steels.

ARTICLE HISTORY

Received: 30 November 2024
Revised: 22 February 2025
Accepted: 2 March 2025

KEYWORDS

Fatigue crack growth rate;
High-strength steel;
Digital image correlation;
Finite element analysis;
Strain energy density factor

1. Introduction

In recent years, high-strength steel has gained extensive attention, since it has been applied in various high-rise and long-span engineering structures including buildings, bridges, etc. However, high-strength steel is susceptible to fatigue crack growth at initial defects under cyclic loading, leading to structural fatigue failure. Therefore, it is indispensable to study the fatigue crack growth rate performance of high-strength steel.

Researchers started to pay attention to fatigue crack growth rate tests using compacted tension (CT) specimens made of different high-strength steels and obtained their material constants in Paris law based on stress intensity factor (SIF) range. Barsom et al.[1] investigated the fatigue crack growth rate of four high-strength steels, HY-80, HY130, 10Ni-Cr-Mo-Co and 12Ni-5Cr-3Mo, by fatigue test; Jesus et al.[2] compared the fatigue behavior between the S355 mild steel and the S690 high strength steel by fatigue crack growth test. The fatigue crack growth rate performance of high-strength steels in China including GB Q460, Q550, Q690 and Q960 were also presented; Tong et al.[3] studied the fatigue behavior of Q460C, Q550D, Q690D and Q960D by fatigue crack growth test; Ma et al.[4] conducted static tension and fatigue crack growth tests of base metal and welded joints of Q550E and established their growth models; Shen et al.[5] investigated fatigue crack growth behaviors of EH690 HSS welded joints in zones of base metal, heat affected zone and weld metal by fatigue crack growth test with various stress ratios; Guo et al.[6] studied the fatigue crack growth performance of Q690D HSS by the test on CT specimens with two plate thicknesses at three stress ratios.

The above researches provide valuable data for high-strength steel fatigue resistance design. However, if attention is paid to test data collection in these researches, it is found that conventional displacement data collecting devices such as extensometers were normally adopted during fatigue crack growth tests while some new non-contact displacement measuring methods like digital image correlation (DIC) were additionally introduced. Panwitt et al.[7] endeavored to measured fatigue crack growth path by DIC; Li et al.[8] proposed a method to determine crack tip position and fracture process zone in concrete based on DIC technique. The use of DIC in fatigue crack growth rate tests of high-strength steels has rarely been reported yet, since DIC is a relatively new method but a promising one.

However, it is worth noting that material constants in above literatures were obtained by fitting only based on a mean curve with a survival probability of 50%, which is absolutely unsafe for fatigue resistance design due to neglection of uncertainties during tests. Inspired by this, researchers began to establish scatter band upper bounds for crack growth curves. Some researchers even compared these upper bounds or mean curves with suggested ones in design codes. Zong et al.[9][10] obtained the fatigue crack growth constants of Q345D and Q690D with CT specimens considering a survival probability of 95% along with a confidence level of 95% and compared them with suggested values in BS7910; Song et al.[11] established fatigue crack growth curves of Ni-Cr-Mo-V steel base metal and welded joints considering strength mismatch effect and compared the mean curves with suggested ones in BS7910; Chen et al.[12] conducted fatigue crack growth tests on Q420C steel under constant amplitude of cyclic loading and compared them with those in BS 7910. However, the comparison of these test results with suggested curves was mostly limited to the code of BS 7910, though fatigue resistance design will surely benefit from the comparison with more codes.

In addition to the use of SIF in fracture analysis, strain energy density factor (SEDF) S is also widely used, which was proposed by Sih[13]. A more detailed comparison between these two approaches will be made in Section 6 in this study. Due to the lack of material constant data, the application of SEDF in fatigue crack growth analysis is rather limited, especially for the analysis of structural steel. Few researches were reported so far. Badaliance[14] postulated the crack growth rate to be a function of the SEDF range and correlated crack growth data of several different materials including the high-strength steel of HP9-4-30 and 300M; Shen[15] conducted fatigue crack growth rate test on CT specimens made of GB Q235B and obtained the material constants related to SEDF. Therefore, more material constant data of high-strength steels are most significant for SEDF approach in crack growth analysis.

To address all the problems raised above, the fatigue crack growth rate performance of structural steels of Q235B, Q355B, Q460C, Q550D and Q690D were studied by static tension test on smooth specimens and fatigue crack growth rate test on CT specimens in this paper. The DIC technique was introduced into the test and strain results around the crack tip were verified by finite element (FE) analysis. Material constants in both Paris law based on SIF range and crack growth rate equations based on SEDF range were obtained by fitting of test results. A thorough survey of fatigue crack growth test results of high-strength steels in relevant literature was conducted and test results were compared. The scatter band upper bound of fatigue crack growth curves for each steel was established and they were compared with suggested curves in various design codes.

The novelty of this study lies in three major aspects: (1) Both the mean and the upper bound of fatigue crack growth curves for Q235B, Q355B, Q460C, Q550D and Q690D were respectively obtained and they were comprehensively compared with suggested curves in various design codes to provide reference to fatigue resistance design in steel components and structures; (2) DIC as a new

non-contact measuring method was introduced into fatigue crack growth tests of high-strength steel and it was presented elaborately; (3) Material constants and curves for fatigue crack growth equations based on SEDF range were proposed for high-strength steels to guide fatigue crack growth analysis based on SEDF.

2. Static tension test

The static tension test was carried out to obtain basic mechanical properties of the five structural steels. A total of 15 smooth specimens were manufactured as shown in Fig.1(a), with 3 specimens for each group of steel grade as shown in Fig.1(b). The main chemical composition of each steel was shown in Table 1. The tension test was conducted on a testing machine of WDW-100 at room temperature as shown in Fig.1(c) and data were collected by an extensometer attached to it. A displacement rate of 10mm/min was exerted on each specimen continuously until the specimen was totally fractured. The material properties including the yield strength σ_y, tensile strength σ_u and elastic modulus E of each specimen was listed in Table 2 and their averages over each group were also listed.

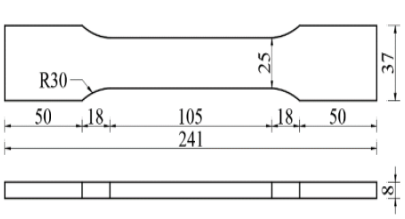

(a) Specimen plain figuration (Unit: mm)

(b) Manufactured specimens

(c) Specimen clamping

Fig. 1 Static tension test

Table 1
Chemical composition of each steel (%)

Steel	C	Si	Mn	P	S	Cr	Ni	Cu
Q235B	0.17	0.17	0.26	0.02	0.015	0.03	0.03	0.01
Q355B	0.21	0.14	0.42	0.022	0.01	0.03	0.02	0.01
Q460C	0.08	0.12	1.45	0.014	0.003	0.031	0.012	0.031
Q550D	0.079	0.17	1.05	0.016	0.003	0.041	0.019	0.020
Q690D	0.15	0.21	1.30	0.015	0.004	0.227	0.009	0.011

Table 2
Static tenstion test results

Steel	σ_y (MPa)	σ_u (MPa)	E (GPa)	Steel	σ_y(MPa)	σ_u (MPa)	E (GPa)
Q235B-1	313.00	447.00	180.12	Q460C-3	470.00	575.00	166.54
Q235B-2	329.00	448.00	176.54	**Q460C Avg**	**472.03**	**581.37**	**180.05**
Q235B-3	322.00	441.00	180.34	Q550D-1	622.00	692.00	185.09
Q235B Avg	**321.33**	**445.33**	**179.00**	Q550D-2	655.00	710.00	180.82
Q355B-1	473.00	583.00	183.42	Q550D-3	636.00	706.00	186.5
Q355B-2	473.00	591.00	180.30	**Q550D Avg**	**637.67**	**702.67**	**184.14**
Q355B-3	460.00	576.00	182.10	Q690D-1	707.00	755.00	194.2
Q355B Avg	**468.67**	**583.33**	**181.94**	Q690D-2	702.00	755.00	167.65
Q460C-1	474.10	582.10	184.9	Q690D-3	705.00	755.00	202.1
Q460C-2	472.00	587.00	188.71	**Q690D Avg**	**704.67**	**755.00**	**187.98**

It is found from Table 2 that mechanical properties of each steel in the specimens meet the requrement proposed by GB 55006-2021[16]. Three indexes including yield strengths, tensile strengths and elastic modulus all generally increase with the steel grade. It is worth noting that all three Q355B specimens are with rather high yield strengths and tensile strengths, which almost overtook those of Q460C specimens. It may mainly stem from the mechanical difference between various steel batches, since only the minumum values instead of maximun values of the yield strength and tensile strength are ruled in GB 55006-2021 and this batch of Q355B certainly meet the demands proposed in this code.

3. Fatigue crack growth rate test

The CT specimen designed according to GB/T 6398-2017[17] was shown in Fig.2(a) and it was with an initial notch with a length of a_{ini}=9+3.75=12.75mm from the center of the bolt. Two specimens were manufactured each for Q235B and Q355B and four specimens were manufactured each for three high-strength steels. The fatigue crack growth rate test was conducted on a fatigue testing machine PWS-100 in room temperature and the clamping of these specimens were shown in Fig.2(b). The crack length was observed with the help of a scale ruler attached to the specimen surface and an electron microscope placed in front of the testing machine. A crack with a length of 5.75mm was first prefabricated further based on the initial notch length of 12.75mm for each specimen by the exertion of sinusoid cyclic loading with a maximum value of F_{max}=37kN, a stress ratio of R=0.1 and a loading frequency of 30Hz. The fatigue crack growth test was subsequently started from a crack length of 5.75+12.75=18.5mm by the exertion of cyclic loading with the same loading as those in the prefabrication stage. The crack length a and the number of cycles N were both recorded at certain crack growth increments until the specimen was fractured with a sharp increase in the relative displacement between the two clamping ends. The failure mode of the specimen Q550D-1 was shown in Fig. 2(c). It is found that the section is clearly divided into several areas: the prefabricated notch, the crack initiation zone, the crack growth zone and the fracture zone. The crack initiation zone is located near the prefabricated notch tip with dark color and smooth section surface. The section surface gets rougher in the crack growth zone characterized by a stable crack growth. The fracture zone undergoes unstable fracture as soon as the crack reaches a critical length. The section surface gets rougher with plastic deformation and the crack grows in more irregular directions, which is similar to the characteristics of a static tension failure mode.

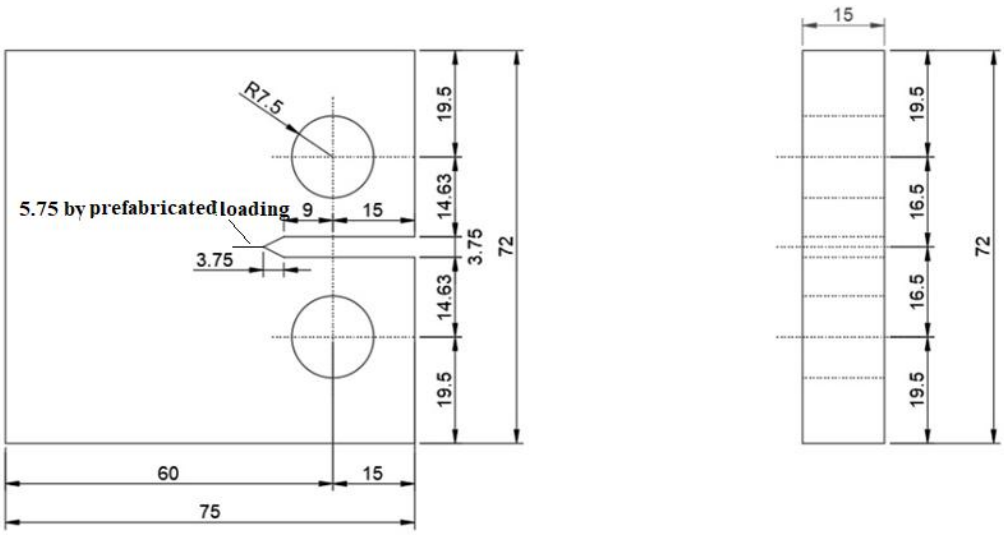

(a)Design of the specimen (Unit: mm)

(b) Clamping of the specimen

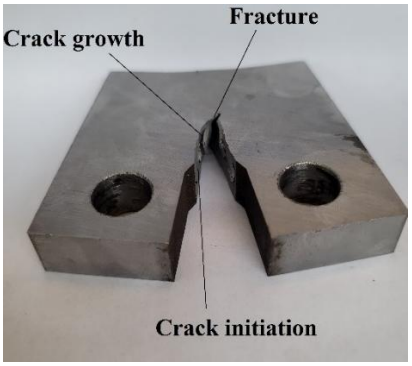

(c) Specimen of Q550D-1 after failure

Fig. 2 Fatigue crack growth rate test

The SIF K in a CT specimen is calculated according to Eq.(1) [17][18]:

$$K = \frac{F}{TW^{0.5}} g\left(\frac{a}{W}\right) \tag{1}$$

where a is the crack length; F is the loading force; T is the plate thickness and it is 15mm; W is the horizontal distance between the action line of the axial force and the far end of the specimen and it is 60mm; $g(a/W)$ is a shaping factor and it is calculated by Eq.(2)(3):

$$g\left(\frac{a}{W}\right) = \frac{(2+\alpha)\left(0.886+4.64\alpha-13.32\alpha^2+14.71\alpha^3-5.6\alpha^4\right)}{(1-\alpha)^{1.5}} \tag{2}$$

$$\alpha = \frac{a}{W},\ 0.2 \le \frac{a}{W} \le 1.0 \tag{3}$$

4. FE analysis

The FE analysis model of the CT specimen was established in the software ANSYS using the eight-node quadratic plane element named PLANE183 as shown in Fig.3(a). The mechanical properties of each steel in Table 2 were adopted in the analysis. Two uniform rows of sector elements were established around the crack tip and each row contained 18 sector elements (each with a sector angle of 10°) with a radius of r=0.1mm, as shown in Fig.3(b). The inner row of elements was simulated by modified PLANE183 with the mid-nodes skewed to the 1/4 point. The mesh size got sparser to 1mm gradually for regions away from the crack tip to save computing cost. A distributed force was applied to the nodes on the upper semicircle of the bolt hole to simulate the force by bolt.

The SIF K was calculated in ANSYS and only the results for typical crack lengths in the specimen Q550D-1 under F_{max}=37kN were given in Table 3 due to limitation on pages while other specimens showed the similar trend. The error, denoted as Er, between the FE analysis result $K_{max\text{-}fem}$ and the empirical solution $K_{max\text{-}solu}$ calculated by Eq.(1) were also listed.

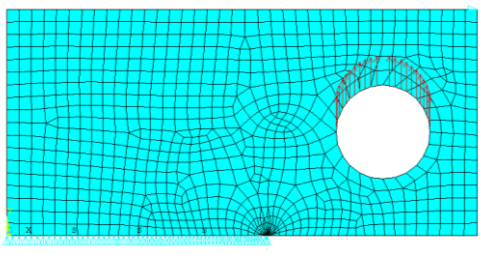

(a) Finite element model

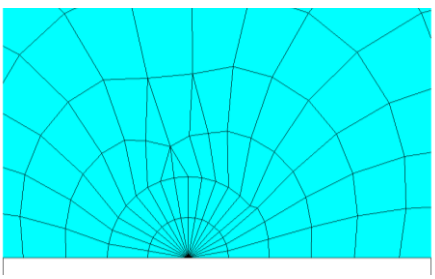

(b) Local meshing

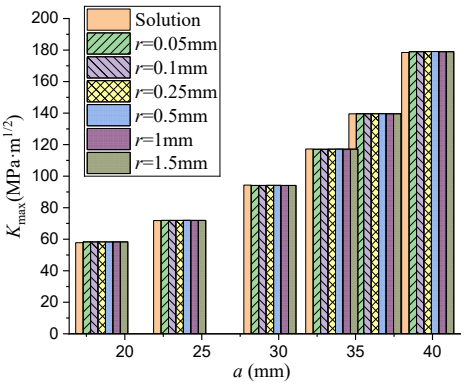

(c) SIFs under crack lengths

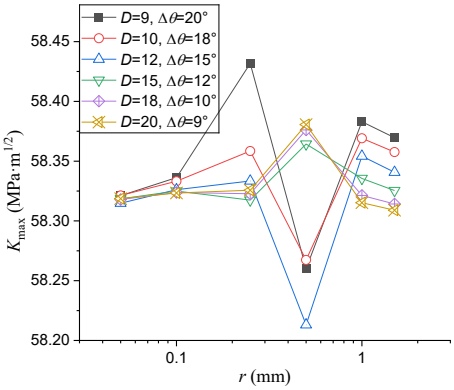

(d) SIFs using different mesh sizes

Fig. 3 Finite element analysis results

Table 3
Comparison of SIF results

a (mm)	$K_{max\text{-}solu}$ (MPa·m$^{1/2}$)	$K_{max\text{-}fem}$ (MPa·m$^{1/2}$)	Er	a (mm)	$K_{max\text{-}solu}$ (MPa·m$^{1/2}$)	$K_{max\text{-}fem}$ (MPa·m$^{1/2}$)	Er
18.5	57.782	58.302	0.90%	33.454	117.252	117.116	0.12%
23.566	71.831	71.959	0.18%	36.258	139.517	139.59	0.05%
29.428	94.332	94.142	0.20%	39.689	178.468	178.969	0.28%

It is found from Table 3 that the SIFs under different crack length obtained by FE analysis and empirical solution agree well with each other with an error less than 0.5%, which proves that the results by FE analysis are with sufficient accuracy. The mesh sensitivity check is indispensable for the SIF results around the crack tip since they are highly sensitive to the nearby mesh size. The number of the first row of sector elements around the crack tip D was fixed at 18 with a sector angle of 10° and the sector radius was changed into r=0.05mm, 0.1mm, 0.25mm, 0.5mm, 1mm and 1.5mm respectively for FE models with each crack length in Table 3. It is worth noting that the mesh size for the region away from the crack tip kept 0.5mm for the previous four radius conditions while it increased to 1mm for the latter two radius conditions to obtain high-quality meshing. The SIF results with various crack length and sector radius were illustrated in Fig.3(c). It is found that those results agree well with each other and all are close to the empirical solutions. It demonstrates that the crack length has little effect on the difference between SIFs obtained with different mesh size. Subsequently, the model with a crack length of a=18.5mm was selected and the number of the first row of sector elements around the crack tip D was change into 9, 10, 12, 15, 18 and 20 (the sector angle $\Delta\theta$ was 20°, 18°, 15°, 12°, 10° and 9°) while the sector radius r was also changed into 0.05mm, 0.1mm, 0.25mm, 0.5mm, 1mm and 1.5mm respectively. The change of SIF results with sector number D and sector radius r were illustrated in Fig.3(d) with a logarithmic coordinate in x-axis. It is found that the SIF gradually decreases and the discrepancy between each result also decreases with the increase in the sector element number D in general. The results of the models with $D \leq 12$ is relatively away from those with $D \geq 15$ for both r=0.25mm and 0.5mm while those with $D \leq 12$ were quite near to those with $D \geq 15$ for other four sector radius conditions. Thus, it is clear that the sector number D should be no less than 15 to get rather accurate results under each radius condition; Furthermore, the SIF results show a trend of decreasing after the first stage of increasing and it finally began to converge when $D \geq 15$. It should be noted that there is a negligible discrepancy rate of around 0.1% between the results with r=0.5mm or r=1mm and those with other four radius conditions, which may result from the difference in mesh sizes away from the crack tip. Therefore, it is concluded from the above analysis that rather accurate results can be obtained with a sector radius of r=1mm and a sector number of D=15 in this FE model.

5. DIC analysis

Comparison of results obtained by DIC analysis and FE analysis needs to be made to verify the accuracy of the test results. DIC is a non-contact measurement method which can calculate the full-field displacements and strains of the observed object. High-contrast and high-density speckle is required on the surface of the object and the images of the object are captured by a HD camera with the help of reliable light source for a 2D DIC analysis. The selected section of images captured called subsets are analyzed based on advanced algorithms which measure displacements of points by correlation between reference subsets before deformation and deformed subsets after deformation, as shown in Fig.4(a). For example, the reference subset before the deformation with a center point P (x, y) becomes the deformed subset with a center point P' (x', y') after the deformation, with a horizontal displacement of u and a vertical displacement of v as shown in Fig.4(b). To get all the information of correlation between the reference subset and the deformed subset, some certain neighboring points (pixels) need to be analyzed. Take the point Q (x+Δx, y+Δy) which becomes Q' (x'+$\Delta x'$, y'+$\Delta y'$) after the deformation for example, the coordinates of it meet Eq.(4) and Eq.(5)[19]:

$$x' + \Delta x' = x + u(P) + \frac{\partial u(P)}{\partial x}\Delta x + \frac{\partial u(P)}{\partial y}\Delta y + \Delta x \tag{4}$$

$$y' + \Delta y' = y + v(P) + \frac{\partial v(P)}{\partial x}\Delta x + \frac{\partial v(P)}{\partial y}\Delta y + \Delta y \tag{5}$$

The unknown horizontal and vertical displacements along with their gradients in the equations are optimized with the best correlation between the subsets for all the pixels. After the correlation, the displacement of discretized subsets of the whole image is tracked and thus the displacement vectors and strain field of the object are further obtained.

Two CT specimens made of GB Q355B were selected to conduct the fatigue test with 2D-DIC analysis. One lateral surface of the specimen was evenly sprayed with matte white paint and black paint to form sharp-contrast and high-density speckles with a size around 0.3mm-0.6mm, as shown in Fig. 4(c). The camera was set firmly on a tripod and the light source was placed at a proper distance from the specimen to keep adequate illumination as shown in Fig.4(d). The full-length video of the test for the specimen was recorded by a high-definition camera with a resolution of 1920×1080 pixels and an FPS of 60. Regarding to the image scale calibration, it was observed that one pixel approximately corresponded to a spatial area of 0.0786 × 0.0786 mm^2 on the object.

As a non-contact measurement method, DIC is inevitably with errors during the test. There are normally two types of errors in DIC analysis: bias errors and variance errors. Bias errors refer to an offset of the mean from the true value while variance errors refer to random errors centered with the mean about the true value. The following main errors during the test were considered and the measures to mitigate them were taken:

(1) Lens distortion. Lens distortion results in some kind of deformation of images, which brings bias error to DIC results. To minimize the effect of lens distortion, the focal length of the camera was adjusted to make the FOV approximately the same size as the specimen in Fig.4(c) and thus the crack to be observed was positioned in the center of the frame where lens distortion was least noticeable.

(2) Out-of-plane motion. This is a main source of bias errors for 2D DIC analysis. The motion of the specimen should be completely parallel to the lens since out-of-plane motion (motion vertical to the lens) brings bias errors to the test. During the calibration stage, the distance of four specimen corners to the

lens was carefully measured and checked to make sure the specimen surface was parallel to the lens. Both the camera and the specimen were carefully adjusted in such a way that the loading and reactions act in the plane of the specimen.

(3) Vibration during the test. There are two types of vibration involved during the test, which are the camera vibration and the specimen vibration. The camera vibration was far smaller than the specimen vibration. As mentioned above, the camera was placed firmly on a tripod and some foam boards were placed between the tripod and ground to avoid potential ground vibration induced by the test machine vibration. The specimen vibration was relatively large and difficult to mitigate. The frequency of the cyclic loading during the fatigue test in DIC analysis was reduced to 2Hz to decrease the effect of the specimen vibration.

(4) Limitation of the camera. The camera was with an FPS of only 60. As mentioned above, the frequency of the cyclic loading during the fatigue test in DIC analysis was adjusted to 2Hz to enhance the accuracy of the video capture and thus there were 30 images for one full cycle. Before the test, the camera was turned on to warm up to a stable working temperature.

To verify the effect of the above error sources, a motionless test was conducted on the two specimens in advance before the crack prefabrication to estimate the accuracy of the DIC system. No loading or deformation was applied on the CT specimens and thus the results including vertical displacement of the notch tip u_y and the strain in the vertical direction ε_y at the notch should ideally be zero. The variation of u_y and ε_y within recorded images was illustrated in Fig.4(e)(f). It is found that both the displacement and the strain fluctuated within these images, and the strain data fell into a more intensive region than the displacement data, since some strain data of the two specimens overlapped each other. The distribution of u_y and ε_y was additionally illustrated in Fig.4(g)(h). It is found that both the displacement and the strain within two specimens demonstrated normal distribution. The mean value *mu* of the vertical displacement is around ±1μm and that of the strain is around ±0.005% (5×10^{-5}), which represents the bias error while the variance $sigma^2$ represents the variance error. Fig.4(h) demonstrates that the variation of ε_y is within ±0.03% ($\pm3\times10^{-4}$), which is far smaller than the vertical strain ε_y in the following fatigue test. Therefore, it is concluded that the above-mentioned errors are relatively small and can be ignored. It is worth noting that the error resulted from vibration during the test cannot be taken into account in the motionless test since the motionless test can only consider the errors in a static condition. However, the results obtained by FE analysis and DIC analysis will be compared in the following paragraph to verify the accuracy of the DIC analysis results.

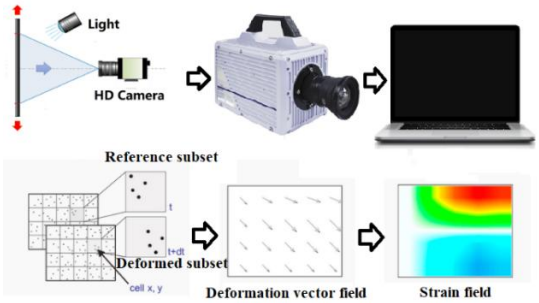

(a) DIC fundamentals

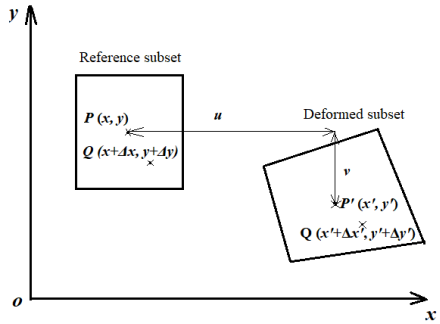

(b) Deformation of subset

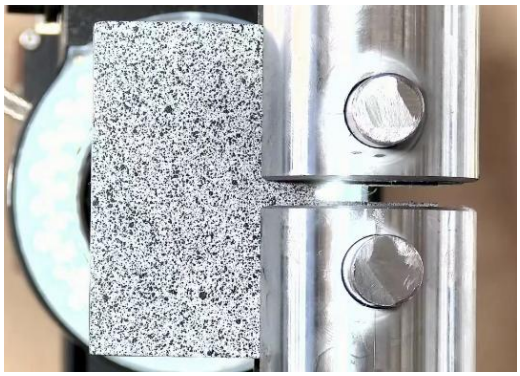

(c) Speckle on the specimen surface

(d) DIC system setup

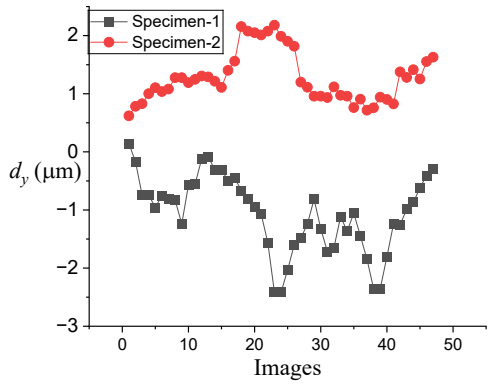

(e) Motionless test displacement with images

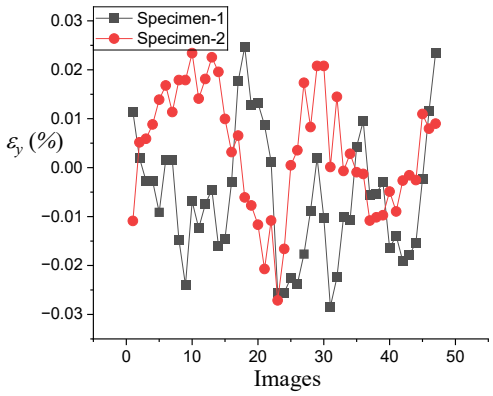

(f) Motionless test strain with images

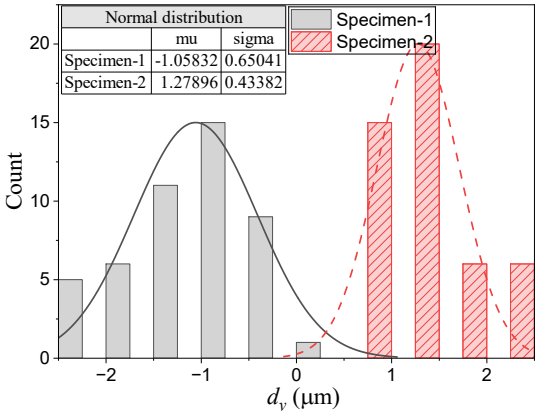

(g) Motionless test displacement distribution

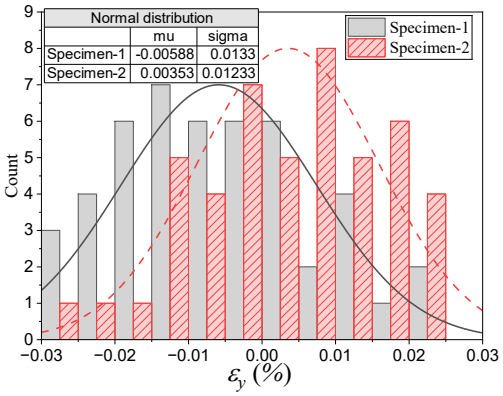

(h) Motionless test strain distribution

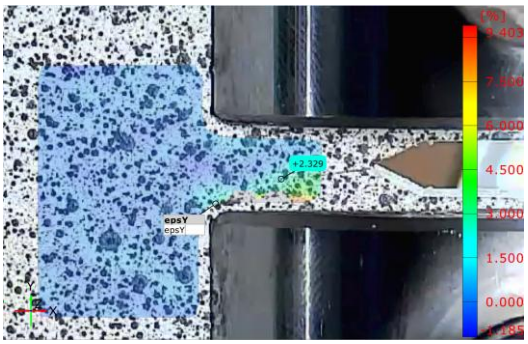

(i) Strain contour of ε_y by DIC for Specimen 1 with a=19.574mm (Unit: %)

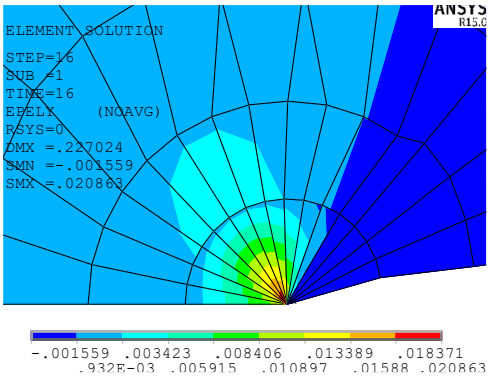

(j) Strain contour of ε_y by FE analysis for Specimen 1 with a=19.574mm (Dimensionless quantity)

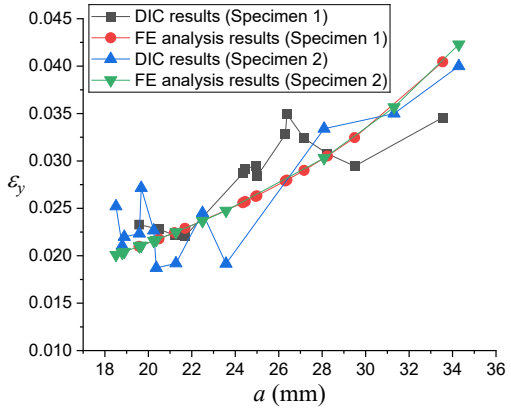

(k) Local strain comparison for DIC and FE analysis

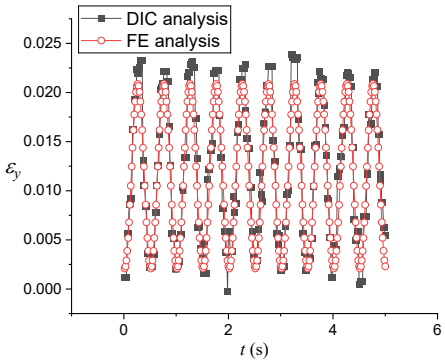

(l) Comparison of local strain time-history for DIC and FE analysis (Specimen 1with a=19.574mm)

Fig. 4 DIC analysis

The prefabrication of the crack was further conducted for these two specimens with the same loading described in Section 4 while the frequency of the cyclic loading was reduced to 2Hz. The videos were further analyzed in the DIC-processing software GOM Correlate. Due to the limitation on pages, only the contour map of the maximum strain within one cycle in the vertical direction (Y-axis direction) ε_y around the crack tip for Specimen 1 with a certain crack length was illustrated in Fig.4(i) and that obtained by FE analysis with the same crack length was illustrated in Fig.4(j). The figure reveals that the strain distribution near the crack tip by DIC analysis generally agrees well with that by FE analysis. All the ε_y values around the crack tip in each crack increment were illustrated in Fig.4(k) to fully compare all the strain data. It is found that most strain data near the crack tip calculated by DIC analysis and by FE analysis agree well with each other, since the discrepancy rate between them for all strain data were within or around 20%, with a maximum of 22% and a minimum of 1%. The comparison of the strain time history near the crack tip for DIC analysis and FE analysis needs to be presented, for the strain was fluctuating during the test. Due to the limitation on pages, only the strain time history in Specimen 1 with a crack length of 19.574mm was illustrated in Fig.4(l) and others showed similar trends. It is found that the strain by these two types of analysis both fluctuate synchronously with the time, with a uniform frequency of 2Hz and a maximum discrepancy rate below 10%. Therefore, it proves the fact that the results obtained by DIC analysis agree well with those by FE analysis and the test results are sufficiently accurate, even with the error resulted from vibration during the test.

6. Fatigue cack growth rate data analysis

Paris law based on the SIF range is shown in Eq.(6):

$$da/dN = C(\Delta K)^m \tag{6}$$

Where N is the number of cycles; da/dN is the crack growth rate; ΔK is the SIF range; C and m are material-dependent constants. Take logarithms on both sides in Eq.(6) to get the linear equation of Eq.(7) and the constants of C and m are obtained through linear fitting of fatigue test data.

$$lg\frac{da}{dN} = lgC + mlg\Delta K \tag{7}$$

SEDF S is defined by the multiplication of total strain energy stored per unit volume with a specific critical distance r away from the point of singularity at the crack tip, as shown in Eq.(8):

$$S = \omega \cdot r = \lim_{\Delta V=0} \frac{\Delta W_t}{\Delta V} \cdot r = \frac{dW_t}{dV} \cdot r \tag{8}$$

where ΔW_t is the total strain energy within a volume of ΔV, thus leading to a strain energy density ω. The use of SEDF is able to determine not only the crack growth rate but also the crack growth direction from its minimum value around the crack tip[20]. The relation of it with SIF in a mode I crack K_I is shown as Eq.(9), while other crack modes are not discussed due to limitation on pages.

$$S = a_{11} K_I^2 \tag{9}$$

$$a_{11} = \frac{1}{16\pi G}(1 + cos\theta)(\kappa - cos\theta) \tag{10}$$

$$G = E/2(1 + \upsilon) \tag{11}$$

$$\kappa = \begin{cases} 3 - 4\upsilon, & \text{plain strain} \\ (3 - \upsilon)/(1 + \upsilon), & \text{plain stress} \end{cases} \tag{12}$$

where a_{11} and κ are coefficients calculated by Eq.(10) and Eq.(12); G is the shear modulus calculated by Eq.(11); υ is the Poisson's ratio; θ is the angle in the polar coordinate around the crack tip. The crack growth rate da/dN is thus calculated by Eq.(13)[14][20]:

$$\frac{da}{dN} = A(\Delta S)^n \tag{13}$$

where ΔS is the SEDF range; A and n are material-dependent constants. The definition of these two constants for each material requires numerous fatigue crack growth tests, similar to Paris law. The use of SEDF in fatigue crack growth analysis is rather limited due to the lack of related test data, which is considered as the most vital shortcoming in this method. It is worth noting that the SEDF range ΔS is deduced into Eq.(14) according to Eq.(9):

$$\Delta S = a_{11}(K_{Imax}^2 - K_{Imin}^2) = 2a_{11}\overline{K}_I \Delta K_I = a_{11}(1 - R^2)K_{Imax}^2 \tag{14}$$

where $\overline{K}_I$ is the mean value of K_I. It is found from Eq.(14) that the use of SEDF range is able to consider the effect stress ratio by the use of mean stress[20]. Eq.(13) is further deduced into the linear equation of Eq.(15) to get a linear relation.

$$lg\frac{da}{dN} = lgA + nlg\Delta S \tag{15}$$

It has been proved that the use of SEDF is able to obtain both rather accurate fatigue crack growth rate results and crack growth direction results[20-23]. Unfortunately, the direct comparison of prediction accuracy between these two methods when dealing with fatigue crack growth is rarely reported in current literature. Choi et al.[22][23] applied both SEDF method and Pris law to fatigue crack growth analysis of in-plane and out-of-plane gusset welded joints to obtain the material constants data while they conducted the crack growth prediction only based on SEDF method; Sih and Tang[24] demonstrated the use of both methods simultaneously in the assurance of reliable time limits in fatigue with reliability analysis while the conclusion cannot be applied to fatigue crack growth test analysis. The above comparison is summarized in Table 4.

Table 4
Comparison of SIF and SEDF methods

	Paris law	Equation based on SEDF
Key index	SIF	SEDF
Key index purpose	To describe the severity of the stress distribution around the crack tip	
Method based on	Stress and strain	Energy
Applicability	Crack growth rate analysis	Crack growth rate & direction analysis
Consider stress ratio	Unable, unless a modification is used	Able
Test data sources	Wide	Limited
Prediction effect	Accurate	

Based on the above knowledge, the fatigue test data were processed by secant method as shown in Eq.(16)[18]:

$$(da/dN)_{\bar{a}} = (a_{i+1} - a_i)/(N_{i+1} - N_i) \tag{16}$$

where $(da/dN)_{\bar{a}}$ is the average crack growth rate over the increment of $(a_{i+1} - a_i)$; The SIF range ΔK and the SEDF range ΔS within each increment is calculated using the average crack length $(a_{i+1} + a_i)/2$.

The relation between the crack length a and the number of cycles N recorded during the crack growth of all specimens was plotted in Fig.5(a), where the crack growth rate (da/dN) is indicated by the slope of each curve. It is found from the figure that the crack growth rates of various steels gradually decrease with the increase of the yield strength and however the trend is not strictly followed. For example, discreteness is found in the a-N curves of Q550D, where the curves of Q550D-1 and Q550D-2 are close to each other with a growth rate even lower than that of all specimens of Q690D, while the curves of Q550D-3 and Q550D-4 are close to each other which fall between those of Q460C and Q690D. This discreteness may be due to the difference in steel batches and randomness in manufacture. It has also been noted by Tong et al[3] that there are some differences in the crack growth test results of different batches of steel plates even with similar strength. It is worth noting that the crack growth rate of the two specimens of Q355B in this test is even slower than that of Q460C due to the fact that they generally share similar yield strengths as listed in Table 2.

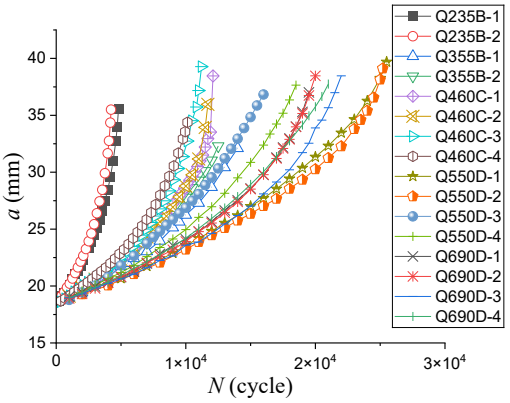

(a) a-N curve

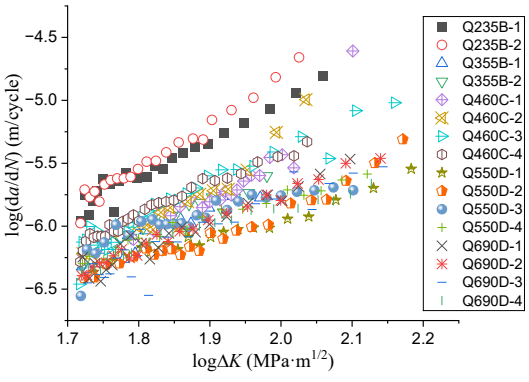

(b) Log(da/dN)-logΔK curve by single specimen

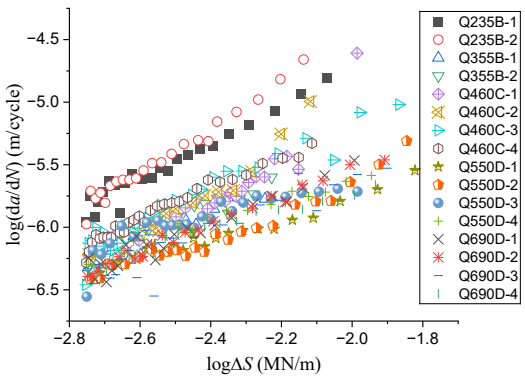

(c) Log(*da*/*dN*)-logΔS curve by single specimen

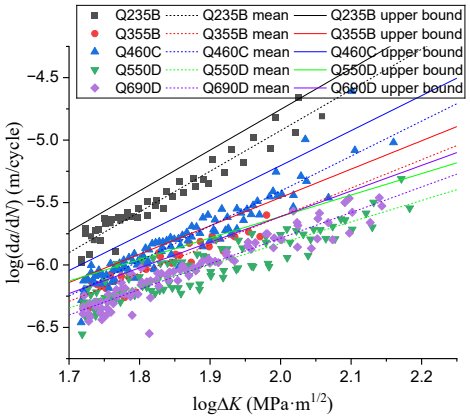

(d) Log(*da*/*dN*)-logΔK curve by specimen groups

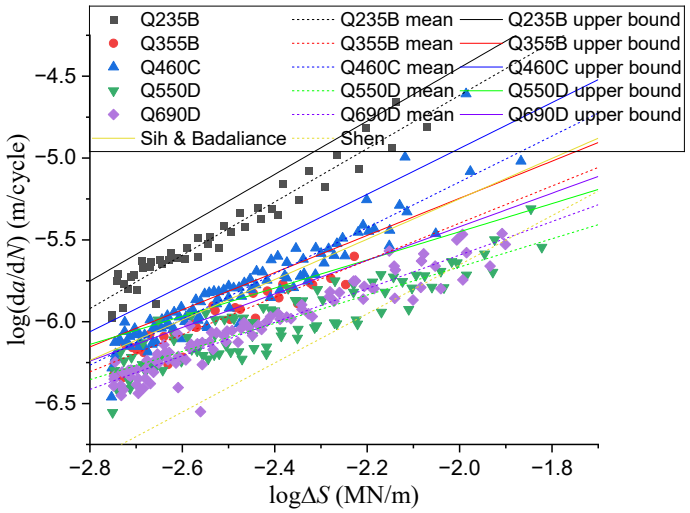

(e) Log(*da*/*dN*)-logΔS curve by specimen groups

Fig. 5 Test data analysis

Table 5
Fitting results of specimens

Specimen	Paris law by SIF range (Unit: da/dN-m/cycle, ΔK-MPa·m$^{1/2}$)				Crack growth rate equation by SEDF range (Unit: da/dN-m/cycle, ΔS-MN/m)			
	m	log$C$	C	R_1^2	n	log$A$	A	R_2^2
Q235B-1	2.978	-10.966	1.081×10^{-11}	0.948	1.489	-1.753	1.766×10^{-2}	0.948
Q235B-2	3.635	-12.087	8.185×10^{-13}	0.973	1.818	-0.838	1.452×10^{-1}	0.973
Average	**3.307**	**-11.526**	**2.979×10^{-12}**	**0.961**	**1.653**	**-1.296**	**5.058×10^{-2}**	**0.961**
Group	**3.258**	**-11.439**	**3.639×10^{-12}**	**0.935**	**1.629**	**-1.359**	**4.375×10^{-2}**	**0.935**
Q355B-1	2.243	-10.129	7.430×10^{-11}	0.811	1.122	-3.189	6.471×10^{-4}	0.811
Q355B-2	2.197	-9.989	1.026×10^{-10}	0.911	1.098	-3.193	6.412×10^{-4}	0.911
Average	**2.220**	**-10.059**	**8.730×10^{-11}**	**0.861**	**1.110**	**-3.191**	**6.442×10^{-4}**	**0.861**
Group	**2.270**	**-10.151**	**7.063×10^{-11}**	**0.857**	**1.135**	**-3.128**	**7.447×10^{-4}**	**0.857**
Q460C-1	3.057	-11.534	2.924×10^{-12}	0.839	1.528	-2.077	8.375×10^{-3}	0.839
Q460C-2	3.407	-12.140	7.244×10^{-13}	0.906	1.704	-1.597	2.529×10^{-2}	0.906
Q460C-3	2.728	-10.867	1.358×10^{-11}	0.931	1.364	-2.426	3.750×10^{-3}	0.931
Q460C-4	2.591	-10.592	2.559×10^{-11}	0.966	1.295	-2.577	2.649×10^{-3}	0.966
Average	**2.946**	**-11.283**	**5.212×10^{-12}**	**0.911**	**1.473**	**-2.169**	**6.776×10^{-3}**	**0.911**
Group	**2.800**	**-11.008**	**9.817×10^{-12}**	**0.894**	**1.400**	**-2.345**	**4.519×10^{-3}**	**0.895**
Q550D-1	1.593	-9.108	7.798×10^{-10}	0.958	0.796	-4.180	6.607×10^{-5}	0.958
Q550D-2	2.153	-10.159	6.934×10^{-11}	0.942	1.077	-3.496	3.192×10^{-4}	0.942
Q550D-3	1.571	-8.897	1.268×10^{-9}	0.768	0.785	-4.037	9.183×10^{-5}	0.736
Q550D-4	1.789	-9.354	4.426×10^{-10}	0.969	0.894	-3.819	1.517×10^{-4}	0.969
Average	**1.776**	**-9.379**	**4.178×10^{-10}**	**0.909**	**0.888**	**-3.883**	**1.309×10^{-4}**	**0.901**
Group	**1.721**	**-9.270**	**5.370×10^{-10}**	**0.803**	**0.861**	**-3.944**	**1.138×10^{-4}**	**0.803**

Q690D-1	2.286	-10.301	5.000×10^{-11}	0.931	1.143	-3.230	5.888×10^{-4}	0.931
Q690D-2	2.233	-10.202	6.281×10^{-11}	0.986	1.116	-3.295	5.070×10^{-4}	0.986
Q690D-3	2.179	-10.155	1.081×10^{-11}	0.854	1.089	-3.414	1.766×10^{-2}	0.986
Q690D-4	1.591	-9.042	8.185×10^{-13}	0.961	0.796	-4.119	1.452×10^{-1}	0.961
Average	**2.072**	**-9.925**	**2.979×10^{-12}**	**0.933**	**1.048**	**-3.470**	**5.058×10^{-2}**	**0.909**
Group	**2.051**	**-9.888**	**3.639×10^{-12}**	**0.902**	**1.026**	**-3.542**	**4.375×10^{-2}**	**0.902**

The relations between the logarithm of the crack growth rate da/dN and the SIF range ΔK or the SEDF range ΔS for each single specimen were illustrated in Fig.5(b)(c) and a nearly linear correlation is found for each specimen. Additionally, the above relations for each group of the same steel were plotted as shown in Fig.5(d)(e). The crack growth constants m, log$C$, n and log$A$ were obtained by fitting using the test data in each single specimen or in specimen groups respectively based on Eq.(7) and Eq.(15). The results along with the average constants over each group were listed in Table 5. The coefficients of determination R_1^2 and R_2^2 for SIF method and SEDF method were given respectively.

It is found from Table 5 that with the increase of the yield strength, m and n both show a generally gradual decreasing trend while the absolute value of log$C$ and log$A$ gradually decreases and increases respectively, with the straight lines gradually moving down in Fig.5(b)-(e), although the trend is not strictly followed. Based on the comparison between the average fitting results over each single specimen and the direct fitting results by specimen group, it is found that they are relatively close to each other with a difference rate less than 5%, which reveals that either method leads to accurate results. It is also found that the coefficient of determination for most specimens are higher than 0.9 although they get slightly lower to around 0.8 in some specimens due to uncertainties, which indicates that linear correlation exists between both lg(da/dN) and lg(ΔK), or lg(da/dN) and lg(ΔS), with generally good fitting effect.

7. Test results comparison and guidance to design

The crack growth test results of high-strength steel CT specimens based on the SIF range ΔK in related literatures were fully summarized in Table 6 and plotted in Fig.6(a). It is found that the straight line of each test result generally moves downward with the increase in the yield strength, indicating a slower crack growth rate, however, which is not strictly followed. Moreover, it is found that the crack growth rate constants of the same steel in this test and in related literatures are relatively close to each other with consistency, which verifies the reasonability of the results obtained in this test. However, there are few crack growth rate test data of structural steel based on SEDF. The limited data from two relevant literatures were listed in Table 7 and represented in Fig.5(e). It is found that the constants obtained in this test is in good agreement with those in these two literatures.

Although it has been reported that scatter of fatigue crack growth of visible cracks is generally lower than that of fatigue crack iniatiaion[36], Table 5 still reveals some sort of uncertainties leading to test result scatter. In general, uncertainties may stem from a wide range of sources including material inhomogeneity, batch differences, specimen production differences, specimen surface quality differences, specimen variability, test load errors, laboratory environment variation, etc. These uncertainties are normally considered by statistical analysis of test data.

The test data for each steel were processed in material groups based on the assumption of a normal distribution in variables. The upper bound for the test data in each group was illustrated in Fig.5(d)(e), which represented a survival probability of α'=95% (5% probability of failure) with a one-sided confidence level of γ=95% (corresponding to an actual survival probability of α=97.7%). The fitted constants for the upper bounds were all listed in Table 8. It is found that almost all the test data falls under the upper bound for each material as shown in Fig.5(d)(e). Each upper bound is considered as a specific design curve for each steel, since it meets the demand of a design curve with a survival probability of α=97.7%.

Table 6
Test constants in literatures based on ΔK (Unit: da/dN-m/cycle, ΔK-MPa·m$^{1/2}$)

Researcher	Steel grade	R	T(mm)	σ_y (MPa)	m	C	lg$C$
Zong et al. [9]	Q345qD	0.1	10.00	363	2.870	9.772×10^{-12}	-11.010
Liao et al. [25]	Q345qD	0.1	13.85	382	2.653	1.970×10^{-11}	-10.705
Tong et al. [3]	Q460C	0.1	10.00	481	2.460	4.140×10^{-11}	-10.383
Ma et al. [4]	Q550E	0.1	8.00	605	2.130	1.549×10^{-10}	-9.810
Tong et al. [3]	Q550D	0.1	10.00	704	2.644	1.530×10^{-11}	-10.816
Guo et al. [6]	Q690D	0.1	15.08	732	2.682	1.866×10^{-11}	-10.729
Tong et al. [3]	Q690D	0.1	10.00	801	1.928	1.920×10^{-10}	-9.718
Tan et al. [26]	Q690	0.1	15.00	≥690	2.215	6.890×10^{-11}	-10.162
Shen et al. [27]	EH690	0.1	12.70	797	2.720	1.090×10^{-11}	-10.963
Zong et al. [10]	Q690D	0.1	10	788	2.600	1.517×10^{-11}	-10.819
Chen et al. [12]	Q420C	0.1	12	430	3.090	4.080×10^{-12}	-11.389
Lukacs et al. [28]	S690QL	0.1	13	791	1.700	8.070×10^{-10}	-9.093
Wang et al. [29]	E690	0.1	2	≥690	2.999	3.531×10^{-12}	-11.452
Yang et al. [30]	Q420B	0.1	20	442	2.580	3.400×10^{-11}	-10.469
Wang et al. [31]	10Ni5CrMoV	0.1	5	811	1.926	2.701×10^{-10}	-9.568
Zhong et al. [32]	EH36	0.1	10	449	2.996	7.775×10^{-12}	-11.109
Duan et al. [33]	HPS 485W	0.1	7.5	≥485	2.840	1.050×10^{-11}	-10.979
Wang et al. [34]	HPS 485W	0.1	12.5	520	2.530	2.190×10^{-11}	-10.660
Song et al. [11]	10CrNi3MoV	0.1	8	710	2.650	1.240×10^{-11}	-10.907
Zong et al. [35]	WNQ570	0.1	10	495	2.800	3.981×10^{-12}	-11.400

Table 7
Test constants in literatures based on ΔS (Unit: da/dN-m/cycle, ΔS-MN/m)

Researcher	Steel grade	R	T(mm)	σ_y (MPa)	n	A	lg$A$
Sih [21] and Badaliance [14]	300M	-	-	1620	1.234	1.660×10^{-3}	-2.781
Shen [15]	Q235B	0.1	14.00	235	1.500	2.230×10^{-3}	-2.652

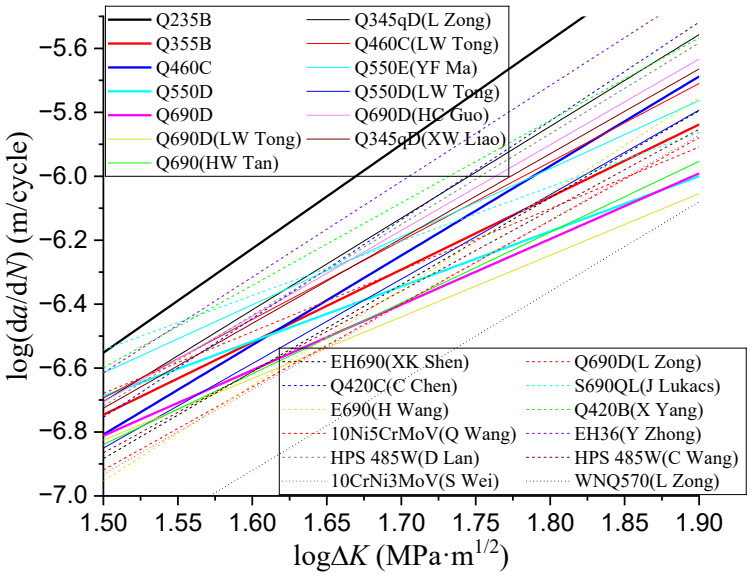

(a) Comparison with results in literatures

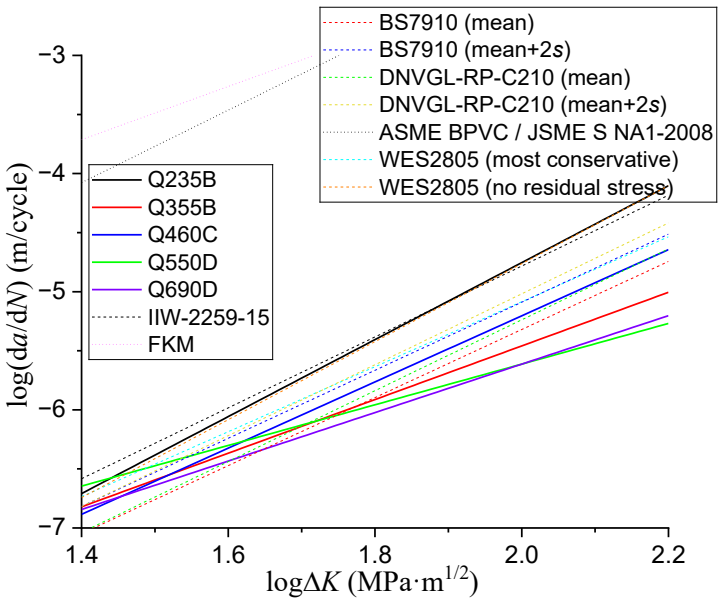

(b) Comparison with design curves

Fig. 6 Comparison of results

Table 8
Fitting results of specimens with α'=95% and γ=95% ($\alpha\approx97.7\%$)

Specimen	Paris law by SIF range (Unit: da/dN-m/cycle, ΔK-MPa·m$^{1/2}$)			Crack growth rate equation by SEDF range (Unit: da/dN-m/cycle, ΔS-MN/m)		
	m	log$C$	C	n	log$A$	A
Q235B	3.258	-11.270	5.369×10^{-12}	1.629	-1.191	6.446×10^{-2}
Q355B	2.270	-9.999	1.002×10^{-10}	1.135	-2.976	1.057×10^{-3}
Q460C	2.800	-10.804	1.570×10^{-11}	1.400	-2.140	7.237×10^{-3}
Q550D	1.721	-9.055	8.812×10^{-10}	0.861	-3.729	1.866×10^{-4}
Q690D	2.051	-9.715	1.926×10^{-10}	1.026	-3.369	4.279×10^{-4}

Several fatigue crack growth design curves based on Paris law have been proposed in design codes and standards. Some typical ones are listed in Table 9. It is worthwhile comparing the design curves in these codes with those upper bounds established in this study. It is worth noting that the comparison is based on the Paris law since SEDF method is adopted in none of these codes. The codes are briefly introduced as follows and the related constants are all listed in Table 9:

(1) IIW-2259-15[37] is the design code suggested by International Institute of Welding (IIW). Generally, it is a code for welded joints but it also gives the suggested crack growth curve constants for the base metal of common steel. The constants listed in Table 9 represent the upper bound with a survival probability α'=95% at a two-sided confidence level of the mean of γ=75% (corresponding to an actual survival probability of α=97.7%, i.e., mean minus two standard deviations 2s).

(2) BS7910 2019[38] is a standard issued by the British Standards Institution, which gives the suggested crack growth curve constants for common steel. It suggests two types of curves: a simplified curve for preliminary screening assessment and a precise two-stage curve for accurate assessment. The Stage b curve for the two-stage type was selected and its mean curve and the upper bound (α=97.7%, i.e., mean minus two standard deviations 2s) were listed respectively.

(3) DNVGL-RP-C210[39][40] is a fatigue design code for offshore steel structures issued by DNV. It also suggests the crack growth curve constants for common steel under air condition. It contains a mean curve and an upper bound curve (α=97.7%, i.e., mean minus two standard deviations 2s).

(4) FKM[41][42] is a German guideline for fracture evaluation. It gives the upper limit of scatter band of steels.

(5) WES2805[43] is the code for fusion welded joints issued by the Japan Welding Engineering Society. It gives two curves for common steel: a most conservative curve and a curve for cracks growing with no residual stress and a stress ratio of R=0.

(6) ASME BPVC[44] and JSME S NA1-2008[45] both gives the same crack growth curve constants for ferritic steel in air environment as shown in Eq.(17). The constants were thus calculated according to Eq.(17).

$$C = 3.78 \times 10^{-12} \cdot 25.72 \cdot (2.88 - R)^{-3.07} \quad (0 \le R < 1) \tag{17}$$

Table 9
Paris law constants in codes (Unit: da/dN-m/cycle, ΔK-MPa·m$^{1/2}$)

No.	Code	Material type	R	m	C	lg$C$
1	IIW-2259-15 (mean+2s, α=97.7%)	Steel	-	3.000	1.650×10^{-11}	-10.783
2	BS7910 2019 (mean)	Steel	<0.5	2.880	8.320×10^{-12}	-11.080
3	BS7910 2019 (mean+2s, α=97.7%)	Steel	<0.5	2.880	1.410×10^{-11}	-10.849
4	DNVGL-RP-C210 (mean)	Steel	-	3.000	5.790×10^{-12}	-11.238
5	DNVGL-RP-C210 (mean+2s, α=97.7%)	Steel	-	3.000	9.604×10^{-12}	-11.018
6	FKM	Steel	-	2.250	1.370×10^{-7}	-6.863
7	WES2805 (most conservative)	Steel	-	2.750	2.600×10^{-11}	-10.585
8	WES2805 (no residual stress and R=0)	Steel	0	3.300	4.340×10^{-12}	-11.363
9	ASME BPVC/ JSME S NA1-2008	Ferritic steel	0.1	3.070	4.213×10^{-9}	-8.375

All the curves were simultanously illustrated in Fig.6(b). It is found that the curve suggested by ASME BPVC 2007 and JSME S NA1-2008 for ferritic steel and that by FKM seem too conservative for all the steels in this study, since they are rather high above all the other curves in the figure. Other curves except these two seem rather close to each other. It is found that the upper bound of Q235B falls above the other upper bounds while IIW-2259-15 and WES2805 are barely enough to cover the upper bound of Q235B, which means these two design curves are applicable to the design of all the steels in this study. However, it must be kept in mind that the above analysis is based on the fact that there are only two specimens involved each for Q235B and Q355B, leading to a tremendous rise in the effect of uncertainty. The comparison of the other three high-strength steels is much simpler, since there are sufficient number of specimens. It is found that all the curves except BS7910 (mean) and DNVGL-RP-210 (mean) fall above the upper bounds of the three high-strength steels in most ranges of logΔK as shown in Fig.6(b). It demonstates that BS7910 (mean+2s), DNVGL-RP-210 (mean+2s), WES2805 and IIW-2259-15 are all applicable to the design of these three high-strength steels, while BS7910 (mean) and DNVGL-RP-210 (mean) are both not applicable due to the neglection of scatter upper bound.

It is worth noting that due to the low m value in Paris law for Q550D, most of the above design curves no longer cover the upper bound of Q550D when logΔK is approxmately smaller than 1.5 MPa·m$^{1/2}$. However, the fatigue crack growth rate analysis based on both SIF range and SEDF range is limited to the stable crack growth stage within which the crack growth rate da/dN is in a straight line with the SIF range ΔK or SEDF range ΔS in a log-log coordinate. The stable crack growth stage is with a growth rate approximately from 10^{-9} to 10^{-5} m/cycle, corresponding to a logΔK of 1.4-2.2 MPa·m$^{1/2}$ in the CT specimens while other ranges of logΔK is not necessary to discuss. Therefore, the above conclusion is still generally applicable to Q550D.

Therefore, each upper bound is applicable to the design of the specific high-strength steel. These upper bounds are considered as the fatigue crack growth design curves for each steel, which can be directly used for the fatigue crack growth rate analysis and design of cracked steel components or structures.

8. Conclusion

(1) The strain results at the crack tip of specimens obtained by FE analysis and DIC analysis are in good agreement with each other, indicating that both are useful tools for the verification of crack growth rate tests.

(2) The crack length has little effect on the difference between SIFs obtained by various mesh sizes while the SIF gradually converges as the angle and the radius of the first row of sector elements at the crack tip decrease in the FE analysis and rather accurate results can be obtained with a sector radius of r=1mm and a sector number of D=15 in this case.

(3) The crack growth rate gradually slows down, with the material constants m and n gradually decreasing and the absolute values of log$C$ and log$A$ gradually decreasing and increasing respectively, as the yield strength increases, although the trend is not strictly followed.

(4) The mean+2s curve in BS7910 and DNVGL-RP-210, along with the curves in WES2805 and IIW-2259-15 are all applicable to the design of Q460C, Q550D and Q690D, while the mean curve in BS7910 and DNVGL-RP-210 are not applicable, and the curves suggested by ASME BPVC or JSME S NA1-2008 for ferritic steel and that by FKM are too conservative.

(5) The scatter band upper bounds established for Q460C, Q550D and Q690D based on either SIF or SEDF with a survival probability 95% along with a one-sided confidence level 95% are able to be considered as design curves applicable to fatigue crack growth analysis and design of these three high-strength steels.

Acknowledgements

This research was supported by the National Natural Science Foundation of China (No.52008202).

Reference

[1] Barsom JM, Imhof EJ, & Rolfe ST . Fatigue-crack growth in high yield-strength steels[J]. Engineering Fracture Mechanics, 1971, 2(4): 301-317.
[2]Jesus DMA, Matos R, Fontoura FB, et al. A comparison of the fatigue behavior between S355 and S690 steel grades[J].Journal of Constructional Steel Research, 2012(79):140-150.
[3] Tong L, Ren Z, Jing S, et al., Experimental study of fatigue crack growth rate of high strength structural steel series[J], Engineering Mechanics, 2020, 37 (12): 191-201+212. (In Chinese)
[4] Ma YF, Cheng EX, Wu XS, et al. Fatigue crack growth of Q550E high strength steel and welded joint[J/OL]. Journal of Civil and Environmental Engineering:1-11[2024-06-07]. (In Chinese)
[5] Shen X ,Gao X ,Shao Y, et al. Investigation on the fatigue crack growth behavior of welded joints in EH690 high-strength marine steel[J].International Journal of Fatigue, 2024(189):108572.

[6] Guo H, Guan X, Pan Y, et al. Experimental research on fatigue crack growth behavior of Q690D high strength steel[J].Journal of Constructional Steel Research, 2024(220):108809.
[7] Panwitt H, Köster P, & Sander M. Fatigue crack growth determination under in-phase and out-of-phase mixed-mode loading conditions using an automated DIC evaluation tool[J]. International Journal of Fatigue, 2022(164): 107122.
[8] Li D, Huang P, Chen Z, et al. Experimental study on fracture and fatigue crack propagation processes in concrete based on DIC technology[J]. Engineering Fracture Mechanics, 2020(235):107166.
[9] Zong L, Shi G, Wang YQ, et al. Experimental study on fatigue crack growth rate of Q345qD bridge steel[J]. China Railway Science, 2015,36(03):37-44. (In Chinese)
[10] Zong L, Guo S, Liao X, et al. Experimental investigation on fatigue crack growth rate of Q690D high strength steel[J]. Journal of Building Structures, 2023, 44(8):217–24. (In Chinese)
[11] Song W, Wang P, Wan D, et al. Fatigue crack growth behavior of Ni-Cr-Mo-V steel welded joints considering strength mismatch effect[J]. International Journal of Fatigue, 2021(151): 106389.
[12] Chen C, Su M, Wang Y, et al. Experimental research on the fatigue crack growth behaviour of Q420C[J]. Journal of Constructional Steel Research, 2022(192):107241.
[13] Sih GC. Strain-energy-density factor applied to mixed mode crack problems[J]. International Journal of fracture, 1974, 10(3): 305-321.
[14] Badaliance R. Application of strain energy density factor to fatigue crack growth analysis[J]. Engineering Fracture Mechanics, 1980, 13(3): 657-666.
[15] Shen S. Research on fatigue property and life prediction of welding joints used in high-rise steel structures based on strain energy density[D]. Southeast University, 2019. (In Chinese)
[16] GB 55006-2021, General code for steel structures[S]. Beijing: China Architecture & Building Press, 2021. (In Chinese)
[17] GB/T 6398-2017, Metallic materials-Fatigue testing-Fatigue crack growth method[S]. Beijing: China Standard Press, 2017. (In Chinese)
[18] ASTM E647, Standard test method for measurement of fatigue crack growth rates[S]. West Conshohocken, PA: American Society for Testing and Materials International, 1995.
[19] Hassan, GM. Deformation measurement in the presence of discontinuities with digital image correlation: A review[J]. Optics and Lasers in Engineering, 2021(137): 106394.
[20] Sih GC, Barthelemy BM. Mixed mode fatigue crack growth predictions[J]. Engineering Fracture Mechanics, 1980,13(3): 439-451.
[21] Sih GC, Faria LDO. Fracture Mechanics Methodology[M]. Springer Netherlands, 1985.
[22] Choi DH, Choi HY . Fatigue life prediction of out-of-plane gusset welded joints using strain energy density factor approach. Theoretical and applied fracture mechanics, 2005, 44(1):16-26.
[23] Choi DH, Choi HY & Lee D. Fatigue life prediction of in-plane gusset welded joints using strain energy density factor approach. Theoretical and applied fracture mechanics, 2006, 45(2):108-116.
[24] Sih GC, Tang KK. Assurance of reliable time limits in fatigue depending on choice of failure simulation: energy density versus stress intensity[J]. Theoretical and applied fracture mechanics, 2011, 55(1):39-51.
[25] Liao X, Wang Y, Qian X, et al. Fatigue crack propagation for Q345qD bridge steel and its butt welds at low temperatures[J].Fatigue & Fracture of Engineering Materials & Structures, 2018, 41(3):675-687.
[26] Tan HM, Hu XQ, Huang D, et al. Fatigue crack propagation performance of Q690 high-strength steel and butt welds[J].Theoretical and Applied Fracture Mechanics, 2023, 126:103988.
[27] Shen X, Gao X, Shao Y, et al. Investigation on the fatigue crack growth behavior of welded joints in EH690 high-strength marine steel[J]. International Journal of Fatigue, 2024,189: 108572.
[28] Lukacs J, Dobosy A, Gaspar M. Fatigue crack propagation limit curves for S690QL and S960M high strength steels and their welded joints[J]. Advanced Materials Research, 2018, 1146(1):44–56.
[29] Wang H, Su B, Hua G, et al. Experiment research on corrosion fatigue crack propagation of marine engineering equipment material E690 high strength steel[J]. Hot Working Technol, 2016, 45(16). (In Chinese)
[30] Yang X, Fan W, Li Z, et al. Experimental and model study on corrosion fatigue crack propagation of Q420B steel in acid rain condition[J]. China Civil Engineering Journal, 2023, 56 (2):1–11. (In Chinese)
[31] Wang Q, Yan Z, Liu X, et al. Understanding of fatigue crack growth behavior in welded joint of a new generation Ni-Cr-Mo-V high strength steel[J]. Engineering Fracture Mechanics, 2018,194:224–39.
[32] Zhong Y, Shao Y, Gao X, et al. Fatigue crack growth of EH36 steel in air and corrosive marine environments[J]. Journal of Constructional Steel Research, 2023, 210:108104.
[33] Duan L, Wang CS & Wang SC. Fatigue Crack Growth Rate Tests of High Performance Steel HPS 485W[C]. 13th International Conference on Fracture, 2013.
[34] Wang CS, Duan L, Zheng L, et al. Fatigue crack growth rate tests of high performance steel HPS 485W for bridges[J]. Engineering Mechanics, 2013:30(6), 212-216.
[35] Zong L, Shi G, & Wang Y. Experimental investigation and numerical simulation on fatigue crack behavior of bridge steel WNQ570 base metal and butt weld[J]. Construction and Building Materials, 2015, 77, 419-429.
[36] Schijve J. Fatigue of Structures and Materials[M]. Heidelberg: Springer Science & Business Media, 2001.
[37] Hobbacher, A. F. Recommendations for fatigue design of welded joints and components[M]. Vol. 47. Cham: Springer International Publishing, 2016.
[38] BS7910, Guide to methods for assessing the acceptability of flaws in metallic structures[S]. London: British Standards Institution, 2005
[39] AS, Det Norske Veritas. Fatigue design of offshore steel structures[M]. Rev. 3 (2011).
[40] Lotsberg I ,Sigurdsson G ,Fjeldstad A , et al. Probabilistic methods for planning of inspection for fatigue cracks in offshore structures[J].Marine Structures, 2016, 46167-192.
[41] Berger C, Blauel JG, Pyttel B, et al. FKM Guideline Fracture Mechanics Proof of Strength for Engineering Components, 2nd revised ed., English version[M], Forschungskuratorium Maschinenbau (FKM), Frankfurt am Main, 2004
[42] Hojo K, Takahashi Y. Comparison of fatigue crack growth curves of Japan, the United States, and European Union Code and Standards[J]. Journal of Pressure Vessel Technology, 2012(134): 031004.
[43] WES 2805, Method of Assessment for Flaws in Fusion Welded Joints With Respect to Brittle Fracture and Fatigue Crack Growth[S], 2007, Tokyo: The Japan Welding Engineering Society.
[44] ASME Boiler and Pressure Vessel Code, XI Rules for Inservice Inspection of Nuclear Power Plant Components[M], 2007, ASME Boiler and Pressure Vessel Committee Subcommittee on Nuclear Power.
[45] JSME S NA1-2008, Codes for Nuclear Power Generation Facilities-Rules on Fitness-for-Service for Nuclear Power Plants[S], 2008, JSME.

Advanced Steel Construction – Vol. 21 No. 6 (2025) 500–510
DOI:10.18057/IJASC.2025.21.6.3

EXPERIMENTAL AND NUMERICAL ANALYSIS ON THE TENSILE-BEARING CAPACITY OF AN INNOVATIVE OFFSHORE FLOATING PHOTOVOLTAIC PLATFORM CONNECTOR

Zhi-Yong Zheng [1, 2], Hong-Bo Liu [1, 3, *], Liu-Lu Guo [3], Ji-Jian Lian [3], Xiang-Yu Yan [4] and Ye Yao [4]

[1] *School of Water Conservancy and Hydroelectric Power, Hebei University of Engineering, Handan 056000, China*
[2] *Hebei Institute of Mechanical and Electrical Technology, Xingtai 054000, China*
[3] *Department of Civil Engineering, Tianjin University, Tianjin 300072, China*
[4] *School of Ocean Energy, Tianjin University of Technology, Tianjin 300384, China*
** (Corresponding author: E-mail: hbliu@tju.edu.cn)*

ABSTRACT

Offshore floating photovoltaic (OFPV) systems have attracted considerable attention from the scientific community because of their broad application prospects. A multi-module configuration interconnected via connectors is typically used in OFPV platforms. The tensile-bearing capacity of the connectors is crucial to ensure the overall safety of OFPV platforms. In this study, the tensile-bearing capacity of an innovative connector was investigated by experiments and numerical simulations. The numerical simulation results conformed well with those from experiments, with a relative error of less than 10%. Subsequently, The tensile mechanism of the connectors was analyzed, leading to the derivation of equations used to determine the tensile-bearing capacity of the OFPV platform connector under two distinct failure modes. Finally, a parametric study was conducted to elucidate the relationship between the tensile-bearing capacity of the connectors and the connecting pipe and baseplate thicknesses. The results obtained from the derived equations agreed well with those from numerical simulations, indicating that the equations could be used to determine the tensile-bearing capacity of OFPV platform connectors. This study lays the theoretical foundation for the design and application of OFPV structures.

ARTICLE HISTORY

Received: 5 February 2025
Revised: 31 May 2025
Accepted: 31 May 2025

KEYWORDS

Offshore floating photovoltaic platform;
Connector;
Tensile-bearing capacity;
Experimental investigation;
Numerical analysis

1. Introduction

The power generation efficiency has been increased by about 5% on average due to the cooling effect caused by contact with seawater [1, 2]. Therefore, OFPV technology has garnered much interest from scholars and experts to optimize the utilization of marine resources and solar energy [3]. This technology primarily involves photovoltaic devices, support structures, and anchoring systems [4, 5]. Although floating photovoltaic technology has reached a relatively mature stage for inland water systems, the harsh marine environment characterized by strong winds and waves as well as corrosive conditions of the saline water poses significant challenges to the large-scale development and deployment of OFPV systems in oceanic settings [6-8]. Multi-module OFPV platforms interconnected via connectors have been developed to address the challenges presented by complex marine environments. In practical applications, this configuration typically consists of hundreds or even thousands of modules and connectors that can interact with significant forces [9, 10]. Thus, the reliability of these connectors is crucial to ensure the overall safety of OFPV platforms, necessitating an exceptionally high load-bearing capacity for the connectors [11]. Currently, The main forms of connectors include: hinged connectors [12-16], chain connections [17-19] and rigid connections [20]. The most widely used type of the connector is the hinged connector. However, the hinged connector restricts too many degrees of freedom[21, 22], only allowing adjacent OFPV platforms to rotate at a certain angle relative to each other, which seriously affects the wave-following performance of the structure. The chain connection releases most degrees of freedom between adjacent OFPV platforms. However, under the action of wave loads, the adjacent platforms might experience severe collisions, which greatly affect the safety of the platform structure. Rigid connection completely restricts the degrees of freedom between adjacent OFPV platforms[23], making the wave-following performance of the structure even worse. Moreover, under the action of wave loads, significant bending moments might be generated at the connectors, which makes this area highly prone to fracture and damage. Meanwhile, many experts [24-31] have conducted in-depth studies on the hydrodynamic responses of multi-module OFPV platforms at different connectors.

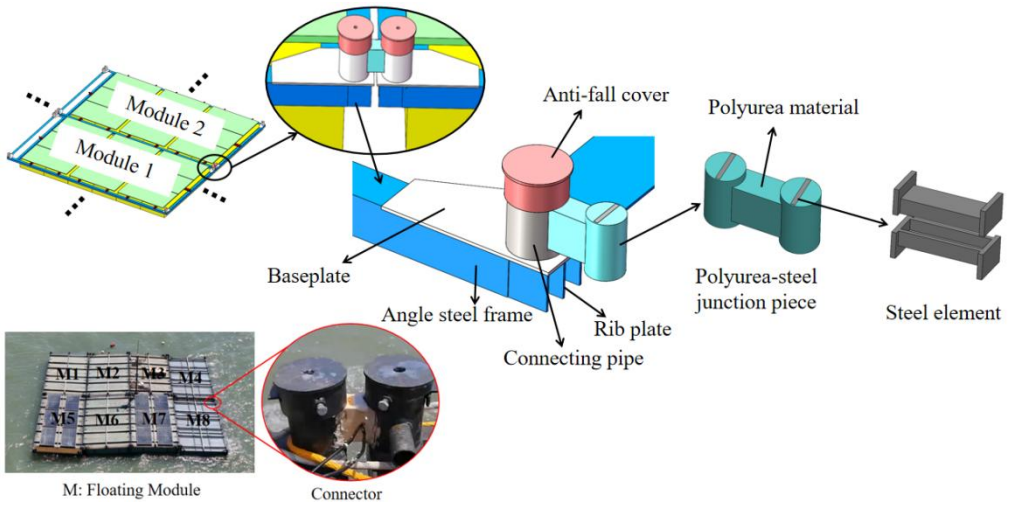

Fig. 1 The configuration of the connector

This paper presents an Innovative connector of the OFPV Platforms, which primarily comprises four components: a baseplate, a connecting pipe, an anti-fall cover, and a polyurea–steel junction component. The configuration of the connector is illustrated in Fig. 1. This connector combines the advantages of most connection forms. Compared with the hinged connector and the rigid connection, this connector releases more degrees of freedom for the OFPV platform and has better wave-following performance. Meanwhile, compared with the chain connection, this connector can not only bear the equivalent tensile force but also have higher impact resistance. More importantly, due to the application of polyurea material, it has higher durability in the marine corrosion environment.

Based on the literature survey, Most of the studies are focused on the hydrodynamic and hydroelastic responses of floating photovoltaic platforms with multiple modules. However, there is a paucity of studies on the mechanical properties of the connectors of the OFPV platforms. According to the research findings of experts, The mechanical properties of the connectors are crucial to ensure the safety of the entire structure[21-23, 32-34]. Accurately determining the tensile-bearing capacity of the connectors not only enhances the design of OFPV platforms but also facilitates the safety assessment of OFPV platforms. This paper presents an in-depth investigation into the tensile performance of this innovative connector utilized in OFPV platforms and introduces a method for calculating the tensile-bearing capacity.

2. Experimental study

2.1. Design of the test specimens

Eighteen test specimens were designed and fabricated for tensile tests using Q235B steel. The variables investigated were the connecting pipe thickness (d = 8, 14, and 20 mm) and baseplate thickness (t = 0, 9 , and 14 mm). The detailed schematic of the specimen is shown in Fig. 2. The variables investigated are presented in Table 1. In this table, 'C' represents 'Connector,' and the first and second digits represent the thicknesses of the connecting pipe and baseplate, respectively. To ensure the reliability of the experimental results, two specimens (designated A and B) were prepared for each group.

Table 1
Details of the test specimens

Notation	d (mm)	t (mm)	Notation	d (mm)	t (mm)
C-8-0	8	0	C-14-14	14	14
C-8-9	8	9	C-20-0	20	0
C-8-14	8	14	C-20-9	20	9
C-14-0	14	0	C-20-14	20	14
C-14-9	14	9			

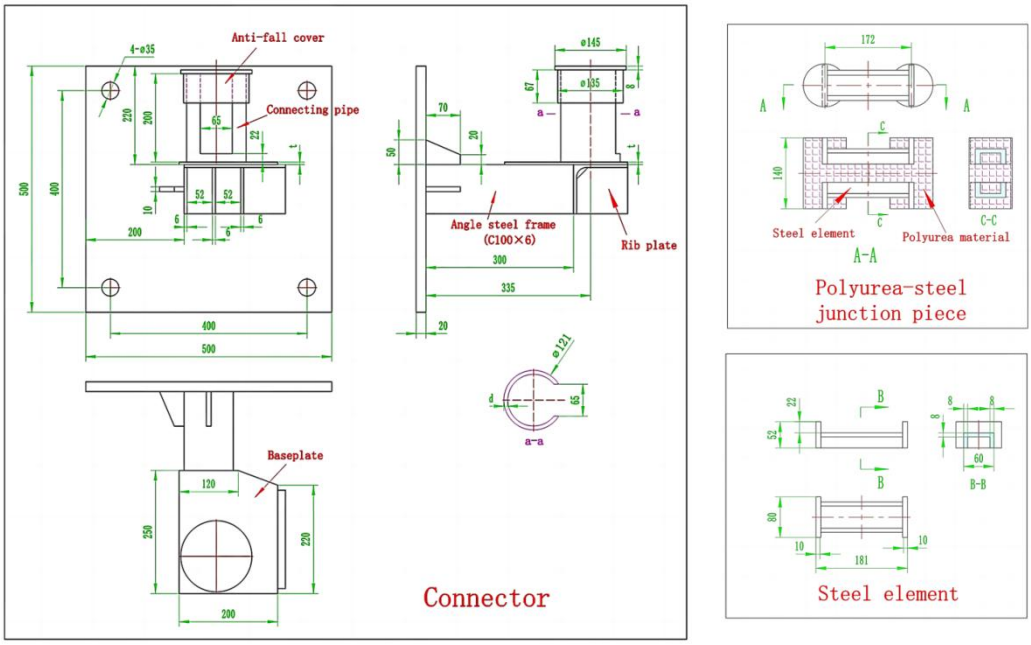

Fig. 2 The detailed schematic of the specimen

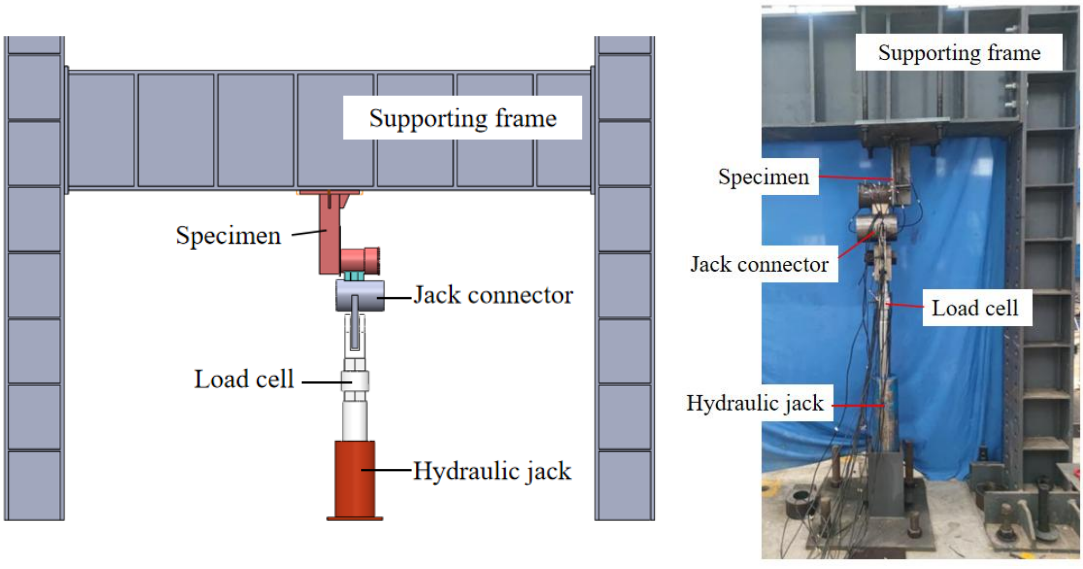

(a) diagram (b) physical drawing

Fig. 3 The experimental setup

2.2. Experimental setup

The experimental setup is shown in Fig. 3. One end of the specimen was fastened to the supporting frame using a connection plate, and the opposite end was connected to a specialized jack interface via a polyurea–steel junction component. The inner diameter of the jack interface matched that of the connecting pipe of the test specimen, whereas its thickness was significantly increased to ensure structural integrity during testing. The hydraulic jack was capable of exerting a force of 50 kN, and a load cell was used to precisely measure the applied force.

The loading procedure was divided into two distinct phases: preloading and formal loading. The preloading phase was conducted to minimize measurement errors that could arise from gaps between the specimen and the loading device. Following this, the formal loading phase involved displacement-controlled loading at a rate of 2 mm/min until the specimen failed or the real-time load decreased to 80% of its peak value.

2.3. Layout of the measurement points

The layout of the displacement and strain measurement points during the experiment is shown in Fig. 4. Linear variable differential transformers (DM1) were installed to measure the displacement along the direction of the applied force. Ten strain gauges were employed to assess the strain at critical locations on the test specimen. Six of these gauges (SG1–SG6) were strategically positioned along the half-circumference of the connecting pipe, specifically at the middle and lower heights of the opening, to monitor the strains within the connecting pipe. In addition, two strain gauges (SG7 and SG8) were affixed on the rear and lateral surfaces of the baseplate to evaluate the strain response. Two strain gauges (SG9 and SG10) were installed on the underside and rear side of the angle steel frame to measure the strains at these locations.

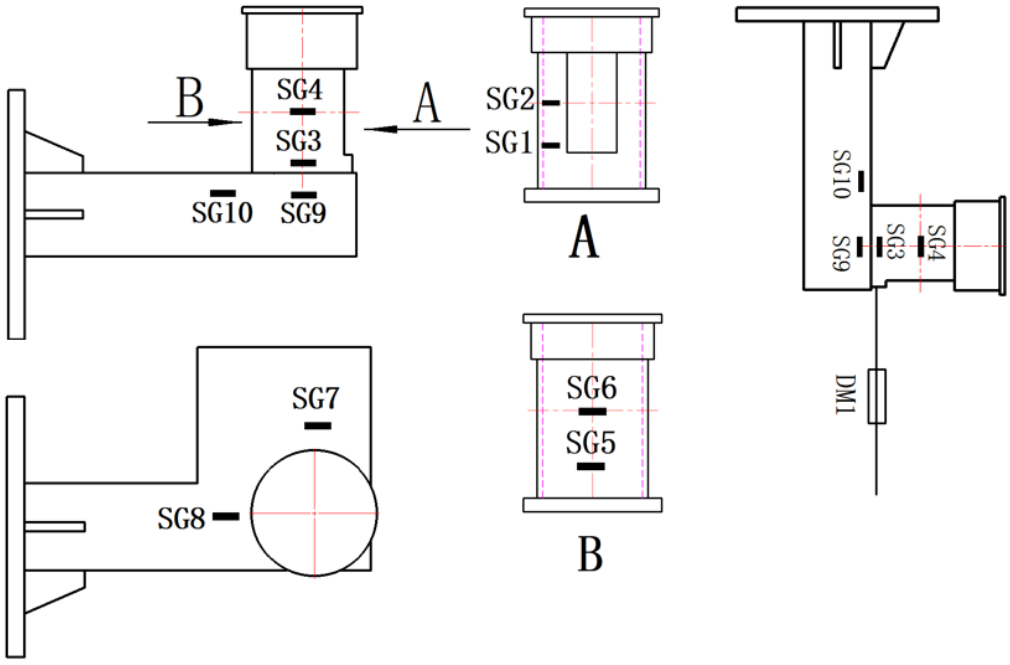

Fig. 4 Schematic diagram of strain gauge and displacement meter arrangement

3. Experimental results

3.1. Failure modes

As shown in Fig. 5, the test specimen exhibited two distinct failure modes: bulging deformation at the opening of the connecting pipe and buckling deformation of the angle steel frame. The two failure modes do not act independently. Their combined effect influences the tensile-bearing capacity of connectors. Additionally, when the connecting pipe fails due to bulging, the angle steel frame undergoes a certain degree of buckling deformation, though it does not yet reach the point of failure, and vice versa. Consequently, two failure modes collectively impact the tensile-bearing capacity of the connectors.

When the connecting pipe thickness was d = 8 mm, the failure mode observed in the test specimen manifested as localized bulging deformation at the opening of the connecting pipe. As the tensile force reached a critical threshold, localized bulging deformation was initiated at this opening, significantly increasing the risk of detachment of the polyurea–steel junction component from the connecting pipe. At this point, the opening of the connecting pipe reached its ultimate strength, leading to a corresponding decrease in the load-bearing capacity of the test specimen.

(a) The opening of connecting pipe has exhibited bulging deformation (b) The angle steel frame has exhibited buckling deformation

Fig. 5 Failure modes of specimen

When the connecting pipe thickness was d = 14 mm, the test specimen exhibited two distinct failure modes: localized bulging deformation at the opening of the connecting pipe and buckling deformation of the angle steel frame. When the baseplate thicknesses were t = 0 and 14 mm, the angle steel frame near the base of the connecting pipe began to deform into folds when subjected to a certain level of tensile force. Subsequently, a significant decrease in the load-bearing capacity of the test specimen was observed. When the baseplate thickness was t = 9 mm, bulging occurred at the opening of the connecting pipe upon reaching a specific tensile force threshold, after which a significant reduction in the tensile-bearing capacity was observed.

When the connecting pipe thickness was d = 20 mm, the failure mode observed in the test specimen was characterized by severe buckling deformation of the angle steel frame adjacent to the connecting pipe. As the tensile force reached a critical threshold, severe buckling deformation was initiated in the angle steel frame located near the bottom of the connecting pipe, resulting in a corresponding decline in the tensile-bearing capacity of the test specimen.

3.2. Load-displacement curves

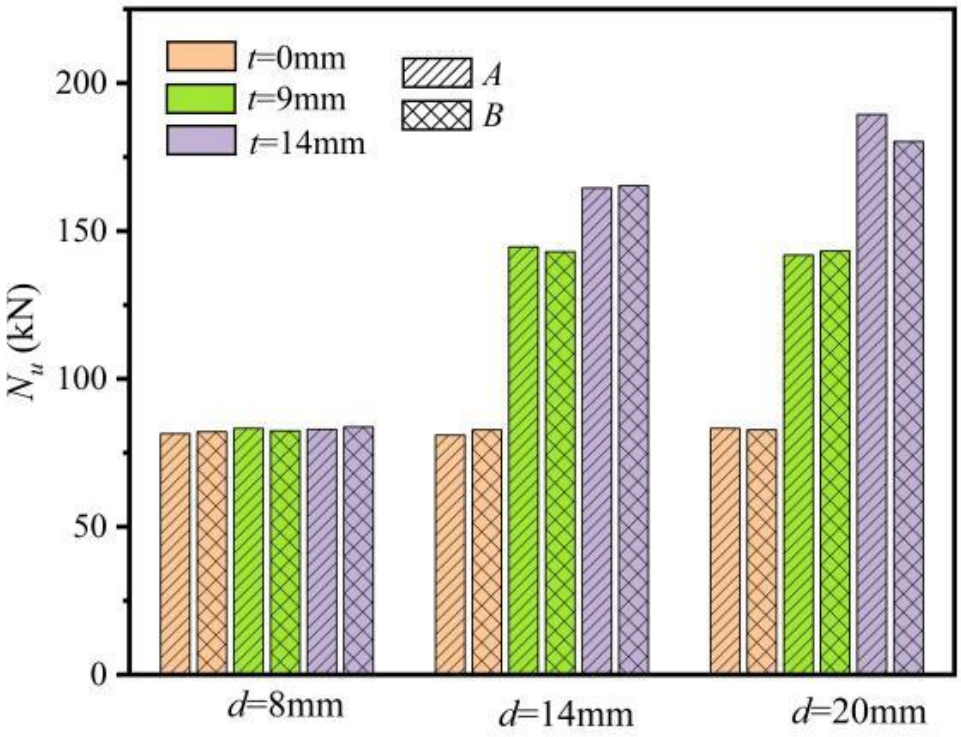

Fig. 6 The column chart of the bearing capacity of the specimen

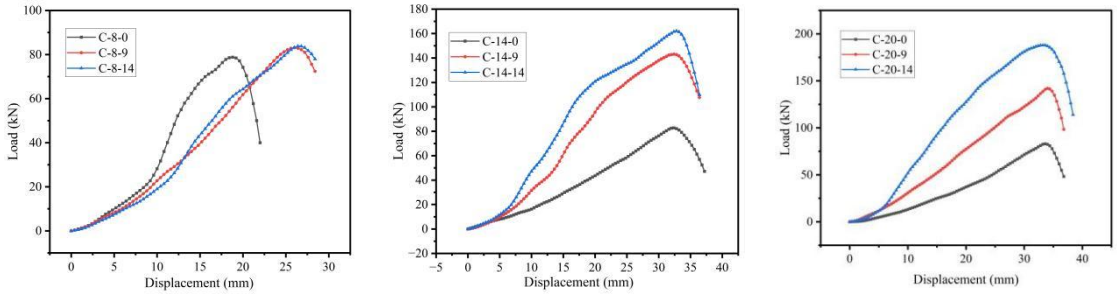

a.d = 8 mm b. d = 14 mm c. d = 20 mm

Fig. 7 Load-displacement curve of specimen

Table 2
The maximum bearing capacity and failure mode of the specimen

Notation	N_{uTEST} (kN)	Failure mode	Notation	N_{uTEST} (kN)	Failure mode
C-8-0A	81.46	D	C-14-9B	142.89	F
C-8-0B	82.07	D	C-14-14A	164.47	D
C-8-9A	83.25	D	C-14-14B	165.23	D
C-8-9B	82.42	D	C-20-0A	83.21	F
C-8-14A	82.89	D	C-20-0B	82.69	F
C-8-14B	83.75	D	C-20-9A	141.82	F
C-14-0A	80.94	F	C-20-9B	143.15	F
C-14-0B	82.74	F	C-20-14A	189.34	F
C-14-9A	144.56	F	C-20-14B	180.21	F

Note: N_{uTEST} is the maximum tensile-bearing capacity of the specimen ascertained from experiments, D is the bulging deformation of the connecting pipe opening, and F is the buckling deformation of the angle steel frame.

The maximum tensile-bearing capacity (Nu) results and load-displacement curves for all test specimens are presented in Fig. 6 and Fig. 7, respectively. The detailed results are summarized in Table 2. It is evident that the tensile-bearing capacity of the test specimens was influenced by the combined effects of the connecting pipe and baseplate thicknesses. Specifically, when d = 8 mm, changes in the baseplate thickness had minimal effect on the tensile-bearing capacity. Conversely, when d = 14 and 20 mm, an increase in the baseplate thickness enhanced the tensile-bearing capacity. Similarly, when t = 0 mm, changes in the connecting pipe thickness had only a minor effect on the tensile-bearing capacity. In contrast, when t = 9 and 14 mm, a higher connecting pipe thickness resulted in a higher tensile-bearing capacity.

3.3. Load-strain curves

Based on the experimental results, the strain measurements at SG4 and SG10 of the test specimens exhibited greater significance. The load–strain curves for all test specimens measured at SG4 and SG10 are shown in Fig. 8 to Fig. 10. It is apparent that the connecting pipe thickness had a pronounced effect on the strains measured at these locations. At SG4 under the same loading conditions, an increase in the connecting pipe thickness resulted in higher strain. Conversely, at SG10 under the same loading conditions, a decrease in the connecting pipe thickness resulted in a higher strain, where the maximum strain was observed when d = 8 mm, which far exceeded those observed when d = 14 and 20 mm. The baseplate thickness also had a considerable effect on the strains measured at SG10. During the initial loading phase, all of the test specimens exhibited similar trends in their strains at this location. However, as the load further increased, the test specimens with thicker baseplates exhibited comparatively higher strains.

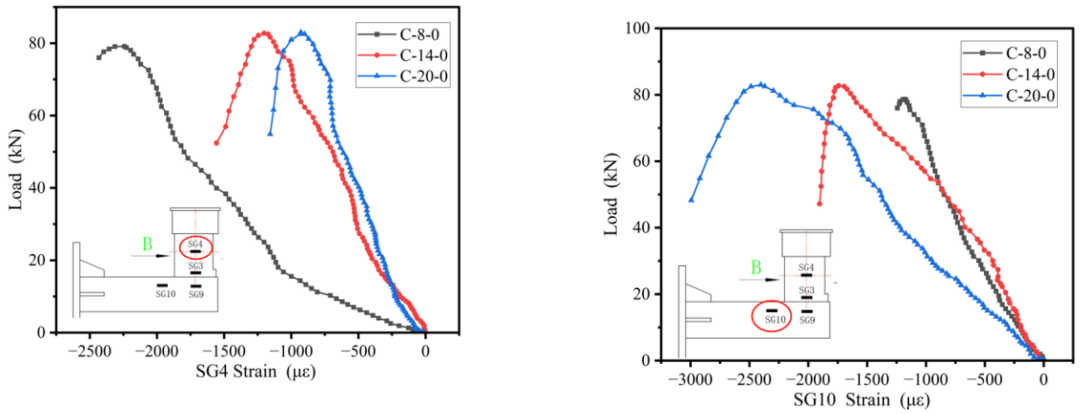

(a) The curve of load-SG4 values (b) The curve of load-SG10 values

Fig. 8 The load-strain curve at the typical position of the specimen when t=0 mm

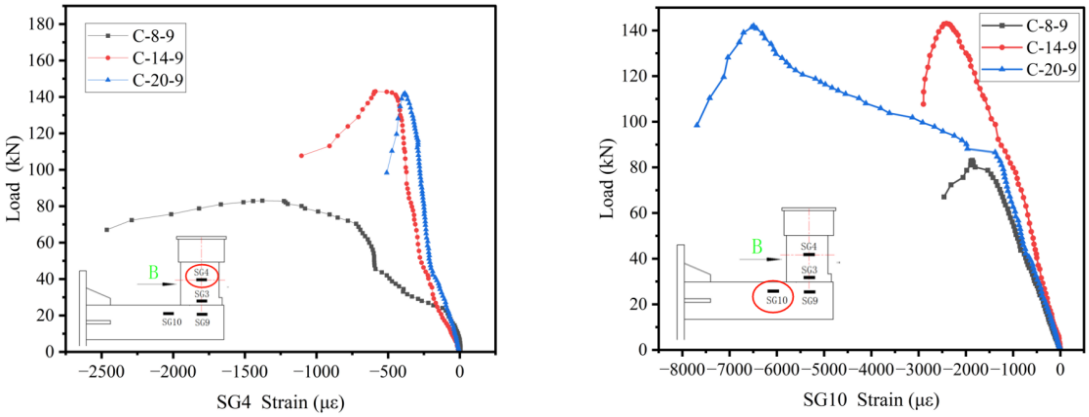

(a) The curve of load-SG4 values (b) The curve of load-SG10 values

Fig. 9 The load-strain curve at the typical position of the specimen when t=9mm

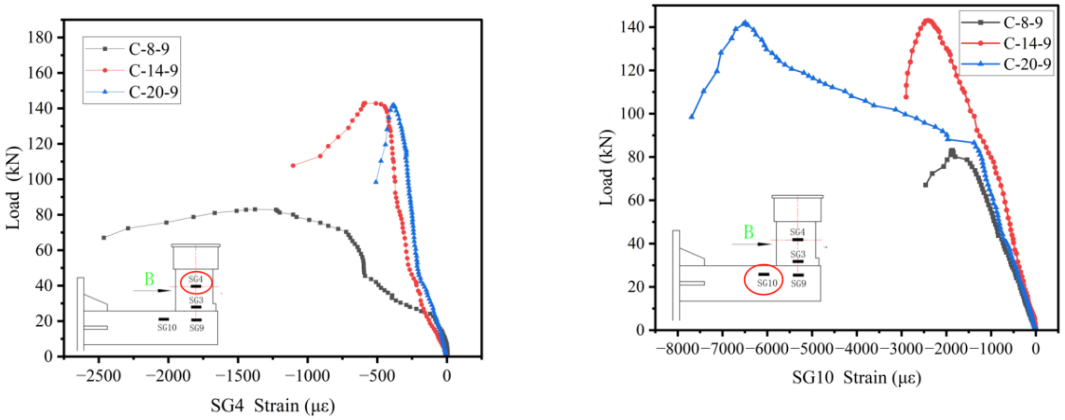

(a) The curve of load-SG4 values (b) The curve of load-SG10 values

Fig. 10 The load-strain curve at the typical position of the specimen when t=14mm

4. Tension mechanism

4.1. Load analysis of the connecting pipe

Neglecting the constraining influence of the angle steel frame at the base of the connecting pipe, this analysis focuses solely on calculating the tensile-bearing capacity of the side-opening connecting pipe. Consider a minute horizontal cross-section at a specified height within the connecting pipe, as shown in Fig. 11(a). The corresponding force distribution is shown in Fig. 11(b). Following the calculations, the bending moment diagram for this cross-section is presented in Fig. 16(c). It is evident that the outer surface of the connecting pipe experienced compression, which was consistent with the compressive strains measured at locations SG1–SG6 in the experiments. The maximum bending moment is calculated by using Eq. 1.

$$dM_{\max} = \frac{\mathrm{d}F}{2\cos\theta}\left[R\sin(\theta-\alpha)+R+\frac{d}{2}\right] \tag{1}$$

Where, Z is the height of the connecting pipe, $\alpha = \arcsin\frac{P}{2R}$, $\theta = \arcsin\frac{P}{2r}$, $dF = \frac{F}{Z}dz$.

The peak stress is observed at the location of the maximum bending moment and this peak stress is determined using Eq. 2.

$$\sigma_{\max} = \frac{dM_a}{W} = \frac{6dM_{\max}}{d^2 dz} \tag{2}$$

where, W is the section modulus in bending, which is a measure of the capacity of the material to resist bending.

The maximum stress can be calculated using Eq.3 by combining Eq.1 and Eq.2.

$$\sigma_{\max} = \frac{F}{d^2}\cdot\frac{3\left[R\sin(\theta-\alpha)+R+\frac{d}{2}\right]}{\cos\theta} \le \sigma_s \tag{3}$$

where, σ_s is the yield strength of the materials.

Based on Eq. 3, the tensile-bearing capacity of the connectors under bulging deformation at the opening of the connecting pipe opening is calculated using Eq. 4.

$$N_{uFOR} = F \le \frac{d^2\sigma_s\cos\theta}{3\left[R\sin(\theta-\alpha)+R+\frac{d}{2}\right]} \tag{4}$$

where N_{uFOR} is the tensile-bearing capacity of the connectors under bulging deformation at the opening of the connecting pipe.

These equations fail to account for the constraining effect of the angle steel frame on the base of the connecting pipe. Consequently, the tensile-bearing capacity of the connectors calculated using Eq. 4 is inadequate, and hence, it is necessary to revise the equation. In addition, considering that the magnitude of $R\sin(\theta-\alpha)$ is notably smaller than R, $R\sin(\theta-\alpha)$ may be omitted from Eq. 4. After applying the correction, the tensile-bearing capacity of the connectors is determined using Eq. 5.

$$N_{uC-FOR} = F \le \frac{d^2\sigma_s\cos\theta}{3\left(R+\frac{d}{2}\right)} \tag{5}$$

where NuC-FOR is the corrected tensile-bearing capacity of the connectors under bulging deformation at the opening of the connecting pipe.

Both Eq. 4 and Eq. 5 indicate that the connecting pipe thickness (d) has a significant effect on the tensile-bearing capacity of the connectors. In particular, an increase in d is associated with a decrease in stress and an increase in the tensile-bearing capacity, which is consistent with the experimental observations.

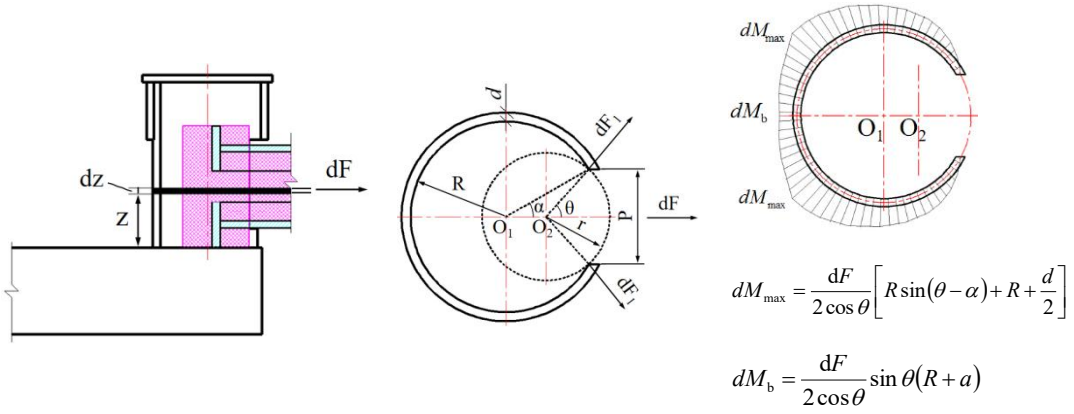

(a) A horizontal cross-sectional diagram of the connecting pipe

(b) Diagram of sectional force distribution

(c) Diagram of sectional bending moment

Fig. 11 Diagram of load analysis for the connecting pipe section

4.2. Force analysis of the angle steel frame

The loading condition at the connector is simplified according to the following procedure, as shown in Fig. 12(a). (1) The effect of the connecting pipe opening on the sectional coefficient is neglected, and the connecting pipe is modeled as a closed pipe. (2) The tensile force is modeled as a uniformly distributed load acting on the connecting pipe. A simplified bending moment diagram for the connector, which is derived from the force analysis, is shown in Fig. 12(b). The maximum bending moment is determined by using Eq. 6.

$$M_{\max} = F\left(\frac{l}{2}+h\right) \tag{6}$$

Where, l is the contact height between the polyurea-steel junction component and the connecting pipe. F is he tensile force of the connectors. h is the vertical distance from the centroid of the angle steel, equipped with a baseplate, to the top surface of the baseplate. As shown in Fig. 13. Mmax is the maximum bending moment induced by the tensile force of the connectors to the centroid axis of the angle steel frame with a baseplate.

$$h = \frac{Bt^2 - Cn^2 - n(C-n)}{2\left[Bt+Cn+(C-n)n\right]} \tag{7}$$

Where, B is the width of the baseplate; t is the height of the baseplate; C is the edge length of the angle steel; n is the thickness of the angle steel.

Therefore, the maximum stress of the angle steel frame is determined by using Eq. 8.

$$\sigma = \frac{Mh}{I_z} = \frac{F\left(\frac{l}{2}+h\right)h}{I_z} \le \sigma_s \tag{8}$$

where, σ is the maximum stress of the angle steel frame; σ_s is the yield strength of steel; I_z is the moment of inertia of the angle steel frame with a baseplate.

By integrating Eq.7 and Eq. 8, the tensile-bearing capacity of the connectors under buckling deformation of the angle steel frame is calculated by using Eq 9.

$$N_{uJF} = F \le \frac{\sigma_s I_Z}{\left(\frac{l}{2}+h\right)h} \tag{9}$$

where, N_{uJF} is the tensile-bearing capacity of the connectors determined from the equation applicable for buckling deformation of the angle steel frame.

It is evident from Eq. 8 and Eq. 9 that the baseplate thickness (t) has a substantial effect on the stress distribution within the angle steel frame. An increase in t is associated with a decrease in stress and an improvement in the tensile-bearing capacity of the connectors, which is consistent with the experimental results. As the value of t increased, the stress within the angle steel frame diminished and the tensile-bearing capacity of the connectors increased, both of which agree with the experimental findings.

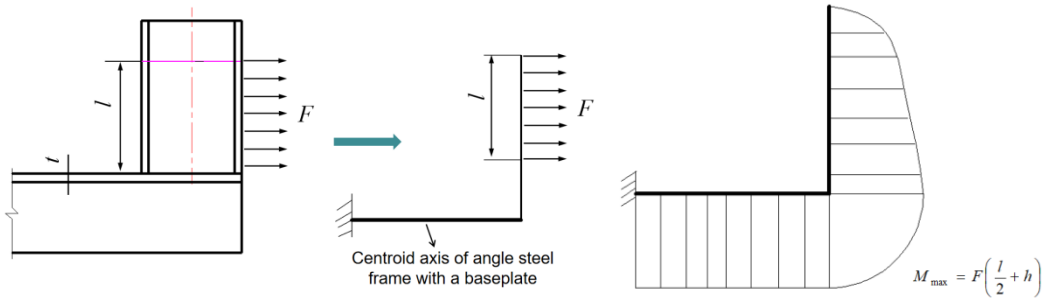

(a) Simplified force diagram of the connector (b) Bending moment diagram of the connector

Fig. 12 Simplified force and bending moment diagram of the connector

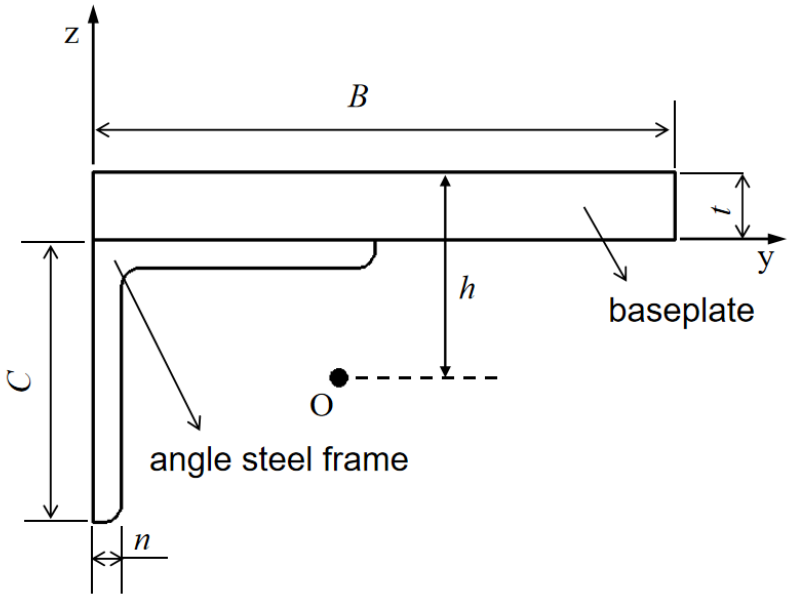

Fig. 13 Section diagram of Angle steel with a baseplate

5. Numerical simulations

5.1. Material properties

Q235B steel was used for the connectors. To determine the properties of the material, tensile tests were conducted following the ISO 6892-1 standard [35], and the properties are tabulated in Table 3. The constitutive model of polyurea is based on the Mooney–Rivlin framework and the specific parameters are listed in Table 4 [36].

Table 3
Average values of the properties of Q235B steel

Materials	E_0 (MPa)	f_y (MPa)	f_u (MPa)	ε_u
Q235B	205700	281.53	432.74	0.22

Note: E_0 is the Young's modulus; f_y is the yield strength of steel; f_u is the ultimate strength ,and ε_u is the corresponding tensile strain.

Table 4
Parameters of the Mooney-Rivlin model Unit: MPa

c_{10}	c_{01}	c_{11}	c_{20}	c_{02}	c_{21}	c_{12}	c_{30}	c_{03}
12.369	8.124	-17.653	7.274	3.062	-0.437	-0.298	0.043	2.94

5.2. Modelling details

The finite element model employs solid elements for simulation, which is comprised of connectors and connection plates. Integrating the polyurea material with the steel elements at a common node treatment to effectively simulate their bonded state as a unified entity. The cylindrical surface of the polyurea-steel junction piece is designed to interface with the inner surface of the connecting pipe, where the latter serves as the contact surface and the former acts as the target surface. The interaction between these surfaces is defined as No Separation contact. A fixed constraint is imposed on the end face of the specimen connection plate, while a tensile displacement is applied to the cylindrical surface of the polyurea-steel junction piece at the opposite end.

5.3. Sensitivity analysis of mesh size

In finite element analysis, the mesh size has a significant effect on the numerical simulation results and computational efficiency. Thus, the effects of mesh size (2, 4, 6, 8, and 10 mm) on the tensile-bearing capacity of the C-8-0 specimen were investigated, and the results are presented in Fig. 14. N_{uFEA} is the maximum tensile-bearing capacity of the test specimen obtained from numerical simulations in Fig. 14. Based on the results, a mesh size of 6 mm was selected to simulate the tensile-bearing capacity of the connectors, since this mesh size achieved a desirable balance between computational efficiency and numerical accuracy.

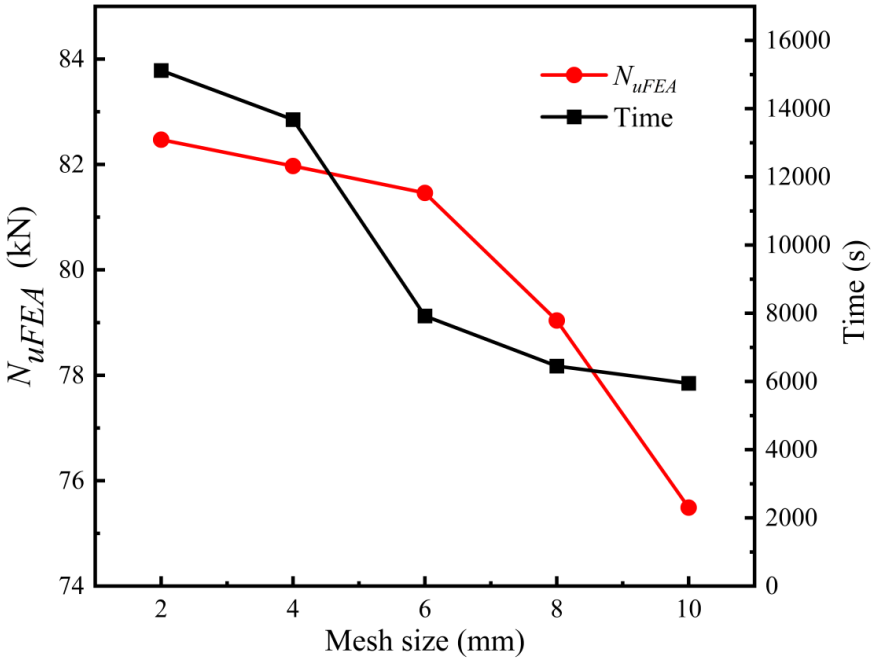

Fig.14 Comparison of simulation efficiency between different mesh sizes

5.4. Validation of the finite element model

The numerical simulation and experimental results for all test specimens were compared, as summarized in Table 5. The relative error between the numerical simulation and experimental results was less than 10%. The failure modes and load-displacement curves of the test specimens are shown in Fig. 14 and Fig. 15, respectively. There was good agreement between the numerical simulation and experimental results, thereby validating that the finite element model was suitable to assess the tensile-bearing capacity of the OFPV platform connector.

Table 5
Comparison between the numerical simulation and experimental results

Notation	N_{uTEST}	N_{uFEA} (kN)	Error	Notation	N_{uTEST}	N_{uFEA} (kN)	Error
C-8-0A	81.46	86.21	5.83%	C-14-9B	142.89	148.36	3.83%
C-8-0B	82.07	86.21	5.04%	C-14-14A	164.47	164.25	0.13%
C-8-9A	83.25	87.24	4.79%	C-14-14B	165.23	164.25	0.59%
C-8-9B	82.42	87.24	5.85%	C-20-0A	83.21	85.68	2.97%
C-8-14A	82.89	86.78	4.69%	C-20-0B	82.69	85.68	3.62%
C-8-14B	83.75	86.78	3.62%	C-20-9A	141.82	149.54	5.44%
C-14-0A	80.94	85.56	5.71%	C-20-9B	143.15	149.52	4.45%
C-14-0B	82.74	85.56	3.41%	C-20-14A	189.34	193.25	2.07%
C-14-9A	144.56	148.36	2.63%	C-20-14B	180.21	193.25	7.24%

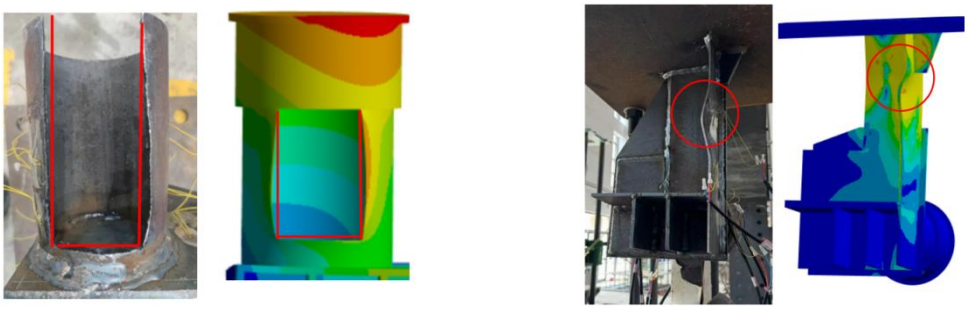

(a) Comparison of bulging deformation of connecting pipe opening (b) Comparison of buckling deformation in angle steel frame

Fig. 14 Comparison of experimental and finite element analysis results for the failure modes

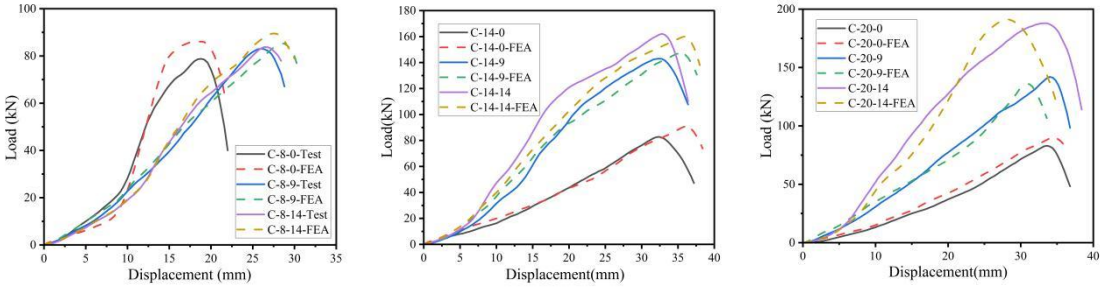

(a) Comparison of load-displacement curves for d=8 mm

(b) Comparison of load-displacement curves for d=14 mm

(c) Comparison of load-displacement curves for d=20 mm

Fig. 15 Comparison of experimental and finite element analysis results for load-displacement curves

5.5. Effect of the connecting pipe thickness

Numerical simulations were conducted using the finite element model to investigate the effect of connecting pipe thickness on the tensile-bearing capacity of the connectors. For simplicity and convenience, the baseplate thickness was set at 0 mm, and the angle steel frame was assumed to remain elastically deformable without yielding or failure. Twenty connecting pipe thicknesses were considered for the numerical simulations, ranging from 1 mm to 20 mm. The tensile-bearing capacities of the connectors for various connecting pipe thicknesses were calculated using Eqs. 4 and 5, and the analytical results were compared with those obtained from numerical simulations. As shown in Fig. 16, the tensile-bearing capacities of the connectors determined using Eq. 4 and Eq. 5 were consistent with those predicted by the finite element model.

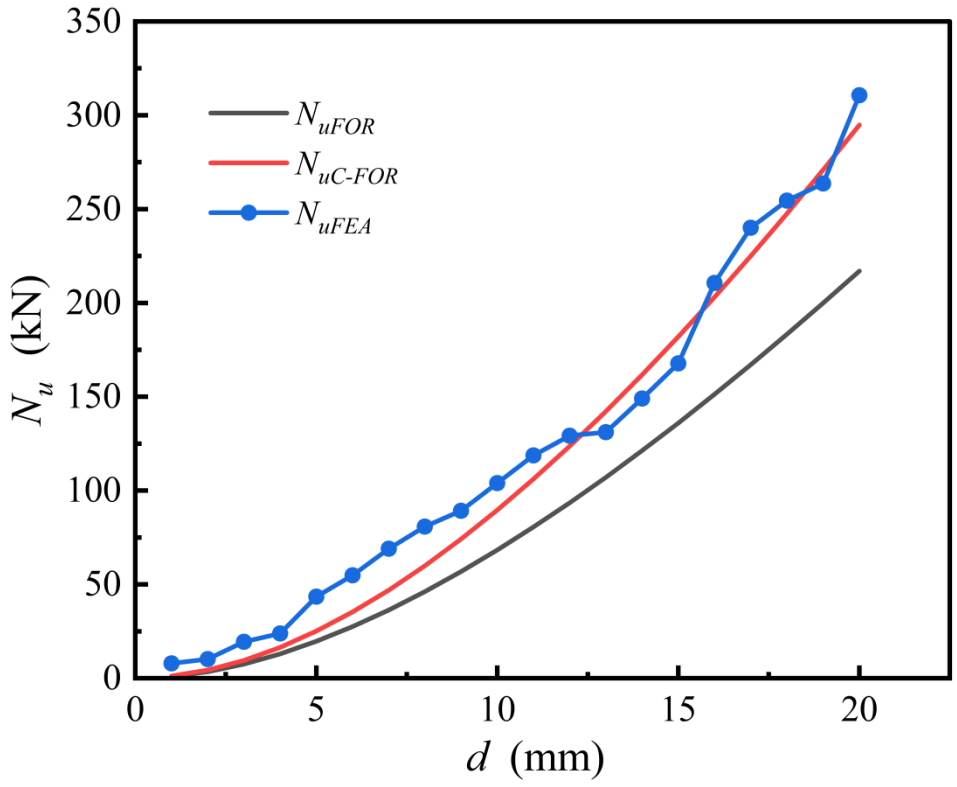

Fig. 16 Comparison of tensile bearing capacity calculated by finite element simulation, Eq.4 and Eq.5

Based on Fig. 16, assuming that the elastic angle steel frame did not yield or fail, the key findings are summarized as follows.

(1) The tensile-bearing capacities of the connectors determined from the unmodified Eq. 4 are substantially lower than those obtained from numerical simulations. This oversight arises from neglecting the effect of the angle steel frame at the bottom of the connecting pipe during the derivation of Eq. 4. With this constraint, the surface stress of the connecting pipe is influenced not only by the horizontal bending moment caused by the connection force acting on the outer side of the connector but also by the vertical bending moment resulting from the connection force applied to the surface of the connector. Hence, the tensile-bearing capacity of the connectors obtained using Eq. 4 is likely to be underestimated.

(2) The tensile-bearing capacities of the connectors obtained using Eq. 5 conform well with those obtained from numerical simulations. In cases where the connecting pipe thickness is minimal, the numerical simulation results surpass the analytical results obtained using Eq. 5. Conversely, in cases where the connecting pipe thickness is substantial, both the numerical simulation and analytical results show excellent agreement, and the trends in the tensile-bearing capacities were consistent. Thus, it can be deduced that Eq. 5 can be used to accurately assess the tensile-bearing capacity of OFPV platform connectors under bulging deformation of the connecting pipe.

(3) The tensile-bearing capacity of the connectors is directly proportional to the square of the connecting pipe thickness.

5.6. Effect of the baseplate thickness

To investigate the effect of baseplate thickness on the tensile-bearing capacity of the connectors and simplify modeling, the connecting pipe thickness was arbitrarily set at 20 mm, assuming that the connecting pipe would not yield. Twenty-one baseplate thicknesses were considered for the numerical simulations, ranging from 0 mm to 20 mm. The tensile-bearing capacities of the connectors were determined for different baseplate thicknesses using Eq 9 and the values were compared with those predicted by the finite element model, as shown in Fig. 17. The results illustrated the relationship between the baseplate thickness and the tensile-bearing capacity of the connectors.

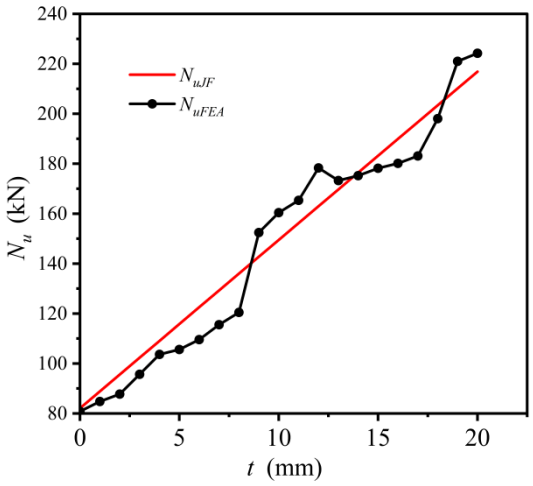

Fig. 17 Comparison of tensile bearing capacity calculated by finite element simulation and Eq.9

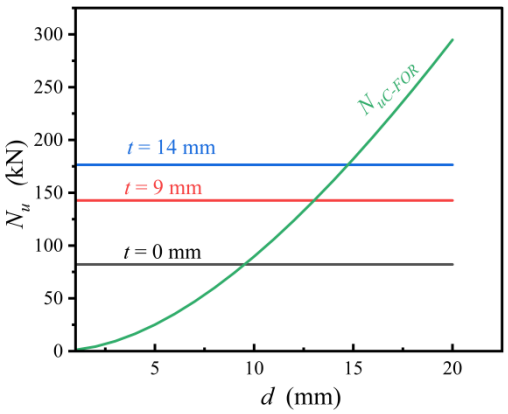

Fig. 18 Diagram of the Calculation Results for Eq.5 and Eq.9

Based on Fig. 17, assuming that the connecting pipe did not yield, the key findings are summarized as follows:

(1) The tensile-bearing capacity of the connectors increases with an increase in the baseplate thickness due to an increase in the moment of inertia (I_z) of the composite section formed by the baseplate and angle steel frame.

(2) The tensile-bearing capacities calculated using Eq. 9 show good agreement with those obtained from numerical simulations, suggesting that the tensile-bearing capacity of the connectors under buckling deformation of the angle steel frame can be accurately determined using Eq. 9.

(3) The tensile-bearing capacity of the connectors exhibits a linear relationship with the baseplate thickness, with a slope of 6.74 kN/mm. This implies that for every 1-mm increase in the baseplate thickness, the tensile-bearing capacity of the connectors increased by 6.74 kN.

5.7. Synergistic effect of the connecting pipe and baseplate thicknesses

The individual effects of the connecting pipe and baseplate thicknesses on the tensile-bearing capacity of the connectors were examined in the previous sections. The tensile-bearing capacities of the connectors under two distinct failure modes can be determined using Eq. 5 and Eq. 9. In practical applications, both the connecting pipe and baseplate thicknesses collectively influence the tensile-bearing capacity of the connectors. To ensure that neither the connecting pipe nor the angle steel frame experiences failure, it is advisable to select the lower value of the tensile-bearing capacities obtained using Eq. 5 and Eq. 9. The tensile-bearing capacities of the connectors were obtained using Eq. 5 and Eq. 9, when t = 0, 9, and 14mm, respectively, as shown in Fig. 18.

Based on Fig. 18, the key findings are summarized as follows:

(1) the tensile-bearing capacity curves obtained using Eq. 5 and Eq. 9 intersected at a particular point. On the left side of this intersection point, the tensile-bearing capacity of the connectors is determined by the bulging deformation at the opening of the connecting pipe, which is proportional to the square of the connecting pipe thickness. On the right side of this intersection point, the tensile-bearing capacity of the connectors is determined by the buckling deformation of the angle steel frame, which is independent of the connecting pipe thickness.

(2) when t = 0 mm, the tensile-bearing capacity at the intersection point of the two curves is associated with a connecting pipe thickness of 8 mm (d = 8 mm). On the left side of the intersection point, increasing the connecting pipe thickness could augment the tensile-bearing capacity of the connectors. On the right side of the intersection point, the tensile-bearing capacity of the connectors is governed by the buckling deformation of the angle steel frame and can be calculated using Eq.9, yielding a constant value. It is worth noting that increasing the connecting pipe thickness does not enhance the tensile-bearing capacity of this connector.

(3) The tensile-bearing capacity of connectors shows a significant increasing trend with the increase of d, but its maximum value is significantly regulated by t. When t = 0mm and d ＜9mm, the tensile-bearing capacity of connectors increases with d to approximately 80 kN. After that, with the increase of d, the bearing capacity no longer increases. By analogy, when t = 14mm and d＜15mm, the tensile-bearing capacity of connectors increases with d to approximately 175kN. After that, with the increase of d, the bearing capacity no longer increases. The increase of t will significantly enhance the positive contribution of d to the tensile-bearing capacity of connectors. There is a synergistic effect between d and t, jointly determining the tensile-bearing capacity of connectors. In practical applications, the smaller of the two is taken.

6. Conclusions

In this study, the tensile-bearing capacity of an innovative connector designed for OFPV platforms is investigated. First, 18 test specimens were designed and fabricated for tensile tests, which yielded the mechanical behavior of the test specimens including the failure modes, load–displacement curves, and load–strain curves. Second, a finite element model was developed and a comprehensive parametric study was conducted. Finally, the tensile mechanism and loading conditions of the connectors were thoroughly analyzed, and equations were derived to determine the tensile-bearing capacity of the connectors under two distinct failure modes. In addition, the tensile-bearing capacities of the connectors determined using the derived equations were compared with those predicted by the finite element model. The conclusions drawn based on the key findings of this study are as follows.

(1) The failure modes of the connectors are primarily categorized into two distinct modes: bulging deformation at the opening of the connecting pipe and buckling deformation of the angle steel frame.

(2) By performing a comprehensive analysis of the stress conditions and deformation mechanisms of the connectors, equations are derived to calculate the tensile-bearing capacity of the connectors under two distinct failure modes. It is advisable to use the smaller value of the tensile-bearing capacities calculated using the derived equations in practical applications.

(3) The thicknesses of the connecting pipe and baseplate have a pronounced effect on the tensile-bearing capacity of the connectors. The combined effect of these parameters is critical to the overall tensile-bearing capacity of the connectors. In cases where bulging deformation occurred at the opening of the connecting pipe, the tensile-bearing capacity is proportional to the square of the connecting pipe thickness. In cases where buckling deformation occurred on the angle steel frame, the tensile-bearing capacity is directly proportional to the baseplate thickness.

(4) For a constant baseplate thickness, the tensile-bearing capacity curves determined using Eq. 5 and Eq. 9 intersect at a particular point. On the left side of the intersection point, the tensile-bearing capacity of the connectors is predominantly determined by the connecting pipe thickness, which can effectively enhance the tensile-bearing capacity of the connectors. On the right side of the intersection point, the tensile-bearing capacity of the connectors is controlled by the buckling deformation of the angle steel frame, and increasing the connecting pipe thickness does not improve the tensile-bearing capacity of the connectors. However, increasing the baseplate thickness could significantly improve the tensile-bearing capacity of the connectors in this case.

(5) The tensile-bearing capacity of connectors shows a significant increasing trend with the increase of the connecting pipe thickness, but its maximum value is significantly regulated by the baseplate thickness. The increase in the baseplate thickness will significantly enhance the positive contribution of the connecting pipe thickness to the tensile-bearing capacity of connectors. There is a synergistic effect between the thickness of the connecting pipe and the baseplate, jointly determining the tensile-bearing

capacity of connectors. In practical applications, the smaller of the two is taken.

Acknowledgements

This research was financially supported by the National Key R& D Program of China (Grant No. 2022YFB4200700), the Natural Science Foundation of Hebei Province (Grant No. E2024402047), the Hebei Graduate Student Innovation Funding Project of China (Grant No. CXZZBS2025180) and the Hebei Key Laboratory of Low-Carbon Construction and Resilience Enhancement of Construction Engineering(Grant No. HKL-LRC-2024-3)

References

[1] Trapani, K. and D.L. Millar, "The thin film flexible floating PV (T3F-PV) array: The concept and development of the prototype.", Renewable Energy, 2014. 71: p. 43-50.
[2] Kjeldstad, Torunn, Lindholm, Dag Marstein, Erik Selj and Josefine, "Cooling of floating photovoltaics and the importance of water temperature.", Solar Energy, 2021. 218: p. 544-551.
[3] Shi. W., Yan, C. J., Ren, Z. R., Yuan, Z. M., Liu, Y. Y., Zheng, S. M., Li, X. and Han, X., "Review on the development of marine floating photovoltaic systems.", Ocean Engineering, 2023. 286: p. 115560.
[4] Sahu, A., N. Yadav and K. Sudhakar, "Floating photovoltaic power plant: A review.", Renewable and Sustainable Energy Reviews, 2016. 66: p. 815-824.
[5] Cazzaniga, R., Cicu, M., Rosa-Clot, M., Rosa-Clot, P., Tina, G. M. and Ventura, C., "Floating photovoltaic plants: Performance analysis and design solutions.", Renewable and Sustainable Energy Reviews, 2018. 81: p. 1730-1741.
[6] Lv, S., Lu, M., Liu, W. Z., Li, X. L., Lv, W. H., Liu, Z., Dong, X. C., Lu, T. H. and Yang, B. W., "Recent advances in longitudinal spatial area marine photovoltaics.", Renewable and Sustainable Energy Reviews, 2025. 208: p. 115036.
[7] Garrod, A., Neda Hussain, S., Ghosh, A., Nahata, S., Wynne, C. and Paver, S., "An assessment of floating photovoltaic systems and energy storage methods: A comprehensive review.", Results in Engineering, 2024. 21: p. 101940.
[8] Ghosh, A., "A comprehensive review of water based PV: Flotavoltaics, under water, offshore & canal top." Ocean Engineering, 2023. 281: p. 115044.
[9] Djalab, A., Djalab, Z., El Hammoumi, A., Tina, G. M., Motahhir, S., and Laouid, A. A. "A comprehensive Review of Floating Photovoltaic Systems: Tech Advances, Marine Environmental Influences on Offshore PV Systems, and Economic Feasibility Analysis." Solar Energy, 2024. 277: p. 112711.
[10] Fan, S., Ma, Z., Liu, T., Zheng, C., and Wang, H., "Innovations and development trends in offshore floating photovoltaic systems: A comprehensive review." Energy Reports, 2025. 13: p. 1950-1958.
[11] Yang, Y., Wang, H., Sun, J., Lu, W., & Shao, L., "Research on multi-body towing performance of a novel star-type floating photovoltaic structure." Ocean Engineering, 2025. 333: p. 121509.
[12] Dai, J., Zhang, C., Lim, H. V., Ang, K. K., Qian, X., Wong, J. L. H. and Wang, C. L., "Design and construction of floating modular photovoltaic system for water reservoirs." Energy, 2020. 191: p. 116549.
[13] Chandrasekaran, S., S.A. Uddin and M. Wahab, "Dynamic Analysis of Semi-submersible Under the Postulated Failure of Restraining System with Buoy." International Journal of Steel Structures, 2021. 21(1): p. 118-131.
[14] Li, Z., D. Chen and X. Feng, "Hydroelastic and expansibility analysis of a modular floating photovoltaic system with multi-directional hinge connections." Ocean Engineering, 2023. 289: p. 116218.
[15] Song, J., Kim, J., Chung, W. C., Jung, D., Kang, Y. J. and Kim, S., "Wave-induced structural response analysis of the supporting frames for multiconnected offshore floating photovoltaic units installed in the inner harbor." Ocean Engineering, 2023. 271: p. 113812.
[16] Yan, C., Shi, W., Han, X., Li, X., and Verma, A. S., "Assessing the dynamic behavior of multiconnected offshore floating photovoltaic systems under combined wave-wind loads: A comprehensive numerical analysis." Sustainable Horizons, 2023. 8: p. 100072.
[17] Luo, W., Zhang, X., Tian, X., Cheng, Z., Wen, B., Li, X. and Luo, Y., "Conceptual design and model test of a pontoon-truss type offshore floating photovoltaic system with soft connection." Ocean Engineering, 2024. 309: p. 118518.
[18] Jiang, Z., Dai, J., Saettone, S., Tørå, G., He, Z., Bashir, M. and Souto-Iglesias, A., "Design and model test of a soft-connected lattice-structured floating solar photovoltaic concept for harsh offshore conditions." Marine Structures, 2023. 90: p. 103426.
[19] Wang, B., Li, Y., Huang, L., Yao, Y. and Qin, Y., "Dynamic analysis of a novel star-type floating photovoltaic system with flexible connectors." Ocean Engineering, 2024. 304: p. 117854.
[20] Pringle, A.M., R.M. Handler and J.M. Pearce, "Aquavoltaics: Synergies for dual use of water area for solar photovoltaic electricity generation and aquaculture." Renewable and Sustainable Energy Reviews, 2017. 80: p. 572-584.
[21] Wang, Y. D., Zhang, Z. Y., Jiang, L. Z., Zeng, L. J. and Liu, J., "Mechanical Properties of Weather-Resistant Steel Beam-to-Column Connections." Advanced Steel Construction, 2024. 20(3): p.253-265.
[22] Ma, H. H., Ma, Y. Y., Fan, F. and Zhang, Y. N., "Seismic performance of single-layer spherical reticulated shells considering joint stiffness and bearing capacity." Advanced Steel Construction, 2022. 18(02): p. 604-616.
[23] Wang, Z. Q., Zheng, Z., MengXiang, J. W. and Jiang, W. Q., "Inversion Method of Uncertain Parameters For Truss Structures Based on Graph Neural Networks." Advanced Steel Construction, 2023. 19(4): p. 366-374.
[24] Jin, C., F.P. Bakti and M. Kim, "Multi-floater-mooring coupled time-domain hydro-elastic analysis in regular and irregular waves." Applied Ocean Research, 2020. 101: p. 102276.
[25] Chen, M., Guo, H., Wang, R., Tao, R. and Cheng, N., "Effects of Gap Resonance on the Hydrodynamics and Dynamics of a Multi-Module Floating System with Narrow Gaps." Journal of Marine Science and Engineering. 2021. 9(11): p. 1256.
[26] Zou, M., Chen, M., Zhu, L., Li, L. and Zhao, W., "A constant parameter time domain model for dynamic modelling of multi-body system with strong hydrodynamic interactions." Ocean Engineering, 2023. 268: p. 113376.
[27] Chen, M., Ouyang, M., Guo, H., and Zhang, C., "A Coupled Hydrodynamic-Structural Model for Flexible Interconnected Multiple Floating Bodies." Journal of Marine Science and Engineering. 2023.11(4): p. 813.
[28] Chen, M., Zou, M., Zhu, L., Ouyang, M., Liang, Q. and Zhao, W., "A fully coupled time domain model capturing nonlinear dynamics of float-over deck installation." Ocean Engineering, 2024. 293: p. 116721.
[29] Du, J., Zhang, D., Zhang, Y., Xu, K., Chang, A. and Zhao, S., "Design and comparative analysis of alternative mooring systems for offshore floating photovoltaics arrays in ultra-shallow water with significant tidal range." Ocean Engineering, 2024. 302: p. 117649.
[30] Yu, J., Cheng, X., Xie, C., Lu, Z., Ding, A., Wang, X. and Zhao,, "Hydrodynamic analysis of three-module semi-submersible platform and its mooring design." Ocean Engineering, 2024. 310: p. 118576.
[31] Zhang, C., Dai, J., Ang, K. K. and Lim, H. V., "Development of compliant modular floating photovoltaic farm for coastal conditions." Renewable and Sustainable Energy Reviews, 2024. 190: p. 114084.
[32] Mashrah, W., Chen, Z. H., Liu, H. B. and Amer, M. A., "Experimental, numerical, and theoretical study on static behaviour of novel steel dovetail joint subjected to axial tensile load." Advanced Steel Construction, 2022. 18(12): p. 453-464.
[33] Si, Q., Ding, Y., Zong, L. and Liu, H., "Mechanical properties and simulation method of structural steel after high cycle fatigue damage." Advanced Steel Construction, 2023. 200(300): p. 400.
[34] Zhang, Z. W., Li, D., Wang, H. J., Qian, H. L., Fang, W. Q., Jing, X. F. and Fan, F. , "Study of mechanical properties of a novel column-beam-column prefabricated steel frame joint." Advanced Steel Construction, 2024. 20(4): p. 0-344.
[35] ISO 6892-1 Metallic materials-Tensile testing-Part1:Method of test at room temperature, 2019.
[36] Li, B. Q. and Zhang, J. L., "Nonlinear Analysis and Design of Surface Waterproof Polyurea Coating with Consideration of Multiple Effects." Journal of Hydraulic Engineering, 2024, 55(04): p. 437-448.

Advanced Steel Construction – Vol. 21 No. 6 (2025) 511–519
DOI:10.18057/IJASC.2025.21.6.4

DYNAMIC RESPONSES OF HIGH-STRENGTH CONCRETE-FILLED HIGH-STRENGTH SQUARE STEEL TUBULAR COLUMNS UNDER VEHICLE COLLISION

Guo-Chang Li, Run-Ze Liu *, Xiao Li, Jia-Long Wang and Yue Zhou

School of Civil Engineering, Shenyang Jianzhu University, Shenyang, Liaoning 110168, China
** (Corresponding author: E-mail: runzeliu1996@163.com)*

ABSTRACT

High-strength concrete-filled high-strength square steel tubular (HCFHST) columns are vital structural elements in modern constructions, such as high-rise and large-span structures, due to their superior strength and reliability. However, during their services, they face challenges from vehicle collisions, which can compromise structural safety. To better understand their dynamic behaviours under vehicle collisions, dynamic constitutive relations for high-strength materials at high strain rates have been verified, firstly. Then, based on the verified simulation model, the working mechanisms of HSCFST columns under truck collision, including internal force development, damage evolution, and energy-dissipation mechanisms, are revealed. Furthermore, the influence of sectional dimensions, steel tube thickness, column height, axial compression ratio, material strengths, vehicle weight, and collision velocity on the anti-collision performance of HSCFST columns is presented. Simulation results indicate that HCFHST columns experience flexural deformation during collisions, and the cargo impact stage is the primary stage for plastic deformation development. The greatest bending moment occurs at the bottom, while the greatest shear force appears at the impact height. As deformation progresses, the steel tube becomes a critical internal force bearing component. The collision velocity, vehicle weight, sectional dimensions, steel tube thickness and steel strength are key factors affecting the anti-collision performance and energy-dissipating capacity of the HCFHST columns. By selecting key parameters according to the parametric study results, the maximum displacement calculation formula for HCFHST columns using the equivalent single degree of freedom method has been established, laying a foundation for the anti-collision design of HCFHST columns.

ARTICLE HISTORY

Received: 10 May 2025
Revised: 11 June 2025
Accepted: 12 June 2025

KEYWORDS

Concrete-Filled Steel Tubular Columns;
High-Strength Materials;
Dynamic Constitutive Relations of Materials;
Vehicle Collisions;
Dynamic Responses

1. Introduction

Modern transportation means have become an indispensable component of people's lives. Traffic safety issues like vehicle collisions are not infrequent and have attracted extensive attention. When a vehicle collides with a building, the consequences are likely significant, with the potential for substantial damage or even structural collapse, resulting in many casualties and property losses. Consequently, impact loads have emerged as a primary concern within civil engineering. Current standards in different countries [1-4] apply the equivalent static method for the anti-impact design, with the basic principle of applying a static load at the collision height. However, this method cannot properly reflect the dynamic behaviour of components to meet the safe requirements and reasonable design. It fails to cover the effect of various parameters on the dynamic response of components and underestimates the damage caused by large trucks and comparable vehicles. Consequently, the revelation of the working mechanisms and dynamic responses of components or structures can facilitate their precise design.

The extensive utilization of high-strength concrete-filled high-strength steel tubular (HCFHST) components in large-span and high-rise structures can be attributed to their high bearing capacity, good ductility, lightweight nature, and compact cross-sectional dimensions [5]. Consequently, researchers have examined the anti-impact behaviour and failure mechanism of HCFHST members through experimental research, numerical simulation, theoretical analysis, and other research methodologies. As demonstrated by Han et al. [6], high-strength concrete-filled steel tubular (HCFST) components exhibit superior toughness and impact resistance in transverse impact tests. Furthermore, a dynamic increase factor expression for the flexural capacity of HCFST components has been proposed, considering steel strengths, steel ratios, cross-sectional dimensions, and impact velocities. Hou et al. [7] have discovered that, due to the distinctive dynamic mechanical properties exhibited by high-strength steel, the impact resistance of CFHSST components is reduced when subjected to high-energy impact conditions in comparison with that of ordinary CFST components. Consequently, it was determined that CFHSST components may manifest evident performance deficiencies when exposed to extreme conditions. Yang et al. [8,9] have revealed the typical dynamic behaviours, loading mechanism, and residual properties of square HCFHST components under lateral impact with axial compression. A m-v-n failure criterion for HCFHST components has been put forward, and the calculation formulas for lateral impact bearing capacity and the maximum displacement calculation were proposed Li et al. [10] demonstrated that HCFHST columns show flexural deformation under impact loads and exhibit excellent impact resistance, as confirmed by a lateral impact test. Additionally, a formula for calculating the energy-dissipating coefficient for columns has been established. In the impact test on HCFHST columns, the aforementioned scholars employed rigid trolleys as a substitute for vehicles, thus neglecting the deformation and damage incurred by vehicles. Moreover, the impact mass and velocity in the aforementioned literature are comparatively minor in terms of vehicle collision, thus rendering it unfeasible to undertake a thorough investigation of the failure modes of the HCFHST columns under vehicle collision through the impact test. Consequently, the information for anti-collision design for the HCFHST column is still limited. Furthermore, due to the elevated expense and protracted duration of full-scale vehicle impact tests, there is currently a lack of experimental research on the dynamic performance of full-scale HCFHST columns in vehicle collisions.

Concerning vehicle impact loads, scholars have focused their research on the dynamic performance of reinforced concrete (RC) piers. However, there are comparatively few numerical simulations on concrete-filled steel tubular (CFST) columns. Saini et al. [11] have verified the feasibility of replacing RC piers with CFST piers through a comparison of the dynamic behaviours of those piers under impact loads. Furthermore, the influence of the key design parameters of CFST piers has been revealed, and the improvement directions of the impact resistance design of CFST piers have been identified. Alam et al. [12] have established a simplified rigid-body-spring model to simulate the vehicle impact of a Chevrolet C2500 truck on full-scale CFST components and those reinforced with CFRP. By comparing the dynamic behaviours with or without the simplified model, it is necessary to consider the vehicle deformation. Yu et al. [13] conducted a study of the dynamic behaviours of CFRP-reinforced CFST columns and CFRP-reinforced hollow steel tubes under vehicle impacts. The findings indicated that CFRP-reinforced CFST columns exhibit superior impact resistance in comparison to CFRP-reinforced hollow steel tubes. Hu et al. [14] have conducted a study on the mechanical properties of CFST piers when subjected to vehicle impacts. An evaluation of CFST piers has been conducted by the United States, European, and Chinese standards, and the applicable scopes of these standards have also been determined. In subsequent research, Hu et al. [15] found that the ratio of the mid-span residual displacement to the column height can be used as an effective index for evaluating the remaining bearing capacity of the CFST columns. Consequently, a prediction model for residual deformation has been formulated. Therefore, by drawing on the research achievements of domestic and foreign scholars on reinforced concrete piers under vehicle impacts, the present paper will examine the anti-collision behaviour of HCFHST columns under vehicle collision.

In this paper, LS-DYNA is employed to analyse the anti-collision behaviours and working mechanisms of HCFHST columns under vehicle collisions. Furthermore, the impacts of parameters, including sectional dimensions, steel tube thickness, column height, axial compression ratio, material strengths, vehicle weight, and impact velocity on the anti-collision performance of HCFHST columns are revealed. A maximum displacement calculation formula of HCFHST columns under vehicle collision is proposed to guide the engineering practice.

2. Modelling of finite element (FE) models

2.1. Modelling

The FE models of the HCFHST column collide with the truck are built with LS-DYNA, as illustrated in Fig. 1. As stated in reference [10], the *CONTACT_AUTOMATIC_SURFACE_TO_SURFACE and *CONTACT_TIED_SURFACE_TO_SURFACE algorithms are chosen to represent the contact within steel and concrete and the contact between steel and steel, respectively. The friction coefficient of the steel-concrete interface and steel-steel interface is taken as 0.6 and 0.15, respectively. To guarantee the accuracy of the simulated results, the Ford F800 SUT developed by NCAC and FHWA was used, which is available at https://thyme.ornl.gov/FHWA/F800WebPage/description/desc2.html. The model can accurately simulate truck-infrastructure interactions under impact, failure modes of the vehicle and post-crash vehicle stability [11,15].

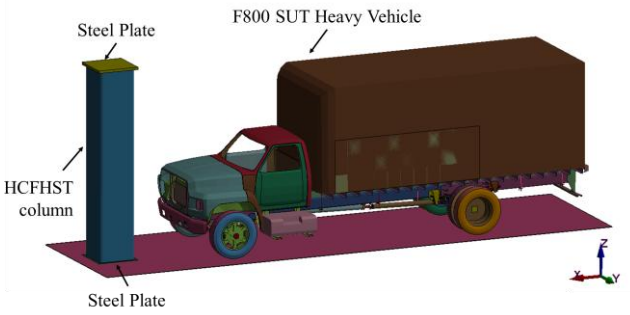

Fig. 1 Established FE model

2.2. Constitutive relations of materials

2.2.1. Selection of constitutive relations for high-strength steel (HSS)

The *MAT_024 is selected to perform the behaviour of HSS [10], with the defined constitutive relation illustrated in Eq. (1). As stated in reference [15], the relationship between yield strength (f_y) and ultimate tensile strength (f_u) has been defined. Meanwhile, the CS model is selected to consider the strain rate effect, and the calculation formula is shown in Eq. (2) [17]. To further confirm the precision and applicability of the CS model and its material parameters, a total of 84 sets of experimental data were collected [18-27], covering a range of steel yield strengths from 420 to 1,000 MPa, and a range of strain rate variations from 0.0002 to 5,293 s^{-1}. The comparison of the collected test data with the calculation results of Eq. (2) is demonstrated in Fig. 2. As exhibited in Fig. 2, the data are distributed close to the prediction line of Eq. (2). The mean, standard deviation (SD) and coefficient of variation (CoV) of the ratio of the calculated DIF to the measured DIF is 0.90, 0.104 and 0.115, respectively. As demonstrated in Fig. 2, the CS model, with material constants of C=6844s^{-1} and p=3.91, is capable of accurately reflecting the mechanical properties of HSS, with a yield strength ranging within 420~1000 MPa and a strain rate ranging within 0.0002~5293 s^{-1}.

$$\sigma = \begin{cases} E_s\varepsilon & (\sigma \le f_y) \\ f_y + 0.01E_s(\varepsilon - \varepsilon_y) & (f_y < \sigma) \end{cases} \tag{1}$$

$$DIF = 1 + (\frac{\dot{\varepsilon}}{C})^{1/p} \tag{2}$$

where, $\dot{\varepsilon}$ is the strain rate; and C and p are material constants.

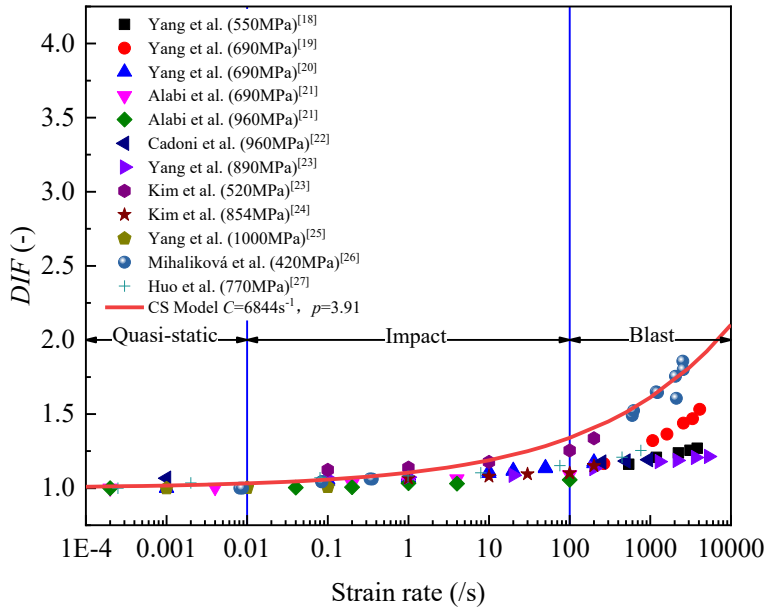

Fig. 2 Verification of the accuracy of CS strain rate model for HSS

2.2.2. Selection of constitutive relations for high-strength concrete (HSC)

The *MAT_72R3 is selected to represent the mechanical properties of high-strength concrete under triaxial compression. The DIF calculation formulas in European specification CEB-FIP (2010) are adopted to reflect the strain rate effect of HSC [28]. The calculation formula of DIF under compression and tension are displayed in Eqs. (3) and (4), respectively. To prove the precision and applicability of the DIF calculation formula, 72 sets of experimental data under dynamic compression [29-33] and 115 sets of experimental data under dynamic tension [34-36] are collected, covering compressive strength ranging within 60~120 MPa. Furthermore, the strain rate variations under dynamic compression and dynamic tension are in the ranges of 0.005~496 s^{-1} and 0.0005~175 s^{-1}, respectively. The collected results were compared with the calculated results of Eqs. (3) and (4), as shown in Fig. 3. The mean, SD, and CoV of the ratio of DIF calculated by Eq. (3) and Eq. (4) to the experimentally measured values are 0.97 and 0.89, 0.204 and 0.356, and 0.211 and 0.398, respectively. This indicates that the DIF calculation formula proposed by CEB-FIP (2010) can accurately reflect the mechanical behaviours of HSC with medium and high strain rates.

$$DIF_{compressive} = \begin{cases} (\dot{\varepsilon}_c/\dot{\varepsilon}_{c0})^{0.014} & \dot{\varepsilon}_c \le 30s^{-1} \\ 0.012(\dot{\varepsilon}_c/\dot{\varepsilon}_{c0})^{1/3} & \dot{\varepsilon}_c > 30s^{-1} \end{cases} \tag{3}$$

$$DIF_{tensile} = \begin{cases} (\dot{\varepsilon}_{ct}/\dot{\varepsilon}_{cto})^{0.018} & \dot{\varepsilon}_{ct} \le 10s^{-1} \\ 0.0062(\dot{\varepsilon}_{ct}/\dot{\varepsilon}_{cto})^{1/3} & \dot{\varepsilon}_{ct} > 10s^{-1} \end{cases} \tag{4}$$

where, $\dot{\varepsilon}_c$ and $\dot{\varepsilon}_{ct}$ are strain rate under compression and tension, respectively; $\dot{\varepsilon}_{c0} = 30 \times 10^{-6}\ s^{-1}$; and $\dot{\varepsilon}_{cto} = 1 \times 10^{-6}\ s^{-1}$.

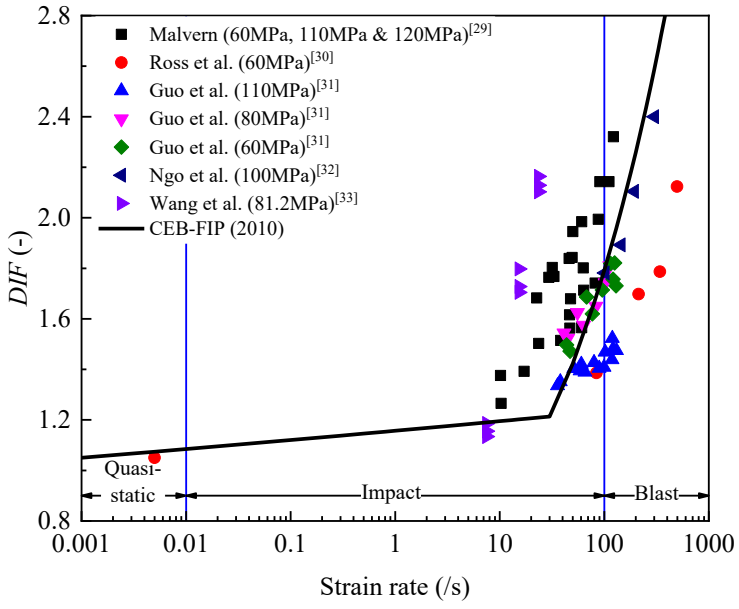

(a) HSC under compression

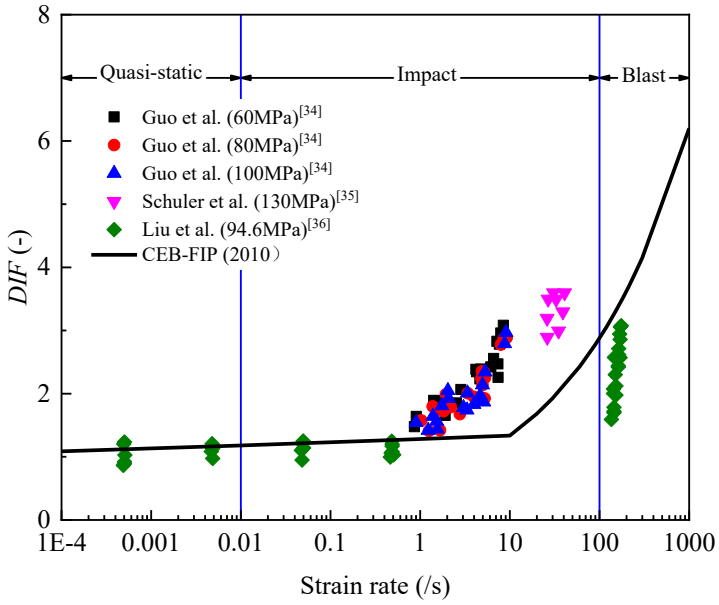

(b) HSC under tension

Fig. 3 Verification of the accuracy of DIF calculation formula for HSC

2.3. Model matrix

In this study, FE models are built to analyse the dynamic behaviours of HCFHST columns under various parameters. A total of 36 full-scale models of HCFHST columns, subjected to vehicle collision, have been established with differing parameters, which are detailed in Table 1.

3. Working mechanisms

To analyse the working mechanism of the typical column, the collision process, development of internal force, evolution of damage, and the energy dissipation mechanism are analysed.

3.1. Collision process

The impact force time-history curve is displayed in Fig. 4(a), and the displacement time-history curve is presented in Fig. 4(b). According to Fig. 4(a), the entire vehicle impact process can be divided into four stages as shown below.

Bumper impact stage (230~249 ms): In the initial collision stage, the bumper contacts the HCFHST column, with a collision height ranging between 520 and 1860 mm. This stage constitutes 18% of the total duration. The overall impact force is minor, exhibiting an increase followed by a subsequent decrease. Since the bumper stiffness is considerably lower than that of the HCFHST column, the impact force achieves its first peak of $0.01F_{max}$ at 238 ms, where F_{max} is the maximum impact force throughout the collision process. Subsequently, the impact force gradually attenuates due to the yield of the bumper. In this phase, the column's displacement is limited, with a displacement of $0.02u_{max}$, where u_{max} denotes the maximum displacement throughout the entire collision process.

Engine impact stage (249~265 ms): The engine has been found to undergo a secondary collision with the bumper as a result of inertia, with the effective collision height extending to 300~1890 mm. The duration of this stage constitutes 15% of the entire collision process. Since the engine exhibits greater stiffness than the bumper, the impact force and column deformation are increased to a greater extent than in the preceding stage. The impact force arrives a peak of $0.06F_{max}$ at 255 ms, and the displacement of the HCFHST column develops to $0.05u_{max}$ at 260 ms, although this remains constrained.

Cockpit impact stage (265~325 ms): The cockpit contacts with the HCFHST column, and the collision height is further extended to 300~2280 mm. This stage occupies 56% of the total duration. Due to the significant difference in stiffness between the cockpit and the HCFHST column, the cockpit is eventually completely crushed. Consequently, the impact force is insignificant at this stage, and its value is stable around $0.01F_{max}$. Furthermore, the displacement of the HCFHST column exhibits stability, with a maximum value of $0.02u_{max}$. It is noticed that the displacement and impact force of the HCFHST column do not significantly change at this stage.

Cargo impact phase (325~337 ms): The cargo container continues to move along the x-axis under the action of inertial force, and its collision range extends to 300~3460 mm. This stage constitutes 11% of the total duration. The trajectory of the cargo in the cargo container has been deflected due to constraints imposed by the residual structure of the cockpit. The collision between the cargo and the HCFHST column occurred at an angle of 2° to the x-axis, with the impact load primarily concentrated at a height of 2240 mm. As the stiffnesses of the cargo and HCFHST are close, the impact force reaches its maximum of 157,902 kN at 326ms. Subsequently, the displacement reaches a peak of 65 mm at 334ms. Then, once the kinetic energy of the cargo is depleted, the impact force gradually decreases to 0 kN, leading to a displacement of 36 mm for the HCFHST column, accompanied by a rebound rate of 55%. It has been determined that this stage represents the main deformation development stage of the HCFHST column under vehicle collision.

Table 1
Key model parameters and simulation results

No.	B (mm)	t (mm)	L (mm)	α (-)	n (-)	f_y (MPa)	f_{cu} (MPa)	m (ton)	v (m/s)	E (kJ)
C1	750	25	3900	12.9%	0.30	890	110	12000	33.3	6667
C2	750	25	3900	12.9%	0.30	770	110	12000	33.3	6667
C3	750	25	3900	12.9%	0.30	690	110	12000	33.3	6667
C4	750	25	3900	12.9%	0.30	620	110	12000	33.3	6667
C5	750	25	3900	12.9%	0.30	550	110	12000	33.3	6667
C6	750	25	3900	12.9%	0.30	460	110	12000	33.3	6667
C7	750	25	3900	12.9%	0.30	890	120	12000	33.3	6667
C8	750	25	3900	12.9%	0.30	890	100	12000	33.3	6667
C9	750	25	3900	12.9%	0.30	890	90	12000	33.3	6667
C10	750	25	3900	12.9%	0.30	890	80	12000	33.3	6667
C11	750	25	3900	12.9%	0.30	890	70	12000	33.3	6667
C12	750	25	3900	12.9%	0.30	890	60	12000	33.3	6667
C13	750	25	4200	12.9%	0.30	890	110	12000	33.3	6667
C14	750	25	4500	12.9%	0.30	890	110	12000	33.3	6667
C15	750	25	4800	12.9%	0.30	890	110	12000	33.3	6667
C16	650	25	3900	14.8%	0.30	890	110	12000	33.3	6667
C17	700	25	3900	13.8%	0.30	890	110	12000	33.3	6667
C18	800	25	3900	12.1%	0.30	890	110	12000	33.3	6667
C19	850	25	3900	11.4%	0.30	890	110	12000	33.3	6667
C20	750	20	3900	10.4%	0.30	890	110	12000	33.3	6667
C21	750	22	3900	11.4%	0.30	890	110	12000	33.3	6667
C22	750	30	3900	15.4%	0.30	890	110	12000	33.3	6667
C23	750	25	3900	12.9%	0.20	890	110	12000	33.3	6667
C24	750	25	3900	12.9%	0.40	890	110	12000	33.3	6667
C25	750	25	3900	12.9%	0.50	890	110	12000	33.3	6667
C26	750	25	3900	12.9%	0.60	890	110	12000	33.3	6667
C27	750	25	3900	12.9%	0.30	890	110	8000	33.3	4444
C28	750	25	3900	12.9%	0.30	890	110	18000	33.3	10000
C29	750	25	3900	12.9%	0.30	890	110	5213.6	33.3	2896
C30	750	25	3900	12.9%	0.30	890	110	12000	16.7	1667
C31	750	25	3900	12.9%	0.30	890	110	12000	25.0	3750
C32	750	25	3900	12.9%	0.30	890	110	12000	41.7	10417
C33	750	25	3900	12.9%	0.30	890	110	12000	33.3	6667
C34	750	25	3900	12.9%	0.30	770	110	12000	33.3	6667
C35	750	25	3900	12.9%	0.30	690	110	12000	33.3	6667
C36	750	25	3900	12.9%	0.30	620	110	12000	33.3	6667

Note: B, t and L are the cross-sectional dimension, wall thickness and column height, respectively; α denotes the steel ratio; n is the axial compression ratio; f_y and f_{cu} are the steel strength and concrete strength, respectively; m is the vehicle weight; v is the impact velocity; and E is the impact energy.

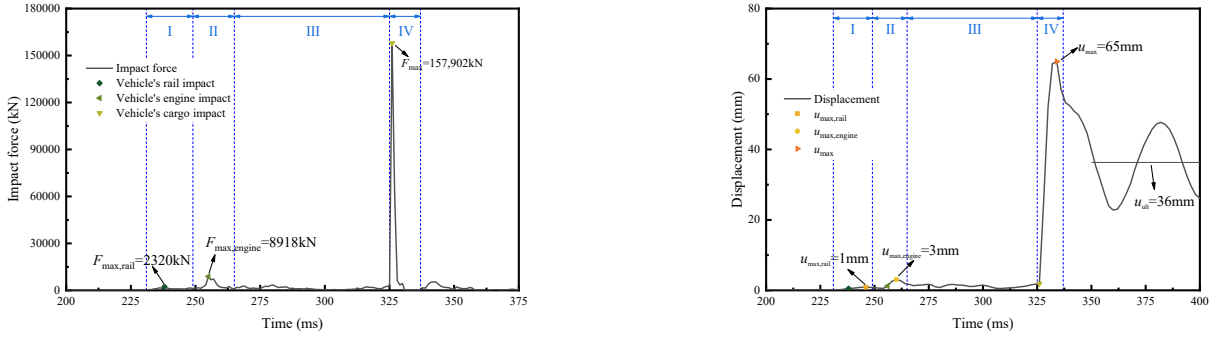

(a) Impact force

(b) Displacement

Fig. 4 Time-history curves

3.2. Development of bending moment

To analyze the damage evolution of the HCFHST columns, the bending moment development is examined in this section. Fig. 5(a) depicts the bending moment in the longitudinal direction at various characteristic points, where 'Max' and 'Min' denote the maximum and minimum value throughout the collision process. The maximum bending moment is 14,174 kN·m at a height of 3000 mm, denoted as M_{max}. In contrast, the minimum bending moment, M_{min}, is recorded at the bottom support, with a value of 15,091 kN·m. This indicates that the greatest bending moment appears at the bottom. As demonstrated in Fig. 5(a), the bending moment remains low, at only $0.15M_{min}$, during the bumper, engine, and cockpit impact stage. With the increase in displacement, the bending moment of the HCFHST column begins to stabilize. During the cargo impact stage, the bending moment gradually rises, ultimately reaching its maximum value.

The bending moment of the HCFHST column and the bending moments borne by each component at the M_{min} section are illustrated in Fig. 5(b). As exhibited in Fig. 5(b), the bending moment gradually increases to 1,520 kN·m during the bumper and engine impact stage, with the bending moment borne by the concrete increasing from 51% to 77% and the corresponding bearing proportion of steel tube decreasing from 49% to 23%. This phenomenon can be attributed to the overall stress of each component are relatively low, as discussed in Section 3.4. During the cockpit impact stage, the bending moment continues to rise, reaching 2,217 kN·m. The increased stress in the steel tube causes an increase in the bending moment, which grows to 29% of its initial value. Consequently, this results in a 6% decrease in the bending moment carried by the concrete. These analyses indicate that concrete is the key component carrying the bending moment during the bumper, engine, and cockpit impact stages. Consequently, the bending moment exhibited a gradual increase, attaining its maximum at 337 ms. Due to the concrete damage and the high stress in the steel tube, the bearing bending moment of the concrete has dropped to 2%, implying that the steel tube constitutes the main bending moment bearing component in the main displacement development stage. In summary, the HCFHST columns produced the greatest bending moment at the bottom under vehicle collisions. In the initial impact stage, concrete is the main component that bears the bending moment in the HCFHST column. Conversely, in the main displacement development stage, the steel tube becomes the critical component that bears the bending moment.

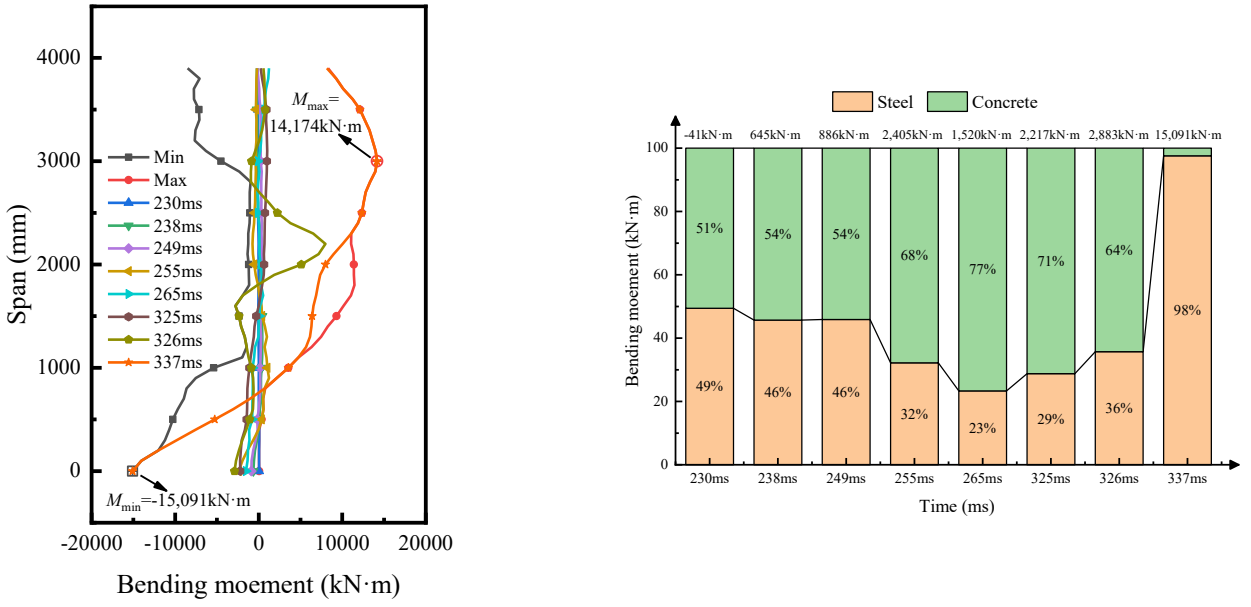

(a) Distribution of bending moment at each characteristic point

(b) Development of the bending moment at M_{min} section

Fig. 5 Development of bending moment of typical column

3.3. Development of shear force

To analyse the damage evolution of the HCFHST column, the shear force development of the HCFHST column is determined. Fig. 6(a) illustrates the shear force at various characteristic points along the longitudinal direction, where 'Max' and 'Min' mean the maximum and minimum shear forces observed during the collision process. The maximum shear force, S_{max}, is recorded at 44,647 kN, while the minimum shear force, S_{min}, is -29,725 kN, both occurring in the collision zone. This indicates that the greatest shear force is experienced in that specific area. As depicted in Fig. 6(a), it is observed that the shear force remains relatively low during the bumper impact, engine impact, and cockpit impact stages, reaching a value of $0.18S_{max}$. However, the shear force gradually increases and reaches its peak in the cargo impact stage.

Fig. 6(b) displays the shear force development of the HCFHST column and its components at the S_{max} section. As plotted in Fig. 6(b), the shear force fluctuates between -1555 kN and 513 kN during the bumper and engine impact stage, owing to low impact force, as explained in Section 3.1. In these stages, the steel tube bears more shear force than the concrete, implying that the steel tube is the critical components that bears the shear force. In the cockpit impact stage, the shear force fluctuates in the range of -1094~1078 kN. During this phase, the bearing shear force of the concrete exceeds that of the steel tube, suggesting that the concrete becomes the main shear force-bearing component. In the cargo impact stage, the maximum shear force reaches -44,647 kN at 326 ms, increasing the shear force bearing proportion of the steel tube to 15%, while the shear force borne by the concrete decreases to 85%. Following this peak, the shear force gradually declines. As the displacement progresses, the shear force carried by the concrete decreases. At 337 ms, the shear force had dropped to 5,560 kN, with the concrete only bearing 20% of the shear force. In contrast, the bearing shear force of the steel tube increased to 80%, indicating that the steel tube becomes the primary component to bear the shear force as the displacement progresses. In conclusion, the highest shear force occurs at the vehicle zone during a vehicle collision, and the steel tube is the main component bearing the shear force.

3.4. Evolution of damage

To examine the damage evolution of HCFHST columns during vehicle collisions, the stress development and effective plastic strain for each component of the HCFHST columns is analysed. Figs. 7 and 8 illustrate the stress and equivalent plastic strain of each component. These figures demonstrate that the HCFHST column undergoes bending deformation during a vehicle collision, with the maximum displacement occurring at the mid-span. During the first three impact stages, the Mises stress in the steel tube reaches $0.67f_y$, suggesting that only elastic deformation has occurred. In this phase, the concrete predominantly undergoes plastic deformation at the point of impact, with its principal stress increasing to $1.10f_{cu}$. Notably, 15% of the concrete in the mid-span section experiences plastic deformation. In the cargo impact stage, plastic deformation is displayed at the impact location on the front collision surface of the steel tube, while the concrete damage is mainly located at the impact location. After the vehicle collision is concluded, the maximum plastic deformation observed in the steel tube occurs at the mid-span section, particularly in the corner area, with a value of 0.099. The concrete in this section incurs complete damage. In summary, the HCFHST column exhibits bending deformation in response to the vehicle collision, with the most significant damage development occurring at the impact location.

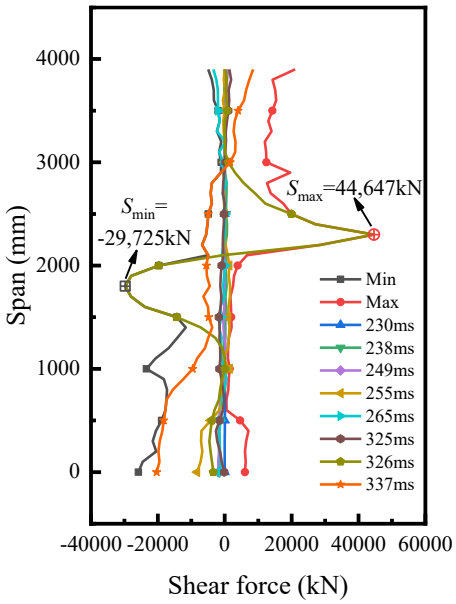

(a) Distribution of shear force at each characteristic point

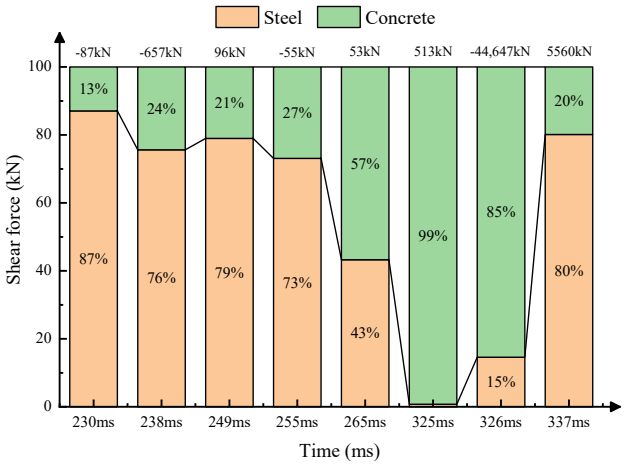

(b) Development of the shear force at S_{max} section

Fig. 6 Development of shear force of typical column

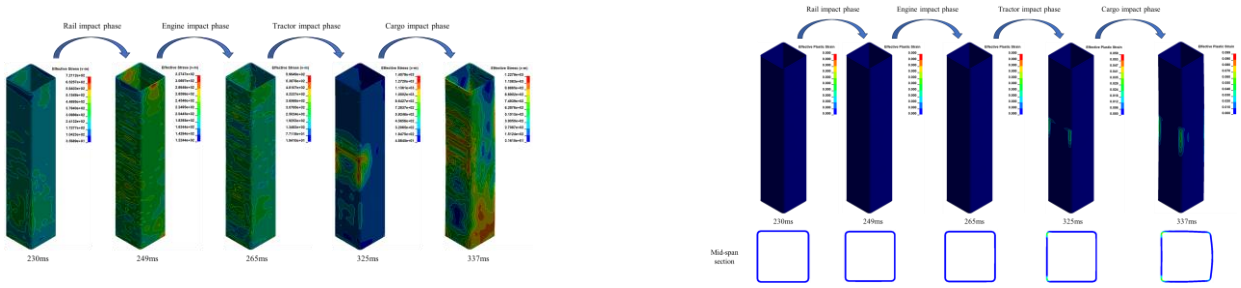

(a) Mises stress (unit: MPa)

(b) Effective plastic strain

Fig. 7 Damage evolution of steel tube in typical column

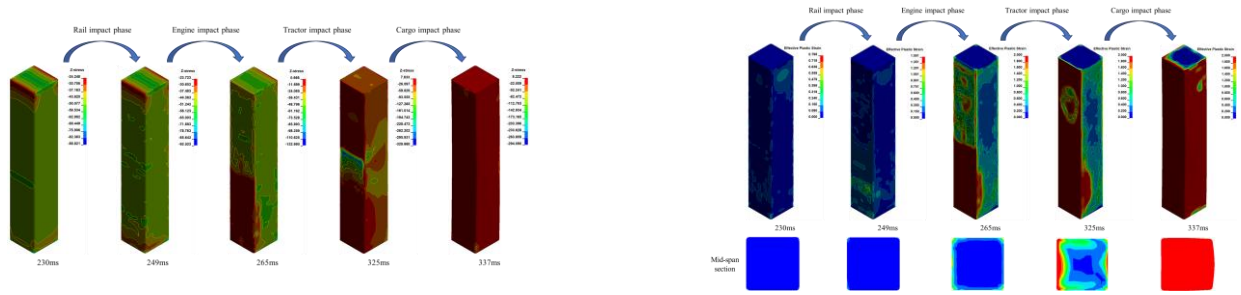

(a) Principle stress (unit: MPa)

(b) Effective plastic strain

Fig. 8 Damage evolution of the concrete in typical column

3.5. Energy dissipating mechanism

Fig. 9 presents the time-history curves of energy and energy dissipated by each component. As illustrated in Fig. 9, the hourglass energy to the total energy (*TE*) ratio is less than 4%, confirming the reliability of the simulation. In the bumper, engine and cockpit impact stage, the dissipated energy of the HCFHST column is less than 0.010*TE*, whilst the energy dissipated by the vehicle can reach up to 0.217*TE*, indicating that the vehicle's deformation predominates in energy dissipation. In the cargo impact stage, the vehicle's kinetic energy rapidly decreases, with the HCFHST column dissipating 0.274*TE*. In this stage, the dissipated energy of concrete and steel tube is approximately 30% and 70%, respectively, indicating that the steel tube is the primary energy-dissipating component. Meanwhile, the vehicle's dissipated energy rises to 0.264*TE*. In summary, the HCFHST column dissipates less energy than the vehicle. The cargo impact stage is the primary energy-dissipating stage, with the steel tube playing a vital role in energy absorption.

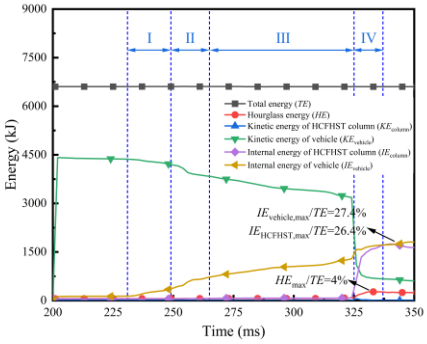

(a) Time-history curves of energy

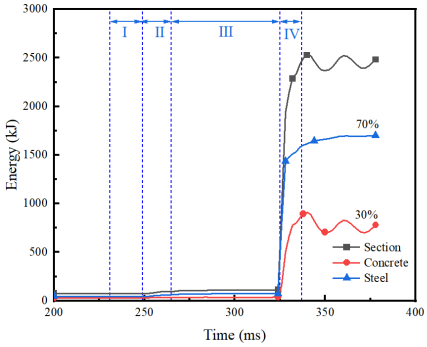

(b) Energy dissipation ratio of each component

Fig. 9 Development of energy

3.6. Parametric analysis

The effects of parameters on the anti-collision behaviours of HCFHST columns are investigated, and the detailed parameters and the corresponding simulation results are shown in Table 1. The impact of parameters on dissipated energy (E_{abs}), maximum displacement (u_{max}) and residual displacement (u_{ult}) of the HCFHST column is displayed in Figs. 10-12, respectively.

Changing sectional dimensions, steel tube thickness and material strength consequently changes the flexural strength and/or flexural stiffness of the HCFHST columns, affecting their dynamic behaviour during vehicle collisions. As demonstrated in Figs. 10-12, increasing the sectional dimension from 650 mm to 850 mm, the E_{abs} of the HCFHST column reduced from 2560 kJ to 2330 kJ, representing a 10% reduction. The u_{max} decreased from 73 mm to 58 mm, indicating a 26% drop, while the u_{ult} remained almost unchanged. This reduction in deformation and plastic energy dissipation is associated with the increase in sectional dimensions, which enhance the column's flexural strength and stiffness. When the steel tube thickness was increased from 20 mm to 30 mm, the E_{abs} by the columns rises from 2310 kJ to 2500 kJ, exhibiting a 10% increase. Additionally, the u_{max} reduces from 66 mm to 56 mm, indicating an 18% decrease, and the u_{ult} diminishes from 35 mm to 31 mm, showing a 13% reduction. These improvements are due to the thicker steel tube, the greater flexural strength and stiffness of the HCFHST column, thereby improving its anti-collision property. As the steel strength increases from 460 MPa to 890 MPa, the E_{abs} of the column reduces from 2600 kJ to 2460 kJ, representing a 6% decrease. Furthermore, the u_{max} reduces from 77 mm to 65 mm, indicating an 18% decrease, and the u_{ult} diminishes from 53 mm to 36 mm, showing a 47% reduction. It is evident that an increase in steel strength results in an enhancement of the flexural strength of the HCFHST column, leading to an increase in the impact resistance of the HCFHST column. When the concrete compressive strength is modified within the range of 60~120 MPa, the alterations in the E_{abs}, u_{max}, and u_{ult} of the column remain within 10%. This indicates that the effect of concrete compressive strength on the dynamic behaviour of the HCFHST column was negligible. To summarize, it can be concluded that the enhancement of the sectional dimension, the steel tube thickness, and the steel strength can lead to a substantial enhancement on the anti-collision performance of the HCFHST columns. Conversely, the concrete compression strength exerts a minor influence on the anti-collision performance of the HCFHST columns.

Increasing the column height, which raises the slenderness ratio, decreases the bending resistance of the HCFHST column. When the column height is increased from 3900 mm to 4800 mm, there is a minor influence on the energy dissipation. However, a slight increase is noted in the maximum and residual displacement, although this increase remains within 5%. Therefore, it can be concluded that the anti-collision properties of the HCFHST column diminish with increased column height. When the axial compression ratio rises from 0.2 to 0.6, the E_{abs} of the column increases from 2380 kJ to 2660 kJ, indicating an 11% enhancement. The increase in u_{max} and u_{ult} of the column also stays within 5%. As discussed in Section 3.4, the HCFHST column exhibits bending deformation during a vehicle collision. As a result, a higher axial compression ratio intensifies the second-order effect on the bending deformation of the column caused by the axial force, ultimately leading to a reduction in the anti-collision property of the HCFHST column.

The increase in impact mass from 5.2 tons to 18 tons led to a substantial rise in E_{abs}, which increased from 100 kJ to 5,040 kJ representing an addition of 49.4 times. The u_{max} rises from 4 mm to 95 mm, and the u_{ult} of the column exhibited an increase from 1 mm to 69 mm. Additionally, when the collision velocity rises from 16.67 m/s to 41.67 m/s, the E_{abs} also increased, from 322 kJ to 4,010 kJ, demonstrating an increment of 11.4 times. The maximum displacement grows from 18 mm to 82 mm, and the residual displacement of the column increases from 5 mm to 52 mm.

The slopes shown in Figs. 10-12 reveal the impact of each parameter on the dynamic behaviours of the HCFHST columns, ranked in descending order: vehicle weight, impact velocity, sectional dimension, steel tube thickness, steel strength, column height, axial compression ratio and concrete compressive strength. Consequently, it is recommended to enhance the anti-collision properties of HCFHST columns by raising the sectional dimension, steel tube thickness, or steel strength.

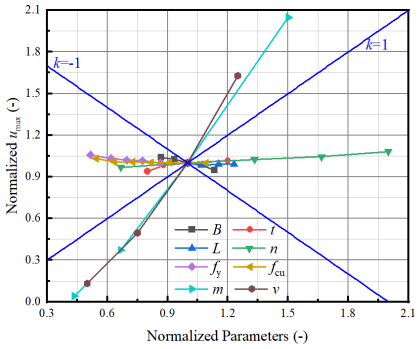

Fig. 10 Influence of parameters on the energy dissipation

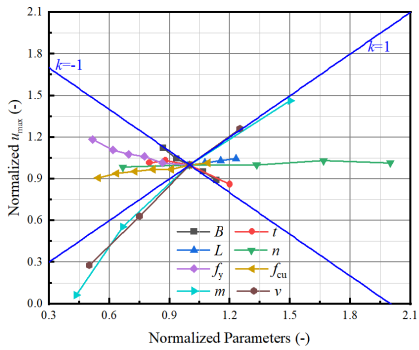

Fig. 11 Influence of parameters on the maximum displacement

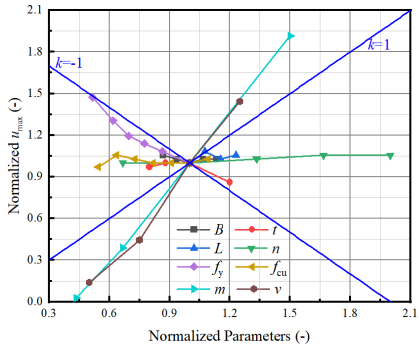

Fig. 12 Influence of parameters on the residual displacement

4. Calculation of maximum displacement

The literature has established a method for calculating the maximum displacement of a column under impact, based on the ideal elastic-plastic model and the equivalent SDOF method. This method assumes that the impactor's kinetic energy is fully converted into the column's internal energy. The formulas for calculating elastic displacements (X_e) and maximum displacements ($X_{m,impact}$) are presented in Eqs. (5) and (6), respectively. The main difference between this study and the findings in the literature [37] is that, in this paper, the vehicle's kinetic energy is not fully transformed into the HCFHST column's internal energy. Therefore, an energy dissipation formula for HCFHSTs column subjected to vehicle collisions is proposed. This formula will be incorporated into Eq. (6) to provide a more accurate calculation of the maximum displacement of the HCFHST column under vehicle collision.

$$X_e = \frac{F_y}{k} \tag{5}$$

$$X_{m,\text{impact}} = \frac{1}{2}\left[\frac{E_{impact}}{k_{\text{LM}}k(1+\alpha)} + X_e\right] \tag{6}$$

where, X_e denote the elastic displacement of the HCFHST column under vehicle collision; the bending resistance, F_y, can be determined as $F_y = \frac{8M_p}{L}$, where M_p is the flexural strength of the HCFHST column, and the calculation formulas detailed in reference [38]; the stiffness, k, can be calculated with $k = \frac{192EI}{L}$, where EI is the flexural stiffness of the column; $X_{m,impact}$ represents the maximum displacement of the column; k_{LM} is the uniformly distributed mass coefficient, which is 0.33 with a fixed-fixed boundary condition; E_{impact} denotes the impact energy; and α is the ratio of the HCFHST column mass to vehicle weight.

Key parameters are selected based on the parametric study in Section 3.6. The regression analysis is used to establish the relationship between the energy dissipation and key parameters, with the prediction formula in Eq. (7). Fig. 13(a) compares simulated and calculated energy dissipation, showing a mean of 1.005 and a SD of 0.031, with 92% of predicted values within a 5% error. These analyses verify that the formula can accurately and precisely predict the energy dissipation of the HCFHST columns. For maximum displacement, Eq. (7) can be substituted into E_{impact} in Eq. (6). Fig. 13(b) compares predicted and simulated maximum displacements, generating a mean of 0.893 and a SD of 0.203, with over 70% of predicted values within a 20% error. While the equivalent SDOF method may slightly underestimate the maximum displacement during vehicle collisions, the prediction accuracy remains acceptable within a 20% error range. Thus, using the energy dissipation formula with the equivalent SDOF method effectively predicts maximum displacement and provides useful guidance for engineering practice.

$$E_{abs} = 2460f(m)f(v)f(f_y)f(t)f(B)f(L) \tag{7}$$

where $f(m) = 0.00285m^2 + 0.0917m - 0.52$, unit in ton; $f(v) = 0.00095v^2 + 0.0045v - 0.21$, unit in m/s; $f(f_y) = 3.16 \times 10^{-7} \times {f_y}^2 - 0.00056f_y + 1.25$, unit in MPa; $f(t) = -0.00106t^2 + 0.0604t + 0.16$, unit in mm; $f(B) = -1.16 \times 10^{-6} \times B^2 + 0.0013B + 0.69$, unit in mm; and $f(L) = 4.54 \times 10^{-8} \times L^2 - 0.0004L + 1.87$, dimensionless.

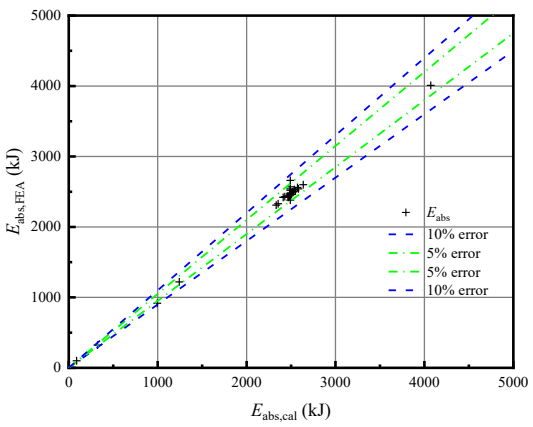

(a) Accuracy of energy dissipating calculation formula

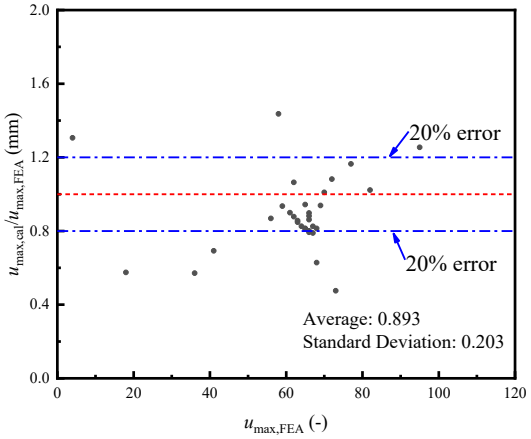

(b) Accuracy of maximum displacement calculation formula

Fig. 13 Accuracy of calculation formula of energy dissipation and maximum displacement of HCFHST column under vehicle collision

5. Conclusions

This paper examines the dynamic performances of HCFHST columns under vehicle collision through numerical simulations. A thorough analysis of working mechanisms for the HCFHST column is conducted, covering the collision process, the development of internal forces, the evolution of damage, and the energy dissipation mechanisms. Through parametric analysis, the impact of parameters such as sectional dimensions, steel tube thickness, column height, axial compression ratio, material strength, vehicle weight and impact velocity on the impact resistance is investigated. Additionally, prediction equations for energy dissipation and maximum displacement of the full-scaled HCFHST columns under vehicle collisions are proposed. Based on the simulation results, the following conclusions can be concluded:

(1) The collected test data proves that the CS model and the CEB-FIP (2010) formula accurately reflect the dynamic performance of HSS and HSC under medium and high strain rate.

(2) The collision process can be categorised into four stages: bumper impact stage, engine impact stage, cockpit impact stage, and cargo impact stage. Among them, the cargo impact stage is the main dynamic behaviour stage of the column. Throughout the entire collision process, the HCFHST column exhibits a bending deformation. The HCFHST column dissipates energy lower than that of the vehicle, and the steel tube, dissipating 70% of the energy within the HCFHST column, is the main energy-dissipating component.

(3) Under a vehicle collision, the HCFHST column generates the greatest bending moment at the bottom and the greatest shear force at the vehicle impact zone. In the initial deformation stage, concrete is the critical internal force bearing component in the HCFHST column. As the displacement progresses, the steel tube takes over as the primary component bearing the internal force.

(4) The parametric results indicate that key factors influencing the dynamic performances of HCFHST columns include impact velocity, impact mass, sectional dimensions, steel tube thickness, and steel strength. Therefore, it is recommended to improve the anti-collision performance of HCFHST columns by raising the sectional dimensions, steel tube thickness, or steel strength.

Acknowledgements

This study is financially supported by the Key Program of National Natural Science Foundation of China, China (51938009), and the General Program of National Natural Science Foundation of China, China (51878419).

References

[1] BS 5400, Steel, concrete and composite bridges, Part 2: Specification for loads, British Standards Institution, London, 1988.
[2] AASHTO-LRFD, AASHTO-LRFD Bridge Design Specifications - Customary US Units, 6th edn, American Association of State Highway and Transportation Officials, Washington, 2020.
[3] BS EN 1991-1-7:2006, Eurocode 1: Actions on structures - Part 1-7: General actions - Accidental actions, European Committee for Standardization, Brussels, 2006.
[4] JGJ D60-2015, General Specification for Design of Highway Bridges and Culverts, China Communications Press, Beijing, 2015. (in Chinese).
[5] G.C. Li, B.W. Chen, Z.J. Yang, H.B. Ge, X. Li, AXIAL BEHAVIOR OF HIGH STRENGTH CONCRETE FILLEDHIGH STRENGTH SQUARE STEEL TUBULAR STUB COLUMNS, Adv Steel Constr 17(2) (2021) 158-168, https://doi.org/10.18057/IJASC.2021.17.2.6.
[6] L. H. Han, C. C. Hou, X. L. Zhao, K. J. Rasmussen, Behaviour of high-strength concrete filled steel tubes under transverse impact loading, J. Constr. Steel Res. 92 (2014) 25-39,

https://doi.org/10.1016/j.jcsr.2013.09.003.
[7] C. Hou, D. Wu, D. Ma, Experimental and numerical study on the impact performance of concrete-filled high-strength steel tube (CFHSST). Thin-Walled Structures 2024, 195:111450, doi:10.1016/j.tws.2023.111450.
[8] X. Yang, H. Yang, S. Zhang, Transverse impact behavior of high-strength concrete filled normal /high-strength square steel tube columns, Int. J. Impact Eng. 139 (2020) 103512, https://doi.org/10.1016/j.ijimpeng.2020.103512.
[9] X. Yang, Z. Zhang, Y. Zhu, W. Ma, J. Chen, D. Li, Dynamic responses and residual capacity of high-strength CFST members subjected to axial impact, J. Constr. Steel Res. 202 (2023) 107800, https://doi.org/10.1016/j.jcsr.2023.107800.
[10] G.C. Li, R.Z. Liu, C. Fang, X. Li, Dynamic responses of high-strength concrete-filled high-strength steel tubular column under lateral impact, J. Constr. Steel Res. 217 (2024) 108663, https://doi.org/10.1016/j.jcsr.2024.108663.
[11] D. Saini, B. Shafei, Performance of Concrete-Filled Steel Tube Bridge Columns Subjected to Vehicle Collision, J. Bridge Eng. 24 (8) (2019) 04019074, https://doi.org/10.1061/(ASCE)BE.1943-5592.0001439.
[12] M. Yu, X.X. Zha, Y.C. Wang, Behaviour of different types of columns under vehicle impact, Proceedings of the 3rd International Conference on Steel and Composite Structures, 2007, pp. 879-884. Manchester, UK.
[13] M. I. Alam, S. Fawzia, X.L. Zhao, Numerical investigation of CFRP strengthened full scale CFST columns subjected to vehicular impact, Eng. Struct. 126 (2016) 292-310, https://doi.org/10.1016/j.engstruct.2016.07.058.
[14] B. Hu, Y.Y. Liu, Vehicular Collision Performance Evaluation of Concrete-Filled Steel Tubular Piers Designed According to Current Codes in the US, Europe, and China, J. Build. Eng. 27 (6) (2022) 04022038, https://doi.org/10.1061/(ASCE)BE.1943-5592.0001889.
[15] B. Hu, H.B. Wang, Vehicular Impact Performance Evaluation Method for CFST Columns Based on Residual Deformation, Int. J. Steel Struct. 24 (2024) 529-549, https://doi.org/10.1007/s13296-024-00834-7.
[16] G.C. Li, B.W. Chen, B.W. Zhu, Z.J. Yang, H.B. Ge, Y.P. Liu, Axially loaded square concrete-filled steel tubular long columns made of high-strength materials: experimental investigation, analytical behavior and design, J. Build. Eng. 58 (2022) 104994, https://doi.org/10.1016/j.jobe.2022.104994.
[17] G.R. Cowper, P. S. Symonds, Strain Hardening and Strain Rate Effects in the Impact Loading of Cantilever Beams. Providence: Brown University, 1958.
[18] H. Yang, X. Yang, A. H. Varma, Y. Zhu, Strain-Rate Effect and Constitutive Models for Q550 High-Strength Structural Steel, Mater. Eng. Perform. 28 (2019) 6626-6637, https://doi.org/10.1007/s11665-019-04431-2.
[19] X. Yang, H. Yang, S. Zhang, Rate-dependent constitutive models of S690 high-strength structural steel, Constr. Build. Mater. 198 (2019) 597-607, https://doi.org/10.1016/j.conbuildmat.2018.11.285.
[20] X. Yang, H. Yang, Z. Lai, S. Zhang, Dynamic tensile behavior of S690 high-strength structural steel at intermediate strain rates, J. Constr. Steel Res. 168 (2020) 105961, https://doi.org/10.1016/j.jcsr.2020.105961.
[21] A.A. Alabi, P.L. Moore, L.C. Wrobel, J.C. Campbell, W. He, Tensile behaviour of S690QL and S960QL under high strain rate, J. Constr. Steel Res. 150 (2018) 570-580, https://doi.org/10.1016/j.jcsr.2018.08.009.
[22] E. Cadoni, D. Forni, Mechanical Behaviour of a Very-High Strength Steel (S960QL) under Extreme conditions of High Strain Rates and Elevated Temperatures, Fire Saf. J. 109 (2019) 102869, https://doi.org/10.1016/j.firesaf.2019.102869.
[23] Y. Zhu, H. Yang, S. Zhang, Dynamic Mechanical Behavior and Constitutive Models of S890 High-Strength Steel at Intermediate and High Strain Rates, J. Mater. Eng. Perform. 29 (2020) 6727–6739, https://doi.org/10.1007/s11665-020-05150-9.
[24] J.H. Kim, D. Kim, H. N. Han, F. Barlat, M.G. Lee, Strain rate dependent tensile behavior of advanced high strength steels: Experiment and constitutive modeling, Mater. Sci. Eng.A 559 (2013) 222-231, https://doi.org/10.1016/j.msea.2012.08.087.
[25] J. Yang, W. Hu, W.R. Wang, G. Shi, X.C. Wei, Relationship Between Strain Rate and Quasi-Static Tensile Behavior of 1000MPa DP Steel, Iron. Steel Res. Int. 23 (7) (2011) 39-42, https://doi.org/10.13228/j.boyuan.issn1001-0963.2011.07.006. (in Chinese)
[26] W. Wang, Y. Ma, M. Yang, P. Jiang, F. Yuan, X. Wu, Strain Rate Effect on Tensile Behavior for a High Specific Strength Steel: From Quasi-Static to Intermediate Strain Rates, METALS-BASEL 8 (1) (2018) 11, https://doi.org/10.3390/met8010011.
[27] J.S. Huo, X. Zeng, H.T. Wang, TENSILE BEHAVIOUR OF TMCP Q690D HIGH-STRENGTH STRUCTURAL STEEL AT STRAIN RATES FROM 0.00025 TO 760 S-1, Adv Steel Constr 18(1) (2022) 488-494, https://doi.org/10.18057/IJASC.2022.18.1.7.
[28] CEB-FIP. Model code 2010: first complete draft. Lausanne: Fédération Internationale du Béton, 2010.
[29] L. E. Malvern, C. A. Ross, Dynamic response of concrete and concrete structures, Second Annual Technical Report, AFOSR Contract No. F49620-83-K007 (1985).
[30] C. A. Ross, D. M. Jerome, J. W. Tedesco, M. L. Hughes, Moisture and Strain Rate Effects on Concrete Strength, Mater. J. 93 (3) (1996) 293-300, https://doi.org/10.14359/9814.
[31] Y.B. Guo, G.F. Gao, L. Jing, V.P.W. Shim, Response of high-strength concrete to dynamic compressive loading, Int. J. Impact Eng. 108 (2017) 114-135, https://doi.org/10.1016/j.ijimpeng.2017.04.015.
[32] T. Ngo, P. Mendis, A. Whittaker, A rate dependent stress-strain relationship model for normal, high and ultra-high strength concrete, Int. J. Prot. Struct. 4 (2013) 451-466, https://doi.org/10.1260/2041-4196.4.3.451.
[33] W. Wang, Z. Zhang, Q. Huo, X. Song, J. Yang, X. Yang, J. Wang, X. Wang, Dynamic Compressive Mechanical Properties of UR50 Ultra-Early-Strength Cement-Based Concrete Material under High Strain Rate on SHPB Test, Mater. 15 (17) (2022) 6154, https://doi.org/10.3390/ma15176154.
[34] Y.B. Guo, G.F. Gao, L. Jing, V.P.W. Shim, Quasi-static and dynamic splitting of high-strength concretes – tensile stress–strain response and effects of strain rate, Int. J. Impact Eng. 125 (2019) 188-211, https://doi.org/10.1016/j.ijimpeng.2018.11.012.
[35] H. Schuler, H. Hansson, Fracture behaviour of High Performance Concrete (HPC) investigated with a Hopkinson-Bar, J. Phys. IV France 134 (2006) 1145-1151, https://doi.org/10.1051/jp4:2006134175.
[36] J. Liu, W. Wang, K. He, D. Kong, X. Dai, X. Zhao, Dynamic tensile and stress wave transmitting characteristics of high strength and high ductility concrete, Constr. Build. Mater. 449 (2024) 138259, https://doi.org/10.1016/j.conbuildmat.2024.138259.
[37] M. Ali, J. Sun, N. Lam, L. Zhang, E. Gad, Simple hand calculation method for estimating deflection generated by the low velocity impact of a solid object, Aust. J. Struct. Eng. 15 (3) (2014) 243-259, http://dx.doi.org/10.7158/S13-006.2014.15.3.
[38] G.C. Li, B.W. Chen, Z.J. Yang, Y.H. Feng, Experimental and numerical behaviour of eccentrically loaded high strength concrete filled high strength square steel tube stub columns, Thin-Walled Struct. 127 (2018) 483–499, https://doi.org/10.1016/j.tws.2018.02.024.

Advanced Steel Construction – Vol. 21 No. 6 (2025) 520–529
DOI:10.18057/IJASC.2025.21.6.5

PARAMETRIC STUDIES ON BENDING CAPACITY OF MECHANICAL JOINTS USING CONCRETE-FILLED STEEL TUBES

Vay Siu Lo [1, 2] and Canh Tuan Nguyen [1, 2, *]

[1] *Ho Chi Minh City University of Technology (HCMUT)*
[2] *Vietnam National University Ho Chi Minh City (VNU-HCM), Ho Chi Minh City, Vietnam*
* *(Corresponding author: E-mail: ctnguyen@hcmut.edu.vn)*

ABSTRACT

This study aimed to conduct an in-depth analysis of mechanical joints using a Concrete-Filled Steel Tube (CFST) for steel tube structures under bending. A series of parametric analyses were performed using finite element models. A conventional theory of CFST structures was applied to calculate the bending resistance of the joint. A key finding of this research was the equivalent strut-tie model to determine the local acting forces in the joint. The internal stress distribution within the concrete core was investigated to define effective areas for the components in compression and tension. Based on analysis results, this study proposed design proportions for the length-to-diameter ratio and the thickness ratio between the connecting steel tube and the main steel tubes. The influence of concrete strength, reinforcement ratios, and the use of shear connectors to prevent slip on the load-bearing capacity were also successfully examined. These findings are critical for simplifying construction practices and optimizing joint performance that might enable more effective and efficient use of CFST in various structural applications. This research revealed the potential of such innovative joint designs to significantly improve the construction method that requires rapid, reliable, and cost-effective solutions.

ARTICLE HISTORY

Received: 14 February 2025
Revised: 13 June 2025
Accepted: 15 June 2025

KEYWORDS

Bending capacity;
Circular steel tube;
Concrete-filled steel tube;
Mechanical joint;
Steel bridge

1. Introduction

Steel tubes are fundamental in structural engineering for their strength, durability, and flexibility [1], with demonstrated high ductility under seismic loading in bridges [2, 3]. Innovations include multiple-pipe bridge columns on varying foundations [4] and extensive use in offshore wind foundations, where steel pipe piles have been experimentally validated [5], supported by theoretical design and static tests for axial and uplift capacity [6], as well as connection analyses for single-pile turbines [7, 8].

Concrete-filled steel tubular (CFST) structures combine material and construction efficiency with fire resistance and environmental benefits [9]. Recent FEA studies have characterized their flexural behavior and stress-strain distributions, leading to strut-tie models for pure bending [10, 11], while experimental comparisons have refined design specifications for bending performance [12, 13]. Advancements in construction technology focus on rapid construction, prefabrication, modular structures, and innovative connection methods for steel pipe columns [14-16]. Advances in prefabrication and modular construction have spurred innovative connections, from bolted CFST girders [17] to mechanical joints like “High-Mecha-Neji” threaded sleeves [18], KASHEEN bolt assemblies [19], and tooth-and-pin mechanisms [20], and slip-joint solutions for offshore monopiles [7, 8]. Despite these developments, on-site welding and complex fabrication still hinder quality consistency and cost reduction in CFST jointing.

Studies on CFST structures involving lightweight aggregate concrete (LAC) and square steel tubes have also provided important foundations for the development of innovative CFST applications. Zhongqiu et al. [21] examined the flexural behavior of LAC-filled steel tubes (LACFST), demonstrating that LAC can maintain effective composite action with the steel tube while reducing structural self-weight. Their results confirmed that LACFST members possess reliable moment capacity and stiffness, and they proposed analytical methods verified through finite element analysis. In a separate study, Li et al. [22] explored the seismic performance of high-strength concrete-filled high-strength square steel tubes (HCFHSTs) under cyclic pure bending. Their experiments and numerical simulations revealed excellent ductility, energy dissipation, and flexural stiffness, even under high-strength material configurations. Further, Yang et al. [23] introduced reinforced hollow square CFSTs (RHCFSTs), integrating prestressed concrete cores and additional reinforcement. Their findings highlighted improved flexural capacity, delayed crack propagation, and enhanced ductility. These studies collectively demonstrate that varying the core concrete material and steel tube geometry significantly influences CFST behavior. Their insights serve as a valuable reference for developing new CFST-based mechanical joints, especially where construction efficiency, weight reduction, and flexural performance are critical.

Recent studies in structural engineering have refined the strut-and-tie model (STM) for designing deep beams in reinforced concrete structures, ensuring safety, and optimizing material use. Various research has enhanced the STM, proposing modifications to codes and innovative methods for design accuracy and reliability. Park et al. [24] introduced an advanced STM method incorporating constitutive laws for cracked reinforced concrete to provide superior capacity estimates for deep beams compared to existing codes. Other studies have recalibrated STM effectiveness factors based on concrete strength and shear span-to-depth ratios, aligning with experimental data and codes like ACI Code-08 and the UK CIRIA Guide #2 [25]. Research on shear design provisions for D-regions in beams highlighted the transition from conventional sectional methods (CSM) to STM, suggesting integration for certain beam configurations [26]. Tuchscherer et al. [27] evaluated deep-beam tests, proposing modifications to ACI 318 and AASHTO LRFD provisions to balance conservatism and accuracy.

The current research was built on previous studies, proposing a new mechanical joint using CFST that maintained bending capacity comparable to steel pipe columns without the joint [28]. This joint can be used for CFST girders, steel pipe piles, and steel pipe columns, aiding accelerated construction. Parametric studies were conducted using finite element models to analyze mechanical joints in CFST structures under bending. The conventional CFST theory was applied to calculate bending resistance, while a new finding assessed local resistance using the strut-tie model of a deep beam. Internal stress fields within the concrete core were investigated to propose effective areas for defining component resistances under compression and tension.

The study proposed design proportions for the length-to-diameter and thickness ratios between the connecting tube and main steel tubes. It examined the influence of concrete strength, reinforcement ratio, and shear connectors on load-bearing capacity. Overall, this research presents a simple, cost-effective mechanical joint using CFST, eliminating the need for site welding or expensive joint solutions while ensuring construction progress.

This paper was organized as follows: Section 2 provided an overview of the proposed mechanical joint utilizing concrete-filled steel tubes, introducing the strut-and-tie model as a framework for analysis. Section 3 delved into the details of the finite element model employed for CFST simulations, along with validation procedures to ensure accuracy. Section 4 presented a comprehensive parametric study, investigating the effects of various factors on joint performance, including effective length, connecting tube thickness, concrete compressive strength, and reinforcement ratio. In Section 5, design proportions and recommendations were derived from the analysis results. Finally, the concluding Section 6 summarized the key findings and offered insights into future research directions.

2. Mechanical joint using concrete-filled steel tube

2.1. The proposed CFST joint

This study proposes a straightforward and cost-effective mechanical joint using CFST that could eliminate the need for site welding or expensive joint solutions while still ensuring construction progress. The continuity of the structure was maintained by using a connecting steel tube to link the two main steel tubes. The rigidity of the connecting tube was enhanced by filling it with reinforced concrete. Additionally, shear connectors might be applied to improve the interaction between the main steel tubes and the joint, ensuring continuity during the load-bearing process. Axial force, shear force, and bending moment can be transferred between the two main tubes through the mechanical joint. The length of the connecting tube was a key parameter affecting the joint's performance. Therefore, this paper aimed to investigate the effects of various parameters on the bending capacity of mechanical joints such as connection length, tube thickness, compressive strength of the concrete core, steel reinforcement ratio, and dowel interactions of shear connectors. Through parametric studies, considerations and proportions were proposed to simplify design practices.

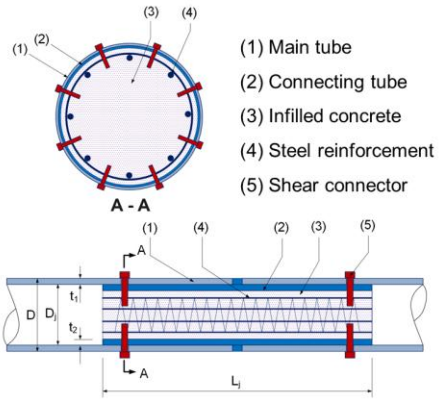

Fig. 1 Steel tubes with a mechanical joint using a concrete-filled steel tube [28]

Figure 1 illustrates the composition of the proposed mechanical joint using a reinforced concrete-filled steel tube where D is the outer diameter of the main tube, D_j is the outer diameter of the connecting tube, t_1 and t_2 are the thicknesses of the main tube and the connecting tube respectively. The connecting tube could be prefabricated and filled with concrete at the factory, then transported to the construction site for erection. This joint could provide load-bearing capacity immediately after installation. For piles constructed using the rotary drilling method or pullout piles, shear connectors could be applied to ensure that torque or uplift force are transmitted effectively through the joint.

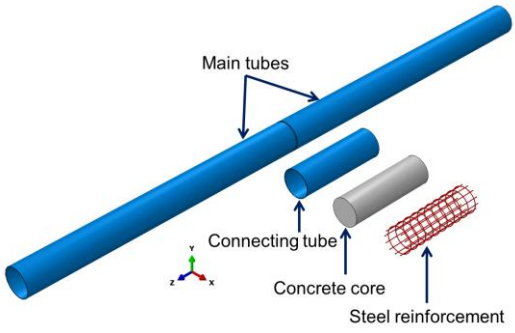

(a)

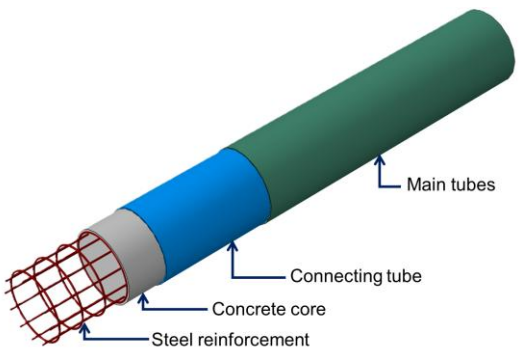

(b)

Fig. 2 Illustration of the mechanical joint model

The simple principal mechanism of the joint is to transmit internal forces between two main steel tubes, effectively functioning as a continuous steel tube. Such performance is achieved through frictional interaction between the inner surface of the main tubes and the outer surface of the connecting tube. Ideally, the outer diameter of the connecting tube would fit the inner diameter of the main tubes. To simplify construction and installation, however, the outer diameter of the connecting tube could be 1 mm to 2 mm smaller than the inner diameter of the main tubes. By analogy with a fitting connection, the main tubes could be heated before installing the connecting tube to improve fitting contact. Fig. 2 illustrates a three-dimensional model of the mechanical joint structure, including a breakdown of its components and a cross-sectional view that details the internal arrangement of the joint. The concrete core could improve local stability for the connecting tube under compressive stress, while the reinforcing steel might enhance the tensile capacity and prevent cracks in the concrete core under tensile stress.

2.2. Bending strength of mechanical joint

Theories of conventional CFSTs under bending can be employed to verify the performance of a mechanical joint with a CFST. The plastic-stress distribution method could be applied to determine the bending capacity of the mechanical joint. This method has been recommended as an adequate solution due to its simplicity and accuracy for CFST structures [15, 29].

The theory for calculating the flexural resistance of CFST has been successfully developed and included in recent design specifications [30-33]. Fig. 3 illustrates the Plastic Stress Distribution Method (PSDM) of a CFST cross-section with steel reinforcement at a critical state. Stress distributions in the steel tube, concrete core, and steel reinforcement are also defined to satisfy the equilibrium conditions under external bending moments transmitted from the main tubes.

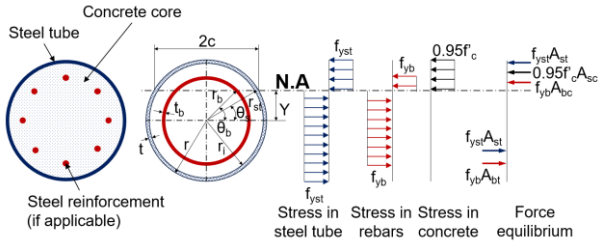

Fig. 3 Plastic stress distribution model of a CFST cross section [30]

The total bending resistance is combined from the contributions of the steel tube, concrete core, and reinforcing bars. By applying the plastic stress distribution method and ignoring axial force, the bending capacity is determined through the equilibrium condition between the external bending moment and the internal bending moments generated by the plastic forces at the centroid of the sectional components. The nominal bending resistance can be calculated as follows [30]:

$$M_n = 0.95 f_c' \left[\left(r_i^2 - y^2 \right) - \frac{c^2}{3} \right] + 4 f_{yst} t c \frac{r_{st}}{r_i} + 4 f_{yb} t_b c_b r_b \tag{1}$$

where,

$$\begin{aligned} &r_{st} = r - t/2; \quad \theta_b = \sin^{-1}\left(y/r_b\right); \quad c_b = r_b \cos\theta_b; \\ &\theta_s = \sin^{-1}\left(y/r_{st}\right); \quad c = r_i \cos\theta_s; \quad t_b = nA_b / 2\pi r_b \end{aligned} \tag{2}$$

in which A_b is the area of a typical steel bar comprising the internal reinforcement (mm^2); c is one-half the chord length of the tube in compression (mm); c_b is one-half the chord length of a notional steel ring equivalent to the internal reinforcement in compression (mm); f_{yb} is yield stress of steel bar (MPa); f_{yst} is yield stress of steel tube (MPa); f_c' is compressive strength of concrete core (MPa); n is number of internal steel reinforcing bars; r is radius to the outside of the steel tube (mm); r_b is radius to the center of the internal reinforcing bars; r_i is radius to the inside of the steel tube (mm); r_{st} is radius to the center of the steel tube (mm); t is the wall thickness of the tube (mm); t_b is the wall thickness of a notional steel ring equivalent to the internal reinforcement (mm); y is distance from the center of the steel tube to the neutral axis (mm); θ_b is angle used to define c_b (rad), θ_b shall be taken as $\pi/2$ if y/r_b is greater than 1 and θ_b shall be taken as $-\pi/2$ if y/r_b is less than -1 (rad); θ_s is angle used to define

c (rad).

This study discovered that the mechanical joint could behave like a deep beam if the ratio between the length of the joint and the diameter of the tube is less than 3.0 [25]. To evaluate the local load-bearing capacity of a deep beam structure, a theory of strut-and-tie model was applied.

2.3. Strut-and-tie model for local resistance estimation

The strut-and-tie model (STM) is a design method used in structural engineering to simplify the complex stress distribution in concrete structures into truss-like models. This model is particularly useful in areas of structures that are complex to analyze using traditional methods, such as beam-column joints, deep beams, corbels, dapped beams, and pile caps. Struts are compression elements carrying compressive stresses across a direct line between nodes. Ties are in tension connecting nodes where tensile forces are expected, effectively holding the structure together under tensile stress. Nodes are the junction points where struts and ties meet. Nodes transfer forces between struts and ties and are critical for the stability of the STM. This method aligns more with actual stress flow in irregularly shaped and heavily loaded parts of structures, offering a more rational approach than traditional beam theory.

The conventional STM is used to simplify complex stress fields in concrete structures by replacing them with truss-like systems of compression struts, tension ties, and nodes. Traditionally, this approach has been applied to reinforced concrete structures, capturing the flow of forces through concrete members. However, in this study, an equivalent STM is proposed to model the local load-bearing capacity of steel mechanical joints in CFST structures. Unlike conventional STM, this model accounts for nonlinear radial pressure distributions and friction forces that develop at the interface of steel tubes in the joint, which are not typically considered in concrete STM applications.

The equivalent STM captures the direct load transmission between steel tubes and the concrete core, reflecting how bending moments in the main tubes create concentrated radial pressures that form struts and ties within the joint. This adaptation allows us to better understand the local mechanical behavior of interference-fit steel joints under combined bending and compression, filling a gap not addressed by traditional STM. This model's novelty lies in its ability to incorporate these localized effects and frictional behavior in steel joints, providing a more realistic assessment of load-bearing capacity in CFST connection.

This study proposed an STM with two concentrated loads to investigate the local load-bearing capacity of the mechanical joint based on the deep-beam theory similar to previous research [24, 25]. The fit connection between outer tubes and an inner tube with different diameters can be considered as a shrink-fit joint without initial contact pressures on the fitting. Due to the small gap between the main tubes and the connecting tube, the joint is fixed and exhibits linear behavior. The interference connection may lead to nonlinear behavior with large angular deformation of the main tubes; pressure concentrations then develop at the joint edges. The friction forces induced by radial pressure could prevent relative slip between the fitting surfaces which may lead to failure of the joint [34]. Fig. 4a presents a proposed load distribution model within the mechanical joint. Bending moments M in the main tubes are transformed into equivalent radical pressure regions which generate concentrated couples N. In this study, the pressures in the longitudinal direction were assumed to be linearly distributed in the range of $L_j/6$ as an active length from edges of the main tubes and connecting tubes. Similar pressure distribution models with active lengths were introduced to investigate the effects of the overlap length on the bending capacity of the slip joint [35, 36].

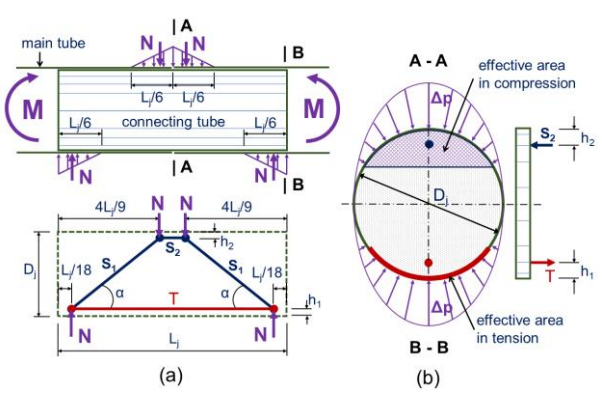

Fig. 4 Proposed strut-and-tie model and equivalent radial pressure in tube section

In the vertical section, the radial pressure is nonlinearly distributed along the half circumference of the connecting tube (see Fig. 4b). To investigate the effects of friction forces, the magnitude Δp can be determined based on similar theory developed from a previous study [34]. From the model, struts S_1 and S_2 in compression and a tie T in tension are identified. It is assumed that internal loads are transferred directly between nodes through the struts in the concrete core.

The tie force T is assumed to be mostly generated along the bottom fiber of the connecting steel tube, neglecting the contributions of the concrete core and reinforcing bars. Strut force S_2 is generated in the top fiber of the cross section. Distances from centers of the tie force T and strut force S_2 to corresponding extreme fibers are h_1 and h_2, respectively. From the force equilibrium conditions, the component struts and tie can be defined as:

$$S_1 = N / \sin\alpha \tag{3a}$$

$$S_2 = T = N / \tan\alpha \tag{3b}$$

where, $\alpha = \text{atan}\left[\left(D_j - h_1 - h_2\right)/\left(7L_j/18\right)\right]$; N is the acting forces on the joint obtained from the bending moment equilibrium condition, $N = 18M/(7L_j)$.

To completely transmit bending moment between main tubes, the local load-bearing capacity of the mechanical joint should be examined by comparing the internal forces obtained from Eqs. (3a) and (3b) with the component strengths formed by effective areas. In this study, stress distributions in the concrete core and the connecting tube were observed to investigate effective areas in tension and in compression of the CFST cross section.

3. Finite element modeling

To examine the behavior of mechanical joints under pure bending, a simply supported beam model was employed with two concentrated loads P positioned at a distance a from the supports. This loading configuration eliminated shear forces and created a region of a constant bending moment between the two load points. The span length was set to 20 times the diameter of the main tubes. Fig. 5 illustrates the loading arrangement, as well as the corresponding bending moment and shear force diagrams. In this scenario, the connecting tube was subjected only to a pure bending moment, $M = Pa$. This setup provided perfect conditions to study the performance of mechanical joints, focusing on the transition of internal moments to ensure the bending capacity of the entire structure.

This type of loading scheme has also been adopted in previous studies to evaluate the flexural behavior of CFST members. Notably, Guochang Li et al. [22] and Zhi-Jian Yang et al. [23] employed similar four-point bending arrangements to generate a pure bending region, enabling accurate assessment of moment resistance and structural ductility in high-strength square CFST beams. The consistency in test setup across studies further validates its effectiveness in capturing the essential flexural characteristics of CFST-based structural systems.

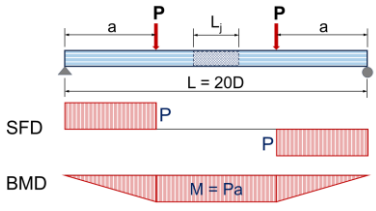

Fig. 5 Simply supported beam under two-point loading condition

A series of finite element models of steel tubes with a mechanical joint using a concrete-filled steel tube were simulated using the ABAQUS analysis software [37]. Fig. 6 illustrates a finite element model of a steel tube beam with a mechanical joint using a concrete-filled steel tube. The joint was located between two concentrated loads spaced two meters apart. To prevent local buckling, bearing stiffeners were created at both supports and at locations of the concentrated loads. A one-millimeter gap was created at the edges of the main steel tubes to model interactions between two tubes. Inside the joint, a smaller-diameter steel tube was embedded and filled with a reinforced concrete core.

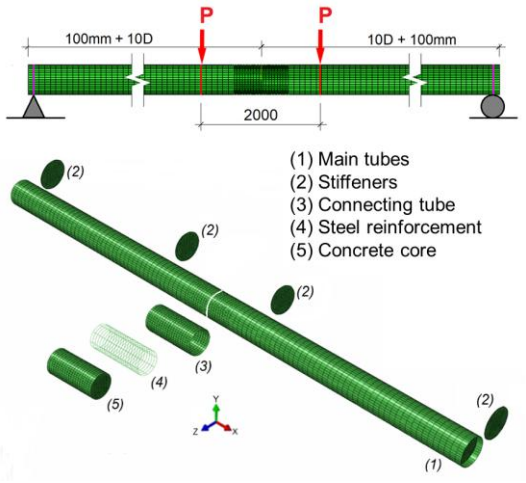

Fig. 6 Finite element model of a steel tube beam with mechanical joint using CFST [28]

3.1. Element types

The main steel tubes, connecting steel tube, and bearing stiffeners were modeled using 4-node shell elements (S4R), while the general-purpose linear brick element (C3D8R) with 8 nodes was employed to simulate the concrete core. Reinforcement bars within the concrete core were modeled as truss elements (T3D2), which could be embedded into the concrete core. The interactions between the two main tubes (see Fig. 7a), between the main tubes and the connecting tube (see Fig. 7b), and between the connecting tube and the concrete core (see Fig. 7c) were modeled using GAP elements, simulating bearing interactions and friction sliding. GAP elements work by incorporating contact mechanics into the finite element model. When the gap between two surfaces closes, the elements apply contact forces that can include both normal and tangential components. The normal component of the contact force typically simulates the bearing pressure, while the tangential component models the frictional resistance to sliding. This dual capability allows GAP elements to accurately reproduce the complex interactions such as those found in mechanical joints, bearings, and other structures where surface contact and friction are critical.

To mitigate slippage and evaluate the impact of the connection between the concrete core and the steel tube, shear connectors were modeled using rigid links in the form of tie interactions. These connectors were arranged along the circumference of the steel tube near the rear end of the connecting steel tube. By employing tie interactions, the shear connectors effectively constrain relative movement between the steel tube and the concrete core, thereby enhancing the structural integrity and load transfer efficiency of the composite system.

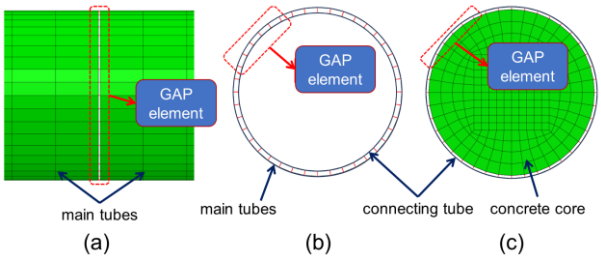

Fig. 7 Modeling surface interactions using GAP elements [28]: (a) edge interaction; (b) tube-tube interaction; (c) tube-core interaction.

Several studies have successfully applied and validated the use of GAP elements in simulating the behavior of concrete-filled steel tube structures. A friction coefficient 0.47 for the GAP element between the steel tube and the concrete core has been proposed based on research by Baltay et al. [38, 39]. Jiho et al. also conducted a series of parametric analyses and successfully validated the simulation method using GAP elements for the interaction between steel and concrete surfaces [12, 15]. For static friction of steel-on-steel contact, the friction coefficient could be estimated between 0.6 and 0.8 in dry air and without lubrication [40-43]. In practical construction, steel tubes are usually coated with a thin prime layer using epoxy-based painting for corrosion protection. The coating layer significantly reduces friction coefficients between two coated steel surfaces. Cabboi et al. [8] confirmed that the presence of the two-coat layer might be the reason for a drastic friction reduction from 0.6 - 0.8 to a possible 0.1 - 0.35 range in slip joint. In this study, a friction coefficient of 0.45 has been proposed for steel-on-steel contact surface with slightly coated layers. This value is also consistent with the friction coefficient proposed in Article 6.13.2.8 by the AASHTO standards when calculating the slip resistance of the bolted connection [30].

The number of meshed elements is crucial to ensure reliable finite element analysis results. In a similar study, Moon et al. [12] also demonstrated that using a minimum of twenty elements along the circumference of a steel tube would yield accurate results. In this study, the steel tubes were divided into forty elements along the circumference to secure the accuracy of analysis results (see Fig. 7). In the longitudinal direction, the region of the joint was meshed more finely than other regions, as illustrated in Fig. 6. The width of the elements within the joint will be half as large as those in other regions. This meshing approach aligned with findings from previous research.

3.2. Material properties

Nonlinear material analysis as well as large deformation analysis were applied to accurately investigate and evaluate the behavior of the structure. To simulate the behavior of the steel tube and reinforcing steel materials, this study employed a three-linear material model that represented the stages of elasticity, full plasticity, and strain hardening. Fig. 8 illustrates the general stress-strain curve for the steel material, assuming an elastic modulus E_s = 200,000 MPa and a Poisson's ratio υ_s = 0.3. The yield strength f_y was defined corresponding to the yield strain ε_y, with the plastic state maintained until the strain reaches 10 ε_y. The ultimate strength f_u was identified at a strain ε_u = 0.1. This steel material model has also been applied and successfully validated in previous studies [12, 13]. In this study, the steel tube had a yield strength f_y = 345 MPa and an ultimate strength f_u = 490 MPa, while the reinforcing steel had a yield strength f_y = 400 MPa and an ultimate strength f_u = 570 MPa.

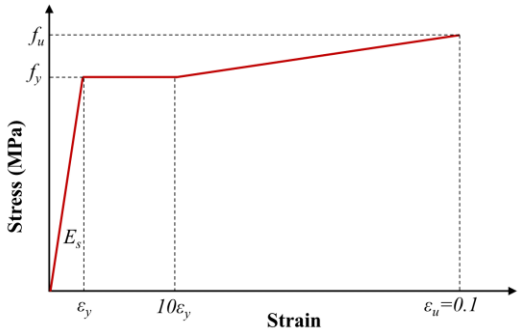

Fig. 8 Material models for steel tubes and steel reinforcement

Recent advancements in concrete modeling have successfully developed damage mechanics and plasticity theory to enhance the predictive accuracy of concrete behavior under various loading conditions. Several studies have proposed different constitutive models emphasizing the non-linear analysis of concrete through improved yield criteria and damage variables that capture both tensile and compressive states. New damage-plasticity approaches were presented to model concrete failure under general triaxial stress covering tension, shear, and multiaxial compression with distinct levels of confinement [44-47].

The nonlinear finite element analysis of concrete materials has been extensively studied in previous research. Moon et al. [12] applied concrete damage models to analyze concrete-filled steel pipe structures. Their research verified the accuracy of the uniaxial stress–strain relationship for unconfined concrete using a plastic failure model in conjunction with the GAP element. This approach effectively simulated the behavior of concrete-filled steel pipe structures through a series of nonlinear finite element parameter analyses. Achieving convergence can be challenging when fully incorporating the nonlinear behavior of concrete, making the choice of an appropriate material model crucial. In this study, the concrete damage plasticity model was adopted, following the work of Lubliner et al. [48] and Lee and Fenves [49]. This model effectively represents concrete behavior under various stress states, particularly when the confining stress remains below four to five times the concrete's compressive strength. Additionally, the dilation angle significantly affects the simulated response of concrete. Based on previous research and a parametric study conducted in this work, a dilation angle of 20 was selected.

The uniaxial stress–strain curve is presented in Fig. 9. In this study, the concrete grade C40 with f_c' = 27 MPa were employed to investigate effects of connecting length, thickness, and reinforcement ratio.

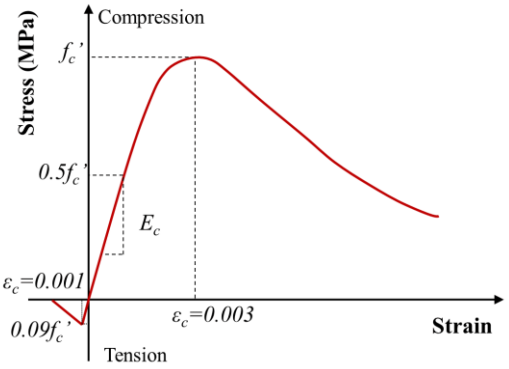

Fig. 9 Material models for infilled concrete

3.3. Bending strength of a steel tube

The mechanical joint was employed to successfully transmit bending moments between main tubes. This means that the joint must produce sufficient load-bearing capacity to prevent failure before main tubes reach the critical bending strength.

This study proposes a method to identify the critical bending moment of the main tubes based on the moment-rotation relationship diagram. The bending strength of the jointless steel tube was used as a benchmark for comparative studies. From finite element analysis results, the corresponding bending moment was determined by using the rotation angle value at the first yield, ϕ_y. The plastic bending moment of a hollow steel tube M_p is defined as:

$$M_p = \lambda M_y = \lambda Z f_y \tag{4}$$

where, M_y is the yielding bending moment, $M_y = Zf_y$; Z is the elastic section modulus of the steel tube; f_y is the yield stress (MPa); λ is shape factor of the section, λ = 1.27 for a circular tube [50].

For a simply supported beam subjected to two concentrated loads (illustrated in Fig. 7), the total rotation angle at a support at first yield is defined as follows:

$$\phi_y = M_y(L-a)/(2EI) \tag{5}$$

where a is the distance from concentrated loads to supports.

3.4. Comparison and verification of bending strength

Previous research has demonstrated the effectiveness of mechanical joints with concrete-filled steel tubes for steel pipe columns. The verification of the bending strength of steel pipe columns using mechanical joints was conducted through finite element analyses by comparing the results to theoretical calculations. The study employed a series of finite element models with varying diameters and joint configurations to simulate the bending behavior under applied loads [28].

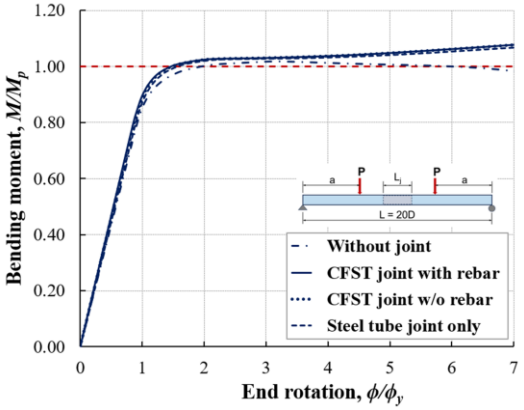

(a) D = 200 mm, L_j = 1000 mm

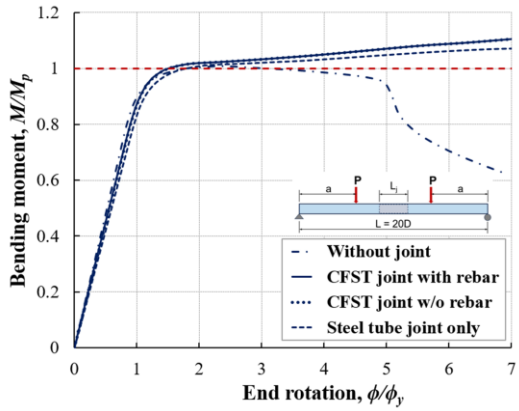

(b) D = 350 mm, L_j = 1000 mm

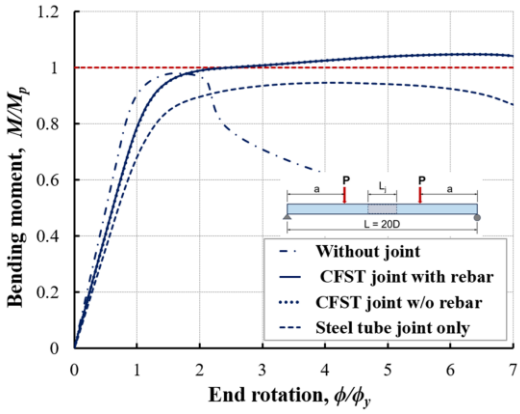

(c) D = 500 mm, L_j = 1000 mm

Fig. 10 Comparison of bending capacity between steel tubes with and without joint

Figure 10 presents the comparative results of the bending strength between steel pipes with and without mechanical joints using CFST. The plastic bending moment M_p from Eq. (4), and the rotation angle at first yield of the tube section, ϕ_y, from Eq. (5) were used as benchmarks for comparison. Furthermore, the comparison was also conducted between joints with and without rebar reinforcement to evaluate their contribution to the overall resistance of the connection. The mechanical joints, filled with reinforced concrete, demonstrated significant improvements in bending capacity compared to pipes without joints. Comparative analysis showed that the proposed mechanical joints could increase the bending strength of steel pipes by up to 21.6%. Stress distributions and deformation patterns were closely observed, indicating that the concrete core within the joint effectively prevented local buckling and contributed to the overall joint rigidity [28]. The findings from this preliminary study serve as the foundation for the current research, where the derived results will be systematically compared with Eqs. (4) and (5) to assess the validity of mechanical joints in steel pipe columns. A detailed discussion on failure mechanisms, including stress distribution within the concrete core and steel pipe connections, will be presented in the following section.

4. Parametric studies and verification

This study conducted a series of parametric analyses using finite element modeling to investigate and assess the efficiency and optimal performance of mechanical joints. The goal was to provide recommendations for the geometric design of these joints with considerations of key geometric parameters including tube diameter, length of the joint, tube thickness, concrete strength, reinforcement ratio, and anchoring effects.

4.1. Effective length of the mechanical joint

For double-tube mechanical joints, the diameter of the connecting tube is determined by the inner diameter of the main tubes. Consequently, this parameter was not examined in this study. Instead, the focus was on investigating the relationship between the main tube diameter and the joint length.

As discussed in the theoretical section, the length of the connecting tube affects the magnitude of the equivalent couple derived from the bending

moment in the main tubes. This couple is considered as an external force acting on the connecting tube. The longer the joint length is, the smaller the magnitude of the couple acts on it. The length of the connecting tube plays a crucial role in ensuring the joint's functionality in transmitting the bending moment from the main tubes through the connecting tube guaranteeing that the joint's load-bearing capacity is always greater than or equal to the bending capacity of the main steel tubes. The joint's load-bearing capacity depends on the frictional interaction on the contact surface between the main tubes and the connecting tube. Such frictional force limits slip and ensure the transmission of the bending moment between the main tubes and the connecting tube. The frictional force depends on the magnitude of the couple acting on the connecting tube and the effective contact surface area.

Table 1 presents the geometric characteristics of the finite element models used for parametric analyses to investigate the impact of connecting length on the load-bearing capacity of the entire structure. Main steel tubes were examined with three different diameters of 200 mm, 350 mm, and 500 mm. The effective span length of the main steel tubes was set to 20 times its diameter. In this study, the length of the connecting tube L_j varied from 200 mm to 1,000 mm at intervals of 100 mm. A total of 27 models were employed in finite element analyses corresponding to different diameters of the main steel tubes. The connecting tube was set to have equal thickness to the main tubes. The models were loaded until failure to construct perfect moment-rotation relationship curves. The bending resistance and deformation of the joints will be examined to assess the performance with different joint lengths. To compare bending resistances, the rotation angle ϕ_y from Eq. (5) will be used as a reference value to determine the corresponding bending moments from the moment-rotation relationship curves for each case.

Table 1
Properties of finite element models with varying length of joint

Model	Main tubes					Connecting tube	
	D (mm)	t (mm)	L (mm)	M_y (kN.m)	ϕ_y (rad)	t_j (mm)	L_j (mm)
D200	200	6	4,000	59.41	0.02591	6	varied
D350	350	8	7,000	247.88	0.02231	8	varied
D500	500	8	10,000	516.46	0.02077	8	varied

The results from the D350 model analysis were used to illustrate the method for determining bending resistance. Fig. 11 presents diagrams of bending moments and rotation angles for various lengths of the joint characterized by the ratio $k = L_j / D$. The horizontal axis represents the ratio between the rotation angle from finite element analyses and that from Eq. (5) for D350 model. The vertical axis illustrates the ratio between the equivalent bending moment computed from the concentrated force P and the distance a from the loaded points to supports and that from Eq. (4). The rotation angle ϕ_y was taken as the standard to determine the corresponding bending resistance for different lengths of the joint. Results indicated that the length of the joint significantly influences the performance and the bending stiffness of the entire structure. Decreasing in length of the joint increased slip between the main tube and the connecting tube causing larger deformation of the joint and reducing efficiency in transmitting bending moments. At rotation angle ϕ_y , as the ratio $k = L_j / D$ increases from 0.57 to 2.86, the ratio of bending resistance M / M_y also increases from 0.32 to 1.11. The bending resistance of steel tubes with a joint length ratio L_j / D = 2.86 is equivalent to that of the steel tube without a joint, with an error of 2.4%. The bending stiffness of the steel tube could be determined based on the slope of the moment-rotation relationship curve. It was also found that bending stiffness of the structure increased with increasing length of the joint.

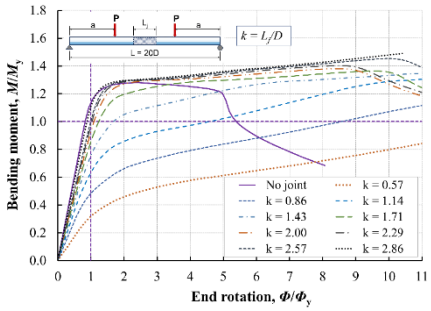

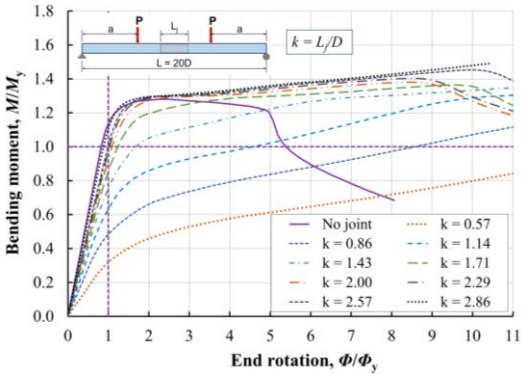

Fig. 11 Bending moment with various lengths of connecting tubes (D = 350 mm)

To investigate the effects of joint lengths on the bending resistance, Fig. 12 summarizes the analysis results of three models D200, D350, and D500. The *x*-axis represents the ratio of joint length to main tube diameter, while the *y*-axis shows the ratio of bending resistance from finite element analysis to the yield moment from Eq. (4). The analysis clearly revealed a correlation between bending resistance and joint length. All models performed linear variation in bending resistance when $L_j / D \leq 2.0$. Within the range $2.0 \leq L_j / D \leq 3.0$, larger diameters could provide faster increase in bending resistance to approach M_y . At L_j / D = 2.0, the differences in bending capacity of the analysis models and M_y were -9.2%, -7.4%, and +0.3% for models D200, D350 and D500, respectively. Models D350 and D500 could provide sufficient bending resistance when $L_j / D \geq 2.5$, while model D200 could only achieve M_y at L_j / D = 3.0. Based on these findings, it can be concluded that the optimal joint length L_j ranges between 2.5 and 3.0 times relative to the main tube diameter D. Therefore, this study recommends an ideal joint length L_j = 3.0 D for main pipe diameters ≤ 200 mm and L_j = 2.5 D for diameters > 200 mm in the design of the mechanical joints using concrete-filled steel tubes. In similar studies on a slip joint connection for single-pole transmission towers and offshore wind turbines using monopiles, the ideal overlap length has been successfully developed and suggested in design standards [50-53]. The overlap length of the slip joint is taken as 1.5 times the diameter which is consistent with findings from this study when the overlap length of a half joint is considered.

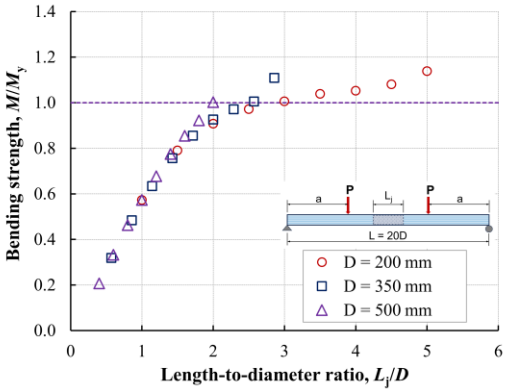

Fig. 12 Variation in bending strength with varying connecting length

In addition to examining the impact of joint length on bending resistance, this study also evaluated its effect on structural deformation, primarily influenced by the gap width between the two main tubes at the discontinuous section. Fig. 13 illustrates the gap width development at the joint section between the main tubes for various joint lengths from models D200, D350, and D500. The horizontal axis represents the ratio of joint length to diameter of the main tube, while the vertical axis represents the gap width relative to the diameter of the main tube at the bottom extreme fiber of the main tube. Results indicated that increasing joint length correlated with reducing gap deformation.

Results revealed that all models D200, D350, and D500 had a similar trend in gap width variation with different joint lengths. Gap width tends to approach 0.5% when $L_j / D \geq 2.5$. Therefore, global structural deformation under bending conditions can be secured by controlling expansion of the gap. The limiting joint length of L_j = 2.5 D suggested in this study is effectively to control gap development of the joint. Moreover, alternative solutions such as

employing shear connectors to enhance the interaction between main tubes, connecting tubes, and the concrete core can also mitigate gap expansion and global deflection. Effects of shear connectors will be explored in a separate follow-up study.

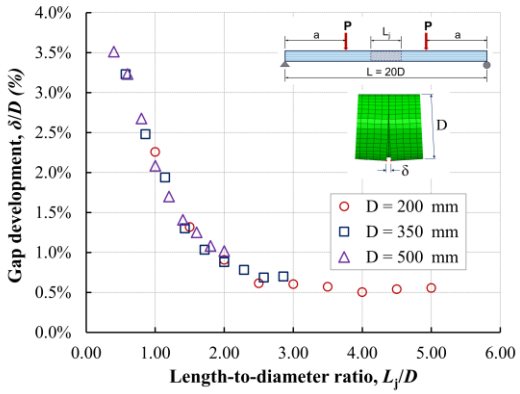

Fig. 13 Variation in gap width with varying joint length

4.2. Effective thickness of the connecting tube

The thickness of the connecting tube is also a critical parameter in the design of mechanical joints using concrete-filled steel tubes. This section investigates the effects of tube thickness on the bending resistance of the steel tube with the mechanical joint. The analysis aimed to propose simplified geometric parameters for the connecting tube thickness. Table 2 outlines the parameters of the finite element analysis models. The length of the joint is selected based on the effective length proposed earlier to maximize the structure's bending resistance. For models D200, D350, and D500, with connecting tube lengths of 600 mm, 900 mm, and 1000 mm respectively, the study explored the bending capacity as the connecting tube thickness varies from 2 mm to 14 mm at interval of 2 mm. This comprehensive investigation aimed to understand how changes in connecting tube thickness impact bending resistance.

Table 2
Properties of finite element models with varying thickness of connecting tube

Model	Main tubes			Connecting tube	
	D (mm)	t (mm)	L (mm)	L_j (mm)	t_j (mm)
D200	200	6	4,000	600	2 to 12
D350	350	8	7,000	900	4 to 14
D500	500	8	10,000	1,000	4 to 14

The thickness of the connecting tube directly impacts its local load-bearing capacity. Despite being filled with concrete, analyses revealed that the connecting steel tube contributed the most load-bearing capacity under both tensile stress and compressive stress. Fig. 14 illustrates how bending resistance of steel tubes varies with changes in pipe thickness. The horizontal axis denotes the ratio of connecting pipe thickness to main pipe thickness, while the vertical axis represents the ratio of bending resistance determined by finite element analysis to the yield moment from Eq. (4).

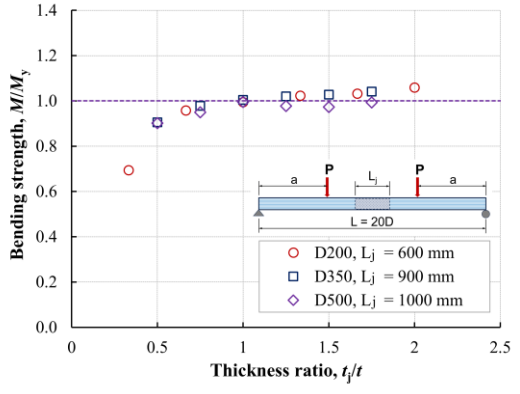

Fig. 14 Effect of thickness of connecting tube on bending strength

Results indicated a significant increase in bending resistance as the thickness increased. All models D200, D350, and D500 exhibited a consistent trend towards approaching the My value when the thickness of the connecting tube equaled that of the main tube (t_j / t = 1.0). Beyond this point, further increases in tube thickness did not yield substantial increases in bending resistance. Based on these findings, this study suggested that for optimal development of bending resistance, the ideal thickness for the connecting tube should equal that of the main steel pipe ($t_j = t$).

4.3. Effects of compressive strength of the concrete and reinforcement ratio

Previous studies revealed that infilled concrete provided a significant contribution to load-bearing capacity of the mechanical joint by improving local stability of the connecting tube [28]. However, the effects of compressive strength of the concrete on the bending capacity were not investigated. It was found that the concrete core could generate local compression strength under strut forces from the STM theory. Therefore, this study examined how compressive strength of the concrete core affected the performance of the joint.

Table 3
List of concrete material employed in parametric studies

Grade	C25	C30	C35	C40	C45	C50	C60	C70	C80
f_c' (MPa)	17	21	24	28	31	34	41	48	55

Table 3 presents data on various concrete types used to examine the impact of compressive strength on the bending resistance of joints. Finite element models employed a general material model, as shown in Fig. 9, to simulate concrete behavior. Compressive strength from grade C25 to C80 was considered in this study where grade C40 was selected as the benchmark for comparing bending resistance across different grades of concrete.

Analysis results indicated that the influence of concrete compressive strength on the bending resistance of the main tube was insignificant. Even at the lowest strength level, grade C25, joints almost provided sufficient bending resistance. Fig. 15 illustrates the analysis results, showing the relationship between compressive strength parameters where grade C40 represented the benchmark value, and the ratio of bending resistance derived from finite element analysis to the M_y value calculated using Eq. (4).

Most cases of failure were observed in the main steel tube due to local instability in the compression zone near the joint area. This study focused solely on main steel tubes connected by mechanical joints using concrete-filled steel tubes. Because these joints were significantly stiffer than the main steel tubes, instability naturally tended to occur in the main steel tube. In cases where the main steel tube was filled with concrete, the influence of concrete strength might become more obvious. It is crucial for the joint to remain undamaged to achieve the ultimate bending resistance of the concrete-filled steel tubes, which far exceed the bending resistance of unfilled steel tubes.

The results also show that concrete with grade C25 is enough to provide the compressive resistance needed for the local strut-and-tie model in the CFST joint area. Because of this, using higher-strength concrete does not significantly increase the overall bending resistance of the mechanical joint. This highlights that the tensile strength mainly comes from the steel tube itself, not from stronger concrete. So, once the concrete strength reaches a minimum level to support local compression, using higher-grade concrete does not help much. Instead, the main factors that affect the bending performance of the CFST system are the steel tube's quality and geometry. This shows that for CFST joints, the steel part plays the key role in providing bending resistance, and concrete only needs to meet a basic strength level.

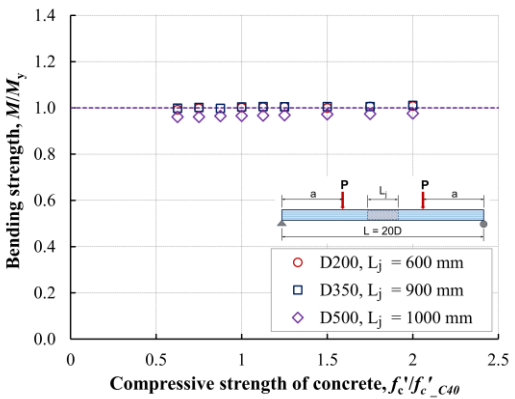

Fig. 15 Effects of compressive strength of concrete on bending strength

Similar to the compressive strength of concrete, analysis results also showed that the influence of the reinforcement ratio on the bending resistance of the structure could be negligible. Both longitudinal and spiral reinforcements were considered in this study. Fig. 16 presents the analysis results from models D200, D350, and D500, indicating that bending resistance remains nearly unchanged with varying reinforcement ratio in the concrete core. This finding aligned with a previous study on the effect of reinforcement on structural bending resistance [28]. It can be inferred that for concrete-filled steel tubes using mechanical joints, additional reinforcement may not be necessary as the steel tube and concrete core could provide sufficient resistance for the steel tube to achieve the ultimate bending capacity. However, in cases where the main steel tube is also filled with concrete, increasing the reinforcement content in the joint could significantly enhance the local resistance of the concrete core, reducing local cracking in the concrete within the tension zone and thereby stabilizing the joint.

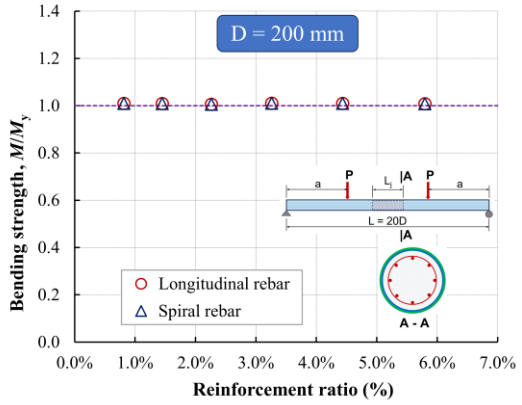

(a) D = 200 mm, L_j = 600 mm

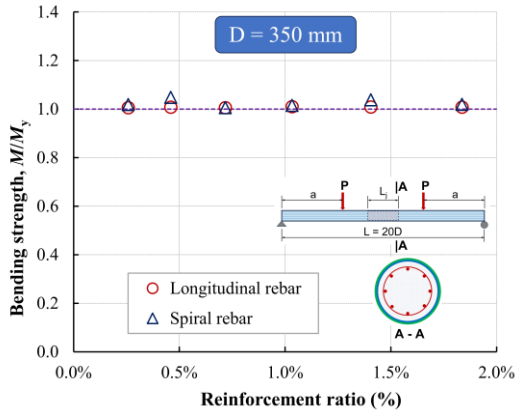

(b) D = 350 mm, L_j = 900 mm

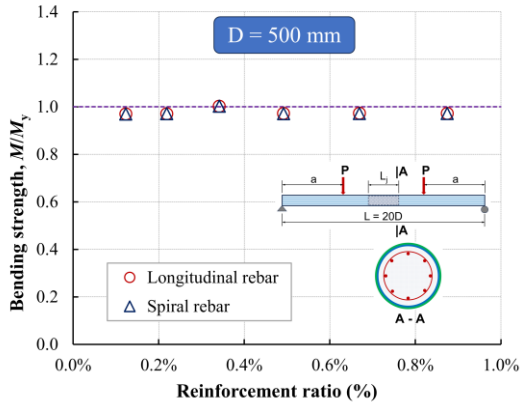

(c) D = 500 mm, L_j = 1,000 mm

Fig. 16 Effects of reinforcement ratio on bending strength

Shear connectors can be employed to prevent slips between main tubes and the connecting tube, as introduced in Fig. 1. Several types of connectors can be considered such as shear studs, steel ribs, and weld joints which will be further investigated in separate experimental studies of the mechanical joint. A finite element analysis was conducted for modal D200 to investigate the bending capacity of the steel tubes with the proposed mechanical joint. Elastic spring elements with appropriate stiffness were applied near the edges of the joint to simulate shear connectors that could partially fix relative displacement between tubes, and the concrete core. Fig. 17 presents comparative results in bending strength between a jointless tube and tubes with mechanical joint with and without shear connectors. The study revealed that the connectors slightly enhanced the structure's bending stiffness by reducing slips between components. At the rotation angle $\phi = \phi_y$, the bending strength with shear connectors was identical to that of a jointless tube and 8.6% greater than that of a structure without shear connectors. However, the impact on maximum bending strength was minimal, as the joint itself provided enough rigidity for the main tubes to reach their maximum capacity before failing due to local buckling.

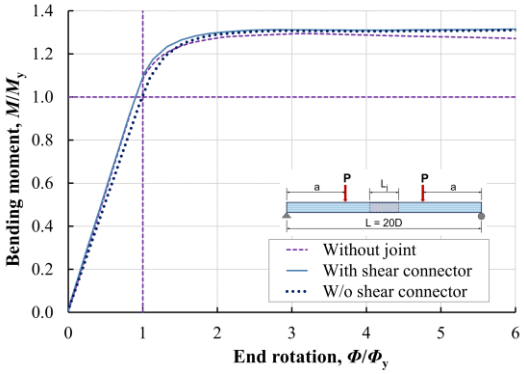

Fig. 17 Effect of anchoring interaction from using shear connectors

5. Design proportions and recommendations

The previous section introduced a strut-tie model with tension and compression areas to assess the local load-bearing capacity of concrete-filled steel tube joints. This tension zone was generated by frictional effects between the main tube and the connecting tube. Local shear force appeared at the contact surface due to friction, creating a longitudinal tensile stress field along the connecting tube. Fig. 18 presents the principal stress distribution at first yield within the joint steel tube and concrete core obtained from finite element analysis of models D200, D350, and D500. The tensile stress field concentrates along the bottom fiber of the steel tube, while the compressive stress field primarily dissipates within the concrete core. Based on such stress distribution, regions for tension and compression are identified and used to compute the structural load-bearing capacity.

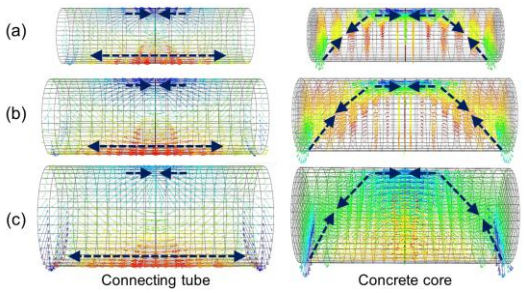

Fig. 18 Principal stress tensors in connecting tubes and concrete cores:

(a) D = 200 mm; (b) D = 350 mm; (c) D = 500 mm

Examining the stress tensor configurations revealed two distinct stress fields within the joint steel tube: tensile stresses along the bottom fiber and compressive stress in the top fiber of the cross sections. The tensile stress field was distributed along the connecting tube, while the compressive stress field was mainly located near the middle region of the joint. Observation of the stress field within the concrete core showed a distribution that aligned well with the proposed strut-tie model in this study. Two main compressive stress fields were generated within the concrete core: a diagonal compressive stress tensor from the bottom left and right edges toward the top fiber and a compressive stress tensor concentrated near the central region of the joint. It is obvious that the connecting steel tube and concrete core simultaneously generated compressive

resistance within the upper section of the joint. In addition, the infilled concrete was constrained by the steel tube, creating a triaxial compression state that could enhance both the strength and strain capacity of the concrete infill. Analysis results successfully verified the proposed theory in this study which can be utilized to compute the load-bearing capacity of mechanical joints using concrete-filled steel tubes based on the strut-tie model. The strut-tie phenomenon became more obvious when the length-to-diameter ratios L_j / D of the joint were less than 3.0. Findings from this study were consistent with those from Lu et al. [11] who proposed a strut-tie model and corresponding effective areas to describe the load transfer mechanism in the circular composite member under pure bending conditions.

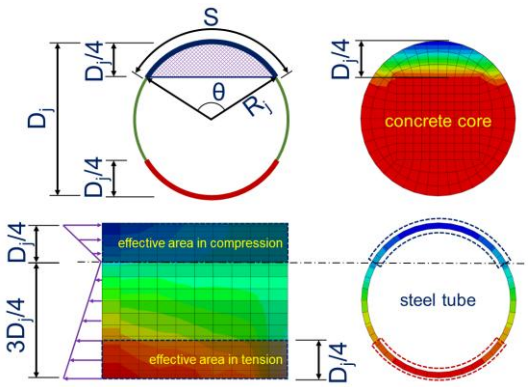

Fig. 19 Effective area of concrete core in compression at first yield

This study focused on developing a method to assess local strengths of the mechanical joint by introducing an approximate theory based on the analysis results to calculate strut and tie strength. Effective cross sections were proposed to define the compression and tension resistances based on the strut-tie model. From finite element analyses, it was found that the compression stress was almost similarly distributed in the range of D_j /4 from the top fiber for all models D200, D350, and D500. Fig. 19 shows the typical stress distribution in the cross section in which the effective areas can be simply defined. The cross section of the joint contributing to compression resistance is considered as a circular segment within D_j /4 from the extreme top fiber. The effective area in compression of the steel tube segment contributing to compression resistance can be proposed as

$$A_{s,c} = \theta D_j t_j / 2 \tag{6}$$

where, $\theta = 2\arcsin\left(\sqrt{3}/2\right)$.

The effective area in compression of the concrete core is equal to the area of the circular segment minus the arc-length area of the steel tube:

$$A_c = \frac{D_j^2}{8}\left(\theta - \sin\theta\right) - A_s \tag{7}$$

The total axial compressive strength of the whole circular segment is defined as follows:

$$S_{2,n} = F_y A_{s,c} + 0.85 f_c^{'} A_c \tag{8}$$

Similarly, the active section in tension of the connecting steel tube to resist the tie force can be assumed as the arc segment in the range of D_j /4 from the bottom extreme fiber as illustrated in Fig. 21. The effective area is defined from the arc-length area as follows:

$$A_{s,t} = \theta D_j t_j / 2 \tag{9}$$

The axial tensile strength of the steel arc segment is defined as follows:

$$T_n = F_y A_{s,t} \tag{10}$$

From the proposed theory of the strut-tie model as presented in Fig. 4, diagonal strut forces were defined from the acting of couple generated by the internal bending moment in main tubes. Several research have successfully developed and proposed theories to define the effective section of the diagonal strut for deep beam [24- 26]. However, most theories only focus on strut-tie models for reinforced concrete beams with rectangular sections. This study observed stress distribution in circular concrete cores from a series of analysis models to find the effective section for the diagonal strut. It was found that compressive stress flow was transmitted through an effective section of an equivalent cylinder as illustrated in Fig. 20. As the length-to-diameter ratio of the joint decreased, the deep-beam effect and the diagonal stress flow became more obvious. In this study, a method to determine the effective concrete section in the strut-and-tie model was proposed. Specifically, the authors selected an equivalent circular section with a diameter $d_e = D_j$ /3 where D_j is the diameter of the CFST joint. This simplification allows for easier calculation of the compression resistance of the diagonal strut within the strut-tie model. The axial compression resistance of the diagonal strut can be obtained as:

$$S_{1,n} = 0.85 f_c^{'} (\pi d_e^2) / 4 \tag{11}$$

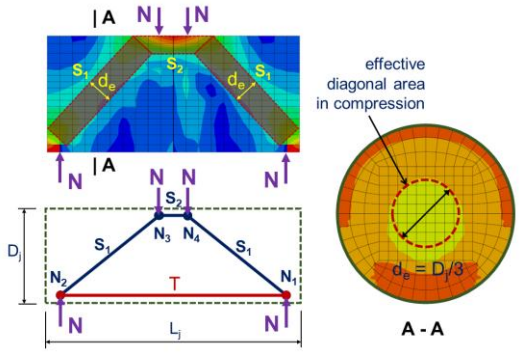

Fig. 20 Assumed effective diagonal area in compression

Local failures of the concrete core at node locations (N_1 to N_4) must be secured by controlling local stresses due to radial pressure Δp generated by couple N as presented in Fig. 20. The magnitude of the radial pressure must not exceed the compressive strength of the concrete. As presented in Fig. 4, the magnitude of Δp can be determined based on the mechanism of the shrink-fit joint [34].

From the previous section, the proportion for connecting length of the mechanical joint was successfully confirmed. To ensure the transmission capacity for the bending moment of the joint, the active length L_j of the joint should be at least three times the diameter D of the main tubes. Findings from this study were consistent with previous achievements in slip joints of towers for offshore wind turbines and power transmission.

Another proportion of the effective thickness of the connecting tube was also proposed. The thickness of the connecting steel tubes should not be less than the thickness of the main tubes, $t_j \geq t$, to secure the rigidity so that the bending moment from main tubes could be completely transmitted through the joint. The connecting steel tube not only provided confining effect for the infilled concrete but also contributed to the tension resistance and compression resistance of the joint based on the strut-tie model theory.

This study also investigated the effects of the compressive strength of the concrete core and the contribution of steel reinforcement on the performance of the mechanical joint. Although variation in concrete strength and reinforcement ratio did not obviously affect the capability of the main tubes for reaching the critical strength since the joint itself could provide sufficient rigidity regardless of the concrete strength, the main tubes completely failed due to local buckling of circular ring in compression. Therefore, the compressive strength of the concrete core is defined by securing the axial compression strength of the strut members under local strut forces. Similarly, the use of steel reinforcement can be neglected in the bending design of the mechanical joint using CFST.

6. Conclusions

The investigation into mechanical joints using CFST offers a promising advancement in structural engineering, particularly for applications involving steel tube structures. This study introduced a new mechanical joint using CFST to enhance construction efficiency by eliminating the need for site welding, thereby maintaining continuity and ensure instant load-bearing capacity post-installation. Key parameters such as the length and thickness of the connecting tube, compressive strength of the concrete core, and reinforcement steel ratio

were extensively analyzed to establish design recommendations. Shear connectors could improve the interaction between the steel tubes and concrete core and structural integrity during load bearing to prevent slip and global deformation. These findings are critical for simplifying construction practices and optimizing joint performance that might enable more effective and efficient use of CFST in various structural applications. Beyond its technical performance, this innovative mechanical joint design also brings substantial economic and logistical advantages. By eliminating the need for on-site welding, construction time is significantly reduced, resulting in faster project delivery and lower labor costs. Furthermore, the design is well-suited to prefabrication, which minimizes site work and improves quality control. Together, these factors lead to significant cost savings and enhanced construction efficiency, making CFST joints an attractive choice for rapid, reliable, and cost-effective structural applications.

To enhance the reliability and applicability of the findings presented in this study, further research is recommended to validate and refine the theoretical models. Future experimental investigations should be conducted to assess the actual performance of the proposed mechanical joint under realistic loading conditions. These studies should focus on verifying theoretical predictions related to bending strength, stiffness, and overall structural behavior of CFST joints.

Moreover, additional research should aim to develop comprehensive design guidelines and contribute to the formulation of new standards for the implementation of the proposed mechanical joint in structural applications. Investigations into the influence of material properties, joint configurations, and varying loading conditions are also necessary to fully understand the behavior and limitations of the proposed joint design. Furthermore, numerical simulations with advanced modeling techniques should be explored to enhance predictive accuracy and optimize design parameters for practical applications.

Acknowledgements

The authors would like to express their gratitude to Ho Chi Minh City University of Technology (HCMUT) – Vietnam National University Ho Chi Minh City (VNU-HCM) for their valuable support in this study.

References

[1] Ishii T., Fujisawa S., and Ohmori A., "Overview and application of steel materials for high-rise buildings", JFE Technical Report, 14(14), 1-8, 2000.
[2] Gao S., Usami T., and Ge H., "Ductility evaluation of steel bridge piers with pipe sections", Journal of Engineering Mechanics, 124(3), 260-267, 1998.
[3] Yasunami H., Terada M., Natori T., and Murakoshi, J, "Numerical Simulation of Steel Pipe Column with Outer Pipe for Seismic Retrofit", Steel Construction Engineering, 5(19), 85-96, 1998.
[4] Shinohara M., Kanaji H., Oniki K., and Kimura, M., "A Proposal of a Bridge Column integrated by Multiple Steel Pipes with Directly-Connected Piles and a Seismic Response Analysis", Journal of Japan Society of Civil Engineers, Ser: C (Geosphere Engineering), 69, 312-325, 2013.
[5] Huo S., Chao Y., Dai G., and Gong, W., "Field test research of inclined large-scale steel pipe pile foundation for offshore wind farms", Journal of Coastal Research, 73, 132-138, 2015.
[6] Li X., Dai G., Zhu M., and Gong, W., "Application of static loading tests to steel pipe piles with large diameters in Chinese offshore wind farms", Ocean Engineering, 186, 106041, 2019.
[7] Segeren M.L., Lourens E.M., Tsouvalas A., and Van Der Zee T.J., "Investigation of a slip joint connection between the monopile and the tower of an offshore wind turbine", IET Renewable Power Generation, 8(4), 422-432, 2014.
[8] Cabboi A., Kamphuis T., Van Veldhuizen E., Segeren M., and Hendrikse H., "Vibration-assisted decommissioning of a slip joint: Application to an offshore wind turbine", Marine Structures, 76, 102931, 2021.
[9] Li G.C., Chen B.W., Yang Z.J., Liu Y.P., and Feng, Y.H., "Experimental and numerical behavior of eccentrically loaded square concrete-filled steel tubular long columns made of high-strength steel and concrete", Thin-Walled Structures, 159, 107289, 2021.
[10] Nakamura S.I., Momiyama Y., Hosaka T., and Homma K., "New technologies of steel/concrete composite bridges", Journal of Constructional Steel Research, 58(1), 99-130, 2002.
[11] Lu H., Han L.H., and Zhao X.L., "Analytical behavior of circular concrete-filled thin-walled steel tubes subjected to bending", Thin-Walled Structures, 47(3), 346-358, 2009.
[12] Moon J., Roeder C.W., Lehman D.E., and Lee, H.E., "Analytical modeling of bending of circular concrete-filled steel tubes", Engineering structures, 42, 349-361, 2012.
[13] Cho J., Moon J., Ko H.J., and Lee, H.E., "Flexural strength evaluation of concrete-filled steel tube (CFST) composite girder", Journal of Constructional Steel Research, 151, 12-24, 2018.
[14] Lehman D.E., and Roeder C.W., Rapid construction of bridge piers with improved seismic performance, Department of Civil Engineer, University of Washington, 2012.
[15] Moon J., Lehman D.E., Roeder C.W., and Lee H.E., "Strength of circular concrete-filled tubes with and without internal reinforcement under combined loading", Journal of Structural Engineering, 139(12), 04013012, 2013.
[16] Stephens M.T., Lehman D.E., and Roeder C.W., "Design of CFST column-to-foundation/cap beam connections for moderate and high seismic regions", Engineering Structures, 122, 323-337, 2016.
[17] Chin W.J., Kang J.Y., Choi E.S., and Lee J.W., "Study on structural behavior characteristics of concrete filled steel tube girder bridges", Korea Institute of Construction Technology, Goyang, Republic of Korea, 2008.
[18] Ichikawa K., Sato R., and Terao N., "Development of Mechanical Joint New "High-Mecha-Neji" for Steel Pipe Piles and Steel Pipe Sheet Piles", JFE Technical Report, No. 25: 9-16, 2020.
[19] Akutagawa H., Takano K., and Tajika H., "Mechanical Joint "KASHEEN" for Large-Diameter Pipe Piles", JFE Technical Report, No. 8: 51-56, 2006.
[20] Masashi K., Yoshiro I., Hironobu M., Yoshinori F., Toshihiko S., Shinji T., Tadachika M., and Hiroyuki T., "Development of the Mechanical "Gachi-cam Joint" for Steel Pipe Piles and Steel Pipe Sheet Piles", Nippon Steel & Sumitomo Metal, Technical Report, No. 113: 34-41, 2016.
[21] Fu Z., Ji B., Maeno H., Eizien A., and Chen J., "Flexural behavior of lightweight aggregate concrete filled steel tube", Advanced Steel Construction, 10(4), 385-403, 2014.
[22] Li G., Qiu Z., Yang Z., Chen B., and Feng Y., "Seismic performance of high strength concrete filled high strength square steel tubes under cyclic pure bending", Advanced Steel Construction, 16(2), 112-123, 2020.
[23] Yang Z-J., Zhang S., Cui W-Z., and Li G-C., "Flexural behavior of reinforced hollow high strength concrete filled square steel tube", Advanced Steel Construction, 20(2), 199-207, 2024.
[24] Park, J.W., and Kuchma, D., "Strut-and-tie model analysis for strength prediction of deep beams", ACI Structural Journal, 104(6), 657, 2007.
[25] El-Zoughiby M.E., El-Metwally S.E., Al-Shora A.T., and Agieb E.E., "Strength prediction of simply supported R/C deep beams using the strut-and-tie method", Arabian Journal for Science and Engineering, 38, 1973-1991, 2013.
[26] Shuraim A.B., "Behavior and shear design provisions of reinforced concrete D-region beams", Journal of King Saud University-Engineering Sciences, 25(1), 65-74, 2013.
[27] Tuchscherer R.G., Birrcher D.B., Williams C.S., Deschenes D.J., and Bayrak O., "Evaluation of Existing Strut-and-Tie Methods and Recommended Improvements", ACI Structural Journal, 111(6), 2014.
[28] Tuan N.C., and Khiem N.T., "A numerical analysis on bending capacity of steel pipe columns using a mechanical joint with concrete-filled steel tube", Journal of Science and Technology in Civil Engineering (JSTCE)-HUCE, 16(4), 87-99, 2022.
[29] Roeder C.W., Lehman D.E., and Bishop E., "Strength and stiffness of circular concrete filled tubes", Journal of Structural Engineering, 136(12), 1545–1553, 2010.
[30] AASHTO LRFD Bridge Design Specification, The American Association of State Highway and Transportation Officials, Washington DC, USA, 2010.
[31] AISC Specification for structural steel buildings, AISC, Chicago, IL; 2010.
[32] ACI Building code requirements for structural concrete and commentary, ACI318-08, Farmington Hills, MI, 2008.
[33] Design of composite steel and concrete structures - Part 1.1: general rules and rules for buildings, Eurocode 4, European Committee for Standardization, Brussels; 2004.
[34] Firouz-Abadi R.D., Mehralian F., Amirabadizadeh H., and Yousefi M., "A Novel Approach to Model the Shrink-Fit Connection", In International Conference on Rotor Dynamics (pp. 25-35), Springer International Publishing, 2023.
[35] Slocum R., and Fairbairn M., "Slip Joints Connections - How Do These Things Work?", In Electrical Transmission and Substation Structures, 363-374, 2015.
[36] Mojto M., Brodnianský J., Recký J., and Tilinger, M., "Modelling and experimental tests of spatial structure focused on slip joints", In Proceedings of International Association for Shell and Spatial Structures (IASS), 18, 1-9, 2020.
[37] ABAQUS standard user's manual version 6.5, Hibbit, Karsson and Sorensen Inc., 2005.
[38] Nolle H., and Richardson R.S.H., "Static friction coefficients for mechanical and structural joints", Wear, 28(1), 1-13, 1974.
[39] Baltay P., and Gjelsvik A., "Coefficient of friction for steel on concrete at high normal stress", Journal of Materials in Civil Engineering, 2(1), 46-49, 1990.
[40] Rabinowicz E., and Tanner R.I., "Friction and wear of materials", Journal of Applied Mechanics, 33(2), 479, 1966.
[41] Fuller D.D., Coefficients of friction, American Institute of physics handbook, 1972.
[42] Blau P.J., Friction science and technology: from concepts to applications, CRC press, 2008.
[43] Hutchings I., and Shipway P., Tribology: friction and wear of engineering materials, Butterworth-heinemann, 2017.
[44] Lubliner J., Oliver J., Oller S., and Oñate E., "A plastic-damage model for concrete", International Journal of solids and structures, 25(3), 299-326, 1989.
[45] Grassl P., and Jirásek M., "Damage-plastic model for concrete failure", International journal of solids and structures, 43(22-23), 7166-7196, 2006.
[46] Sarikaya A., and Erkmen R.E., "A plastic-damage model for concrete under compression", International Journal of Mechanical Sciences, 150, 584-593, 2019.
[47] Wong M.B., Plastic analysis and design of steel structures, Burlington (MA), Butterworth, 2009.
[48] Lubliner J., Oliver J., Oller S., and Oñate E., "A plastic-damage model for concrete", International Journal of Solids and Structures, 25, 299–329, 1989.
[49] Lee J., and Fenves G.L., "Plastic-damage model for cyclic loading of concrete structures". Journal of Engineering Mechanics, ASCE, 124(8), 892–900, 1998.
[50] Kiessling F., Nefzger P., Nolasco J.F., and Kaintzyk U., Requirements on loading and strength. In: Overhead Power Lines, Power Systems, Springer, Berlin, Heidelberg, 2003
[51] Slocum R., and Fairbairn M., "Slip Joints Connections - How Do These Things Work?", Electrical Transmission and Substation Structures, 363-374, 2015.
[52] Brodniansky J., Recký J., Magura M., Klas T., and Botló M., "Slip joint connection of conical towers subjected to bending and torsion", Advances and Trends in Engineering Sciences and Technologies III, 55-60, CRC Press, 2019.
[53] Mojto M., and Cabboi A., "The mechanical behaviour of a slip joint for an offshore wind turbine: First monitoring and modelling results", Thin-Walled Structures, 196, 111482, 2024.

Advanced Steel Construction – Vol. 21 No. 6 (2025) 530–541
DOI: 10.18057/IJASC.2025.21.6.6

STUDY ON HUMAN-INDUCED VIBRATION OF AN INNOVATIVE SPATIAL CABLE-SUPPORTED FLOOR SYSTEM

Qi An [1, *], Hang-Qi Zheng [1], Yu-Hao Dong [1], Xiu-Jun Wang [2], Yan-Song Diao [1] and Zhong-Hua Wang [2]

[1] *School of Civil Engineering, Qingdao University of Technology, Qingdao 266520, China*
[2] *The Fourth Construction Co., Ltd. of China Construction Eighth Engineering Division, Qingdao 266000, China*
**(Corresponding Author: E–mail: anqi@qut.edu.cn)*

ABSTRACT

The growing demand for expansive indoor spaces in public buildings has necessitated the development of an innovative spatial cable-supported floor system (SCSFS). Experimental results revealed that the first-order natural frequency of the test floor is 17.58 Hz, with a damping ratio of 0.028. Among the four types of loads analyzed, jumping loads induced the most significant human-induced vibration acceleration responses in the floor system, whereas walking loads had a relatively minor impact. Numerical simulations further demonstrated that parameters such as the arrangement of cable-strut system, beam height, cable cross-sectional area, and sag of cable-strut system significantly influence the natural frequency of the floor system. Moreover, these parameters, along with steel beam cross-section type and floor slab thickness, play a critical role in the acceleration response. Conversely, changes in the cross-sectional area of the struts, boundary conditions, and prestress levels were found to have minimal impact on both natural frequency and acceleration responses. This study elucidates the natural vibration characteristics and human-induced vibration mechanisms of the SCSFS, identifies the effects of key structural parameters on human-induced vibration responses, and provides a theoretical and technical foundation for the practical engineering application of SCSFS. The findings possess substantial scientific and engineering value.

ARTICLE HISTORY

Received: 18 March 2025
Revised: 22 July 2025
Accepted: 2 August 2025

KEYWORDS

Spatial cable-supported floor system;
Large-span floor system structures;
Human-induced vibration;
Comfort analysis;
Numerical simulation

1. Introduction

In the field of contemporary architecture, with the increasing complexity of functional requirements and the continuous innovation of spatial concepts, long-span floor systems have become the core structural solution for realizing ultra-large-span column-free spaces.

Compared with small and medium-span floor systems (such as concrete floors, composite floors, and timber floors [1]) which feature diverse forms and mature technologies, the development of long-span floor systems [2-9] still faces significant challenges in terms of structural form innovation and research depth. In engineering practice, long-span requirements are primarily met through four types of floor systems: prestressed concrete floors [10-12], steel truss composite floors [13-15], open-web sandwich floors [16-17], and cable-supported floors [18-20]. However, with the continuous increase in architectural span requirements, the limitations of existing mainstream systems have gradually become apparent: long-span prestressed concrete floors face severe challenges in crack control and excessive self-weight [21]; the load-bearing capacity of steel truss composite floors relies on steel truss systems, which consist of upper chords, lower chords, web members, and other components connected via dense joints, resulting in complex component layouts and low space utilization; open-web sandwich floors have limited spanning capacity; cable-supported floors still require further research and technical breakthroughs in terms of refined node design, construction tension control, and adaptability to complex spatial forms.

Therefore, exploring and developing innovative structural solutions that can more efficiently synergize the performance of different materials, optimize key structural details, and enhance overall stability and space utilization has become a crucial research direction for advancing the development of modern architectural spaces.

In response to these limitations, this study introduces a novel spatial cable-supported floor system (SCSFS) designed for large-span applications [22], as illustrated in Fig. 1. The SCSFS comprises two main components: an upper rigid composite floor system and a lower spatial cable-strut system. The upper rigid composite floor system integrates concrete floor slabs with intersecting steel beams, while the lower spatial cable-strut system includes inner and outer rings, radially arranged cables, and circumferential cables. The lower ends of the struts connect to the radial and circumferential cables, and the upper ends connect to the steel beams via universal rotational nodes.

Compared to existing large-span floor systems, the SCSFS offers several key advantages:

1) It leverages the compressive performance of concrete slabs to bear vertical loads and relies on the tensile properties of cables to transmit horizontal forces. Compared with traditional structures (e.g., unidirectionally loaded steel beam-concrete composite floors), the SCSFS achieves improved structural load-bearing efficiency and enhanced spanning capacity, making it adaptable to the requirements of larger-span buildings. The lower cable-strut system can provide reliable support for the upper rigid slab system, while the material advantages—high compressive strength of concrete and high tensile strength of cables—are fully utilized.
2) The cable-strut system adopts a spatial arrangement, which effectively restrains the lateral displacement of the lower nodes of struts, thereby ensuring the support stability of the cable-strut system.
3) The upper nodes of struts are designed to allow universal rotation, ensuring that struts only bear axial forces.
4) The cable-strut system features a simple layout with favorable visual effects; additionally, pipelines can be routed freely through the structure, resulting in high utilization efficiency of architectural space.
5) Steel beams, cables, and struts are all prefabricated components, leading to a high degree of prefabrication and accelerated construction speed.

Owing to its efficient material utilization, the Spatial Cable-Supported Floor System (SCSFS) typically features smaller component cross-sections. While this enables long spans and structural lightweighting, it also results in relatively low overall structural damping. Such characteristics—low damping, light weight, and long span—render the system prone to significant vibration responses under human-induced loads (e.g., walking, jumping, and rhythmic movements). Critically, once vibrations are excited, their attenuation process is often slow. Sustained or excessive vibrations not only severely compromise occupant comfort and disrupt normal functionality but may even trigger crowd panic or safety incidents in extreme cases. Historical and modern engineering cases—such as bridge resonance induced by specific step frequencies, severe oscillations of pedestrian bridges caused by synchronized pedestrian movements, and building-wide vibrations from fitness activities—have repeatedly demonstrated the potential risks of long-span lightweight structures under human-induced excitation [23-25].

Given the prominence of such vibration issues, major international technical standards (e.g., ISO-10137) [26] and Chinese specifications (e.g., Technical Standard for Vibration Comfort of Building Floor Structure (JGJ/T 441—2019)) [27] have provided important design guidelines and methods for human-induced vibration control. However, existing regulatory frameworks are primarily based on extensive field measurements and simplified models of traditional floor systems, such as conventional beam-slab structures, composite beams, or grid structures. As an innovative spatial tensioned cable-supported composite structure, the SCSFS exhibits unique natural vibration characteristics (frequency, mode shape) and peak acceleration responses under human-induced loads that cannot be accurately described by prediction models or limit criteria established for traditional structures. Consequently, significant doubts exist regarding the applicability and reliability of directly applying existing code provisions and evaluation methods to the human-induced vibration analysis of SCSFS. Specialized theoretical and experimental research on this novel system is therefore urgently required.

Given the pronounced human-induced vibration issues of SCSFS and the inability of existing research and specifications to directly address them, this

study systematically investigates the human-induced vibration of SCSFS through experimental and numerical simulation methods. It focuses on addressing the following key issues: (1) the natural vibration characteristics and human-induced vibration response patterns of SCSFS; (2) the influence laws of critical structural parameters on the human-induced vibration responses of SCSFS. The findings aim to provide reference for the engineering application of SCSFS.

2. Human-induced vibration testing scheme

2.1. Specimen design and fabrication

To align with the experimental setup, a spatial cable-supported floor system with a span of 4.5m × 4.5m was designed, as illustrated in Fig. 2. The outer frame employs box-shaped steel beams with a cross-section specification of □100×8 mm (height × thickness, unit: mm). Internally, H-shaped steel beams with a cross-section of H100×50×4×8 mm (height × flange width × web thickness × flange thickness, unit: mm) were used. High-strength round steel rods with a tensile strength of 650 MPa and a diameter of 20 mm serve as cables, while the struts feature a cross-section of P57×4 mm (diameter × thickness, unit: mm). The floor slab comprises 40-mm-thick reinforced concrete using C30-grade concrete. The steel beams in both longitudinal and transverse directions are connected, while the perimeter beams are welded to steel short columns at their intersections. The floor system is supported by pre-constructed concrete edge columns. Specifically, the steel short columns (Support A) are welded to embedded plates atop the concrete columns, while the steel short columns (Support B) rest directly on steel plates atop the concrete columns. Elsewhere, the bases of the steel beams are directly supported on the concrete column tops. The connections between steel short columns and cables, between cables, and between cables and struts are articulated. During construction, a 5-kN prestress was applied to the cables by rotating the cable-end tensioners. The construction process of the experimental floor system is illustrated in Fig. 3.

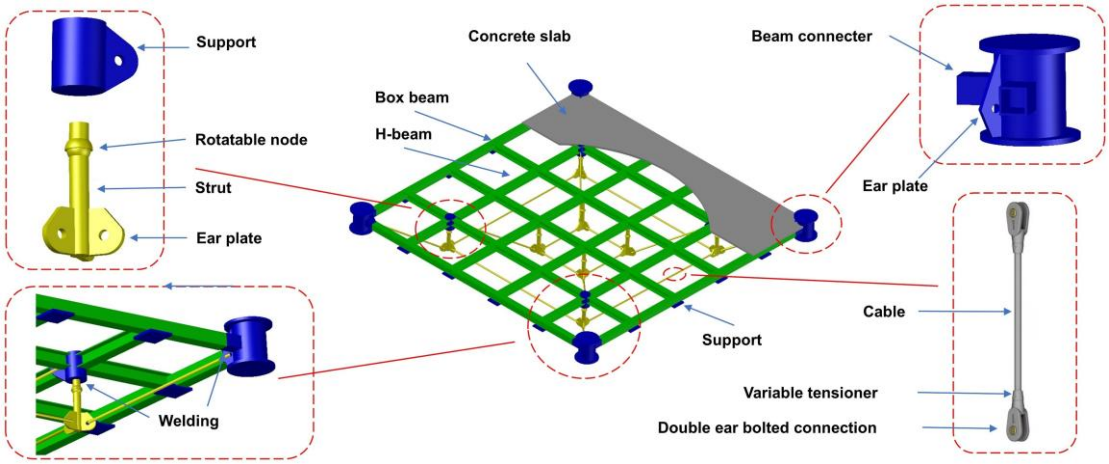

Fig. 1 Schematic diagram of the SCSFS structure

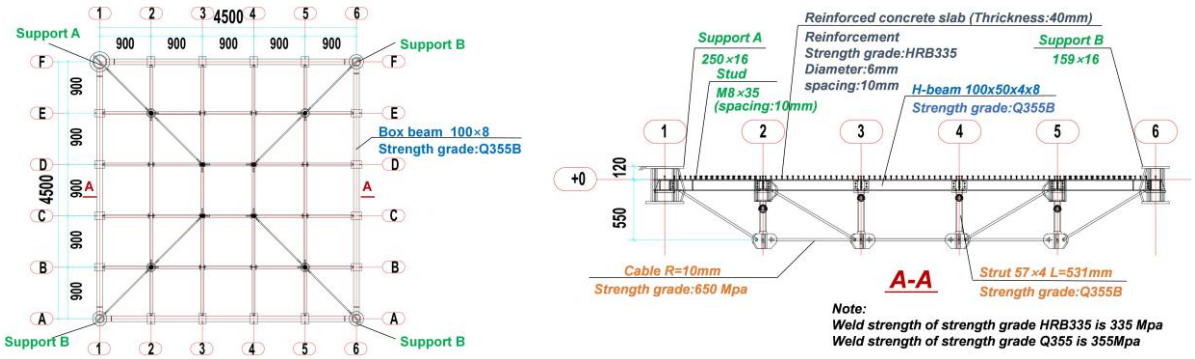

(a) Layout plan

(b) Cross-sectional schematic

Fig. 2 Geometric dimensions and embedment details of the specimens (unit: mm)

(a) Steel reinforcement binding

(b) Formwork removal of concrete columns and beams

(c) Assembly of the steel beam grid

(d) Installation of struts and cables

(e) Concrete slab construction

(f) Completed floor system

Fig. 3 Construction process of the test floor

2.2. Loading scheme

Four volunteers were enlisted to apply human-induced loads to the test floor. The loading process was divided into two stages. In the first stage, a free vibration test was conducted. The volunteers applied an impact load to the test floor and then remained stationary to capture the structure's natural vibration characteristics. This stage aimed to accurately determine the natural frequency and damping ratio of the test floor.

In the second stage, the volunteers applied various types of human-induced loads, including impact, stepping, jumping, walking, and running, following predefined activity patterns. To ensure consistent excitation frequencies, a metronome was employed to regulate the volunteers' movement frequencies. This stage was designed to evaluate the human-induced vibration responses of the test floor under different load types. The volunteers' body weights are listed in Table 1, while the detailed test descriptions are provided in Table 2. The loading regions for human-induced loads are shown in Fig. 4, where A1 and A2 represent areas for impact, stepping, and jumping activities, and P1–P2 denote the walking and running paths. The loading scenarios are depicted in Fig. 5.

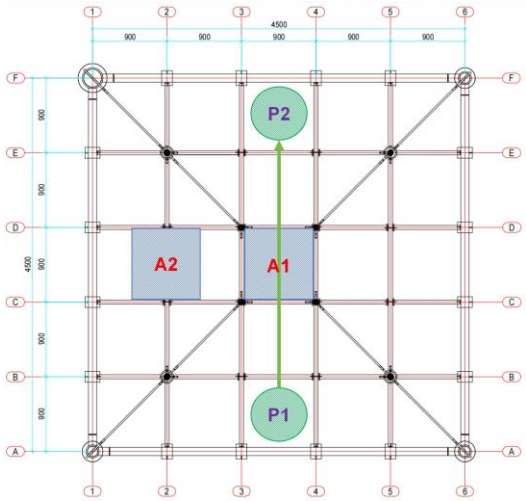

Fig. 4 Schematic diagram of the human-induced load application area

Table 1
Volunteer body weights

volunteer	1	2	3	4
weight(kg)	95	89	74	75

2.3. Measurement scheme

Since human-induced vibrations of floor systems are primarily vertical, only the vertical acceleration responses of the test floor were measured. Acceleration sensors were used at the test site to collect the vibration acceleration of the test floor, with the specific measurement scheme shown in Fig. 6. Human perception of vibration directly depends on the interaction with the contact surface, i.e., the vibration characteristics of the floor surface. Since the lower cable-strut system is not in direct contact with the human body, its vibration does not affect human perception, and thus monitoring of the lower cable-strut system is unnecessary. Moreover, considering that the vibration at the mid-span of the test floor is the most intense, acceleration sensors are arranged at the mid-span of the structure to ensure accurate capture of the maximum acceleration response of the structure.

(a) Stepping (b) Jumping

(c) Walking (d) Running

Fig. 5 On-site application of human-induced loads

3. Human-induced vibration test results and discussion

3.1. Free vibration test

The natural vibration characteristics of the test floor were determined using the results of Test 1. The heel-drop impact method was employed to obtain the free vibration acceleration decay curve, as shown in Fig. 7a. The frequency response was derived using Fast Fourier Transform (FFT), as depicted in Fig. 7b. The results indicate that the structural components exhibit typical single-periodic decay characteristics and can be modeled as a damped generalized single-degree-of-freedom system. The peak response was observed at 17.58 Hz, indicating that the first natural frequency of the test floor is 17.58 Hz. Based on the time history data, the logarithmic decrement method was applied, yielding a structural damping ratio of 0.028[28-30].

Table 2
Description of human-induced load tests

Test	description	Activity areas	Activity frequency(Hz)	Velocity (m/s)	volunteer
1	Four persons performing heel impact	A1	——	——	1、2、3、4
2	One person stepping	A1	1.89	——	2
3	Two persons stepping	A1	1.92	——	1、2
4	Three persons stepping	A1	2.00	——	1、2、4
5	Four persons stepping	A1	2.17	——	1、2、3、4
6	One person stepping	A2	1.92	——	2
7	Two persons stepping	A2	2.08	——	1、2
8	Three persons stepping	A2	2.22	——	1、2、4
9	Four persons stepping	A2	2.22	——	1、2、3、4
10	One person jumping	A1	2.33	——	2
11	Two persons jumping	A1	2.17	——	1、2
12	Three persons jumping	A1	2.00	——	1、2、4

Test	description	Activity areas	Activity frequency(Hz)	Velocity (m/s)	volunteer
13	Four persons jumping	A1	2.70	——	1、2、3、4
14	One person jumping	A2	3.03	——	2
15	Two persons jumping	A2	2.94	——	1、2
16	Three persons jumping	A2	3.03	——	1、2、4
17	Four persons jumping	A2	3.03	——	1、2、3、4
18	One person walking	P1—P2	1.66	1.33	2
19	Two persons walking	P1—P2	1.82	1.44	1、2
20	Three persons walking	P1—P2	1.50	1.00	1、2、4
21	Four persons walking	P1—P2	1.85	1.06	1、2、3、4
22	One person running	P1—P2	2.86	2.22	2
23	Two persons running	P1—P2	2.50	2.01	1、2
24	Three persons running	P1—P2	3.00	2.40	1、2、4
25	Four persons running	P1—P2	2.93	2.35	1、2、3、4

Note: The activity frequency of volunteers is calculated as "number of activity steps/time" in the experiment, and all frequencies fall within the range specified in ISO 10137 [26](1.2 – 2.4 Hz for walking, 2 – 4 Hz for running, and 1.5 – 3.5 Hz for jumping). Treading is approximately regarded as a scenario under walking.

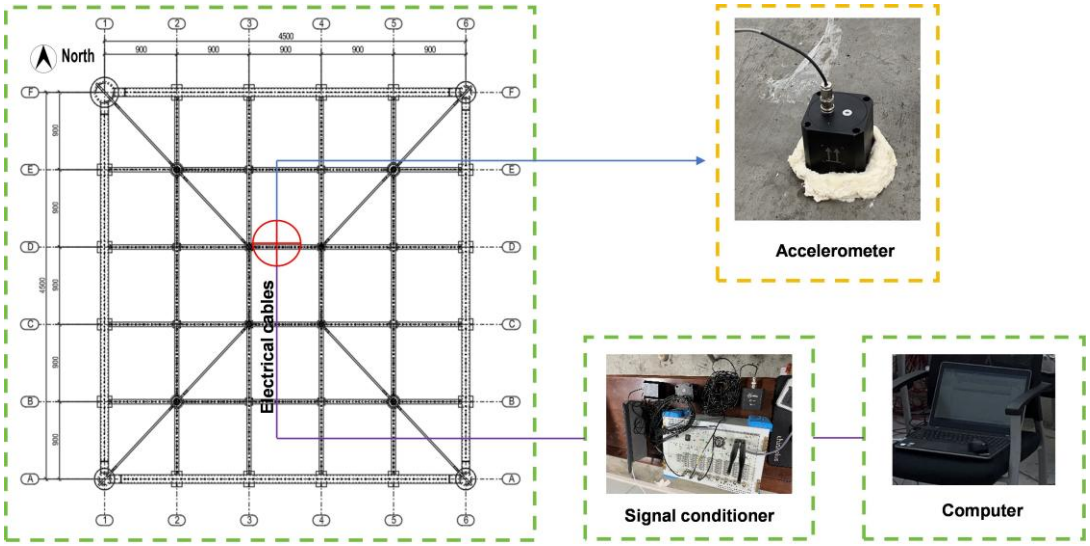

Fig. 6 Data acquisition system and typical measuring points

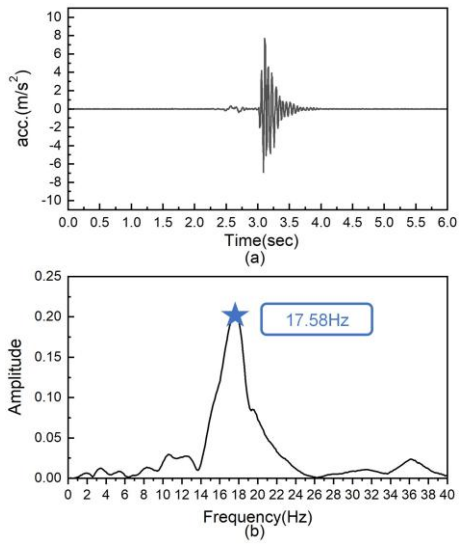

Fig. 7 Time histories and FFT results for Test 1

3.2. Human-induced vibration test

3.2.1. Stepping test

The stepping test was analyzed based on the results of Test 2. Fig. 8 illustrates that the time span between vibration peaks in the time history (i.e., the period from one peak to the next) is 0.53 seconds, corresponding to a stepping frequency of 1.89 Hz and a peak acceleration of 1.281 m/s². The FFT analysis reveals that the primary acceleration components are concentrated in the frequency ranges of 11.12–16.41 Hz and 17.22–22.51 Hz, with a peak observed at 19.34 Hz, which is ten times the stepping frequency.

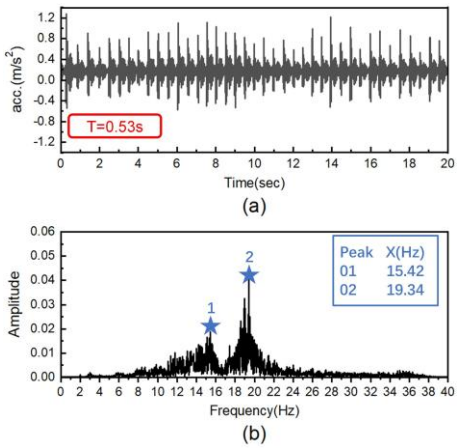

Fig. 8 Acceleration response for Test 2 (a. Time histories; b. FFT)

3.2.2. Jumping test

Due to space constraints, the jumping test was analyzed using representative results from Test 10. As shown in Fig. 9, the time history reveals a peak period

of 0.43 seconds, corresponding to a jumping frequency of 2.33 Hz and a peak acceleration of 1.121 m/s². The FFT analysis indicates primary acceleration components at 2.36 Hz, 4.65 Hz, 7.05 Hz, 9.41 Hz, 11.81 Hz, 13.84 Hz, and within the range of 16.83–19.95 Hz, with a peak observed at 18.75 Hz, which is eight times the jumping frequency.

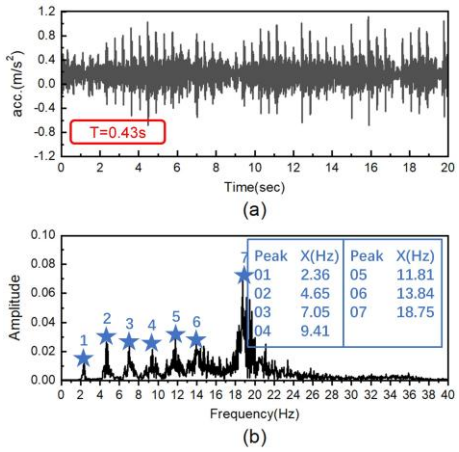

Fig. 9 Acceleration response for Test 10 (a. Time histories; b. FFT)

3.2.3. Walking test

The walking test was analyzed based on representative results from Test 21. Fig. 10 shows a peak period of 0.54 seconds, corresponding to a walking frequency of 1.85 Hz and a peak acceleration of 1.173 m/s². The FFT results show a peak at 18.55 Hz, which is ten times the walking frequency.

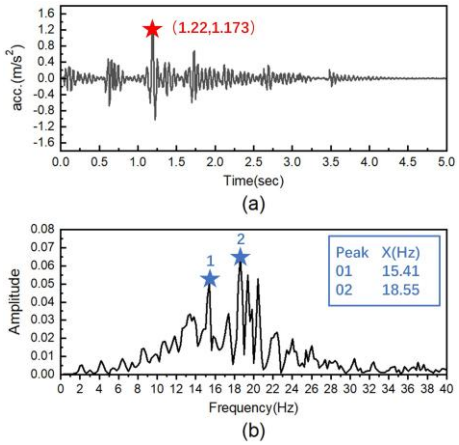

Fig. 10 Acceleration response for Test 21 (a. Time histories; b. FFT)

3.2.4. Running test

The running test was analyzed using the results of Test 22. Fig. 11 shows a time history peak period of 0.35 seconds, corresponding to a running frequency of 2.86 Hz and a peak acceleration of 0.996 m/s². The FFT analysis indicates primary acceleration components within the ranges of 2.00–3.83 Hz and 8.05–24.26 Hz, with a peak observed at 19.67 Hz, which is seven times the running frequency.

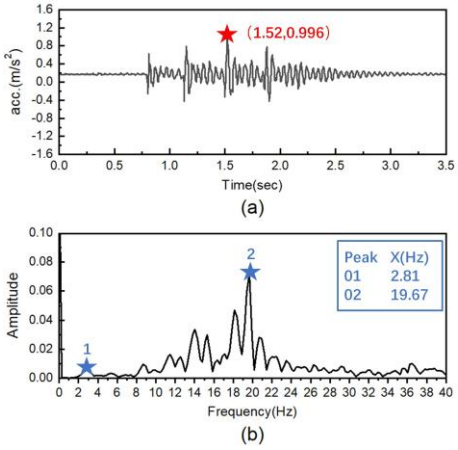

Fig. 11 Acceleration response for Test 22 (a. Time histories; b. FFT)

3.2.5. Summary and discussion of human-induced vibration responses

The peak acceleration responses across all test cases are summarized in Table 3. The results indicate that the peak accelerations of Tests 2–5 are greater than those of Tests 6–9, while the peak accelerations of Tests 10–13 exceed those of Tests 14–17. Since the acceleration sensors are arranged in the mid-span region, when excitation is applied at the mid-span, the floor vibration is dominated by the first-order mode shape, with the mid-span being the area of maximum vibration response. Additionally, the excitation positions in Tests 10–13 are closer to the sensors (see Table 2 for details), resulting in higher acceleration signals. The peak accelerations under jumping loads in Tests 10–13 are significantly higher than those induced by other types of loads. Tests 18–21 correspond to peak accelerations under walking loads, which are relatively small.

In accordance with the Technical Standard for Vibration Comfort of Building Floor Structure [27], the peak accelerations of Tests 2–25 all exceed the specified peak acceleration limits, indicating that the test floor has significant issues regarding human-induced vibrations.

Table 3
Summary of peak responses to human-induced vibration

stepping		jumping		walking		running	
test number	peak acceleration(m/s²)	test number	peak acceleration(m/s²)	test number	peak acceleration(m/s²)	test number	peak acceleration(m/s²)
2	1.281	10	1.121	18	0.46	22	0.996
3	0.973	11	5.852	19	0.281	23	0.868
4	1.275	12	4.86	20	0.962	24	1.231
5	1.633	13	4.412	21	1.173	25	0.978
6	0.516	14	1.301	——	——	——	——
7	0.613	15	1.497	——	——	——	——
8	1.275	16	3.135	——	——	——	——
9	1.497	17	2.716	——	——	——	——

4. Finite element analysis

4.1. Modeling scheme

The finite element model of the Test floor was developed using the ABAQUS software, as illustrated in Fig. 12. The steel beams beneath the slab were modeled using beam elements (B31), with Young's modulus, density, and Poisson's ratio (PRXY) defined as 2.06e11 N/mm², 7850 kg/m³, and 0.3, respectively. The concrete slab was modeled using shell elements (S4R), with corresponding values of 3e10 N/mm², 2400 kg/m³, and 0.2. Truss elements (T3D2) were employed to simulate the struts and cables beneath the slab, sharing the same material properties as the steel beams. The boundary conditions were

set to align with the experimental setup, where one corner of the floor system (RP-1) was restrained in all three translational directions, while the other three corners and steel beam supports (RP-2) were constrained in the vertical direction only.

The load point (LP1) corresponded to the location of jumping and stepping loads, while single-running loads were applied along route LR1, and four-person walking loads were applied along route LR2. The magnitude and frequency of the loads were consistent with those in the experiment, and the acceleration response was measured at the same location as the applied load (LP1). Table 5 summarizes the parameters of the finite element model.

Human-induced loads were simulated using the Fourier series model specified in ISO 10137 [26], as expressed in Equation (1):

$$F_v(t) = Q\left[1 + \sum_{n=1}^{k} \alpha_{n,v} \sin\left(2\pi n f t + \phi_{n,v}\right)\right] \quad (1)$$

In the equation, Q represents the individual weight (N), n is the harmonic order, k is the number of harmonics, $\alpha_{n,v}$ is the Fourier coefficient for the nth harmonic, f is the step frequency, and $\phi_{n,v}$ is the phase of the nth harmonic (rad). Parameters of the load model are determined based on Table 4. To enable effective comparison between finite element analysis results and on-site measured data, the fundamental frequency adopts the actual excitation frequencies obtained from on-site measurement statistics. The moving load is applied in the following manner: the position of the load action is dynamically adjusted along the longitudinal direction of the floor system. When a load is applied at a new position, the load at the previous position is removed simultaneously. The step distance is set to 720 mm, and the time interval for position switching is equal to the step frequency. Moreover, at each action position, a complete time history curve of single-step walking force is applied to simulate the moving effect of real walking loads.

Table 4
Parameter values of human-induced load model

Type of Motion	Frequency (Hz)	First Three Fourier Coefficients		
		α_1	α_2	α_3
Stepping	1.89	0.33	0.1	0.06
Jumping	2.33	1.40	0.4	0.10
	2.50	1.40	0.4	0.10
Walking	1.85	0.31	0.1	0.06
Running	2.86	1.40	0.4	0.10
	2.50	1.40	0.4	0.10

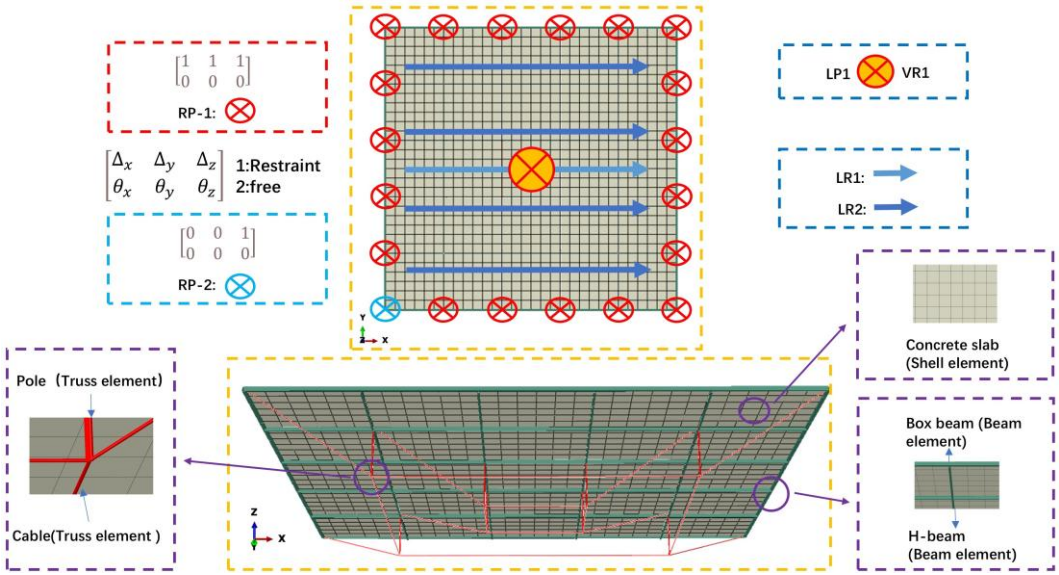

Fig. 12 Finite element model of the test floor

Table 5
Description of finite element model parameters

Model Number	Parameter Information										
	Floor Area (mm^2)	Sag (mm)	Slab Thickness (mm)	Beam Height (mm)	Beam Section Type	Cable Cross-sectional Area (mm^2)	Strut Cross-sectional Area (mm^2)	Cable Prestress (KN)	Inner Cables	Outer Cables	Boundary condition
Test floor	4500*4500	1293	50	100	H	314	1381	5	√	√	A
SCSFS-1	13500*13500	1293	50	100	H	314	1381	5	√	√	A
SCSFS-2	13500*13500	1293	50	100	H	314	1381	5	×	×	A
SCSFS-3	13500*13500	1293	50	100	H	314	1381	5	×	√	A
SCSFS-4	13500*13500	1293	50	100	H	314	1381	5	√	×	A
SCSFS-5	13500*13500	1293	50	100	box	314	1381	5	√	√	A
SCSFS-6	13500*13500	1293	60	100	H	314	1381	5	√	√	A
SCSFS-7	13500*13500	1293	70	100	H	314	1381	5	√	√	A
SCSFS-8	13500*13500	1293	80	100	H	314	1381	5	√	√	A
SCSFS-9	13500*13500	1293	90	100	H	314	1381	5	√	√	A
SCSFS-10	13500*13500	1293	100	100	H	314	1381	5	√	√	A
SCSFS-11	13500*13500	1293	50	125	H	314	1381	5	√	√	A
SCSFS-12	13500*13500	1293	50	150	H	314	1381	5	√	√	A

SCSFS-13	13500*13500	1293	50	175	H	314	1381	5	√	√	A
SCSFS-14	13500*13500	1293	50	200	H	314	1381	5	√	√	A
SCSFS-15	13500*13500	1293	50	100	H	392.5	1381	5	√	√	A
SCSFS-16	13500*13500	1293	50	100	H	471	1381	5	√	√	A
SCSFS-17	13500*13500	1293	50	100	H	549.5	1381	5	√	√	A
SCSFS-18	13500*13500	1293	50	100	H	628	1381	5	√	√	A
SCSFS-19	13500*13500	1293	50	100	H	314	1727	5	√	√	A
SCSFS-20	13500*13500	1293	50	100	H	314	2072	5	√	√	A
SCSFS-21	13500*13500	1293	50	100	H	314	2417.8	5	√	√	A
SCSFS-22	13500*13500	1293	50	100	H	314	2763.2	5	√	√	A
SCSFS-23	13500*13500	1293	50	100	H	314	1381	5	√	√	B
SCSFS-24	13500*13500	1293	50	100	H	314	1381	5	√	√	C
SCSFS-25	13500*13500	1293	50	100	H	314	1381	5	√	√	D
SCSFS-26	13500*13500	1293	50	100	H	314	1381	10	√	√	A
SCSFS-27	13500*13500	1293	50	100	H	314	1381	15	√	√	A
SCSFS-28	13500*13500	1293	50	100	H	314	1381	20	√	√	A
SCSFS-29	13500*13500	906	50	100	H	314	1381	5	√	√	A
SCSFS-30	13500*13500	1035	50	100	H	314	1381	5	√	√	A
SCSFS-31	13500*13500	1164	50	100	H	314	1381	5	√	√	A
SCSFS-32	13500*13500	1422	50	100	H	314	1381	5	√	√	A
SCSFS-33	13500*13500	1293	120	250	H	900	1381	5	√	√	A
SCSFS-34	13500*13500	1164	140	250	H	900	1381	5	√	√	A
SCSFS-35	13500*13500	1422	260	300	H	1500	1381	5	√	√	A

Note: Boundary condition A—corner three-way translational constraints, the rest only constraints vertical translational constraints; Boundary condition B—All use three-way translation constraints; Boundary condition C—Release the tangential translational constraints of the floor system and apply only the translational constraints in the other two directions; Boundary condition D—releases the normal translational constraints of the floor system and applies only the translational constraints in the other two directions.

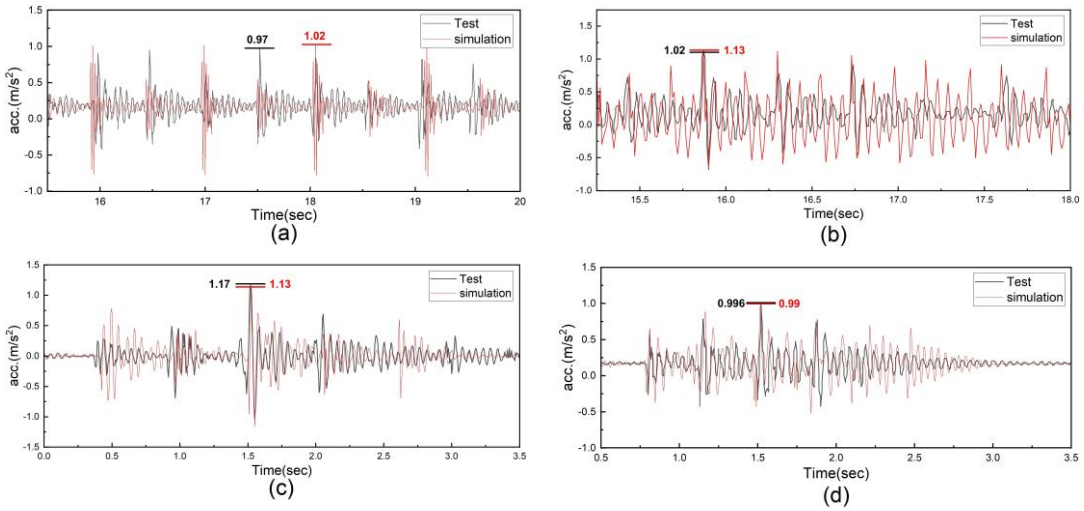

Fig. 13 Comparison of simulated and measured dynamic responses of the floor system (a. Dynamic response under single-person stepping load; b. Dynamic response under single-person jumping load; c. Dynamic response under four-person walking load; d. Dynamic response under single-person running load).

Table 6
Numerical simulation results of natural characteristics for SCSFS-1

Mode Shape Number	1	2	3
Frequency (Hz)	2.68	2.89	4.45
Mode Shape	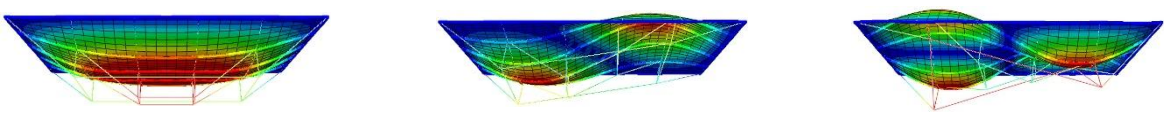		

4.2. Validation of the modeling scheme

Based on the aforementioned finite element model (TEST FLOOR), a finite element analysis was conducted, and the results were compared with the experimental data. In terms of natural frequency, the first-order frequency obtained from the finite element analysis was 18.11 Hz, while the first-order

natural frequency measured in the experiment was 17.58 Hz, with an error of 3%. According to relevant studies [31-33], an error of 3% is acceptable.

Fig. 13 presents the comparison of human-induced vibration responses obtained from experiments and FEA. Under single-person stepping, single-person jumping, four-person walking, and single-person running loads, the peak accelerations obtained from the numerical simulations were 1.02 m/s², 1.13 m/s²,1.13 m/s², and 0.99 m/s², respectively, while the experimentally measured peak accelerations were 0.97 m/s², 1.02 m/s², 1.17 m/s², and 0.996 m/s², respectively. The errors between the numerical simulations and the experimentally measured peak accelerations were 5%, 10%, 3%, and 1%, respectively. The 10% error corresponding to the jumping load is mainly attributed to the fact that the finite element analysis adopts the standard load model specified in the ISO 10137 [26] standard. However, in the actual test, there are significant individual differences among volunteers in terms of jumping movements, jumping heights, and motor abilities, resulting in deviations between the actual load and the standard model in the specification, which in turn leads to this error.

In summary, the numerical simulations were able to accurately reflect the dynamic response characteristics of the floor system under various loads. Although minor errors were present, the overall trends and peak patterns were consistent, validating the reliability of the adopted modeling approach in predicting the dynamic response of the floor system.

4.3. Human-induced vibration of SCSFS-1

Given that the test floor was subsequently scheduled for static load tests, larger cross-sectional dimensions were designed for safety considerations. This resulted in increased stiffness and a higher natural frequency, which deviated from the typical frequency range of human-induced loads (1.5 Hz–3.5 Hz). To further investigate the vibration response mechanism of the floor under such loads while maintaining the structural configuration unchanged, a validated finite element scheme was employed to establish a floor model with a span exceeding 10 m. This model not only embodies the characteristics of large-span floors but also brings the floor's frequency closer to the excitation frequency of human activities, thereby more comprehensively revealing the vibration characteristics of the floor under human-induced loads. The key parameters of the adjusted model (SCSFS-1) are listed in Table 5.

Load application areas and acceleration measurement points are shown in Fig. 12. LP1 denotes the application point for jumping and stepping loads, while LR1 and VR1 represent the routes and central point for running and walking loads. The load excitation time histories were calculated using Equation (1), in which the individual weight Q was taken as 0.882kN and the excitation frequency f was set to 2.5 Hz.

4.3.1. Natural vibration characteristics

The natural vibration characteristics of the modified finite element model were analyzed, as summarized in Table 6. The first-order natural frequency of SCSFS-1 was 2.68 Hz, corresponding to a half-wave mode. The second-order natural frequency was 2.89 Hz, with two half-wave modes, while the third-order frequency was 4.45 Hz, featuring four half-wave modes.

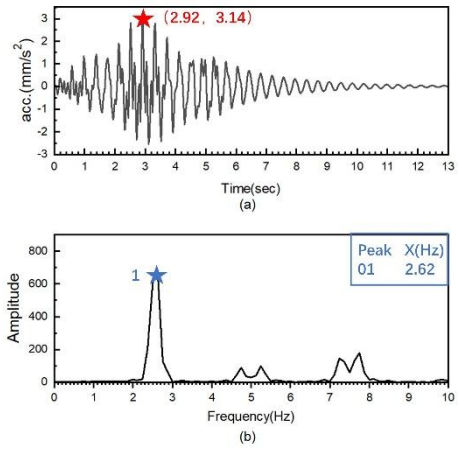

Fig. 14 Time histories and FFT results of SCSFS-1 under running load

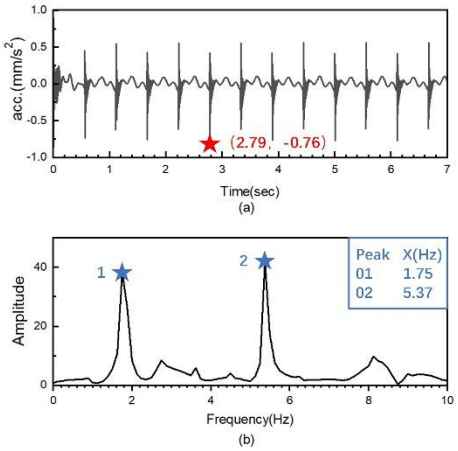

Fig. 15 Time histories and FFT results of SCSFS-1 under stepping load

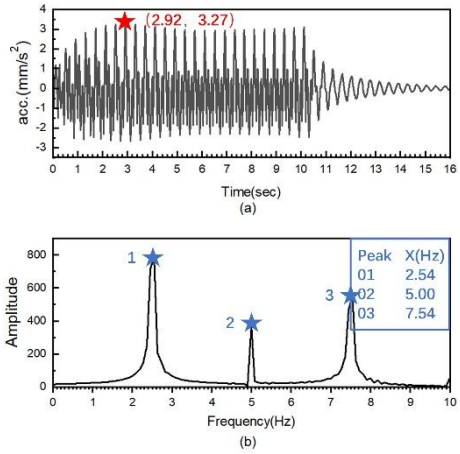

Fig. 16 Time histories and FFT results of SCSFS-1 under jumping load

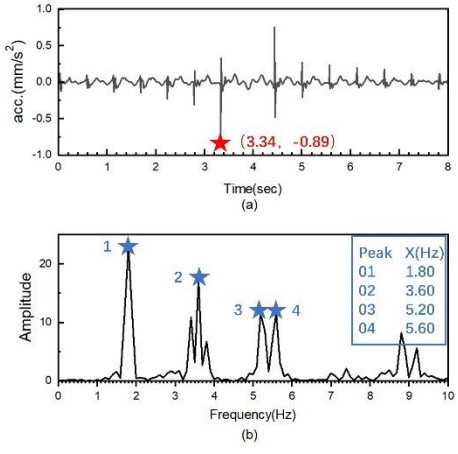

Fig. 17 Time histories and FFT results of SCSFS-1 under walking load

4.3.2. Human-induced vibration response

Under running loads (Fig. 14), the peak acceleration was 3.14 m/s², with dominant FFT components observed in the ranges of 2.2–3.0 Hz, 4.5–5.5 Hz, and 7–8 Hz. A peak occurred at 2.62 Hz, primarily exciting the first-order mode (2.68 Hz).

For stepping loads (Fig. 15), the peak acceleration was 0.76 m/s², with FFT components concentrated in the ranges of 1.0–2.2 Hz and 5.1–6.4 Hz. A peak was observed at 5.37 Hz.

Under jumping loads (Fig. 16), the peak acceleration reached 3.27 m/s², with FFT components in the ranges of 2–3 Hz, 4.8–5.2 Hz, and 7–8 Hz. A peak at 2.54 Hz primarily excited the first-order mode.

Finally, for walking loads (Fig. 17), the peak acceleration was 0.89 m/s², with FFT components appearing in the ranges of 1.6–2.0 Hz, 3.2–4.0 Hz, 4.8–6.0 Hz, and 8.2–9.8 Hz. A peak at 1.8 Hz was observed.

4.4. Parametric analysis

Key parameters of the floor system, including the arrangement of cable-

strut system, slab thickness, steel beam section type, beam height, cable cross-sectional area, strut cross-sectional area, boundary conditions, cable prestress, and sag of cable-strut system, were selected to investigate their influence on the human-induced vibration responses of the floor system. The model parameters are listed in Table 5. Given that the human-induced vibration responses of the floor system are most significant under jumping and running loads, these two load types were applied as excitations during the parametric analysis.

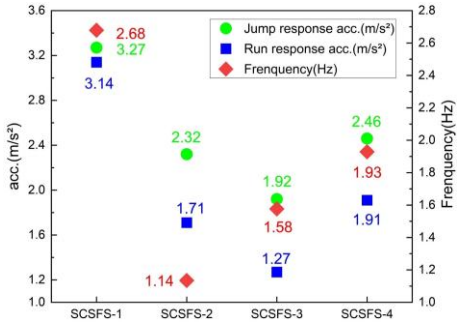

Fig. 18 Natural frequency and peak acceleration under different arrangements of cable-strut system

4.4.1. Arrangement of cable-strut system

Fig. 18 illustrates the effects of four different arrangements of cable-strut system configurations on the floor system's natural frequency and peak acceleration under jumping and running loads.

In terms of natural vibration characteristics, using the natural frequency of SCSFS-1 (2.68 Hz) as the baseline, the frequency changes for SCSFS-2, SCSFS-3, and SCSFS-4 were -57.5%, -41.0%, and -30.0%, respectively.

In terms of human-induced vibration response under running load, using the acceleration response of SCSFS-1 (3.14 m/s²) as the baseline, the changes in acceleration response for SCSFS-2, SCSFS-3, and SCSFS-4 were -45.5%, -59.6%, and -39.2%, respectively. Under jumping load, using the acceleration response of SCSFS-1 (3.27 m/s²) as the baseline, the changes in acceleration response for SCSFS-2, SCSFS-3, and SCSFS-4 were -29.1%, -41.3%, and -24.8%, respectively.

These data indicate that the inner-ring cables contribute significantly more to enhancing the floor system's stiffness than the outer-ring cables. Specifically, the outer-ring cables reduce the acceleration response, whereas the inner-ring cables lead to an increase in the acceleration response. This phenomenon stems from the fact that the structural vibration response is determined by the combined action of multiple factors, such as mass, stiffness, load type, and load frequency, rather than being solely dependent on stiffness. Meanwhile, the actual vibration of the floor system is dominated by the superposition of multiple modes rather than a single mode. When the inner-ring cables significantly increase the structural stiffness, elevating the structural frequency to a level close to or even consistent with the excitation frequency of human-induced loads, resonance effects may be triggered, thereby amplifying the human-induced vibration response of the structure.

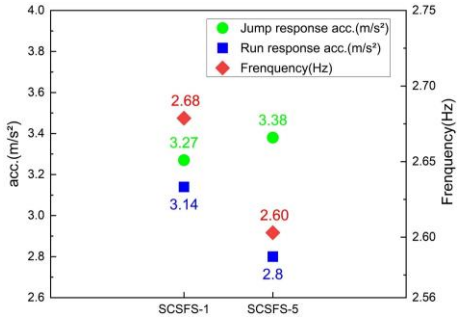

Fig. 19 Natural frequency and peak acceleration under different steel beam cross-section types

4.4.2. Steel beam section type

Fig. 19 illustrates the effects of the steel beam section type on the floor system's natural frequency and peak acceleration under jumping and running loads.

In terms of natural vibration characteristics, the natural frequency of SCSFS-1 was 2.68 Hz, which was approximately 2.9% higher than that of SCSFS-5 (2.60 Hz). This difference was primarily attributed to the increase in mass, which partially offset the enhancement in stiffness.

In terms of human-induced vibration response under running load, the acceleration response of SCSFS-1 was 3.14 m/s², which was significantly higher than that of SCSFS-5 (2.80 m/s²), with a difference of approximately 12.14%. Under jumping load, the acceleration response of SCSFS-1 was 3.27 m/s², which was lower than that of SCSFS-5 (3.38 m/s²), with a difference of approximately 3.36%.

These data indicate that the steel beam section type not only influences the natural frequency of the floor system but also affects the acceleration response, with distinct response trends observed under different load types.

4.4.3. Slab thickness

Fig. 20 demonstrates the effects of varying slab thickness on the floor system's natural frequency and peak acceleration under jumping and running loads.

In terms of natural vibration characteristics, using the natural frequency of SCSFS-1 (2.68 Hz) as the baseline, the frequency changes for SCSFS-6, SCSFS-7, SCSFS-8, SCSFS-9, and SCSFS-10 were -2.6%, -3.4%, -3.0%, -1.9%, and 0%, respectively.

In terms of human-induced vibration response under running load, using the acceleration response of SCSFS-1 (3.14 m/s²) as the baseline, the changes in acceleration response for SCSFS-6, SCSFS-7, SCSFS-8, SCSFS-9, and SCSFS-10 were -32.5%, -38.5%, -45.2%, -55.1%, and -64.6%, respectively. Under jumping load, using the acceleration response of SCSFS-1 (3.27 m/s²) as the baseline, the changes in acceleration response for SCSFS-6, SCSFS-7, SCSFS-8, SCSFS-9, and SCSFS-10 were -21.4%, -34.9%, -43.7%, -54.4%, and -63.6%, respectively.

These data indicate that an increase in slab thickness initially reduces the natural frequency of the floor system, followed by an increase, while the acceleration response gradually decreases.

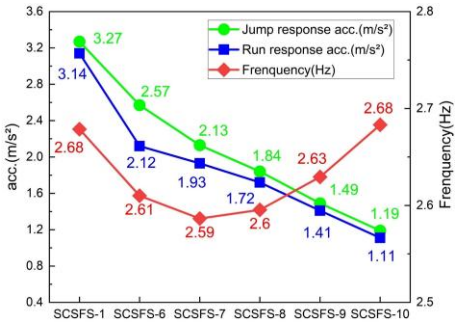

Fig. 20 Natural frequency and peak acceleration under different slab thicknesses

4.4.4. Beam height

Fig. 21 presents the effects of varying beam height on the floor system's natural frequency and peak acceleration under jumping and running loads.

In terms of natural vibration characteristics, when the beam height was increased from 100 mm (SCSFS-1) to 200 mm (SCSFS-14), the natural frequency was increased by 19%.

In terms of human-induced vibration response under running load, as the beam height was increased from 100 mm to 200 mm, the acceleration response of the floor system exhibited a significant decreasing trend, with a total reduction of 79%. Under jumping load, when the beam height was increased from 100 mm to 200 mm, the acceleration response of the floor system also demonstrated a gradual decreasing trend, with an overall reduction of 63%.

These data indicate that an increase in beam height leads to a gradual rise in the natural frequency of the floor system, while the acceleration response progressively decreases.

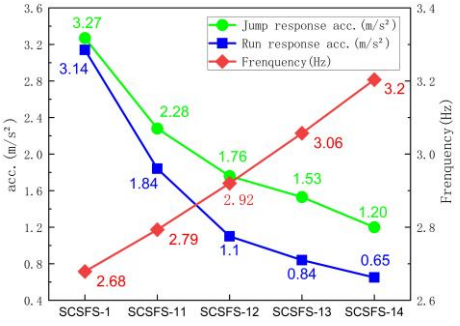

Fig. 21 Natural frequency and peak acceleration under different beam heights

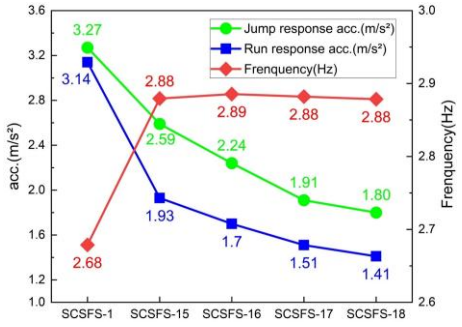

Fig. 22 Natural frequency and peak acceleration under different cable cross-sectional areas

4.4.5. Cable cross-sectional area

Fig. 22 illustrates the influence of varying cable cross-sectional areas on the natural frequency of the floor system and its peak acceleration under jumping and running loads.

In terms of natural vibration characteristics, when the cable cross-sectional area was increased from 314 mm² (SCSFS-1) to 392.5 mm² (SCSFS-15), the natural frequency was increased by approximately 7.5%, and the first-order vibration mode of the floor system transitioned from one half-wave to two half-waves. When the cable cross-sectional area was further increased from 392.5 mm² to 628 mm² (SCSFS-18), the natural frequency remained almost unchanged. This phenomenon was attributed to the fact that the first-order vibration mode of the floor system had already transitioned to two half-waves, at which point the change in cable cross-sectional area had a relatively minor influence.

In terms of human-induced vibration response under running load, as the cable cross-sectional area was increased from 314 mm² to 628 mm², the acceleration response exhibited a decreasing trend, with a total reduction of 55.1%. Under jumping load, when the cable cross-sectional area was increased from 314 mm² to 628 mm², the acceleration response gradually decreased, with a total reduction of 45.0%.

These data indicate that increasing the cable cross-sectional area can significantly reduce the acceleration response and enhance the natural frequency of the floor system, although it may lead to changes in the vibration mode shapes of the floor system.

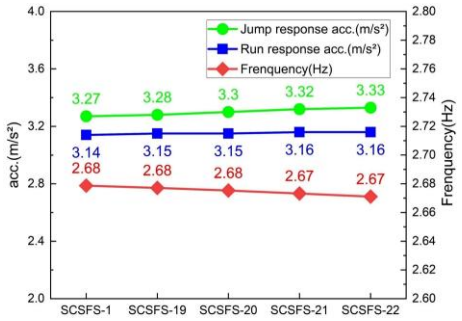

Fig. 23 Natural frequency and peak acceleration under different strut cross-sectional areas

4.4.6. Strut cross-sectional area

Fig. 23 depicts the impact of varying strut cross-sectional areas on the natural frequency of the floor system and its peak acceleration under jumping and running loads.

In terms of natural vibration characteristics, the increase in strut cross-sectional area had a limited influence on the natural frequency, with a variation not exceeding 0.02 Hz. In terms of human-induced vibration response, the variation in acceleration response did not exceed 0.06 m/s². These data indicate that changes in strut cross-sectional area have a minor influence on both the natural frequency and acceleration response of the floor system.

4.4.7. Floor system boundary condition

Fig. 24 illustrates the influence of different boundary conditions on the natural frequency of the floor system and its peak acceleration under jumping and running loads.

Under different constraint conditions, the variation range of the natural vibration frequency is extremely limited, not exceeding 0.02 Hz, and the variation is less than 1%. Under the action of running and jumping loads, the variation range of the acceleration response of each model is also small, with a variation of less than 1%. These data indicate that the boundary conditions of the floor have a relatively small impact on the natural vibration frequency and acceleration response of the floor.

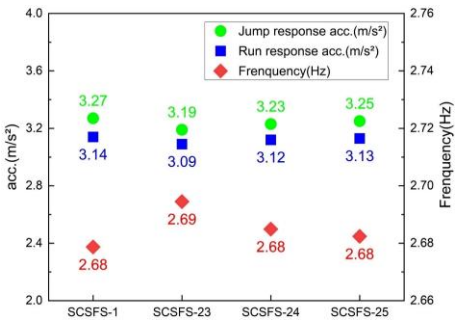

Fig. 24 Natural frequency and peak acceleration under different floor system boundary conditions

4.4.8. Cable prestress

Fig. 25 illustrates the effect of varying cable prestress on the natural frequency and peak acceleration of the floor system under jumping and running loads.

The research results show that under the prestress conditions of 5kN, 10kN, 15kN, and 20kN, the natural frequency of the floor system remains unchanged, and the peak acceleration remains basically consistent. This is attributed to the fact that the boundary conditions of the floor system fully release the horizontal constraints, causing the prestress of the cables to be entirely borne and compressed by the upper rigid structure. A self-balancing state is formed between the "improvement of geometric stiffness" by the cables and the "reduction of geometric stiffness due to compression" of the upper structure. The influences of the two on the geometric stiffness offset each other, so the prestress has no significant impact on the overall dynamic response.

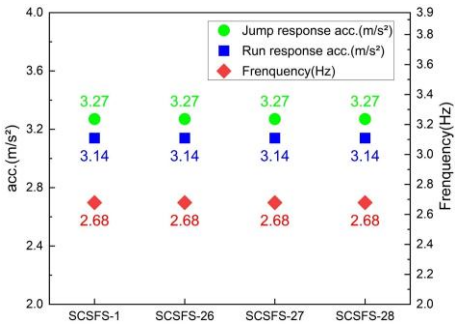

Fig. 25 Natural frequency and peak acceleration under different cable prestress levels

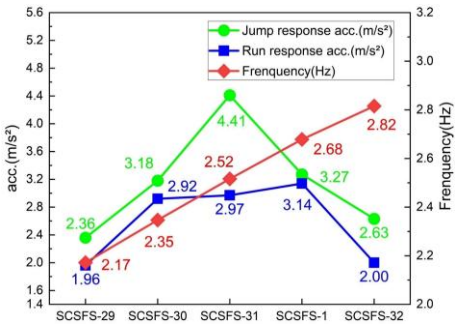

Fig. 26 Natural frequency and peak acceleration under different sags

4.4.9. Sag of cable-strut system

Fig. 26 illustrates the influence of different sags (where sag refers to the vertical distance along the vertical direction between the two ends of the cable) on the natural frequency of the floor system and its peak acceleration under jumping and running loads.

In terms of natural vibration characteristics, when the sag was increased from 906 mm (SCSFS-29) to 1422 mm (SCSFS-32), the natural frequency was increased by approximately 30%.

In terms of human-induced vibration response under running load, using the acceleration response of SCSFS-29 (1.96 m/s²) as the baseline, the changes in acceleration response for SCSFS-30, SCSFS-31, SCSFS-1, and SCSFS-32

were 49.0%, 51.5%, 60.2%, and 2.0%, respectively. Under jumping load, using the acceleration response of SCSFS-29 (2.36 m/s²) as the baseline, the changes in acceleration response for SCSFS-30, SCSFS-31, SCSFS-1, and SCSFS-32 were 34.7%, 86.9%, 38.6%, and 11.4%, respectively.

These data indicate that as the sag increases, the natural frequency of the floor system gradually rises, while the acceleration response exhibits a trend of initial increase followed by a decrease.

4.5. Vibration control schemes based on comfort limit requirements

Fig. 27 presents the models that meet the comfort limit requirements. By adjusting the sag, slab thickness, and beam height, the peak acceleration of the floor system has been reduced. The same excitation method as used in the parameter influence analysis in Section 4.4 was adopted herein.

In accordance with the Technical Standard for Vibration Comfort of Building Floor Structure [27], SCSFS-33, SCSFS-34, and SCSFS-35 satisfy the limit requirements for such spaces as dance halls, performance stages, spectator stands, indoor sports venues, and gyms dedicated to aerobic exercises. Specifically, during normal use, the first-order vertical natural frequency of the floor system should not be less than 4 Hz, and the effective maximum vertical vibration acceleration should not exceed 0.5 m/s².

SCSFS-35 meets the requirements for spaces including shopping malls, restaurants, public transportation waiting halls, theaters, cinemas, auditoriums, and exhibition halls. For these venues, the first-order vertical natural frequency of the floor system should not be less than 3 Hz, and the peak vertical vibration acceleration should not exceed 0.15 m/s².

4.6. Comparative analysis of natural vibration characteristics of typical floor systems

To clarify the differences among the spatial cable-supported floor system (SCSFS-1), steel-concrete composite floor system (SCSFS-2), and steel truss composite floor system, a comparative group was established through numerical simulation. Specifically, based on SCSFS-1, two comparative models were constructed: one is SCSFS-2 with cables and struts removed, and the other is a steel truss composite floor system where cables and struts are replaced by steel trusses with the same material consumption maintained. The relevant comparison results are presented in Table 7.

The natural vibration frequency of the SCSFS-1 system is 2.68 Hz. Although it is lower than 3.29 Hz of the steel truss composite floor system, it is significantly higher than 1.14 Hz of the steel-concrete composite floor system (SCSFS-2). This indicates that the presence of cables can enhance the floor stiffness, optimize the vibration characteristics of the floor to a certain extent, and reduce the risk of comfort problems caused by human-induced vibration.

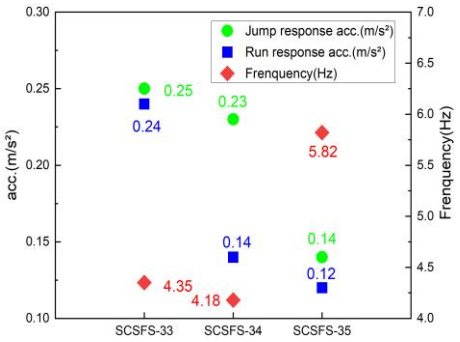

Fig. 27 Vibration response indices of SCSFS models meeting comfort requirements for different venues

Table 7
Numerical simulation comparison of natural vibration characteristics of three typical floor systems

Name	SCSFS - 1	Steel - Concrete Composite Floor (SCSFS - 2)	Steel Truss Composite Floor
First - order Natural Vibration Frequency (Hz)	2.68	1.14	3.29
Mode Shape	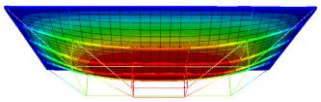	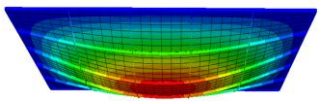	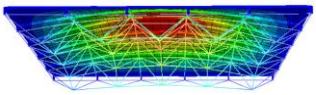

Note: The steel-concrete composite floor (SCSFS-2) is developed from SCSFS-1 by removing the cables and struts; the steel truss composite floor is developed from SCSFS-1 by replacing the cables and struts with steel trusses, ensuring that the material consumption of SCSFS-1 is consistent with that of the steel truss composite floor.

5. Conclusions

This study systematically investigated the dynamic response of the spatial cable-supported floor system under various human-induced loads through on-site experiments and numerical simulations, with a focus on the natural vibration characteristics, human-induced vibration responses, and the impact of key structural parameters on vibration behavior. The experimental loading included free vibration tests and multiple human-induced vibration tests, covering four common excitation types: stepping, jumping, walking, and running. The main findings are as follows:

1) The test floor exhibited a first-order natural frequency of 17.58 Hz and a damping ratio of 0.028. Significant vibration issues were observed under human-induced loads, with jumping loads having the most pronounced effect on acceleration response, resulting in a maximum peak response of 5.852 m/s². In contrast, walking loads produced minimal effects on acceleration response.
2) The cross-sectional type of steel beams influenced not only the natural frequency of the floor system but also its acceleration response. Different load types resulted in varying response trends. Increasing the slab thickness initially reduced the natural frequency of the floor system but subsequently led to an increase, while acceleration responses progressively decreased. Conversely, increasing the beam height consistently elevated the natural frequency and concurrently reduced the acceleration response.
3) The cable-strut system significantly improved the natural frequency of the floor system. The inner-ring cables contributed more to stiffness enhancement than the outer-ring cables. Both inner- and outer-ring cables affected the acceleration response of the floor system: outer-ring cables reduced acceleration responses, whereas inner-ring cables increased them. Increasing the cable cross-sectional area markedly reduced acceleration responses and improved the natural frequency of the floor system, although it could alter the vibration mode shapes. The presence or absence of cable prestress had no observable effect on the natural frequency or acceleration responses of the floor system.
4) The cross-sectional area of struts and the boundary conditions of the floor system had minimal influence on the natural frequency and acceleration responses. With increasing sag, the natural frequency of the floor system gradually increased, while acceleration responses exhibited a trend of initial increase followed by a decrease.
5) It is possible to reduce the vibration response of the floor and increase its natural vibration frequency by optimizing the key structural parameters of the floor (multi - parameter coordination), so that all indicators meet the comfort limit requirements of the Technical Standard for Vibration Comfort of Building Floor Structures [27], providing a quantifiable engineering solution for floor vibration control.

Acknowledgements

The project received financial support from the Shandong Provincial Natural Science Foundation, China (Grant No. ZR2020QE243).

References

[1] Bazli M, Heitzmann M, Ashrafi H, "Long-span timber flooring systems: A systematic review

from structural performance and design considerations to constructability and sustainability aspects", Journal of Building Engineering, 48, 103981, 2022.
[2] Zhang X, Li Q, Wang Y, et al., "Numerical and Experimental Study on the Dynamic Behavior of an Innovative Steel-Concrete Composite Hollow Waffle Floor", International Journal of Structural Stability & Dynamics, 20(8), 0, 2020.
[3] Choe L, et al., "Behavior and Limit States of Long-Span Composite Floor Beams with Simple Shear Connections Subject to Compartment Fires: Experimental Evaluation", Journal of Structural Engineering, 146(6), 1 – 14, 2020.
[4] Tan M, Wu Y, Pan W, et al., "Optimal Design of a Novel Large-Span Cable-Supported Steel – Concrete Composite Floor System", Buildings, 14(1), 113, 2024.
[5] Zhou L, Huang Y, Chen B, et al., "Seismic Behavior of Large-Span Open-Web Floors Consisting of I-Shaped Steel Chords and Steel Tube Webs", Advances in Civil Engineering, 2020, 1 – 14, 2020.
[6] Cao L, Li J, Zheng X, Chen Y F, "Vibration behavior of large span composite steel bar truss-reinforced concrete floor due to human activity", Steel and Composite Structures, An International Journal, 37(4), 391 – 404, 2020.
[7] Yang S, Wang G, Xu Q, He J, Yang M, Su C, "Dynamic Response Study of Space Large-Span Structure under Stochastic Crowd-Loading Excitation", Buildings, 14(5), 1203, 2024.
[8] Wu Y, Pan W, Luo Y, "Economical Design Comparison of Large-Span Composite Floor Systems with I Beams and Corrugated Web Beams", Buildings, 13(1940), 1940, 2023.
[9] Tsavdaridis K D, McKinley B, Kacaroglu B N, Corfar D-A, Lawson R M, "Bending test of long-span ultra-shallow floor beam (USFB) with two lightweight concretes", Structures, 66, 106895, 2024.
[10] Zhou X H, et al., "Experimental and analytical studies on the vibration serviceability of pre-stressed cable RC truss floor systems", Journal of Sound and Vibration, 361, 130 – 147, 2016.
[11] Han T, Liang S, Zhu X, et al., "Experimental study on the flexural behavior of large-span prestressed and steel-reinforced concrete slabs", Engineering Structures, 337, 120533, 2025.
[12] Huang L, Jie H, Zeng B, Zhou Z, Li L, "Experimental and numerical investigation on the mechanism of large-span floor system characterized by biaxially prestressed steel reinforced concrete beams", Structures, 69, 107443, 2024.
[13] Yang X, Wang, et al., "Experimental Study and Numerical Simulation on Mechanical Properties of the Bottom Plate in the Assembled Composite Slab with Additional Steel Trusses", Advances in Civil Engineering, 1 – 8, 2021.
[14] Liu J P, et al., "Vibration performance of composite steel-bar truss slab with steel girder", Steel and Composite Structures, 30(6), 577 – 589, 2019.
[15] Cao L, et al., "Experimental studies on vibration serviceability of composite steel-bar truss slab with steel girder under human activities", STEEL AND COMPOSITE STRUCTURES, 40(5), 663 – 678, 2021.
[16] Hu L, Ma, et al., "Research and application of U-shaped steel plate-concrete composite open-web sandwich slab structure with high strength bolts", Journal of Building Structures, 33(7), 61 – 69, 2012. (in Chinese)
[17] Luan H Q, et al., "Investigation on structural behavior of an innovative orthogonal-diagonal steel open-web sandwich floor system", Advances in Structural Engineering, 19(2), 353 – 371, 2016.
[18] Zhou X H, et al., "Experimental and analytical studies on the vibration serviceability of pre-stressed cable RC truss floor systems", Journal of Sound and Vibration, 361, 130 – 147, 2016.
[19] Qiao W T, et al., "EXPERIMENTAL STUDY ON THE FUNDAMENTAL MECHANICAL FEATURES OF CABLE-SUPPORTED RIBBED BEAM COMPOSITE SLAB STRUCTURE", Advanced Steel Construction: An International Journal, 13(2), 96 – 116, 2017.
[20] Qiao W T, et al., "Mechanical features of cable-supported ribbed beam composite slab structure", STEEL AND COMPOSITE STRUCTURES, 25(5), 523 – 534, 2017.
[21] Li M, Zhang J, Song B, et al., "Experimental and numerical investigation on flexural performance of non-prestressed concrete precast bottom slab with a removable section steel and three ribs", Structures, 79, 109441, 2025.
[22] An Q., Wang Y., "Spatial cable-supported floor system: ZL 201910759335.4" [Patent], 2019. (in Chinese)
[23] Ivanovic S, Pavic A, Reynolds P, "Vibration serviceability of footbridges under human-induced excitation: A literature review", Journal of Sound and Vibration, 279(1 – 2), 1 – 74, 2005.
[24] Belykh I, Bocian M, Champneys A R, et al., "Emergence of the London Millennium Bridge instability without synchronization", Nature Communications, 12, 2021.
[25] Lee S H, Lee K K, Woo S S, et al., "Global vertical mode vibrations due to human group rhythmic movement in a 39-story building structure", Engineering Structures, 57, 296 – 305, 2013.
[26] International Organization for Standardization, "ISO 10137: 2007. Bases for design of structures—serviceability of buildings and walkways against vibration", Geneva, Switzerland, 2007.
[27] Technical standard for vibration comfort of building floor structure: JGJ/T 441-2019, China Architecture and Construction Press, 2020. (in Chinese)
[28] Cao L, Liu, et al., "Experimental and analytical studies on the vibration serviceability of long-span prestressed concrete floor", Earthquake Engineering and Engineering Vibration, 17(2), 417–28, 2018.
[29] Liang H, Xie, et al., "Identification of Dynamic Parameters of Pedestrian Walking Model Based on a Coupled Pedestrian-Structure System", APPLIED SCIENCES-BASEL, 11(14), 6407, 2021.
[30] Fahmy Y G M, Sidky A N M, "An experimental investigation of composite floor vibration due to human activities. A case study", HBRC Journal, 8(3), 228–238, 2012.
[31] Zhang X, Wang, et al., "Experimental and Analytical Study on the Vibration Performance of U-Shaped Steel-Concrete Composite Hollow Waffle Slab", Shock & Vibration, 2020(1), 1–15, 2020.
[32] Brownjohn J M W, Pan T C, et al., "Floor Vibration Serviceability in a Multistory Factory Building", Journal of Performance of Constructed Facilities, 30(1), 1–14, 2016.
[33] Liu J P, Huang S, Li J, et al., "Vibration Serviceability of Large-span Steel–Concrete Composite Beam with Precast Hollow Core Slabs Under Walking Impact", Engineering, 19, 93–104, 2021.

Advanced Steel Construction – Vol. 21 No. 6 (2025) 542–550
DOI:10.18057/IJASC.2025.21.6.7

EVALUATION OF MECHANICAL PROPERTIES OF NEW MODULAR STEEL CHANNEL TRUSS BEAMS UNDER ECCENTRIC LOADING

Shao-Chun Ma [1, 2, 3, *], Yi-Ming Liu [1, 3], Li Zhang [4] and Yun-Chi Xia [4]

[1] *School of Civil Engineering and Architecture / Kaifeng Research Center for Engineering Repair and Material Recycle, Henan University, Henan Kaifeng 475004, China*
[2] *Yellow River Laboratory (Henan), Henan Zhengzhou 450000, China*
[3] *Henan Province Research Center for Intelligence Conservation and Restoration of Historical Buildings, Henan Kaifeng 475004, China*
[4] *China Construction Seventh Engineering Bureau Co, Ltd, Henan Zhengzhou 450016, China*
** (Corresponding author: E-mail: scma@vip.henu.edu.cn)*

ABSTRACT

In order to address the challenges presented by the large size of conventional truss beams and the difficulties in hoisting, transportation, and installation. This paper proposes a new type of modular steel channel truss beams, which are formed by splicing the truss beam splices with high-strength bolts. This study conducted standard-load and overload destructive tests on six full-scale specimens under eccentric loads. It focused on the mechanical properties and damage characteristics of modular beams, along with evaluating the effectiveness of high-strength bolt splicing nodes. The results showed that the new type of modular steel channel truss beams possess excellent bending resistance and toughness. At the point where the ultimate bearing capacity is reached, the compression diagonal web buckles, causing damage to the modular beam. However, the high-strength bolt connection nodes remain intact. It shows that the overall toughness of the modular beam is significantly improved by the ability of the tensile action of connection nodes to absorb more deformation forces. The numerical model is established by simulation software and validated by comparing the calculations to the test results. The results are in close agreement, verifying the reliability of the finite element model. Additionally, the flexural performance of the modular beam is significantly influenced by the thickness of the compressed diagonal web. The flexural capacity of the composite beam depends on the critical load at which buckling damage occurs in the compressed diagonal web. Through numerical simulation, parameter optimization for the modular beam was conducted, and the optimal thickness of the compressed diagonal web was obtained. The calculation formula for the bending capacity applicable to the new modular beam is determined using the effective width method. This formula serves as the foundation for the theoretical design and practical engineering application of modular beams.

ARTICLE HISTORY

Received: 24 April 2024
Revised: 31 March 2025
Accepted: 6 May 2025

KEYWORDS

Channel steel modular beam;
Mechanical property;
Load-displacement curve;
High-strength bolt;
Numerical simulation

1. Introduction

Prefabricated construction is a product of the industrialization of the construction industry, which can achieve the goals of low energy consumption, short construction periods, high efficiency, and less pollution [1]. Compared to concrete structures, steel structures are lighter in weight, have lower foundation costs, and are more economical [2]. Steel is a ductile, versatile, and recyclable material [3]. Therefore, steel structures have significant development advantages and promising application prospects. It is of great significance for the healthy development of prefabricated buildings.

The integrated floor covering consists of compressed steel plate-concrete composite floor slab and channel steel truss beams. This design offers several advantages, including a reasonable force transmission path, high space utilization, and convenient pipeline arrangement [4-5]. As an important component of integrated building systems, truss beams have been extensively studied by scholars. Liu et al. [6] proposed a new type of double-layer steel-concrete combined wall with steel trusses as stiffening ribs. The steel truss enhances the steel plate's resistance to local buckling. Davis et al. [7] conducted an experimental study on an asymmetric I-beam floor structure using a full-scale model. The structure can withstand five times the live load under normal use. Hazal et al. [8] conducted full-scale tests and numerical simulations on steel-concrete composite trusses. They found that filling the compression chord members with concrete can effectively prevent local buckling. Leal et al. [9] proposed a steel-concrete composite floor slab system that consists of thin-walled steel trusses. The system can resist local buckling due to the collaboration of three different types of shear connectors, which provide sufficient stiffness and bending strength. Chen et al. [10] conducted a bending capacity test on five concrete floor slab specimens with lightweight steel truss beams. They found that the bending capacity of the floor slab was linearly related to the area of steel in tension and the height of the section. Jia et al. [11] evaluated the performance of truss beams and determined that the damage was primarily caused by the yielding of chord rods and the buckling of diagonal web rods. No significant damage was observed in the upper and lower columns and nodes. However, current research on truss beams primarily focuses on alterations in their mechanical properties when exposed to symmetrical loading. Modern engineering demonstrates that truss beams are influenced by various factors and complex forces. In their study of cold-formed steel roof frames, Doaa et al. [12] found that the loading method significantly impacts the bearing capacity, stiffness, and energy absorption capacity of the specimens. When two loading points are used instead of one, the energy dissipation capacity increases by 28%. Abdallah E et al. [13] found that the internal bending capacity of the face is significantly affected by the eccentric load in the numerical analysis of beam-CHS column-strut plate connection nodes. Cao et al. [14] simulation analysis of rectangular stainless steel tube concrete columns to investigate the impact of length-to-width ratio and relative eccentricity on the distribution of longitudinal stresses in the cross-section. The formula for calculating the compressive load capacity under eccentric load is provided. In conclusion, prolonged eccentric loading on truss beams can lead to a complicated stress scenario that could negatively impact the structure, posing a safety hazard [15-16]. Therefore, it is necessary to evaluate the performance of trusses under asymmetric loads to serve practical engineering.

Effective node connections are crucial for prefabricated concrete structures. Bolted connection nodes are widely used in practical engineering due to their convenience of construction and superior performance [17-18]. Elsabbagh et al. [19] conducted a parametric study of bolted semi-rigid nodes using the finite element method (FEM) and concluded that the shear values in the upper part of the connection significantly influence the mechanical properties of bolted connection nodes. Wang et al. [20] proposed a new type of bolted end plate connection (BEPC) for precast concrete column-column nodes. Low-cycle repeated loading tests demonstrated its excellent seismic performance, with minimal impact from the node position. Li et al. [21] proposed a formula for calculating the yield moment. They conducted low-cycle repeated loading tests on four foot-size specimens of bolted flange spliced nodes with varying flange thicknesses and different stiffening rib configurations. Fan et al. [22] conducted an experimental investigation into the performance and damage mechanism of a new type of self-tightening one-sided bolted node (STOSB). The seismic performance of this node is greatly affected by the end plate stiffness and column flange thickness. Liu et al. [23] conducted straight shear tests on bolted nodes to investigate the mechanical behavior and damage modes of bolted connections. The studies indicate that bolted connections can effectively reduce the deflection of truss beams and improve the overall comfort of the building's vibration [24]. It is recommended that bolted connections be used as much as possible in practical projects.

Currently, the truss beams used in real construction projects are typically monolithic. However, the substantial dimensions and weight of prefabricated components pose significant challenges to the standardization of production, transportation, and installation, as depicted in Fig. 1. The irrational design of truss beams, the occurrence of varying degrees of damage during transportation,

and the non-standardized installation of these components are prone to safety hazards to the engineering structure, and may even result in casualties or property losses, as illustrated in Fig.2. To address the aforementioned problems, this paper proposes a new type of modular steel channel truss beam spliced together with high-strength bolts. The force performance and damage mechanism were investigated through standard-load and overload destructive tests under eccentric loads. And analyzed the bending capacity through the finite element analysis tool for the extension study. The main factors that control the bending capacity were identified through theoretical analysis based on the principle of equal critical force.

Fig. 1 Hoisting of large-span steel truss

Fig. 2 Steel truss instability failure

2. Experimental design

2.1. Specimen design

The modular steel channel truss beam is a new type of beam commonly used in high-rise assembled monolithic floor cover structure systems, as shown in Fig. 3. It is the key component of the main structural floor plate force. To study its mechanical properties under standard-load and overload destructive tests, six full-scale specimens were designed and fabricated for two distinct groups, labeled E_i and F_i. Where: E represents standard-load test, F represents overload destructive test, and i = 1, 2, 3.

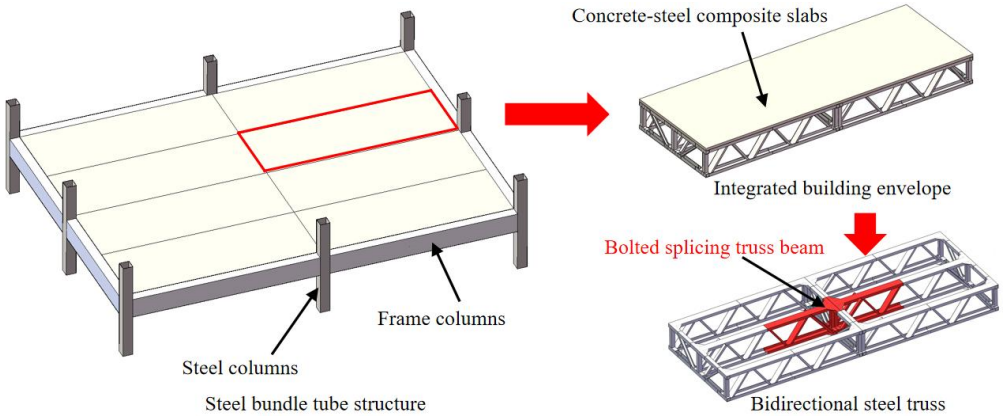

Fig. 3 Three-dimensional schematic diagram of new modular steel channel truss beam structure system

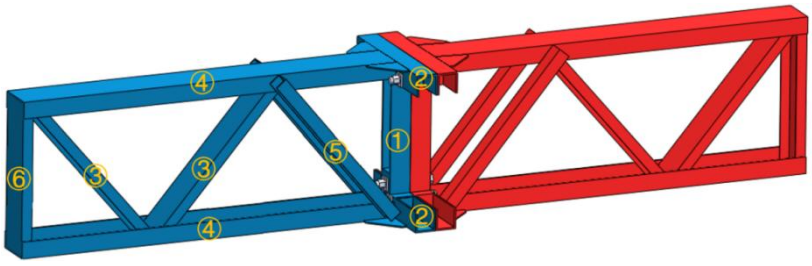

(a) Overall model

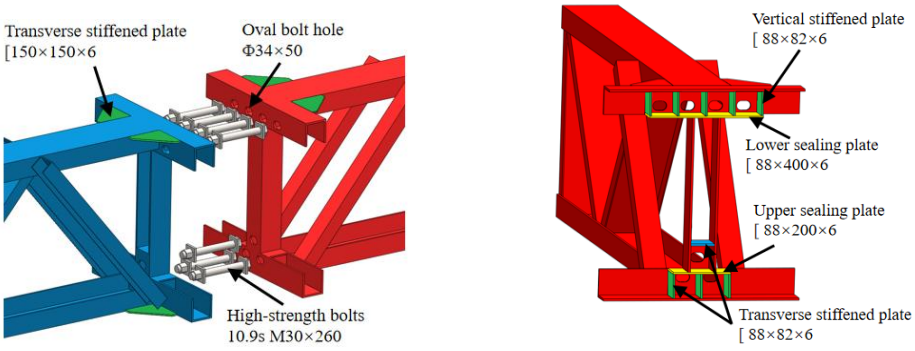

(b) Bolt splice node (c) Internal structure

Fig. 4 Three-dimensional schematic diagram of new modular steel channel truss beams

Referring to the design regulations of steel frame beams, supporting member regulations, and node structure requirements in GB50018-2002 Technical Code for Cold-Formed Thin-Walled Steel Structures [25] and Steel Structure Residential Main Component Dimension Guidelines 2020 [26], the

structure of the new modular steel channel truss beam is shown in Fig. 4, which consists of two identical main truss splices and seven sets of high-strength bolts. The members are constructed using Q345B channel steel. The top and lower chords of the main truss splice ① have a cross-section size of 200mm×80mm×8mm. The upper and lower chords of the secondary truss ②, which is perpendicular to the assembled main truss, have a cross-section size of 100mm×100mm×8mm. The end web ③ has a cross-section size of 150mm×50mm×4mm, while the vertical web ④ has a cross-section size of 100mm×100mm×8mm at the splicing location. The inner diagonal web ⑤ has a cross-section size of 180mm×50mm×4mm, while the outer diagonal web ⑥ has a cross-section size of 80mm×60mm×4mm. The bolt holes are reinforced with a 6mm thick lower sealing plate and a vertical reinforcement plate. Additionally, a 150mm×150mm×6mm horizontal reinforcement plate is installed at the intersection of the main truss and the secondary truss. High-strength, grade 10.9 friction-type bolts are utilized. Each group of high-strength bolts consists of a bolt rod, a nut, and two washers. The bolt rod has a diameter of 30 mm and a length of 260 mm.

In order to measure the displacement change of the specimen and the strain of the main rods during the loading process, it is essential to install the displacement meter, dial indicator, and strain gauges as shown in Fig 5.

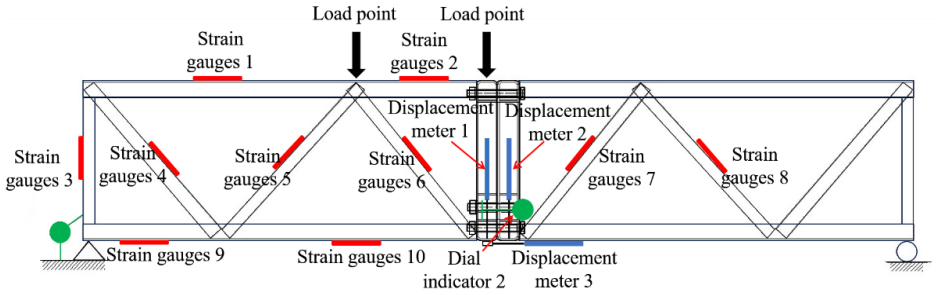

Fig. 5 Positions of measurement points

2.2. Loading set-up

The beam specimen underwent vertical loading using an electro-hydraulic servo-hydraulic loading system. To ensure a reasonable distribution and transfer of the load, the three-point centralized loading method was adopted. Eccentric loading was applied using loading blocks, with the eccentric loading points located at the splicing nodes of the modular steel channel truss beam and the intersection of the chords on one side. The hinged connection is formed between the two ends beam and the bearing. An anti-tipping device [27] is vertically arranged on the modular steel channel truss beam to restrict its out-of-plane deflection and prevent eccentric tipping during loading. The field-loading device is depicted in Fig. 6.

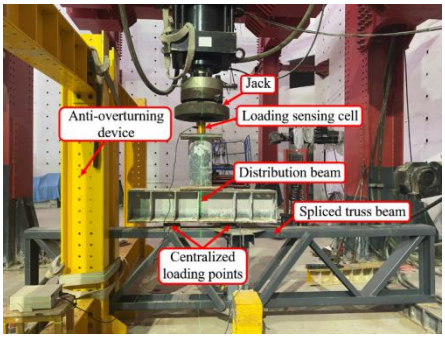

Fig. 6 Field loading device

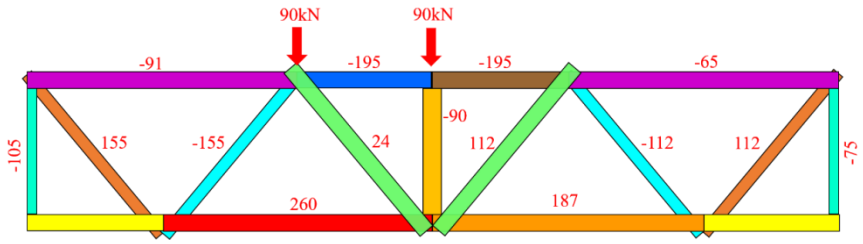

Fig. 7 Axial force diagram of the truss beam

2.2.1. Determine the bearing capacity for serviceability limit state

Before conducting the standard load test, it is necessary to determine the design value of the test loading by theoretically calculating the bearing capacity. To facilitate this calculation, the elastic deformation and constraint effect between adjacent bars are ignored. The node of the modular steel channel truss beam is regarded as a smoothly articulated node, and the axial force for each rod is calculated based on principles of structural mechanics. The calculation sketch is shown in Fig. 7. According to the specifications, the maximum tensile force of the lower suspension bar under standard combined load is 260 kN. In this load, the total value of the eccentric load corresponding to the upper part of the specimen is 180 kN, which is the maximum load limit for the standard load test.

2.2.2. Loading test

Pre-loading test: The pre-loading test is conducted on the specimen of the modular steel channel truss beam to eliminate any assembly gaps and verify the functionality of the testing equipment. The preloading load is controlled at 30% of the design load [28].

Standard load test: Each level of load increment is 10 kN, with a loading interval of 10 minutes. The load is incrementally increased to the standard load of 180 kN before being halted. 1 hour after unloading 20 kN at each level, the interval remains 10 minutes until completely unloaded.

Overload destructive test: The loading method and requirements are the same as the standard test. In the later stage, the load increment is 5 kN for each level, and the time interval remains unchanged. When the following conditions are met, the limit state of load-carrying capacity is considered to be reached, and loading is stopped: (1) specimen bars are bent or destabilized; (2) the maximum deflection reaches 1/50 of the support span [29].

3. Test results and analysis

3.1. Analysis of experimental phenomena

3.1.1. Standard load test phenomena

During the standard load test, the three specimens exhibited similar test phenomena. As the load increased during the early stage of loading, both the vertical displacement in the span and the tension displacement under the beam continued to increase. However, the vertical displacement in the span increased at a much faster rate than the tension displacement under the beam. When loaded to 180 kN, the vertical displacement in the span and the tension displacement under the beam reached their maximum values. The test results indicate that no relative slip occurred at each connection node, no tensile deformation occurred at bolted joints, and the specimen remained undamaged and in good condition. Under the action of eccentric load, the specimen can effectively and function normally within the design load range, meeting the specified requirements. During the unloading stage, the structural deformation gradually recovered as the load decreased. After complete unloading, the residual deformation was negligible. The results of the test are presented in Fig. 8.

(a) Pre-test (b) Load to 180kN (c) After unloading

Fig. 8 Standard load test

3.1.2. Overload destructive test phenomenon

Before loading to 180 kN, the test phenomena were not significant for each specimen. When the vertical load exceeded the design value, the beam still demonstrated stable flexural performance. As the load continued to increase, the displacement of the specimen gradually increased, indicating that it was in the elastic deformation state. At the load close to the ultimate bearing capacity of 327.9 kN, the beam experienced a sudden large deformation, accompanied by a loud ringing sound, destroying the member and the cessation of loading. The damage to the specimen is shown in Fig. 9. The test results indicate that yield deformation occurred first in the diagonal web on the eccentrically loaded side. The top channel steel of the vertical web bar bulged outward, and the upper chord bar buckled upward on both sides. Additionally, a downward bending phenomenon occurred in the middle of the span, resulting in obvious deflection deformation. The deformation characteristics of the rods were similar when the three specimens were damaged, as shown in Fig. 9(b)-(d). The main damaged parts are the compressed diagonal web bar on the eccentric loading side and the vertical web bar at the beam end. The stresses on both sides of the beam are uneven under the action of eccentric loading, indicating that different loading methods have a significant impact on the operational performance of the beams. Different loading methods of eccentric load have a great influence on the working performance of the beam. It is important to note that this analysis is based solely on objective evaluations and technical terminology. The deformation of the vertical web at the beam end occurred at the flange, while the web did not show obvious deformation. The primary reason is that the weak zone of the channel steel is located near the stress point in the opening, making it susceptible to bending and damage when compressed.

(a) Overall damage diagram for modular beams

(b) F1 localized damage diagram (c) F2 localized damage diagram (d) F3 localized damage diagram

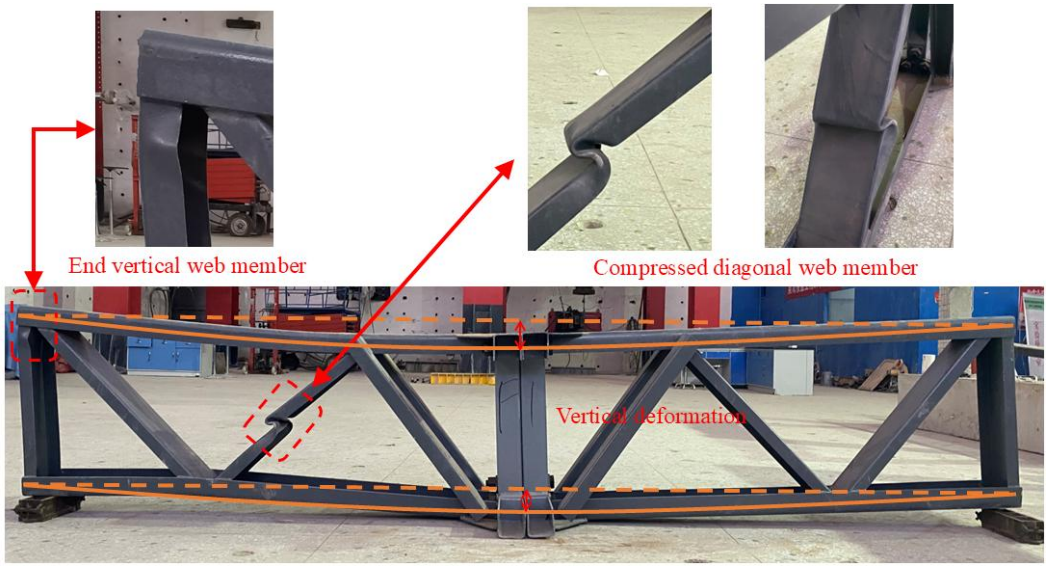

(e) Deformation and local failure of F1 specimen

Fig. 9 Damage diagram of modular steel channel truss beams

3.1.3. Failure analysis of high-strength bolts

After unloading the test, the specimen was removed to observe the residual damage of the high-strength bolts under eccentric loading. Fig. 10(a) shows the splicing surface of the modular steel channel truss beam, with the bolt holes remaining intact. The contact part of the spliced surface did not show any significant damage, indicating that the high-strength bolts effectively fastened the connection and prevented relative slip on the spliced surface. Fig. 10(b) shows the disassembled high-strength bolts. The bending deformation of the bolt rods is not significant, indicating good resistance to bending and safety margins. The high-strength bolt connection is reliable and effective in the event of modular steel channel truss beam destruction, making it suitable for practical engineering projects.

(a) Modular beam splice surface (b) High-strength bolts

Fig. 10 Damage diagram of splicing surface

Table 1
Main test parameters

Standard load test								Overload destructive test						
No	P_y kN	δ_y mm	Δ_y mm	δ_r mm	Δ_r	δ_r/δ_y	Δ_r/Δ_y	No	P_u kN	δ_u mm	Δ_u mm	P_u/P_y	μ_y	Δ_u/δ_u
E_1	180.0	8.69	1.94	1.53	0.43	0.18	0.22	F_1	327.6	48.34	5.71	1.80	5.56	0.12
E_2	180.2	9.31	2.07	1.49	0.43	0.16	0.21	F_2	326.5	50.07	5.89	1.79	5.38	0.11
E_3	179.8	8.40	1.76	1.55	0.39	0.18	0.22	F_3	329.7	49.65	6.34	1.82	5.91	0.12
$\bar{E}$	180.0	8.80	1.92	1.52	0.42	0.17	0.21	$\bar{F}$	327.9	49.35	5.98	1.81	5.61	0.11

3.2. Load-bearing capacity analysis

The main test parameters obtained from the standard load test and the overload destructive test are shown in Table 1. P_y and P_u are the vertical loads for the serviceability limit state and the overload ultimate limit state, respectively. δ_y and δ_u are the mid-span deflections of the modular beams in these two limit states. Δ_y and Δ_u are the tensile sizes of the modular beam joints in these two limit states. δ_r and Δ_r are the mid-span deflections of the modular beams after complete unloading and the magnitude of tensors at the joints; μ_y is the modular beam ductility coefficient.

Table 1 shows that the vertical deflection of t the modular steel channel truss beam at the rod connection under the standard load is minimal, with an average value of 8.80 mm. According to Appendix A.1.1 of Code for Design of Steel Structures, the allowable deflection of bending truss members is $l/400$. The length of the combined beam is 3900 mm. The maximum allowable deflection can be calculated as 9.75 mm, and the vertical deflection of the combined beam meets the code requirements. The specimen joints do not show any apparent deformation, and the average tensile size is 1.92 mm. After complete unloading, the tensile sizes were reduced to 1.52mm, with a recovery rate of 83%. The beam's tension size is 0.42 mm, with a recovery rate of 79%. Within the normal load range, the deformation of the channel steel truss module beam specimen is relatively small, indicating good toughness.

In the overload destructive test, the modular steel channel truss beam exhibited a maximum vertical deformation of 49.35 mm and a ductility coefficient of 5.61. The ultimate load-carrying capacity was 327.9 kN, which is 1.82 times the ultimate load of normal use. This indicates that the modular steel channel truss beam has a sufficient safety margin. When the modular beam was damaged, the tensile size under the beam in the middle of the span was only 5.98 mm, which accounted for just 11% of the vertical displacement in the same location. This is because all the members of the modular beam adopt channel steel, with a relatively small moment of inertia of the cross-section and a relatively large slenderness ratio. Its tensile strength is much greater than its compressive strength. Under the action of loads, it is prone to compressive failure. The load acts directly on the upper chord bar. The upper chord bar is vertically compressed, while the lower chord bar is horizontally tensioned. Consequently, the vertical deformation of the upper chord bar is much larger than the horizontal elongation dimension of the lower chord bar. Meanwhile, the high-strength bolts effectively connected and fastened the beam, limiting its deformation in the middle of the span. It is recommended to promote the use of high-strength bolt connections in actual engineering applications of assembled buildings.

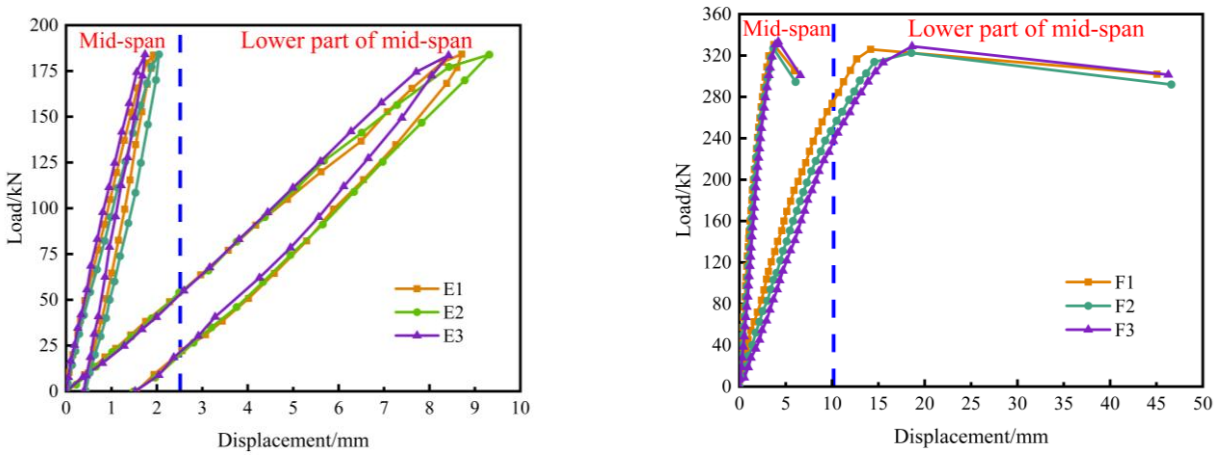

(a) Standard load effects (b) Over load effects

Fig. 11 Load-deflection curves in the mid-span

3.3. Load-displacement curve analysis

The load-displacement curves of the modular steel channel truss beam are shown in Fig. 11. It is not difficult to determine that the specimen is basically in the elastic working state during the standard load test, as the load-displacement relationship changes linearly. During the unloading process, the vertical displacement within the span and the tensile displacement beneath the beam of the specimen gradually decrease, while the slope of the load-deflection curve indicates a slow decrease. It indicates that the gap in the connection part of the specimen is not completely closed during the unloading process, which demonstrates its good energy absorption capacity and relatively ample safety margin.

From the analysis of Fig. 11, it can be seen that the specimen undergoes elastic and elastoplastic stages during the loading process of overload destructive tests. (1) Elastic Stage: At the beginning of loading, the relationship between load and displacement is linear. With the increase in load, the displacement gradually increases, and the standard load test is basically in the elastic-plastic stage. (2) Elastic-plastic stage: As the load is gradually increased to the ultimate load, the displacement growth rate accelerates. When the ultimate load is reached, the compression member of the modular steel channel truss beam undergoes buckling deformation. This results in a decrease in overall bearing capacity, as well as a significant increase in mid-span deflection and under-beam tensile displacement.

Under the same vertical load, the mid-span vertical displacement is much larger than the tensile displacement underneath the beam. Under the vertical load, the assembled main truss experiences the largest mid-span bending moment and deformation. During the overall stress analysis of the modular beam, the lower tensile displacement is relatively small, and the high-strength bolts exhibit good connection performance.

3.4. Load-strain curve analysis

Fig. 12 shows the load-strain curve of the modular beam. The measured strain is negative when the bar is compressed and positive when it is pulled during the test. Under eccentric load, the upper chord bar (where strain gauges 1 and 2 are located) is compressed, while the lower chord bar (where strain gauges 9 and 10 are located) is under tension. The diagonal web bar is under tension when inclined outward and under compression when inclined inward. The direction of the force of the vertical web bar is opposite to that of the diagonal web bar. The web bar inclined towards strain gauges 4, 6, and 7 is the tensile web bar, while the one inclined towards strain gauges 5 and 8 is the compressive web bar. The vertical web bar at the end of strain gauge 3 is under compression.

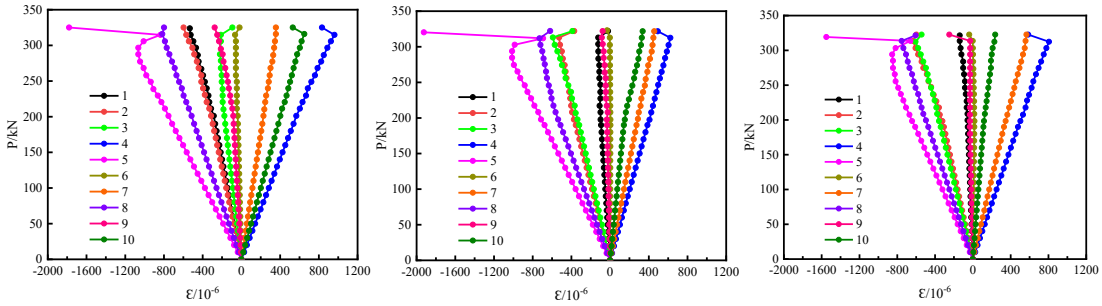

(a) Specimen F1 (b) Specimen F2 (c) Specimen F3

Fig. 12 Load-strain curves

By comparing and analyzing the load-strain curves in Fig. 13, it can be observed that the overall trend of the load-strain curves of the three specimens is essentially the same. During the entire loading process, the strains on the upper and lower chord bars are relatively small. The compressed diagonal web of strain gauge 5 is located at the eccentric loading point, where the strain growth rate is the largest. The strain growth rate of the tensile inclined web corresponding to strain gauge 4 is the second highest. During the overload destructive test, both the diagonal web bar of strain gauge 5 and the vertical web bar at the end of strain gauge 3 of the modular beam were damaged. Under the same load, the strain values of the compressed diagonal web bars were greater than those of the end vertical web bars. When the ultimate load was reached, both underwent abrupt changes. Therefore, under asymmetric loading, the compressed diagonal web buckled and was damaged before the end vertical web bar.

4. Parameter optimization and evaluation

In the overall stress process of the modular beam, the compressed diagonal web at the loading point is the first to reach the ultimate strength and damage. Therefore, the mechanical properties of the overall modular beam can be enhanced by strengthening the weak part. In order to investigate the main influencing factors of web size on the mechanical properties of the modular steel channel truss beam, the web thickness can be optimized. Except for the varying thickness of the compression-inclined web, all other parameters remain unchanged. The thickness (t) of the compression-inclined web is set at 4.5mm, 5mm, 5.5mm, 6mm, 6.5mm, and 7mm, respectively.

The load-displacement curves of modular beams with varying thicknesses of diagonal web bars are depicted in Fig. 13. As the thickness of the compression diagonal web increases, the stiffness and load-bearing capacity of the modular steel channel truss beam also increase, leading to a gradual reduction in mid-span deflection. When the thickness of the compression diagonal web is 5mm, the ultimate load-carrying capacity of the modular beam is 411.8 kN, which represents an increase of 16.59% compared to the initial value. When the thickness is 6mm and 7mm, the ultimate load capacity is 463.2kN and 472.2kN respectively, which is 31.14% and 33.69% higher than the initial value.

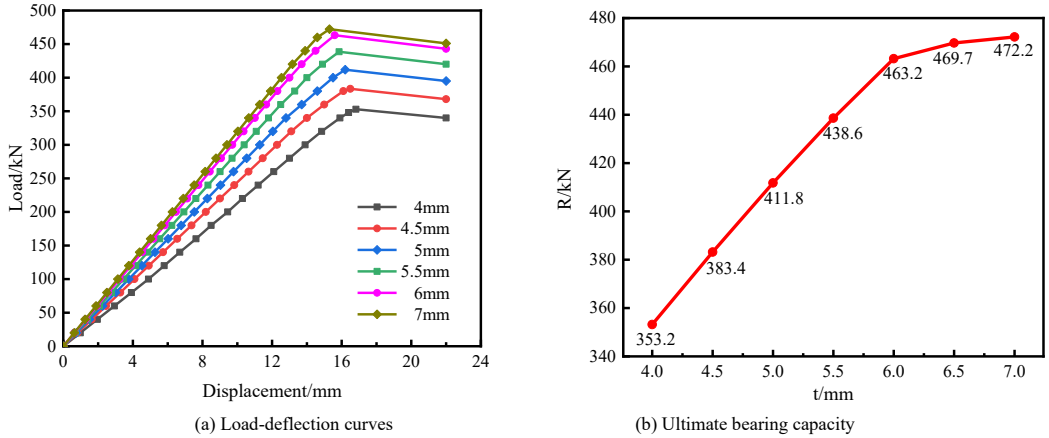

(a) Load-deflection curves (b) Ultimate bearing capacity

Fig. 13 Comparison of bearing capacity for different inclined web thicknesses

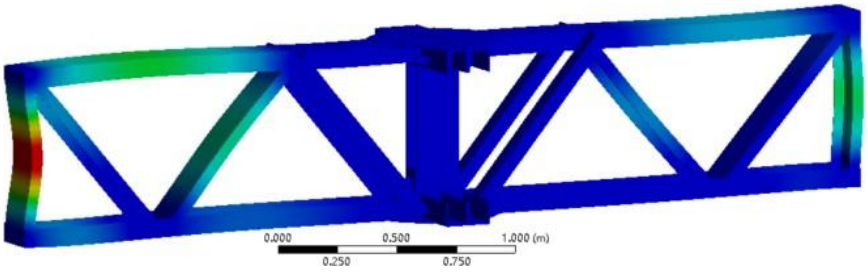

Fig. 14 Modular Beam Damage Patterns with compressive web thickness of 7mm

When the web thickness is less than 6mm, the ultimate load-carrying capacity of the modular beam is linearly related to the web thickness. With the gradual increase in the web thickness, the rise in the load-carrying capacity of the modular beam gradually diminishes. The ultimate load-carrying capacity of the compression-inclined web thickness increases from 6mm to 7mm by only 1.9%. When the thickness of the compressive web is 7 mm, the damage condition of the modular beam is shown in Fig. 14. At this time, the compressed vertical web at the end of the modular beam has priority over the compressed diagonal web and is subject to damage. However, the material properties of the compressed diagonal web are not fully utilized. When the thickness of the compressed inclined web exceeds 6 mm, the impact of increasing the web thickness on the load-carrying capacity of the modular beam is not significant. In order to fully utilize the material performance and achieve better economic outcomes, the thickness of the pressurized inclined web should be controlled in the structural design.

5. The bending capacity calculation of modular beams

5.1. Theoretical model

The stress distribution of modular beams is relatively complex in practical engineering. Therefore, it is common to assume that the stiffness and bearing capacity of each rod and connection in the modular beam are infinite. Without considering the effect of rod deformation on the bearing capacity of the modular steel channel truss beam, it is regarded as an ideal truss for simplified calculations. The simplified calculation model of the modular beam is shown in Fig. 15. By comparing and analyzing the test results and finite element simulation results of the modular beam, it can be observed that the compressed diagonal web bar is the weakest part of the modular beam. When the compressive web bar reaches the critical buckling load, the frame's modular beam is damaged as a whole. Therefore, the overall flexural load capacity of the modular beam can be calculated by inversely analyzing the ultimate load capacity of the stressed diagonal web bar. This calculation is of significant importance for the theoretical design of the modular beam.

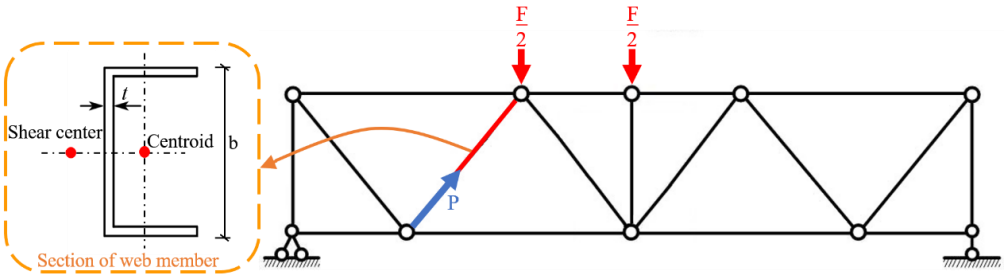

Fig. 15 Simplified computational model of modular beams

The modular steel channel truss beam with stressed diagonal web bars studied in this paper is a uniaxially symmetric channel. The shear center is located outside the back side of the channel, indicating that the axial pressure on the bar does not act on the shear center. When the bar is bent, torsional deformation occurs around the shear center, which is coupled with bending, resulting in bending and buckling of the bar. The critical load is less than both the bending critical load around the axis of symmetry and the pure torsional critical load.

The calculation of bending and torsional buckling is based on the principle of equal critical forces. This is achieved by converting it into bending and buckling of equivalent sections to determine the converted slenderness ratio. According to the Technical Specifications for Cold-Formed Thin-Walled Steel Structures, the stability coefficient is determined by meeting the requirements for bending buckling (axial compression bar). Additionally, the critical force for bending and twisting buckling is calculated. Formula (1) can be utilized to determine the critical buckling load of the compression diagonal web.

$$Pmax = \varphi A_e f \tag{1}$$

Conversion of length to slenderness ratio λ gets the length to slenderness ratio at its maximum value (maximum reduction degree), to wit:

$$\lambda = max\{\lambda_x,\ \lambda_y,\ \lambda_\omega\} \tag{2}$$

In the formula:λ_x ,λ_y is the length-to-finish ratio of the member to the x-axis and y-axis of the main axis of the cross-section;λ_ω is the converted length to slenderness ratio for bending and twisting flexure;

A_e is the effective cross-sectional area, The effective cross-sectional area is determined by first calculating the effective width of the compressed plate member using the effective width method.

$$b_e = \begin{cases} b_c & \dfrac{b}{t} \leqslant 18\alpha\rho \\ \left(\sqrt{\dfrac{21.8\alpha\rho}{b}} - 0.1\right) b_c & 18\alpha\rho < \dfrac{b}{t} < 38\alpha\rho \\ \dfrac{25\alpha\rho}{b} b_c & \dfrac{b}{t} \geqslant 38\alpha\rho \end{cases} \tag{3}$$

$$\alpha = 1.15 - 0.15\psi \tag{4}$$

$$\rho = \sqrt{205\frac{k_1 k}{\sigma_1}} \tag{5}$$

Where: b is the width of the plate; b_e is the effective width of the plate; ψ is the unevenness coefficient of compressive stress distribution; max compressive stress $\sigma_1 = \varphi f$; k is the coefficient of compressive stability of the plate; and k_1 is the plate group constraint coefficient.

In the simplified calculation model of the modular beam, the eccentric load F applied to the modular beam is calculated as 1.17 times of the axial force P of the compressed diagonal web bar using the structural mechanics solution. Therefore, the ultimate bending capacity $Fmax$ can be calculated according to formula (6).

$$Fmax = 1.17\varphi A_e f \tag{6}$$

5.2. Comparative analysis of theoretical and simulation results

Based on the results of the finite element analysis, it is evident that the compression-inclined web is the first part of the modular beam to sustain damage when its thickness is less than 6mm. Therefore, specimens with compression web thicknesses of 4mm, 4.5mm, 5mm, 5.5mm, and 6mm were selected for testing. The ultimate bending capacity ($Fmax$) was calculated and compared with the simulated ultimate bearing capacity (R) to draw valuable conclusions.

Table 2
Comparison of calculation and simulation results

No	t (mm)	$Fmax$ (kN)	R (kN)	$Fmax/R$	$(Fmax-R)/R$
1	4	363.9	353.2	1.03	3.03%
2	4.5	399.2	383.4	1.04	4.12%
3	5	430.5	411.8	1.05	4.54%
4	5.5	462.3	438.6	1.05	5.40%
5	6	495.3	463.2	1.07	6.93%
Mean				1.05	4.81%
Standard deviation				0.0146	0.0146

Table 2 shows that the calculated results of the compression-inclined web specimens with varying thicknesses closely align with the simulation results, with a ratio of 1.05, a standard deviation of 0.0146, and an average deviation amplitude of approximately 5%. It is concluded that the deviation rate tends to increase with the increase in web thickness. It is hypothesized that the error is due to the initial eccentricity of the modular beam under asymmetric loading. There appears to be a deviation between the calculated results based on the ideal articulated truss and the actual truss members. In addition, as the web thickness increases, the ultimate load capacity of the modular beam gradually rises, and the deformation of each member also increases. This aspect is neglected in the ideal modular beam model, leading to an increase in the deviation of the calculation results. Overall, the variance between the calculated and simulated results is relatively minor. It shows that the formula for the bending capacity of the modular beam, derived using the effective width method can be utilized in the design and calculation of new modular steel channel truss beams.

6. Conclusions

1. The new modular steel channel truss beam presented in this paper demonstrates improved bending resistance and toughness. The modular beam meets the normal use requirements stipulated in the code with high stiffness and low deformation. The results of the overload destructive test indicate that the ultimate bearing capacity exceeds the standard load by a factor of 1.82, while the ductility coefficient is 5.61, and the modular beam possesses a higher safety reserve capacity.

2. The shear performance of the high-strength bolt splicing node performs satisfactorily. While the new modular beam is damaged, the bending deformation of bolt rods and the slip of node splicing surface are not obvious. This indicates that using high-strength bolts for connections is relatively safe and enhances the modular beams' overall toughness. It is recommended to promote the application of high-strength bolt splicing nodes in practical projects.

3. According to the comparative analysis of the test and simulation results, the bending capacity of the modular beam depends on the critical load at which buckling damage occurs in the compressed diagonal web. On the premise of making full use of the material properties while taking economic factors into consideration, by increasing the thickness of the compressed diagonal web member from 4 mm to 6 mm, the ultimate bearing capacity of the new composite beam can be increased by 31.14%. This paper presents a formula for calculating the bending capacity of the new modular beam using the effective width method. The calculated results show a high level of concordance with the simulation results. The results can serve as a foundation for the structural, theoretical design, and practical engineering application of this new type of modular steel channel truss beam.

Acknowledgements

The authors would like to express heartfelt gratitude to the financial support by China Postdoctoral Science Foundation funded project (No. 2018M632805), Key scientific and technological project of Henan Province (No. 232102321066), Key scientific and technological project of Kaifeng City (No. 2303001).

References

[1] Li XJ, Xie WJ, Yang T, et al. Carbon emission evaluation of prefabricated concrete composite plates during the building materialization stage. Building and Environment, 2023, 232.110045. DOI:10.1016/j.buildenv.2023.110045.

[2] Khan K, Chen ZH, Liu JD, et al. State-of-the-Art on Technological Developments and Adaptability of Prefabricated Industrial Steel Buildings. Applied Sciences, 2023, 13(2): 685-685.

[3] Chen ZH, Khan K, Khan A, et al. Exploration of the multidirectional stability and response of prefabricated volumetric modular steel structures. Journal of Constructional Steel Research, 2021, 184.04022236. DOI:10.1061/JSENDH.STENG-11610.

[4] Simões SL, Silva LC, Tankova T, et al. Performance of modular hybrid cold-formed/tubular structural system. Structures, 2021, 30:1006-1019.

[5] Sangeetha P. Analytical Study on the Behaviour of Composite Space Truss Structures with Openings in a Concrete Slab. Civil and Environmental Engineering Reports, 2020, 30(3): 265-280.

[6] Liu ZH, Shu GP, Luo KR, et al. Performance of double-skin truss-reinforced composite wall under axial compression. Journal of Constructional Steel Research, 2023, 202.107778. DOI:10.1016/j.jcsr.2023.107778.

[7] Davis S, Stoddard E, Yarnold MT. Full-Scale Floor System Testing for Future Hot-Rolled Asymmetric Steel I-Beams. Journal of Structural Engineering, 2023, 149(2).04022236. DOI:10.1061/JSENDH.STENG-11610.

[8] Güldür H, Baran E, Topkaya C. Experimental and numerical analysis of cold-formed steel floor trusses with concrete filled compression chord. Engineering Structures, 2021, 234.111813. DOI:10.1016/j.engstruct.2020.111813.

[9] Leal L, Batista E. Experimental investigation of composite floor system with thin-walled steel trussed beams and partially prefabricated concrete slab. Const Steel Res, 2020, 172:106172. DOI:10.1016/j.jcsr.2020.106172.

[10] Chen Y, Quan CR, Feng L, et al. Experimental study on lightweight steel truss concrete slab. Building Science, 2020,36(01):54-60.

[11] Jia B, Ding J, Ding ZY, et al. Experimental Research on the Mechanical Behavior of Steel Frame Joints Using High-Strength Bolt Connection with Tapping Steel Plate. Progress in steel Building Structures, 2021,23(01):48-58.

[12] Bondok D, Salim H, Urgessa G. Quasi-static responses and associated failure mechanisms of cold-formed steel roof trusses. Engineering Structures, 2021, 231.111741. DOI:10.1016/j.engstruct.2020.111741.

[13] Abdallah E, El Aghoury Ihab, Mohamed IS, et al. Numerical investigation of branch plate-to-CHS connection under eccentric shear loading. Ain Shams Engineering Journal, 2023, 14(6).102139. DOI:10.1016/j.asej.2023.102139.

[14] Cao B, Zhu LF, Jiang XT, et al. An Investigation of Compression Bearing Capacity of Concrete-Filled Rectangular Stainless Steel Tubular Columns under Axial Load and Eccentric Axial Load. Sustainability, 2022, 14(14): 8946-8946.

[15] Wu CC, Fan FR, Cheng Z, et al. Behavior of steel reinforced UHPC-filled stainless steel tubular columns under eccentric loads. Journal of Constructional Steel Research, 2023,203.107806. DOI:10.1016/j.jcsr.2023.107806.

[16] Diao MZ, Guan H, Xue HZ, et al. Load-Resistant Mechanism and Failure Behaviour of RC Flat Plate Slab-Column Joints Under Concentric and Eccentric Loading. Springer Nature Singapore, 2023: 917-928.

[17] Yin LF, Niu Y, Quan G, et al. A numerical investigation of new types of bolted joints for cold-formed steel moment-resisting frame buildings. Journal of Building Engineering, 2023, 65.105738. DOI:10.1016/j.jobe.2022.105738.

[18] Guo XY, Amr R, Rahulreddy C, et al. Seismic Resistance of GFRP Bolted Joints with Carbon Nanotubes. Journal of Engineering Mechanics, 2018, 144(11): 04018106. DOI:10.1061/(ASCE)EM.1943-7889.0001528.

[19] Ashraf E, Tarek S, Salah N, et al. Behavior of extended end-plate bolted connections subjected to monotonic and cyclic loads. Engineering Structures, 2019, 190: 142-159.

[20] Wang ZQ, Xiong F, Chen J, et al. Experimental and Numerical Analyses on the Seismic Performance of a Novel Precast Concrete Column-column Joints with Bolted End-plate Connection. KSCE Journal of Civil Engineering, 2022, 26(11): 4746-4759.

[21] Tao YL, Chen XS, Liu XC. Seismic performance of CFST column bolted flange splice joints with connecting plates and rebar hooks. Engineering Structures, 2022, 267.114662. DOI：10.1016/j.engstruct.2022.114662.

[22] Fan SG, Xie SW, Wang K, et al. Seismic behaviour of novel self-tightening one-side bolted joints of prefabricated steel structures. Journal of Building Engineering, 2022, 56:104823. DOI：10.1016/j.jobe.2022.104823.

[23] Liu HL, Yang GY, Guo YJ, et al. Experimental Study on the Shear Deformation Characteristics and Mechanical Properties of Bolted Joints. International Journal of Geomechanics, 2023, 23(1). DOI:10.1061/(ASCE)GM.1943-5622.0002641.

[24] Zhang AL, Xie ZQ, Zhang YX, et al. Shaking table test of a prefabricated steel frame structure with all-bolted connections. Engineering Structures, 2021, 248. DOI:10.1016/j.engstruct.2021.113273.

[25] GB50018-2002 Technical code of cold-formed thin-wall steel structures. China Planning Press,

2002.
[26] Ministry of Construction of the People's Republic of China. Guide to the dimensions of main components for steel structure houses. China Construction Industry Press, 2021.
[27] Wang Y, Li T. Experimental and Numerical Investigation on Bending Capacity of Steel concrete Composite Truss Girder. The Open Civil Engineering Journal, 2015, 9(1): 943-949.
[28] Ma SC, Tan SL, Pan YH, et al. Experimental study on fiber-reinforced ceramsite concrete composite wall panel and correction of seismic damage model. Structures, 2024, 59: 105805.
[29] Liu WZ, Cui SQ. Experimental Study and Parametric Analysis on Flexural Performance of Bilateral Prestressed Composite Concrete Slabs with Steel Truss. Industrial Construction, 2021, 51(02):32-39+31.

Advanced Steel Construction – Vol. 21 No. 6 (2025) 551–560
DOI:10.18057/IJASC.2025.21.6.8

ESTIMATION OF DEFORMATION CAPACITY OF CIRCULAR HOLLOW SECTION BASED ON STRAIN

Heng-Li Fu [1, 2], Gan-Ping Shu [1, 2, *], Jin Zhang [3], Bao-Feng Zheng [1, 2], Li-Bo Wang [1, 2] and Zhan-Peng Chen [1, 2]

[1] *Key Laboratory of Concrete and Prestressed Concrete Structures of Ministry of Education, Southeast University, Nanjing 210096, China*
[2] *School of Civil Engineering, Southeast University, Nanjing 210096, China*
[3] *ARTS Group Co., Ltd., Suzhou 215123, China*
** (Corresponding author: E-mail: shuganping@seu.edu.cn)*

ABSTRACT

The deformation evaluation of steel members is an important part of the performance-based seismic design of steel structures. The strain-based deformation capacity is not susceptible to load and boundary conditions, and can directly reflect the ductility of the component. According to the mechanical properties of steel circular hollow section (CHS) beam-columns in engineering structures, this paper proposes a strain-based ductility coefficient derived from the equivalent plastic zone to estimate their deformation capacity. Six typical circular hollow section steel components were subjected to quasi-static tests, with different diameter-to-thickness ratio and axial compression ratio as the test parameters. Based on the experimental results, a validated and reliable finite element model was established to analyze the effects of various factors on the strain ductility coefficient of steel circular hollow sections under quasi-static loading. The results indicated that the strain ductility coefficient decreased with increasing diameter-to-thickness ratio and axial compression ratio. A recommended empirical formula for the strain ductility coefficient of circular hollow section beam-columns was proposed using regression analysis. The empirical formula has high accuracy, serving as a reference for promoting the application of performance-based seismic design in steel structures.

ARTICLE HISTORY

Received: 21 April 2025
Revised: 21 May 2025
Accepted: 26 May 2025

KEYWORDS

Quasi-static test;
Circular hollow section;
Strain ductility coefficient;
Performance-based seismic design

1. Introduction

In the past few decades, the focus of seismic design has shifted from "strength" to "performance" [1]. Performance-based seismic design is currently a hot topic in structural seismic research. Deformation is an important indicator for measuring structural performance levels, and the current performance-based design theory primarily emphasizes nonlinear deformation at both the structural and component levels. Circular hollow sections are commonly used as the main structural members due to their advantages such as high strength-to-weight ratio, excellent seismic performance, ease of construction, and controllable quality [2].Therefore, it is essential to accurately estimate their deformation capacity to ensure a rational seismic design of the overall structure.

Performance-based seismic design for engineering structures was first proposed by scholars from the United States and Japan in the 1990s [3]. In Japan, JACI 2000 defines performance objectives, explicitly specifying the performance standards that different types of buildings should achieve under earthquake action. It also sets different seismic performance targets for buildings based on varying levels of seismic intensity. The concept of performance-based seismic design was first formally introduced in the United States in 1995 through the publication of the document Vision 2000, which laid the foundation for the development of performance-based design methodologies [4]. FEMA 273 [5] was the first performance-based seismic design code, mainly outlining seismic performance objectives, performance classification, and design methods. In 2010, the United States issued the document TBI-2010 High-Rise Building Performance-Based Seismic Design Guidelines [6], a new performance-based seismic design method that provides clear performance evaluation criteria for the whole structure and its structural components. The structural design standards such as FEMA 356 [7], ASCE 41-13 [8] and ASCE 41-17 [9] also explain performance-based design. For the performance-based seismic design of steel structures, Chinese standards, Standard for design of steel structures (GB 50017-2017) [10] and Code for seismic design of buildings (GB/T 50011-2010) [11], provide relevant provisions. However, these codes primarily rely on load-bearing capacity checks and construction detailing requirements, without specifying deformation limits for different performance levels.

In recent years, extensive research has been carried out by scholars worldwide on the seismic behavior of structural members. Fan et al. [12] conducted static tests on three steel tubular columns with low axial compression ratios, mainly to investigate the effects of diameter-to-thickness ratio and axial compression ratio on the deformation performance of steel tubular columns. Xin et al. [13]conducted experimental and numerical investigations into the global buckling behaviour of circular hollow section (CHS) beam-columns fabricated from both normal and high strength structural steels, and proposed improved stability design approaches. Zheng et al. [14]conducted a study on the seismic behaviour of hot-rolled stainless steel circular hollow section (CHS) beam-columns. Their experimental findings revealed that these members primarily failed through local buckling at the ends, and demonstrated good seismic performance owing to the inherent ductility of stainless steel. Xing et al. [15]investigated the hysteretic performance of circular hollow section (CHS) steel members subjected to cyclic axial loads and lateral displacements. The results showed that, compared to tension-dominated members, those under various levels of compressive force exhibited more pronounced global deformations. Wang et al. [16] used finite element method to study the hysteretic properties such as ultimate bearing capacity, ductility coefficient and energy dissipation coefficient of circular steel pipe members to provide a basis for failure mechanism analysis of large-span space structures under seismic action. Mohamed Elchalakani et al. [17] conducted cyclic bending tests on cold-formed round tubes, mainly to investigate the effect of diameter-to-thickness and length-to-finish ratios on the ductility of the members and to derive the limiting values of length-to-finish ratios of the members applied to seismic design. Guo et al. [18] investigated the seismic performance of steel circular hollow section after being subjected to lateral impact loading, the test results showed that the impact height had a negative effect on the deformation capacity of steel circular hollow sections and proposed a simplified hysteresis model considering the effects of a combination of impact height and axial horizontal loading. Fang et al. [19] conducted an experimental study on the seismic performance of elliptical circular hollow section columns to investigate the effects of different tube thicknesses, axial compression ratios, and bending directions on the damage pattern, yield strength, and ductility of the members. Zhang et al. [20] proposed the use of strain-based ductility indices to enhance the applicability of the fiber model and developed an empirical formula for the strain ductility of H-shaped sections. At present, there are few studies on the deformation capacity of circular hollow section under different axial compression ratios.

In structural elastoplastic analysis, beam-column members are typically modeled using plastic hinge or fiber-based approaches. The deformation indices, rotation angle (θ) and curvature (φ), are primarily applied in the plastic hinge model. Meanwhile, for beam-column members, it is challenging to define the moment-rotation relationship while considering the coupling effect of moment and axial force. On the other hand, strain indices are more applicable to the fiber model. The yield strain (ε_y) is solely dependent on the material properties and is not influenced by the geometric characteristics of the member or loading boundary conditions. In elastoplastic analysis, the material strain response in the fiber model can be directly obtained. Therefore, evaluating the performance of steel members based on strain indices offers high applicability and convenience. At present, there are few studies on circular hollow sections based on deformation capacity under various axial pressure ratios. Therefore, a systematic study on the ductility of circular hollow sections is of reference

significance for improving the seismic performance-based evaluation criteria.

2. Experimental programme

2.1. Design principles

Steel frame is the most common steel structure system in engineering applications, which is mainly composed of frame columns and frame beams. Fig. 1 shows the stress form of typical steel frame under in-plane bending moment. The main mechanical characteristics of the frame column can be equivalent to the cantilever column component intercepted from the inflection point to the fixed end. Therefore, the cantilever column component is taken as the test component in this paper.

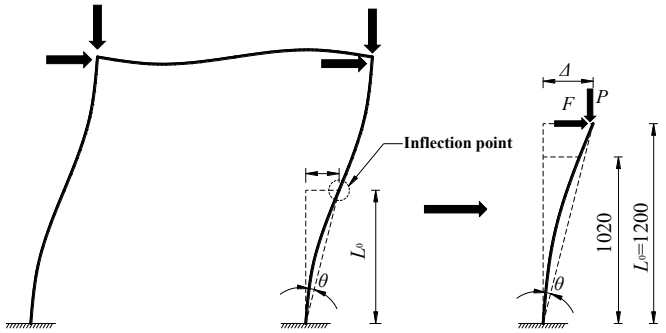

Fig. 1 typical steel frame and column equivalent cantilever members

2.2. Description of the components

Six Q355 circular hollow section components were tested under a combination of vertical load and cyclic horizontal displacement. The cross-section grades of the components in this study cover common engineering types, corresponding to cross-section grades 1 to 4 specified in the Chinese standard GB50017-2017 [10]. These grades are mainly determined by steel type and diameter-thickness ratio. In addition, axial compression ratios of 0.2, 0.4, and 0.6 were set to examine the effects of different axial compression ratios on the behavior of circular hollow sections. The nominal cross-sectional dimensions $D \times t$ (D and t represent the diameter and thickness of the CHS component, respectively) of the CHS component are 219 × 8, 219 × 6, 219 × 4 and 219 × 3.5. Due to the uncommon sizes of 219 × 4 and 219 × 3.5 circular hollow sections, this batch of CHS component was obtained by machining 219 × 6 the CHS component. The dimensions of each component are shown in Table 1. The cross-sectional schematic is shown in Fig. 2. The component labels in Table 1 consist of three parts, with the first part "S1", "S2", "S3", and "S4" representing cross-section grade 1, cross-section grade 2, cross-section grade 3, and cross-section grade 4, respectively. The "219 × 8" in the second part represents the nominal diameter and nominal thickness of the component section. The numbers "0.2", "0.4", and "0.6" in the third part represent different axial compression ratios n ($n=P/Af_y$), where P is the constant axial load applied and A is the measured cross-sectional area, f_y is the yield stress of steel. The fourth part represents the loading mode, where "C" represents loop loading. For example, component S1-219 × 8-0.2-C represents a circular hollow section with a cross-sectional grade of 1, a cross-sectional diameter of 219mm, a thickness of 8mm, and an axial compression ratio of 0.2, subjected to cyclic loading.

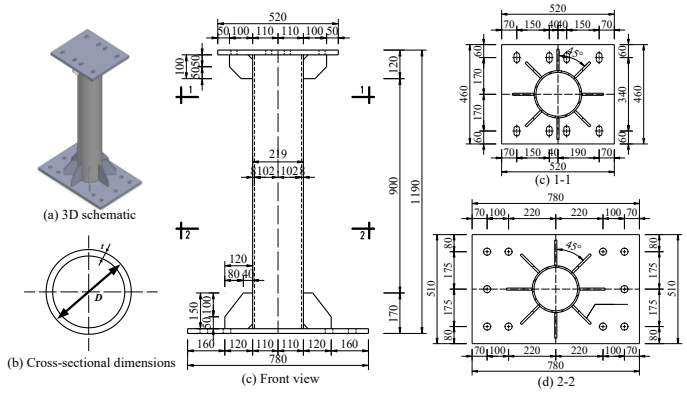

Fig. 2 Details of test component A-C-219×8-0.2 (unit: mm)

Table 1
Main design parameters of test components

Component number	Grade	D(mm)	t(mm)	n	D/t	Cross-section Grade
A-C-219×8-0.2	355	219	8	0.2	27.375	S1
A-C-219×8-0.4	355	219	8	0.4	27.375	S1
A-C-219×8-0.6	355	219	8	0.6	27.375	S1
A-C-219×6-0.2	355	219	6	0.2	36.5	S2
A-C-219×4-0.2	355	219	4	0.2	54.75	S3
A-C-219×3.5-0.2	355	219	3.5	0.2	63	S4

In order to avoid the influence of weld seams and enable more direct observation of the failure modes and deformation capacity of circular steel members, seamless round steel pipes were used for all components in this study. For better mechanical performance and installation reliability, 20 mm thick end plates were attached to both ends of the circular hollow section by welding. Stiffening ribs were welded at 45-degree intervals at both ends of the component to enhance its stiffness and prevent end failure during the loading process. It is worth noting that all stiffeners are made of the same steel as the component. The dimensions and parameters of the component are detailed in Fig. 2.

2.3. Material tests

The material properties of the CHS component were obtained through tensile testing. The test components were made from seamless round steel pipes with four different thicknesses: 8.00 mm, 6.00 mm, 4.00 mm, and 3.50 mm. Therefore, 12 samples with varying thicknesses were cut along the rolling direction from the same batch of plates as the loaded components. The tensile tests were executed according to GB/T 228.1 [21]. The length of the 8.00 mm components was 250 mm, while the lengths of the 6.00 mm, 4.00 mm, and 3.50 mm components were 240 mm. The experiments were conducted using an MTS testing machine, and deformation was recorded with a 50 mm extensometer. The loading rate was initially set to 0.5 mm/min until the strain reached 2.5%. After this, the loading rate was increased to 2 mm/min until the components fractured. Table 2 summarizes the average results of the material performance parameters, where t represents the thickness of the component, f_y is the yield strength, f_u is the ultimate tensile strength, E is the Young's modulus and e is the elongation rate.

Table 2
Material properties

Grade	t(mm)	fy (MPa)	fu (MPa)	E (GPa)	e
355	8	371.04	546.29	192.85	31
355	6	361.68	547.61	229.23	31
355	4	375.31	573.60	234.21	25
355	3.5	377.01	567.08	227.212	29

2.4. Geometric imperfection measurement

Initial geometric defects are commonly present in round steel pipes during the manufacturing process, which can influence the test results. Therefore, this study employed laser scanning technology to measure the initial geometric defects of the components [22]. Prior to scanning, marker spots were applied to the component surface. A handheld laser scanner was used to measure the 3D profile of the outer surface, recording point clouds at different scanning positions. The scanning data was then fed back to a computer to create a real-time model of the point cloud, with a measurement accuracy of 0.01 mm, as shown in Fig. 3.

The measurement results of each sample indicate that the defect amplitude varies slightly for each cross-section and height. Select five different cross-sections 150mm above the stiffening ribs at the bottom of the sample, with an interval of 150mm between each cross-section for analysis, and select 200 data points for each cross-section to form the curve shown in Fig. 4. The outer surface contour distribution of cross-sections A-C-219 × 8, A-C-219 × 6, A-C-219 × 4, and A-C-219 × 3.5 is shown in Fig. 5. The consistent results indicate that each cross-section has two radius peaks, which means the cross-section is approximately elliptical. Local defects in each component are strictly controlled within 1/200 of the diameter, meeting the requirements of GB 50205-2020 [23].

Fig. 3 Laser scanner test

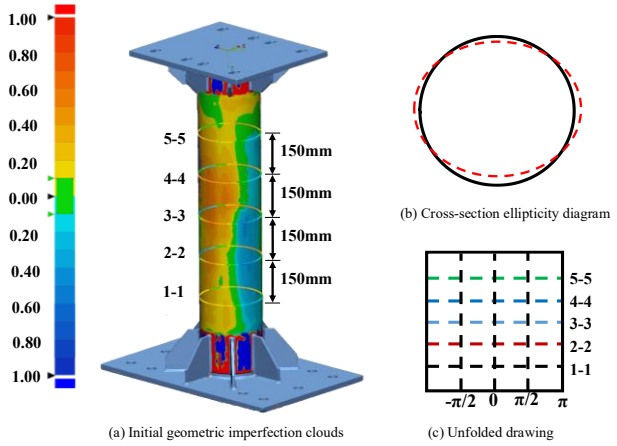

(a) Initial geometric imperfection clouds (b) Cross-section ellipticity diagram (c) Unfolded drawing

Fig. 4 Component imperfection distribution

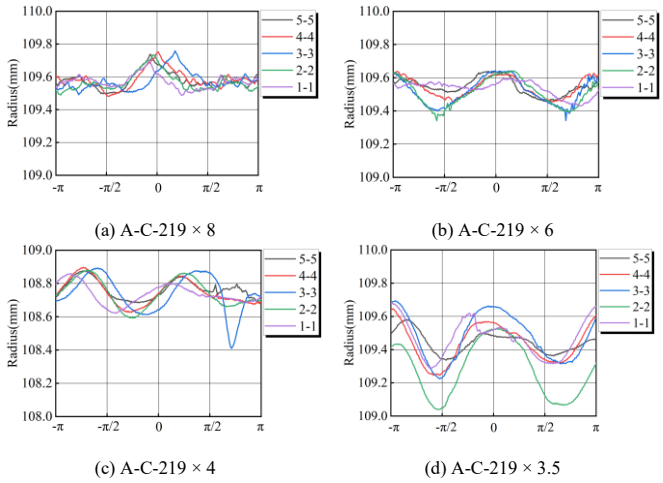

(a) A-C-219 × 8 (b) A-C-219 × 6

(c) A-C-219 × 4 (d) A-C-219 × 3.5

Fig. 5 Distribution of outer-surface curves of components

2.5. Test setup

The experimental loading device is shown in Fig. 6, which is used for quasi-static testing of steel components. The bottom of the component is fixed to the base using M30 high-strength bolts, while the top is connected to the loading beam via a connector and pin shaft. Additionally, the experimental device is equipped with a four-bar linkage to constrain the outer surface of the component, ensuring that there is no out of plane displacement during the loading process. During the experiment, a 1000kN hydraulic jack was first used at the top to apply axial force. After maintaining stability, the MTS electro-hydraulic servo actuator (maximum load of 500kN) was used to drive the distribution beam to apply horizontal load until the experiment was stopped.

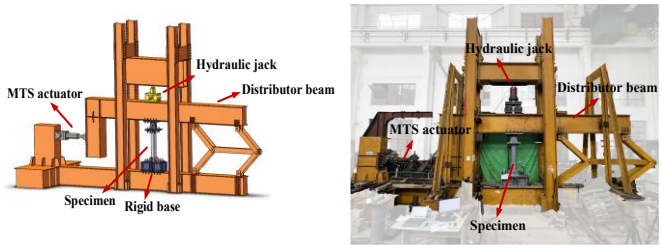

(a) Schematic diagram (b) Photo of the site layout

Fig. 6 Test setup

Several sensors were employed in the experimental setup. The constant axial force was applied and monitored using a hydraulic jack, while the lateral force was measured by an MTS hydraulic actuator. As shown in Fig. 7(a), nine linear variable displacement sensors were installed to monitor the displacement response throughout the testing period. D1 and D2 were used to measure the horizontal displacement within the top plane of the column; D3 monitored the horizontal displacement outside the top plane of the column; D4 measured the horizontal displacement within the column plane; D5 monitored the horizontal displacement outside the column plane; D6 measured the horizontal slip within the base plane of the column; D7 monitored the horizontal slip outside the column base plane; and D8 and D9 were used to monitor the rotation of the column base.

As shown in Fig. 7(b)(c), a series of strain gauges were installed, and Digital Image Correlation (DIC) non-contact measurement technology was used to track the deformation response during the test. This method was primarily employed to determine the bottom bulge and the height of the equivalent plastic zone of the column.

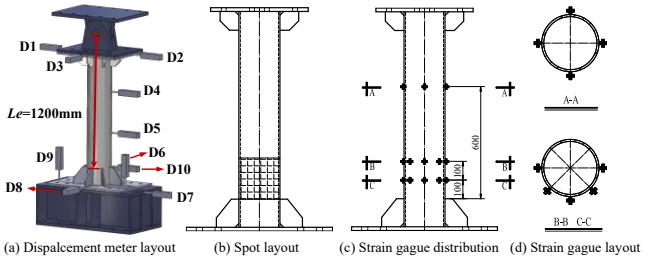

(a) Dispalcement meter layout (b) Spot layout (c) Strain gague distribution (d) Strain gague layout

Fig. 7 Component measurement programme

2.6. Loading protocol

The cyclic tests followed the non-uniform cyclic loading protocol outlined in ANSI/AISC 341 [24], using a quasi-static drift angle θ control. As illustrated in Fig. 9, the drift angle was calculated as $\theta = \Delta/L_e$, where Δ represents the horizontal displacement at the top of the component, and L_e denotes its effective length. The drift angle loading sequence included 0.375%, 0.50%, 0.75%, 1.0%, 1.5%, and 2.0%. Specifically, drift angles of 0.375%, 0.50%, and 0.75% were applied for six cycles each, while the 1.0% drift angle was applied for four cycles. For the remaining drift levels, two cycles were applied per level, with the drift angle increasing by 1.0% every two cycles thereafter, as illustrated in Fig. 10. To manage the overall test duration, different displacement rates were adopted: a rate of 0.2 mm/s was used when Δ equaled 0.00375 L_e; for displacements below 0.03 L_e, a rate of 0.5 mm/s was applied; and for values exceeding 0.03 L_e, the rate was increased to 1 mm/s. Both monotonic and cyclic loading processes continued until either distinct local buckling developed at the specimen's base or a sudden decline was detected in the load-displacement response.

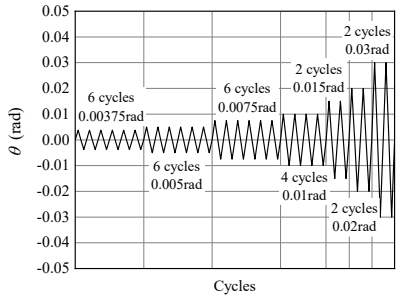

Fig. 8 Cyclic loading protocol

3. Test results

3.1. Experimental phenomena

The deformation development and failure phenomena of each component are similar. Six steel circular hollow sections undergo three stages of elasticity, elastoplasticity and failure in constant axial compression and low-cycle repeated tests. The final failure mode is shown in Fig. 9. Taking the typical component A-C-219×4-0.2 as an example, the test process and phenomenon are described in detail.

In the early stage of loading, before the drift angle reached 0.015, the transverse and longitudinal strain values of the circular hollow section were small, and the component exhibited no apparent phenomena (Fig. 10a). When the drift angle reached 0.015, slight bulging appeared on the right side of the component (Fig. 10b). As the drift angle increased to 0.02, buckling in the right compression zone became more pronounced. When the drift angle reached 0.03, annular deformation occurred, and the steel circular hollow section experienced severe buckling. When the drift angle reached 0.04, the circular hollow section deformed excessively, and the accumulated residual deformation led to a 'lantern'-shaped buckling. The component underwent significant plastic deformation, its load-bearing capacity was greatly reduced, and the test was completed.

Fig. 9 Final failure mode of the component

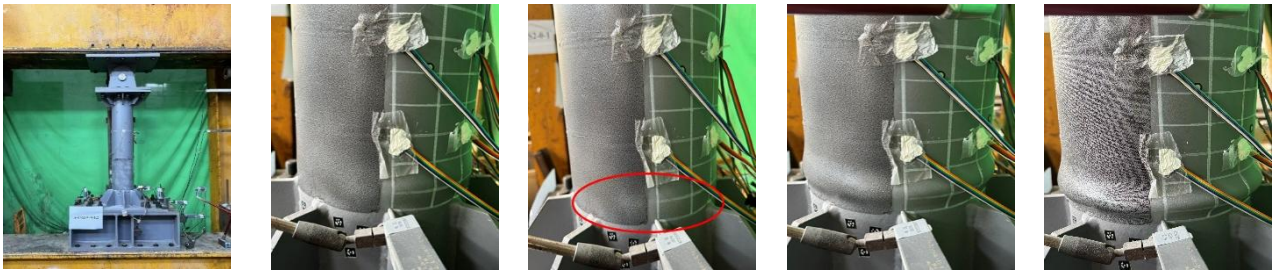

(a) Initial stage of test (b) $\theta = 0.015$ (c) $\theta = 0.02$ (d) $\theta = 0.03$ (e) $\theta = 0.04$

Fig. 10 Process of component failure

(a) A-C-219×8-0.2 (b) A-C-219×8-0.4 (c) A-C-219×8-0.6

(d) A-C-219×6-0.2 (e) A-C-219×4-0.2 (f) A-C-219×3.5-0.2

Fig. 11 Failure mode of test piece

The final failure mode of each component was shown in Fig. 11. Each component behaved similarly to the typical specimen A-C-219×4-0.2. Local buckling occurred at the end of the component, forming a ring-like buckling of the circular hollow section and resulting in large plastic deformation. However, components A-C-219×8-0.2 and A-C-219×8-0.4 exhibited tearing and cracking of the circular hollow section near the stiffener. Since the stiffener was directly welded onto the circular hollow section, the component was relatively weak at the welding location. In the middle and late stages of loading, the upper portion of the steel circular hollow section near the stiffener tore or cracked, leading to the termination of the test. However, the failure of the components occurred after reaching the ultimate bearing capacity, and was not caused by a decrease in bearing capacity due to weld crack.

3.2. Hysteretic responses

The hysteretic behavior of a structural component under cyclic loading reflects its deformation characteristics during repeated loading, which is typically represented by the moment–drift angle curve. The total bending moment M comprises a first-order moment M_1, induced by the applied lateral force, and a second-order moment M_2, resulting from the axial load acting on the lateral displacement at the column top. The moment-rotation hysteresis curve of the circular steel circular hollow section component under cyclic loading is shown in Fig. 12, where the abscissa is the drift angle of the loading part of the component, and the ordinate is the bending moment applied to the component. By comparing the hysteresis curves and characteristics of each component, the following conclusions can be drawn : 1) The hysteresis curves of each component show a relatively full spindle shape and have good energy dissipation capacity. 2) Each component experiences elastic stage, yield stage and failure stage. 3) After the peak load, the bearing capacity of each component did not decrease sharply, showing the characteristics of ductile failure. 4) With the increase of axial compression ratio, the hysteresis curve area of the component decreases and the energy dissipation capacity decreases. 5) Under the coaxial pressure ratio, the drift angle of local buckling of the component with cross-section grade S1 is larger than that of the component with cross-section grade S2, and presents a certain rule. Therefore, with the increase of the diameter-thickness ratio, the local buckling of the component occurs earlier.

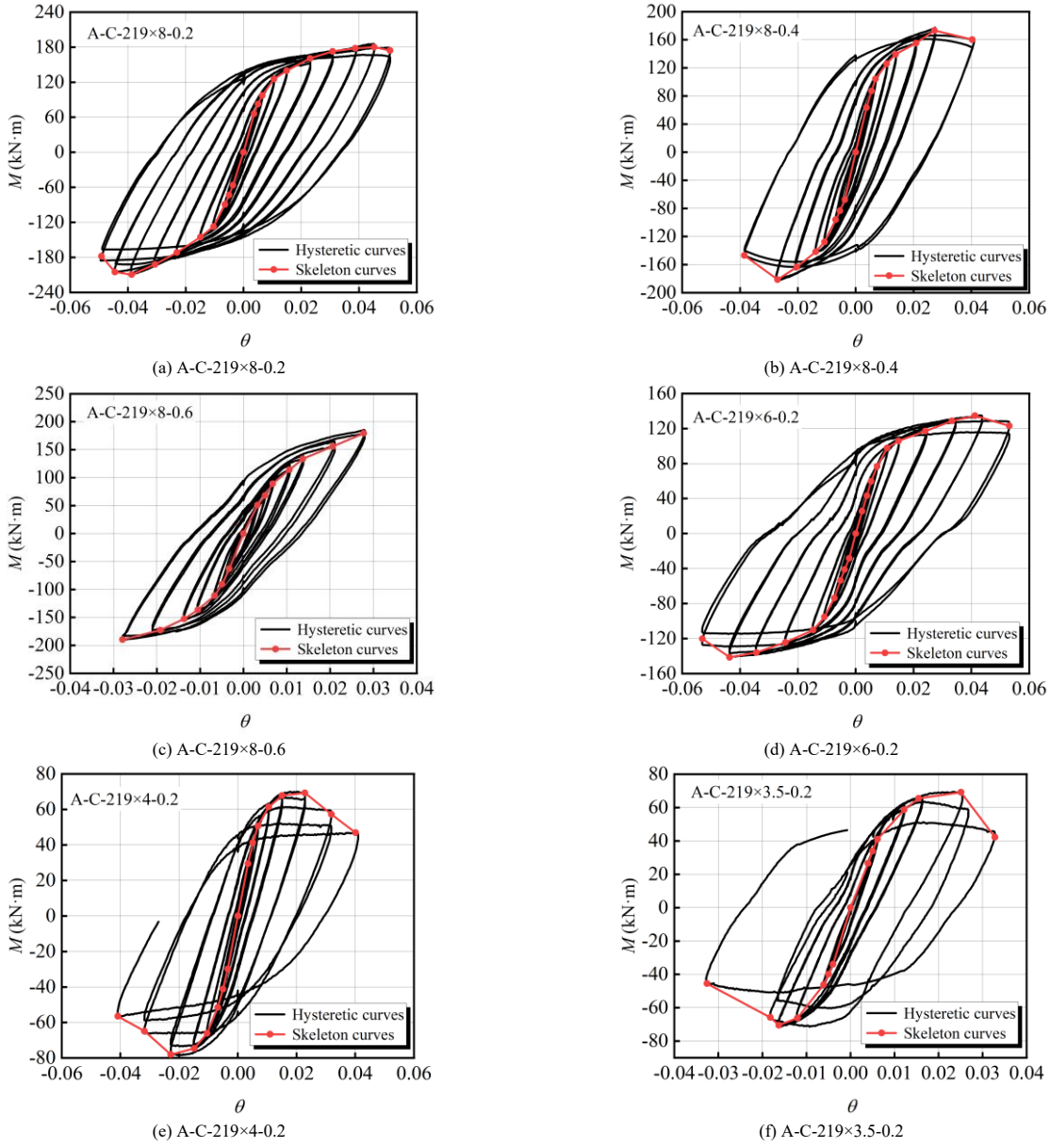

(a) A-C-219×8-0.2 (b) A-C-219×8-0.4

(c) A-C-219×8-0.6 (d) A-C-219×6-0.2

(e) A-C-219×4-0.2 (f) A-C-219×3.5-0.2

Fig. 12 Hysteretic loops and skeleton curves of components

3.2.1. Measurement of plastic zone length

The distance from the peak or trough of the member's buckling waveform to the root of the member is defined as half of the equivalent plastic zone length. The Digital Image Correlation (DIC) technique can accurately measure the component plastic zone length L_h [25]. According to the theory of elasticity [26], the flexural half-wave length of a circular pipe section is the distance from the crest to the trough of the wave, which is calculated by the formula (1), which can be approximated as half of the equivalent plastic zone length of a circular pipe section, i.e., $L_h/2$.

DIC technology can record the deformation development of the component in real time, and the corresponding local buckling length in the limit state is taken as the equivalent plastic zone length L_h of the component. Taking the component A-C-219×4-0.2 as an example, the plastic zone length L_h is accurately measured in the data processing software, as shown in Fig. 15. The measured value of the component and the approximate value calculated by Eq. (1) are listed in Table 3. It can be seen that the calculated value of the formula is close to the measured value.

The Digital Image Correlation (DIC) technique enables real-time recording of the deformation evolution of test components. Taking component A-C-219×4-0.2 as an example, L_h was accurately measured using the data processing software as illustrated in Fig. 15. The measured values of the components, along with the approximate values calculated using Eq. (1), are listed in Table 3. It can be observed that the calculated results show good agreement with the experimental measurements.

$$L_{cr}=1.72\sqrt{(R-\frac{t}{2})t} \quad (1)$$

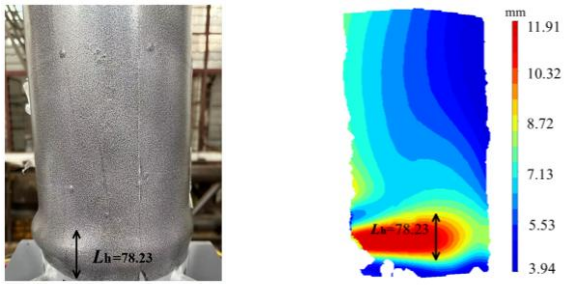

Fig. 13 Measurement of L_h for test component A-C-219×4-0.2

Table 3
Equivalent plastic zone length

Component number	Measured value	Formula value	Error
A-C-219×8-0.2	110.33	99.92	9.41%
A-C-219×8-0.4	110.25	99.92	9.32%
A-C-219×8-0.6	110.36	99.92	9.4%
A-C-219×6-0.2	85.33	88.34	3.56%
A-C-219×4-0.2	78.23	71.32	8.85%
A-C-219×3.5-0.2	65.62	66.80	1.83%

4. Definition of strain ductility coefficient

4.1. Equivalent plastic zone

The experiment shows that the region near the maximum bending moment of the steel member with circular pipe section is also the concentrated area of plastic and local buckling deformation of the member. Based on the stress characteristics of cantilever members, the area of local instability is defined as the 'equivalent plastic zone ' [27], and the following assumptions are made when defining the equivalent plastic energy consumption area [28]:

(1) The curvature is assumed to be constant throughout the equivalent plastic zone and the bending moment is taken as the maximum value occurring within this zone;

(2) Ignore the shear deformation in the equivalent plastic zone of the flexural members [29];

(3) The flexural member is divided into elastic section and equivalent plastic zone. The local buckling of the members occurs in the equivalent plastic zone, and the elastic segment remains elastic throughout the loading process;

(4) No overall bending torsional instability of members

4.2. Curvature of equivalent plastic zone

According to the assumptions (3) and (4) in Section 4.1, the total horizontal displacement of the cantilever member Δ is composed of the horizontal displacement of the elastic section Δ_{es} and the deformation of the equivalent plastic zone Δ_h. As shown in Fig. 14, the deformation of the equivalent plastic zone consists of the deflection deformation Δ_{h1}, the rotational deformation of equivalent plastic zone Δ_{h2} and the shear deformation of the equivalent plastic zone Δ_{h3}. Since the shear deformation of the equivalent plastic zone is small, the shear deformation of the equivalent plastic zone Δ_{h3} is ignored according to assumption (2) in section 4.1.

$$\Delta = \Delta_{es}+\Delta_{h1}+\Delta_{h2}+\Delta_{h3} \quad (2)$$

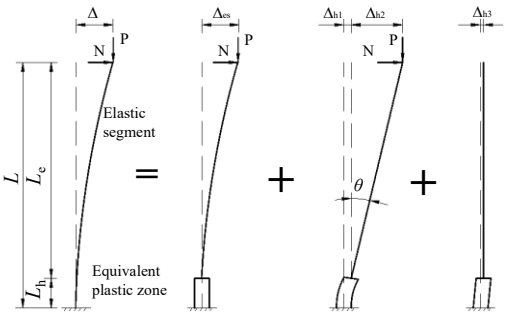

Fig. 14 Decomposition diagram of component deformation

The horizontal displacement of the elastic segment is calculated in Eq. (3). The notation used in this equation is as follows: Δ_f and Δ_s represent the elastic bending deformation and shear deformation of the elastic segment of the cantilever component; F is the lateral load at the top of the cantilever component; E and G are the elastic modulus and shear modulus of the steel material, respectively; I is the moment of inertia of the cross-section of the cantilever component; A is the cross-sectional area of the cantilever component; L_e is the length of the elastic segment; κ is the coefficient of shear stress non-uniformity, with a typical value of 10/9 for circular hollow section cross-sections [30].

$$\Delta_{es} = \Delta_f + \Delta_s = \frac{FL_e^3}{3EI} + \frac{FL_e}{\kappa GA} \quad (3)$$

Based on assumption (1) in section 4.1, it is assumed that the curvature of the section is uniform in the equivalent plastic zone. Therefore, the average curvature of the equivalent plastic zone is expressed by Eq. (4), where R is the radius of curvature of the plastic energy plastic zone.

$$\varphi = \frac{1}{R} \quad (4)$$

According to the schematic diagram, the calculation formula of bending deformation in the equivalent plastic zone of the member is given by Eq. (5), where θ is the section angle at the end of the plastic zone. When θ is small, Eq. (5) can be simplified as Eq. (6). In Eq. (6), L_h is the length of equivalent plastic zone.

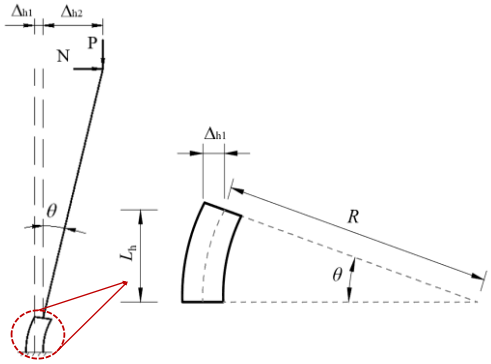

Fig. 15 Calculation diagram

$$\Delta_{h1} = R(1-\cos\theta) = 2R\sin^2\frac{\theta}{2} \quad (5)$$

$$\Delta_{h1} \approx 2R\left(\frac{\theta}{2}\right)^2 = \frac{R\theta^2}{2} = \frac{L_h^2}{2}\varphi \quad (6)$$

The deformation Δ_{h2} induced by the rotation of the equivalent plastic energy is given by Eq. (7). By substituting Δ_{h1} and Δ_{h2} into Eq. (1), the formula for the equivalent plastic zone curvature is derived as Eq. (8).

$$\Delta_{h2} = \theta L_e = \varphi L_h L_e \quad (7)$$

$$\varphi = \frac{\Delta-\Delta_{es}}{L_eL_h + L_h^2/2} = \frac{\Delta-\Delta_{es}}{(L-L_h/2)L_h} \quad (8)$$

Where Δ_{es} is the horizontal displacement of the elastic section, which can be directly calculated based on elastic theory, and Δ is the horizontal displacement at the loading point of the member, which can be directly extracted from the calculation results of the cantilever member. Therefore, the average curvature of the equivalent plastic zone can be determined using the equivalent plastic length L_h, the total horizontal displacement of the member Δ, and the horizontal displacement of the elastic section Δ_{es}.

4.3. Equivalent strain

According to the assumption that the section curvature in the equivalent plastic zone is equal, the strain in the equivalent plastic zone can be calculated by Eq. (9).

$$\varepsilon_{max} = \varepsilon_0 + \varepsilon_f = n\varepsilon_y + \frac{\varphi h}{2} \quad (9)$$

The notation used in this equation is as follows: ε_0 is the strain caused by axial pressure, ε_f is the section edge strain caused by bending, n is the axial compression ratio, ε_y is the yield strain, and h is the section height. Therefore, the effect of the ultimate deformation of the member is changed into Eq. (10).

$$\varepsilon_u = n\varepsilon_y + \frac{\varphi_u h}{2} \quad (10)$$

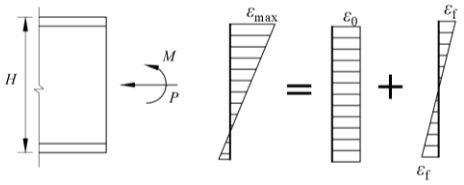

Fig. 16 Equivalent strain in the plastic zone

4.4. Strain ductility coefficient

In reference [18], the ratio of the strain corresponding to the reduction of the ultimate load of the member to 85 % to the strain corresponding to the yield of the section edge of the member is defined as the ' strain ductility coefficient ' [31]. The strain ductility coefficient can directly represent the plastic deformation development ability of the component. In the equation of strain ductility coefficient (11), ε_y is the strain corresponding to the yield of the section edge of the member and ε_u is the ultimate strain of the section. In this paper, ε_u is defined as the strain in the plastic zone corresponding to the 15% reduction of the peak load [32].Where Δ_{es} denotes the horizontal displacement of the elastic section and it can be calculated using equation(2); where Δ is obtained from loading tests; L_h can be approximated by Eq. (1); L denotes the member length and h represents the diameter of the circular cross-section.

$$\mu_\varepsilon = \frac{\varepsilon_u - \varepsilon_y}{\varepsilon_y} \quad (11)$$

$$\mu_\varepsilon = \frac{2(n-1)\varepsilon_y + \frac{(\Delta - \Delta_{es})h}{(L - L_h/2)L_h}}{\varepsilon_y} \quad (12)$$

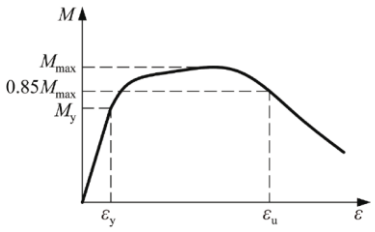

Fig. 17 Ultimate deformation of components

5. Numerical modeling

5.1. Establishment of finite element models

The finite element model of the component was established by ABAQUS. The ' S4R ' shell element had been widely used to simulate the cross-section members under various loading conditions. Therefore, the S4R shell element was used for the steel circular hollow section components and stiffeners in this paper. A mesh sensitivity analysis was first conducted with mesh sizes of 15 mm, 10 mm, and 5 mm. The results indicate that: (i) the 15 mm mesh significantly improved computational efficiency but led to reduced accuracy, with deviations exceeding 3% compared to the 10 mm mesh; (ii) the 5 mm mesh yielded results that were in close agreement with those of the 10 mm mesh, with average discrepancies within 1%. Considering both computational efficiency and accuracy, a mesh size of 10 mm was ultimately selected for subsequent analyses [33]. The bottom and top of the model were coupled to points RP2 and RP1 respectively, which had been successfully applied in Ref. [34]. Fixed boundary conditions were applied at the bottom of the model, while the top was constrained against out-of-plane displacement and rotation. The vertical pressure and reciprocating horizontal displacement were applied at the centroid point RP1. The loading system was described in the previous chapter. The same axial pressure as the test is used in the calculation and analysis.

The steel constitutive model used in the parametric analysis adopted a nonlinear combined hardening material model. The key parameters were taken from Ref. [35], as shown in Table 2. For the verification model, the elastic modulus and yield strength of the steel were determined based on the test results in Table 4.The first-order buckling mode obtained from the eigenvalue analysis was applied to the model as the initial geometric imperfection. For the local initial geometric defects of the verification model, the measured values of the 3D-scanned components were used. For the model of parametric analysis, the maximum value of local initial geometric defects was taken as 1/10 of the wall thickness [22].

Table 4
Basic parameters of the cyclic material model adopted in the FE modelling

Grade	$\sigma_{\|0}$ (MPa)	E (MPa)	C_1 (MPa)	γ_1	C_2 (MPa)	γ_2	C_3 (MPa)	γ_3	C_4 (MPa)	γ_4
Q355	355	206000	7993	175	6773	116	2136	34	1450	29

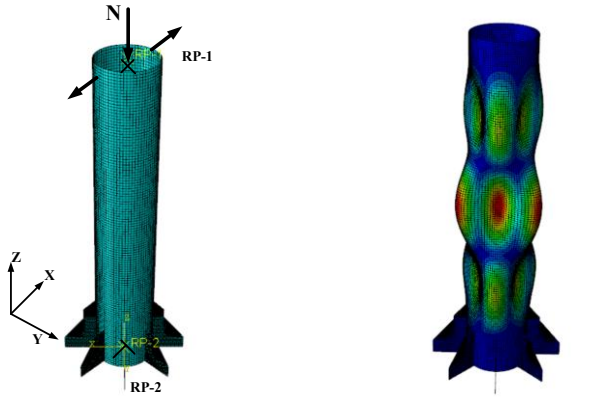

(a) FE model (b) Local buckling mode

Fig.18 Finite element model

5.2. Finite element model validation

The FE model was verified based on the experimental results of 6 components. Fig. 19 shows the failure mode of the component A-C-219×6-0.2 from both the finite element model and the test components, as well as the deformation corresponding to the plastic zone length at the same time. It was observed that the finite element model accurately simulated the local buckling at the bottom of the component and other components exhibited similar failure phenomena which were consistent with the test results. Fig. 20 shows the comparison of the bending-drift angle curve and the skeleton curve of the six component tests and the FE model. The results indicated that the shapes of the skeleton curve of the ultimate bending moment of the test and the finite element simulations were basically the same and matched well. In general, the established finite element model accurately reproduced the mechanical behavior of the circular steel circular hollow sections under cyclic loading and was suitable for subsequent parametric analysis.

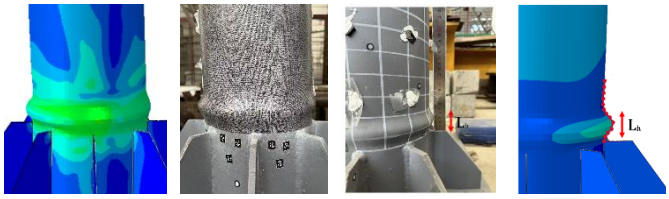

(a) FE failure mode (b) Experimental failure mode (c) Component plastic zone length (d) FE plastic zone length

Fig. 19 Comparison between finite element method and experiment

6. Analysis of parametric analysis results

6.1. Parametric study

The parameter study of the verified finite element model was conducted to expand the database, considering the diameter-thickness ratio, axial compression ratio, and loading system of compression-bending members as the main factors. For the model used for parameter analysis, the elastic modulus of steel is E = 206 kN / mm, the yield strength of steel is f_y = 355 MPa, and the Poisson 's ratio is v = 0.3. The diameter-thickness ratio of steel members with circular hollow section ranges from 20 to 66, with a total of 8 different groups of values designed. The axial compression ratios are 0.2, 0.3, 0.4, 0.5, and 0.6, with 5 different groups of values. The materials considered are primarily Q355. For modeling convenience, the length of the members is set to 1200 mm, with boundary conditions and the loading system identical to those of the previously verified finite element model.

6.2. Analysis of factors influencing the strain ductility coefficient

The parametric analysis provided the basis for calculating key limit state parameters, including total displacement and plastic zone length. The strain ductility coefficient of each component is then calculated according to the definition of the strain ductility coefficient, and the effects of different factors are analysed.

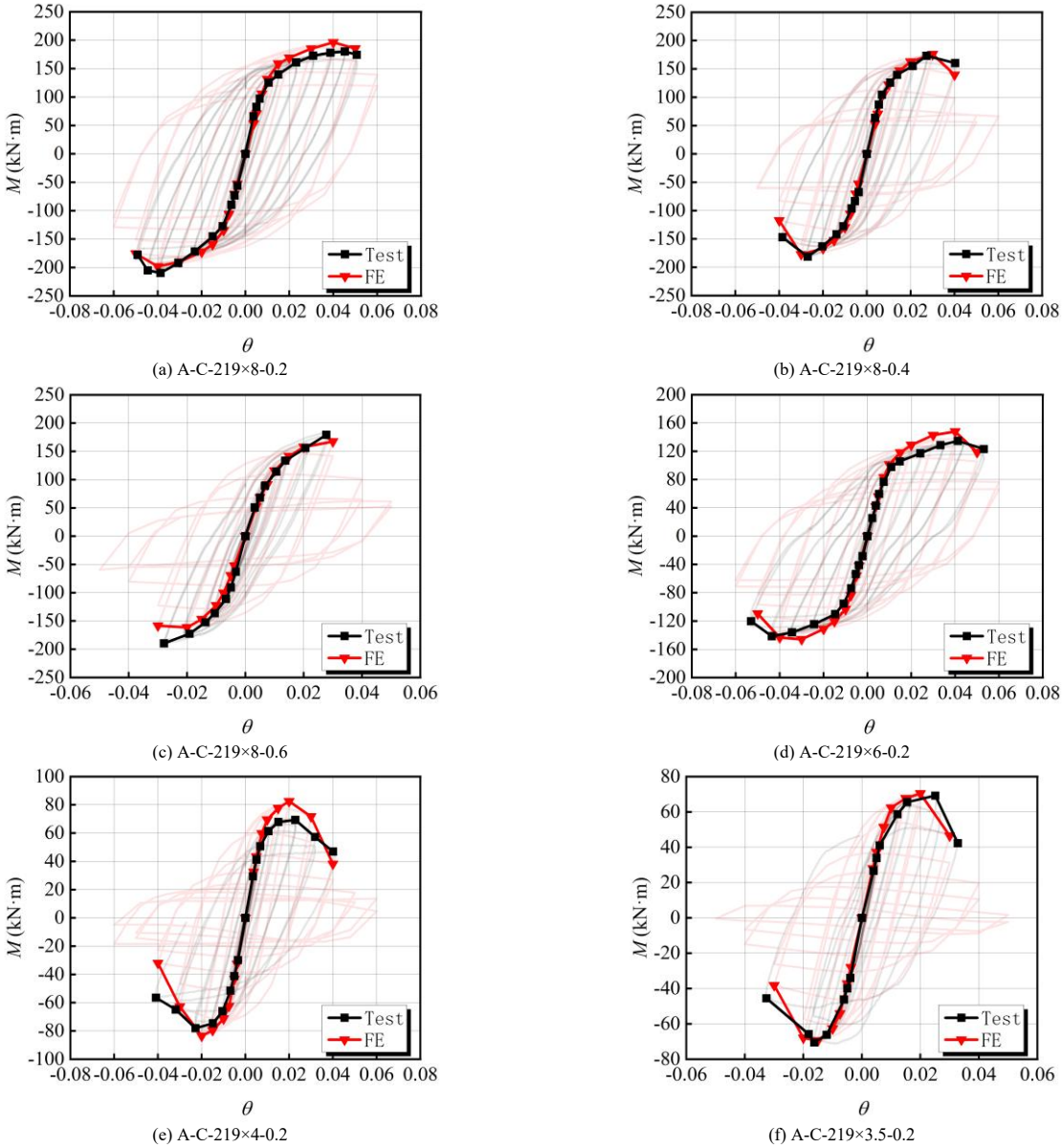

(a) A-C-219×8-0.2 (b) A-C-219×8-0.4

(c) A-C-219×8-0.6 (d) A-C-219×6-0.2

(e) A-C-219×4-0.2 (f) A-C-219×3.5-0.2

Fig. 20 Comparison of hysteresis curve and skeleton curve between experimental and finite element simulation

6.2.1. Impact of loading protocol

The deformation capacity of circular section members under two loading systems was investigated using finite element simulations. These two loading protocols are symmetrical cyclic loading protocol and collapse-consistent loading protocol. The symmetrically cyclic loading protocol, which corresponds to the experimental procedure described above, is a commonly used method in the seismic performance evaluation of structural components. The collapse-consistent loading protocol was proposed by LIGNOS in 2014 [36]. The collapse-consistent loading protocol inserts a large one-way push-over displacement between several elastic-plastic loading cycles, which is considered to be more in line with the characteristics of seismic action.

The bending moment-displacement curves of circular section steel members with axial compression ratio of 0.2 section under collapse-consistent loading protocol and symmetrically cyclic loading protocol are compared, as shown in Fig. 21. The symmetrically cyclic loading protocol is usually more unfavorable than the earthquake action, and the collapse-consistent loading protocol can be regarded as a typical seismic wave as a disordered loading system. Table 5 is the comparison of strain ductility coefficient of the components under the two loading protocols. The analysis results indicate that:(1) The strain ductility coefficient under the collapse-consistent loading protocol are consistently higher than those obtained under symmetrically cyclic loading protocol;(2) The rate of strength degradation after the component reaches its peak load under the collapse-consistent loading protocol is significantly lower than that under symmetrically cyclic loading protocol;(3) For components with the same diameter-to-thickness ratio, a higher axial compression ratio leads to a larger difference in strain ductility coefficient between the two loading protocols. Since structural components were more vulnerable under symmetric cyclic loading, only symmetric cyclic loading was adopted in the subsequent parametric analyses.

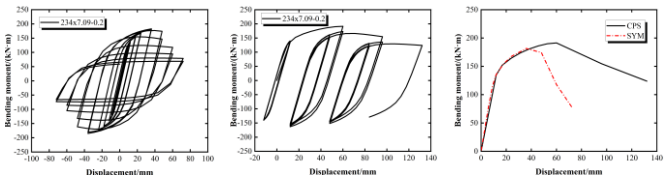

(a) Symmetrically cyclic loading protocol n-0.2 (a) Collapse-consistent loading protocol n-0.2 (c) Skeleton curve comparison n-0.2

Fig. 21 Comparison of bending moment-displacement curves under different loading protocols

6.2.2. Effect of diameter-thickness ratio

Fig. 21 shows the distribution of strain ductility coefficients of models with different diameter-to-thickness ratios under horizontal reciprocating loads. It shows that the diameter-to-thickness ratio of the circular cross-section steel members has a significant effect on the strain ductility coefficient. Generally, as the diameter-to-thickness ratio increases, the strain ductility coefficient of the model decreases.

Table 5

Comparison of strain ductility coefficient of components under different loading protocols

Component number	Collapse-consistent loading protocol	Symmetrically cyclic loading protocol	Ratio
234x7.09-0.2	48.13	25.45	1.89
234x7.09-0.4	37.4	18.08	2.06
234x7.09-0.6	32.26	9.85	3.27
234x5.08-0.2	35.79	22.4	1.59
234x5.08-0.4	23.54	13.41	1.75
234x5.08-0.6	17.29	8.4	2.05
234x3.96-0.2	25.92	17.87	1.45
234x3.96-0.4	17.16	10.35	1.65
234x3.96-0.6	10.37	5.62	1.84
234x3.54-0.2	21.72	17.2	1.26
234x3.54-0.4	14.74	10.61	1.38
234x3.54-0.6	7.46	5.23	1.42

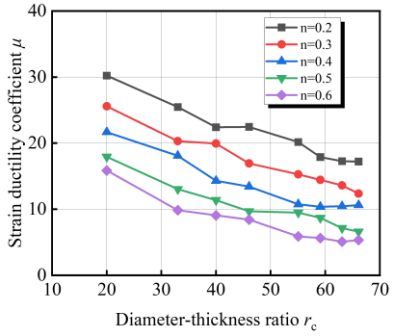

Fig. 22 Influence of diameter to thickness ratio

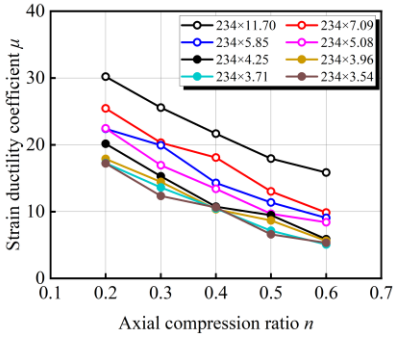

Fig. 23 Effect of axial compression ratio

6.2.3. Effect of axial compression ratio

The variation of the strain ductility coefficient of circular cross-section steel members under horizontal cyclic loading with axial compression ratios of 0.2, 0.3, 0.4, 0.5, and 0.6 is shown in the Fig. 22. As shown in Fig. 22, the strain ductility coefficient of the compression-bending circular cross-section steel members decreases as the axial compression ratio increases.

6.2.4. Empirical formula for strain ductility factor

The analysis of the results indicates that for compression-bending members, both the diameter-to-thickness ratio and the axial compression ratio of the component section are important factors affecting the strain ductility coefficient of the compression-bending steel members. Among them, the axial compression ratio is negatively correlated with the strain ductility coefficient and the diameter-thickness ratio of the member is inversely correlated with the strain ductility coefficient. Therefore, the functional relationship of the strain ductility coefficient of steel members with circular hollow section is shown in the following equation (13).

$$\mu_{fc} = \frac{a}{r_c} + b r_c^{c} (1 - kn)^{d} \quad (13)$$

Where r_c (r_c=D/t)is the diameter-to-thickness ratio, n is the axial pressure ratio, and a, b, c, and d are constants to be determined. Based on the regression analysis of the parameter analysis results in this study, the values of the aforementioned constants can be determined. The empirical formula for calculating the strain ductility coefficient of Q355 members is given as follows:

$$\mu_{fc} = \frac{300}{r_c} + 50 r_c^{-0.2} (1 - 1.4n)^{1.6} \quad (14)$$

Fig. 24 shows the comparison between the calculated and experimental values of the test members obtained according to the strain ductility coefficient empirical formula. The experimental value is the result of the test of six specimens according to the formula (14) in section 4.3 ; the calculated value is the result of fitting according to formula 14. It can be seen that the calculated values have a high degree of agreement with the tested and simulated values. Therefore, the strain ductility coefficient formula can be reliably used to predict the strain-based deformation capacity of circular cross-section steel members.

Since the 219×3.5 circular hollow section was fabricated from 219×6 circular circular hollow section, manufacturing deviations resulted in an actual wall thickness smaller than the design thickness. Consequently, the obtained strain ductility coefficients was relatively low, leading to a higher relative error.

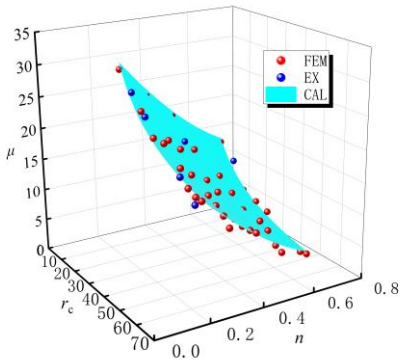

Fig. 24 Comparison of calculated strain ductility coefficient values with simulated and experimental values

Table 6

Comparison between experimental and calculated values of strain ductility coefficient

Component number	Experimental value	Calculated value	Error
A-C-219×8-0.2	27.57	26.20	4.96%
A-C-219×8-0.4	18.55	17.89	3.55%
A-C-219×8-0.6	13.77	12.33	10.45%
A-C-219×6-0.2	24.90	22.98	7.71%
A-C-219×4-0.2	18.84	18.75	0.47%
A-C-219×3.5-0.2	16.08	17.72	10.19%

7. Conclusion

This paper proposes a strain ductility coefficient based on the equivalent plastic zone to evaluate the deformation of circular hollow section steel components. The effects of different parameters on the strain ductility coefficient are investigated by conducting low circumferential reciprocating tests and finite element analysis. Based on the research results, this paper proposes an empirical formula for the strain ductility coefficient. The main conclusions are as follows:

(1) For circular hollow section steel members with different diameter-to-thickness ratios, local buckling occurs at the bottom under cyclic loading. According to the principle of equal total deformation of members, the strain-based ductility coefficient is proposed to provide a theoretical basis for evaluating the deformation capacity of members.

(2) According to the test and finite element result, the ultimate strain and strain ductility coefficient of the circular cross-section steel member decreases with the increase of the member diameter-to-thickness ratio and axial pressure ratio.

(3) Based on the finite element and experimental results, this paper proposes a suggested empirical formula for the strain ductility coefficient. The empirical formula is accurate and effective, as demonstrated by comparisons with experimental data and finite element (FE) results, with a maximum error not exceeding 15%.

It is important to note that the experimental program in this study was conducted using steel with a nominal yield strength of 355 MPa. Moreover, the proposed Equation (14) does not account for the influence of different steel strength grades. As the strength of steel increases, a reduction in ductility is typically observed. To enhance the applicability and generalization of the proposed equation and conclusions, further investigations are required to incorporate the effect of steel strength and develop appropriate modifications. In addition, the present study is focused on circular steel members governed by a local buckling failure mode. Other potential failure mechanisms, such as shear failure, global instability, and fatigue damage, involve distinct deformation characteristics and failure mechanisms, and they are not within the scope of the conclusions of this study.

References

[1] M.J. Priestley, Performance based seismic design. In: 12th World Conferences on Earthquake Engineering, 2000, pp. 2831-2852.

[2] M. Elchalakani, X.L. Zhao, R.H. Grzebieta, Plastic mechanism analysis of circular tubes under pure bending, International Journal of Mechanical Sciences 2002;44:1117–1143.

[3] Dalal Sejal P, Vasanwala, Desai A K, Performance based seismic design of structure: A review. International journal of civil and structural engineering 2011;1:795-803.

[4] SEAOC. A framework for performance-based engineering: Vision 2000. California: Structural Engineering Association of California, 1995.

[5] FEMA-273 Nehrp guidelines for the seismic rehabilitation of buildings. Washnigton, DC: Federal Emergency Management Agency; 1997.

[6] TBI Guidelines Working Group. Guidelines for performance-based seismic design of tall buildings. California, peer report: Pacific Earthquake Engineering Research Center; 2010.

[7] FEMA 356. FEMA-356 Prestandard and Commentary for the Seismic Rehabilitation of Buildings. Washnigton, DC: Federal Emergency Management Agency; 2000.

[8] ASCE 41-13. ASCE41–13 Seismic Evaluation and Retrofit of Existing Buildings. Reston, VA: American Society of Civil Engineers; 2014.

[9] ASCE 41-17. Seismic Evaluation and Retrofit of Existing Buildings. Reston, Virginia: American Society of Civil Engineers, Ed.; American Society of Civil Engineers; 2017.

[10] GB 50017—2017. Standard for design of steel structures. Beijing: China Architecture & Building Press; 2018 [in Chinese].

[11] GB 50011-2010. Code for seismic design of buildings. Beijing: China Architecture & Building Press; 2018 [in Chinese].

[12] Fan Zhong, Chai huijuan, Chen Yuchen, et al. Deformation Performance of Steel Pipe Columns. Journal of Tianjin University(Science and Technology) 2021;54:133-143 [in Chinese].

[13] X. Meng, L. Gardner, Stability and design of normal and high strength steel CHS beam-columns, Engineering Structures 251 (2021) 113361.

[14] B. Zheng, Z. Chen, J. Yao, H. Fu, L. Wang, G. Shu, Tests on seismic performance of hot-rolled stainless steel circular hollow section beam-columns, Structures 74 (2025) 108611.

[15] J. Xing, Y. Tian, Q. Yang, Y. Huang, G. Xu, Hysteretic performance of CHS steel members under cyclically fluctuating axial loads and lateral displacement, Engineering Structures 199 (2019) 109602.

[16] Wang kaifei, Shaofangfang, et al. Research on hysteretic behavior of steel circular-tube members under constant compression and cyclic bending. Journal of Building Structures 2010;31:35-38 [in Chinese].

[17] M. Elchalakani, X.-L. Zhao, R. Grzebieta, Cyclic bending tests to determine fully ductile section slenderness limits for Cold-Formed circular hollow sections, Journal of Structural Engineering 130 (2004) 1001–1010.

[18] Z. Guo, J. Yang, Z. Li, Y. Chen, Experimental investigation on hysteretic behavior of circular hollow steel tubular columns after lateral impacts, Engineering Structures 232 (2021) 111861.

[19] C. Fang, F. Wang, C. Wang, Y. Zheng, Cyclic behavior of oval hollow section (OHS) beam-columns, Thin-Walled Structures 161 (2021) 107430.

[20] J. Zhang, G.-P. Shu, D. Yang, L.-L. Yang, Estimation of deformation capacity of steel beam-columns based on strain ductility coefficient, Structures 46 (2022) 1517–1531.

[21] GB/T 228.1-2021. Metallic materials-Tensile testing-Part 1:Method of test at room temperature. Beijing: China Standards Press; 2021 [in Chinese]

[22] Xu Y, Wu B, Zheng B. Full-field geometric imperfection and effect on cross-section capacity of circular steel tubes. J Construction Steel Res 2023;201:107749.

[23] GB 50205-2020. Standard for acceptance of construction quality of steel structures. Beijing: China Planning Press; 2020 [in Chinese].

[24] American Institute of Steel Construction (ANS//AISC), ANS/AISC 341-16. Seismic Provisions for Structural Steel Buildings, Illinois, USA, 2016.

[25] K. Wei, F. Yuan, X. Shao, Z. Chen, G. Wu, X. He, High-speed multi-camera 3D DIC measurement of the deformation of cassette structure with large shaking table, Mechanical Systems and Signal Processing 177 (2022) 109273.

[26] Timoshenko S, Gere J. Theory of elastic stability (International student edition). McGREW - Hill international book company; 1963.

[27] X. Cheng, D. Duan, A. Ali, Y. Chen, Constitutive model for thin-walled H-sections bent about weak-axis considering local buckling, Structures 25 (2020) 56–71.

[28] X. Cheng, Chen yiyi, Hinge zone model of H-section steel members and hinge zone length. journal of tongji university 2016;44: 677-684 [in Chinese].

[29] X. Cheng, Cross-section Classification and Hysteretic Behavior of Non-plastic-hinge H-section Steel Beam-columns. Tongji University Press;2017.

[30] Shi Binghua, Common formulas for calculating the non-uniformity coefficient of shear stress distribution in typical cross-sections, Journal of Building Structures 1984;66-69[in Chinese].

[31] Jin Zhang, Research and application of performance-based seismic design method and performance evaluation criteria for multistory steel structures. Nanjing: Southeast university; 2023 [in Chinese].

[32] JGJ 101—2015. Specification for seismic test of buildings. Beijing: China Architecture & Building Press; 2015 [in Chinese].

[33] Y. Wu, S. Fan, H. Zhou, Y. Guo, Q. Wu, Cyclic behaviour of diagonally stiffened stainless steel plate shear walls with two-side connections: Experiment, simulation and design, Engineering Structures 268 (2022) 114756.

[34] Chen, B. Zheng, G. Shu, Classification criteria for austenitic stainless steel H-section under cyclic loading about major-axis, Journal of Constructional Steel Research 214 (2024) 108460.

[35] Shi Y, Wang M, Wang Y. Experimental study of structural steel constitutive relationship under cyclic loading. J Build Mater 2012;15:293–300 [in Chinese].

[36] Suzuki Y, Lignos DG. Development of loading protocols for experimental testing of steel columns subjected to combined high axial load and lateral drift demands near collapse. Proc., 10th National Conf. on earthquake engineering. Anchorage, AK: Earthquake Engineering Research Institute; 2014.